UNIVERSITAT POLITÈCNICA
DE CATALUNYA
BARCELONATECH

Real-time solutions of parametric thermo-hydro-mechanical problems with proper generalized decomposition

Arash Moaven

Real-time solutions of parametric Thermo-Hydro-Mechanical problems with Proper Generalized Decomposition

By

Arash Moaven

Supervisors:

Prof. Sergio Zlotnik

Prof. Thierry J. Massart

A thesis submitted to the

Universidad Politécnica de Cataluña

And

Université libre de Bruxelles

In partial fulfillment of the requirements for the degree of Doctor in Engineering Sciences

Barcelona, 31st of May 2023

“ Beginning to think is beginning to be undermined. ”

Albert Camus

Abstract

Real-time solutions of parametric Thermo-Hydro-Mechanical problems with Proper Generalized Decomposition

Arash Moaven

The Proper Generalized Decomposition (PGD) is a mathematical framework belonging to the Model Order Reduction (MOR) class of techniques. To the best of the author's knowledge, this methodology has not been applied to transient coupled Thermo-Hydro-Mechanical (THM) problems in porous media. THM models have been developed for various geo-environmental applications, such as enhanced oil recovery, geothermal energy extraction, and deep geological repositories. This thesis studies the application of the PGD technique to THM problems, drawing inspiration from the concept of deep geological repositories. The study demonstrates how the PGD methodology can be used to obtain real-time solutions to THM problems, using a simplified deep geological repository as an example.

The developed generalized solutions provided by PGD are perfectly suited to be used in multi-query situations, such as parameter identification and calibration procedures, optimization, or uncertainty quantification. The extremely fast response obtained after the training phase opens the doors to real-time inversions, control situations, or simply increasing the accuracy of the inverse identification procedures by allowing a much larger number of evaluations of the objective function when compared to traditional discretization techniques.

This work presents two main contributions. First, it provides a detailed description of the separated discrete operators that are required in the PGD methodology when material parameters, geometrical parameters, or a combination of both are considered. This is done in the context of transient coupled THM problems. Second, the study investigates several configurations related to the use of the PGD methodology in the context of coupled problems and transient problems.

Two models of a simplified deep geological repository problem are presented to show the capabilities of the proposed methodology. The first one is parametrized by the physical properties of the host rock (elastic modulus, thermal conductivity, hydraulic conductivity). This would be useful, for example, in the solution of an inverse problem to characterize the actual properties of the rock. The second model addresses a geometrical parametrization that controls the distance between the canisters when

the repository is set to a grid canister. This is intended for the development useful to study and design the repository and to determine, for example, an optimal distance avoiding temperature runouts.

The study as a whole employs a combination of techniques (PGD with the modeling of coupled THM processes in porous media) to produce a range of solutions and an efficient solver that functions in real-time.

Acknowledgments

As a conscious being, I am keenly aware that my current state is intertwined with both the past and the future, driven by my dreams and motivations. The profound influence of my experiences and environment has shaped my internal perceptions since birth. The presence of others exerts a powerful force, serving as motivation and propelling me forward to fulfill my endeavors.

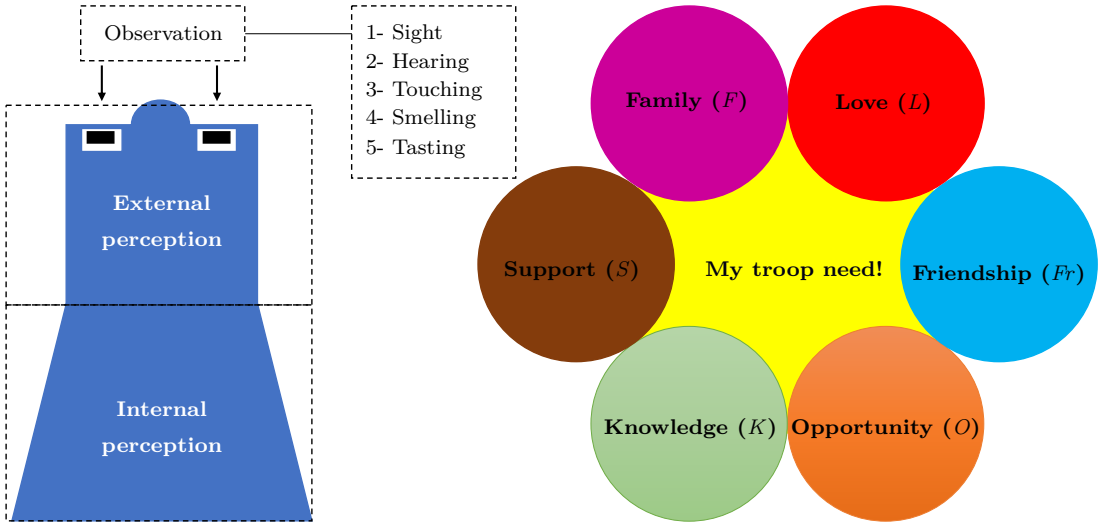

(A) (B)

The Figure (A) above presents a simplified representation of how our world as individuals is divided into two realms: the external and the internal. The internal perceptions form an infinite world that is uniquely defined by each individual. It is clear that the presence of external individuals influences our internal perceptions. Within the realm of internal perceptions, there exist numerous individual worlds, such as basic needs (nature) and values (nurture). To simplify, let us focus on one concept: the need for social connection, friendship, and belonging within a society-the human beings that surround us. I call it my troop need.

My troop need, as illustrated in Figure (B), carries profound significance for me as it reflects my deepest emotions and feelings. When it harmoniously aligns with my internal perception of the need for human connection, I am empowered to persevere on my journey with unwavering conviction. To simplify matters, I have defined six distinct dimensions that directly correspond to the need for social connection: family, love, friendship, opportunity, knowledge, and support. These dimensions serve as

driving forces, fueling my motivation and propelling me towards the attainment of my goals.

In my troop need, rooted in the concepts of family (F), love (L), and support (S), I find my foundation in my parents, Javad (my dad) and Homa (my mom), who have been constant pillars of support throughout my life. Words cannot adequately express my deep gratitude and emotions. Additionally, my sister Niloofar and my brother Ali have always stood by my side, unwavering in their support. Above all, I consider myself incredibly fortunate to have a partner in life who embodies the essence of family (F), love (L), friendship (Fr), and support (S): my wife, Kiana. My love for you knows no bounds. Thank you all for being there for me.

To ensure that I include everyone who has been by my side, I would like to express my love and gratitude to each individual by acknowledging them based on the different dimensions of my troop need. By mentioning their names, I can convey my appreciation for their presence and support in each aspect of my life. Here are the individuals who hold a special place in my heart:

- S and O and K: **Sergio and Thierry.**
- F and L and S: **Mom, Dad, Niloofar, Ali, Mehrnaz and Mehdi.**
- F and L and Fr and S: **Kiana.**
- F and Fr and S: **Sogol, Reza, Sadegh, Abazar, Shiva, Yasaman, Babak and Siamak.**
- Fr and S: **Arash, Amir, Shokoufeh, David, Pavlina, Olga, Peter, Fernanda, Dagmar, Dietmar, Edgar, Alberto, Álvaro, Alex, Arti, Arezoo, Eli, Bardia, Hamzeh, Yannick, Lelde and Yasmin.**
- S: **Lelia, Silvia and Sue.**

Contents

Abstract **v**

Acknowledgments **vii**

Contents **ix**

List of Figures **xiii**

List of Tables **xxi**

List of Symbols **xxiii**

1 Introduction **1**
1.1 Multi-physical processes in porous media 2
1.2 Application of multi-physical modeling in deep geological repositories 4
1.3 THM modeling assumptions used in the thesis 8
1.4 Computational cost 10
1.4.1 Model Order Reduction 11
1.4.2 POD and RB in THM processes in porous media 13
1.4.3 Application of PGD on coupled THM models 14
1.5 Proper Generalized Decomposition (PGD) 14
1.6 Outline and objective of this work 16

2 Governing equations and discretization **19**
2.1 Governing equations 19
2.1.1 Constitutive laws 20
2.1.2 The field equations 22
2.2 Weak form and discretization 25
2.2.1 Weak form 25
2.2.2 FEM formulation 26

3 Proper Generalized Decomposition for parametric problems **31**

3.1 Steady-state thermal problem . . . 32
3.1.1 Discretization . . . 33
3.1.2 Parametric problem . . . 33
3.2 Encapsulated PGD methodology . . . 35
3.2.1 Proper Generalized Decomposition work in principle . . . 35
3.2.2 Enrichment iteration . . . 39
3.2.3 Fixed-point iteration . . . 40
3.2.4 Convergence control and stopping criteria . . . 41
3.3 An example of a PGD solution . . . 42

4 Application of PGD to THM problems 47
4.1 Parametric problem . . . 48
4.2 Space-time discretization of parametric THM . . . 51
4.3 PGD applied to parametric THM problem . . . 53
4.3.1 Separable operators for material parameters . . . 55
4.3.2 Separable operators for geometric parameter . . . 57

5 Methodology validation 63
5.1 Problem statement . . . 63
5.1.1 Analytical solution . . . 66
5.1.2 Finite Element Method validation . . . 67
5.1.3 Parametric problem . . . 69
5.2 Results of the academic problem . . . 71
5.3 Discussion and analysis of the results . . . 73

6 Application to a simplified model of engineered barrier system 81
6.1 Common features and concepts of problems . . . 81
6.1.1 Heat source . . . 84
6.1.2 Boundary conditions . . . 86
6.1.3 The computation of time-dependent thermal boundary conditions 87
6.1.4 Initial conditions . . . 90
6.1.5 Parametric definition . . . 90
6.2 Results for a three material parameters problem . . . 92
6.2.1 Generalized solutions for thermal boundary conditions . . . 95
6.2.2 Accuracy of the generalized solution . . . 97
6.2.3 The efficiency of the generalized solution . . . 103
6.2.4 Possible exploitations of the generalized solution . . . 106
6.3 Results for a geometrically parametrized problem . . . 107

7 Discussion on the development of the numerical methodology 111
7.1 Effects of PGD solver stopping criteria on accuracy and efficiency . . . 112
7.2 Effect of PGD compression . . . 117
7.3 Use of a Δ-solver methodology . . . 122

7.4 Previous time step as starting point for PGD linear solver 124

8 Conclusions and future work **127**
8.1 Summary of the contributions 127
8.1.1 Separable operators and time integration of THM for PGD . . 128
8.1.2 The validation of methodology 128
8.1.3 Exploring PGD on a simplified model of engineered barrier system 129
8.2 Conclusions and recommendations 130
8.3 Future work 131

A Separated operators for PGD **135**
A.1 Material parameters 135
A.2 Geometric parameter 138
A.3 The four-parameter case 143

Bibliography **155**

List of Figures

1.1 Schematic representation of porous medium with three phases. 2

1.2 Schematic view of a multi-barrier system re-sketched from [129]. 5

1.3 (A) A deep geological repository re-sketched from [152], and (B) THM processes due to heat emitted from HLW and thermally induced stresses at the buffer and host rock and water circulation due to thermal expansion. 6

1.4 Multi-physical processes occurring in a fully saturated two-phase porous medium, presented here in a simplified form by using two colors; blue for the liquid phase and brown for the solid phase. Heat transport occurs solely through conduction (Fourier's law), while water transport is driven exclusively by diffusion (Darcy's law). 9

1.5 This illustration shows a thermally one-way coupled THM model, where thermal effects impact the hydraulic and mechanical parts, but not vice versa. Biot's concept defines the bi-directionality of hydraulic and mechanical parts, determining how much of the initial volumetric loading transfers between the solid skeleton and fluid. 10

1.6 The Proper Generalized Decomposition (PGD) technique consists of two stages: offline and online. The offline stage requires a significant computational cost, while the online stage can be performed in real-time. The PGD solver employs two iterative procedures: enrichment iterations and fixed-point iterations. The enrichment iterations compute the mode successively, while the fixed-point iterations compute each mode iteratively. By providing input data to the encapsulated PGD solver as will be explained, we can perform these two iterative procedures within specified tolerances. 15

2.1 (A) Porosity (ϕ) in a fully saturated medium is determined by the proportion of fluid volume (V_f) to the overall volume (V). (B) shows the mass of each phase per unit volume. 20

2.2 The THM process. 20

2.3 Boundaries and domain of a generic axisymmetric problem are presented. Here, Ω represents the spatial domain of the problem, while Γ_{t}, Γ_{r}, Γ_{b}, and Γ_{l} are the boundaries at the top, right, bottom, and left of Ω, respectively. 23

3.1 (A) Axisymmetric cylinder, (B) geometry, and (C) boundaries and domain. 32
3.2 Scheme of the three main ingredients of the PGD methodology for the solution of parametric linear systems of equations. Inputs and outputs (gray boxes) are given in separated formats (ingredient 1). An enrichment iteration (ingredient 2) sequentially adds terms to the approximated unknown function $\mathbf{T}(\mu)$. A simple fixed-point method (ingredient 3) is used to deal with the nonlinearities introduced by the separated unknown function. In the figure, σ_m corresponds to the amplitude of the m term of $\mathbf{T}(\mu)$, η_{tol} is the tolerance used to stop the enrichment iteration, ϵ and ϵ_σ are the errors estimates for the fixed-point iterations (defined in Equations (3.36) and (3.37)), and ϵ_{tol} is the tolerance of the fixed-point. 38
3.3 Relative amplitude versus modes. 44
3.4 (A) Three modes of normalized spatial functions, and (B) three modes of normalized parametric functions. 44
3.5 Temperature field result (A) and relative error (B) of PGD at $\mu = 1.5\ \frac{\mathrm{W}}{\mathrm{m}^{\circ}\mathrm{C}}$. 45
3.6 (A) The generalized solution of temperature as a function of space and parameter, and (B) relative error of the whole domain (spatial and parametric). 45

4.1 The entire spatial domain ($\Omega(\mu_L) = \Omega_1 \cup \Omega_2(\mu_L)$) is divided into two subdomains. The left half of the model, which includes the canister, buffer, backfill, and some part of the host rock, is fixed (Ω_1). The right half of the model, which represents the host rock between canisters ($\Omega_2(\mu_L)$), is controlled by the geometric parameter (μ_L). This parameter affects the $\Omega_2(\mu_L)$ domain only by shortening or elongating the radial direction. . . 49
4.2 The systematic procedure of seeking a generalized solution of parametric THM. It presents that for solving this problem by Encapsulated PGD toolbox, it is necessary to define the input data in separated formats. The generalized solutions are the separated unknowns, a collection of $\mathrm{n_t}$ parametric objects of $\mathbf{T}^i(\boldsymbol{\mu})$ and $\mathbf{U}^i(\boldsymbol{\mu})$. 54
4.3 Mapping of the domain problem from the reference domain to the model domain is accomplished using the mapping function $M(R, Z, \mu_L)$. This function explicitly affects the Ω_2 domain, while Ω_1 remains fixed. The figure illustrates the generic concept of reference domain geometry and demonstrates how the geometric parameter μ_L influences it through the mapping function. 57
4.4 Mapping of the domain problem affects the element. So, the size of bilinear quadrilateral elements will be changed from the reference domain (le_R and le_Z) to the model domain (le_r and le_z). 58

4.5 (A) The parental element is mapped by $\mathbf{J}$ to the reference element, (B) it is the reference element, $\hat{\mathbf{J}}$ maps it to the model element, and (C) it is the model element. 59

5.1 (A) Axisymmetric cylinder under uniform stress, (B) geometry, and (C) boundaries and domain. 64

5.2 Convergence plots at (A) day 1, (B) day 10, (C) day 100, and (D) day 356 demonstrate that reducing the element size (h) results in a decreasing L_2 norm of the error. The observed convergence order of two aligns with the expected behavior for the linear elements utilized in this study. 68

5.3 Space solution of the validation problem for time = 185 days and parameters $\boldsymbol{\mu}^* = [5\,\frac{\mathrm{W}}{\mathrm{m}\,^\circ\mathrm{C}}, 3\times10^{-12}\,\frac{\mathrm{m}}{\mathrm{s}}, 55600\,\mathrm{MPa}, -0.1\,\mathrm{m}]$. Several PGD solutions computed for different PGD-enrichment tolerances (η_{tol}) are displayed alongside the FE solution. As the tolerance is reduced, the error of PGD in comparison to FE diminishes. It is worth noting that in the case of the thermal field, the solutions for all tolerances are on top of the FE. 72

5.4 Time solution of the validation problem for $z = 9.75\,\mathrm{m}$ and parameters $\boldsymbol{\mu}^* = [1.5\,\frac{\mathrm{W}}{\mathrm{m}\,^\circ\mathrm{C}}, 3\times10^{-12}\,\frac{\mathrm{m}}{\mathrm{s}}, 55600\,\mathrm{MPa}, -0.1\,\mathrm{m}]$. Several PGD solutions computed for different PGD-enrichment tolerances (η_{tol}) are shown together with the FE solution. When the tolerance is being reduced, the error of PGD with respect to FE vanishes. Note that in the case of the thermal field, the solution for all tolerances are on top of the FE. 73

5.5 Effect of a decrease of the enrichment tolerance, the accuracy of global error for temperature ($\epsilon_{\mathrm{G}}^{\mathrm{T}}$), pressure ($\epsilon_{\mathrm{G}}^{\mathrm{p}}$), and displacement ($\epsilon_{\mathrm{G}}^{\mathbf{u}}$) increases. 74

5.6 The global errors in each time slice by assigning $\eta_{\mathrm{tol}} = 10^{-6}$, for all the fields output are less than 10^{-3}; however, for temperature $\epsilon_t^{\mathrm{T}}(t)$, the global errors are 10^4 more accurate than the pressure $\epsilon_t^{\mathrm{p}}(t)$ and displacement $\epsilon_t^{\mathbf{u}}(t)$. 75

5.7 The representation structure of the error explaining the parametric space comprises two blocks: (A) blocks corresponding to the values of the "outer" parameters, namely hydraulic conductivity and geometric parameter, and (B) blocks matching the variations of the "inner" parameters, namely elastic modulus and thermal conductivity. 76

5.8 The vertical axis represents the selected parametric combinations, and the horizontal axis is the time. This figure presents the local error for pressure (A) and displacement (B) for 81 various parametric combinations, which have been taken from the minimum, maximum, and middle points of the four parametric ranges. The color bar represents the local error (Equation (5.21)) in each selected parametric combination versus time, which is the relative error of the PGD solution with respect to FEM for every time and parameter combination 77

5.9 This figure aims to explain the presence of a distinct blue square in the upper right corner of Figure 5.8-A, which represents a specific combination. This particular combination achieves a faster attainment of steady-state compared to the other combinations in Figure 5.8-A, resulting in significantly improved accuracy. The figure consists of nine plots illustrating the evolution of pressure over time for different parametric combinations. The maximum hydraulic conductivity ($\mu_\kappa^{\max}$) is held constant, while the geometric parameter ($\mu_L^{\min}$) remains unchanged. The plots are grouped based on variations in heat conductivity and elastic modulus values. . . . 78

6.1 The deep geological repository is divided into two main barriers: one is the low permeability host rock as a natural barrier, and the other one is the engineered barrier system. The engineered barrier system consists of three main components, which are a canister (which contains the HLW), buffer, and backfill materials. 82

6.2 The model problem and its geometry are re-sketched from [149]. 83

6.3 Side view of the engineered barrier system in the deep geological repository (A). The top view of the repository (B) illustrates the continuous backfill, which is approximated using an axisymmetric geometry. Additionally, it depicts the inter-distance between canisters (L), which will be investigated as a geometrical parameter in this context. 83

6.4 Power evolution versus time in the year to simulate the HLW as the heat source. 85

6.5 Hydraulic (A) mechanical (B) and thermal (C) boundary conditions. . . 86

6.6 Based on the global deep geological repository model (A), a large scale model (B) is extracted to solve and find the temperatures to prescribe as a function of time on the top and bottom boundaries of the smaller model (C). 88

6.7 In this problem, the first pre-processing step consists of solving the steady-state problem to define the initial conditions (Equation (6.8)) and extracting the output in separated forms (A). The second pre-processing step involves solving the parametric thermal problem of the auxiliary large-scale model (Equation (6.7)) and extracting the average separated thermal values for the top and bottom boundaries of the small model (B). In BCs PGD BOX, T^t_{top} and T^t_{bottom} represent the separated thermal boundary conditions for the time slice t for the top and bottom boundaries of the smaller model, respectively. 93

6.8 Generalized solution to the parametric coupled THM problem at hand. It shows that the separated unknowns for each time slice will be found by providing the ICs PGD BOX, BCs PGD BOX, and all the separated matrices and vectors. 94

6.9 Figures (A) and (B) present the prescribed temperature versus time for the top and bottom boundaries of the small-scale model, respectively. They show that the results of the PGD solver are in agreement with the FEM for $\mu_\kappa = 1.5\,\frac{\mathrm{W}}{\mathrm{m}\,^\circ\mathrm{C}}$. 96

6.10 Relative error of the whole domain (time and heat conductivity of the rock) for prescribed temperature on top (A) and bottom (B). 97

6.11 (A) Result of temperature versus time for a fixed coordinate in space ($r = 0.8\,\mathrm{m}$ and $z = 17.5\,\mathrm{m}$) in the rock material with a particularized point in parametric space $\mu_\kappa = 1.5\,\frac{\mathrm{W}}{\mathrm{m}\,^\circ\mathrm{C}}$, and (B) Temperature field output at $t = 100\,\mathrm{year}$ for the same particularized point in parametric space. . . 99

6.12 Global errors of the thermal solution in each time slice are less than 10^{-5}, quantifying the accuracy of the generalized solutions in the whole domain of time, spatial and parametric space. 100

6.13 (A) Behavior of the global error for pressure versus time, (B) Global error of displacement versus time. For both cases, the effect of a smaller enrichment tolerance $\eta_{\mathrm{tol}} = 10^{-6}$ is illustrated. For $\eta_{\mathrm{tol}} = 10^{-6}$, the accuracy for the whole domain of time for both cases is almost less than 10^{-3}. 101

6.14 (A), (C) and (E) illustrate the results for pressure, radial displacement, and vertical displacement versus time, respectively. These results correspond to a specific point in the parametric space, $\boldsymbol{\mu}^* = [1.5\,\frac{\mathrm{W}}{\mathrm{m}\,^\circ\mathrm{C}}, 3 \times 10^{-14}\,\frac{\mathrm{m}}{\mathrm{s}}, 68000\,\mathrm{MPa}]$, and a fixed coordinate in space ($r = 0.8\,\mathrm{m}$ and $z = 17.5\,\mathrm{m}$) , which is located in the rock material close to the buffer. The results demonstrate agreement with the FEM solutions over time. (B), (D) and (F) display the field results for the same specific point in the parametric space at a time slice of $t = 10\,\mathrm{years}$ for pressure, radial displacement, and vertical displacement, respectively. These results further confirm the accuracy of the methodology. 102

6.15 Number of modes (M^t) versus time slice (t) for finding the solution of Equation (6.15) as an offline stage procedure: (A), number of modes as a function of time. (B) illustration of the enrichment procedure for the time slice year $t = 10\,\mathrm{year}$, for which 361 Modes are required to reach the enrichment tolerance ($\eta_{\mathrm{tol}} = 10^{-6}$). 104

6.16 The computational cost of the PGD solver depends on building the generalized solution (offline stage), while for FEM solvers, the cost increases beyond the Break-Even Point (BEP) of solving 802 models. In cases where a large number of models are required, such as in parametric identification problems needing 13,050 models, classical FEM models can take up to 200 days, while the PGD solver takes only 12 days, making it 16.67 times faster. Thus, using the PGD solver is more advantageous, depending on the problem's objective. 105

6.17 A generalized solution enables the investigation of the output sensitivity of the problem by making slight changes to the values of the input parameters within their specified range. Specifically, (A) focuses on a specific coordinate ($\mathbf{x}^*$) where temperature monitoring is required as the heat conductivity of the rock changes over time. In (B), a three-dimensional plot illustrates the variation of temperature over time and the heat conductivity at that particular spatial coordinate ($\mathbf{x}^*$). The color bar indicates the corresponding temperature values. 106

6.18 The variation of temperature error (A), pressure error (B), and displacement error (C) is observed across the entire domain of the geometric parameter and time. The color bar represents the corresponding relative errors ($\epsilon_{\mathrm{G}}(t, \mu_L)$). 108

6.19 The parametric response of temperature with respect to the geometric parameter (μ_L) and time (t) was evaluated for the buffer adjacent to the canister (B). In some studies, the maximum temperature of the buffer has been analyzed as part of the design criteria for a repository. Thus, this coordinate ($\mathbf{x}^*$) holds significance in determining the optimal spacing between canisters to ensure that the maximum allowable temperature in the buffer is not exceeded (A). The color bar represents the corresponding temperature values. 108

7.1 Global errors in each time slice for a different combination of stopping criteria for the pore pressure (A) and the displacement (B) fields. Combinations of Υ_3 and Υ_4 are seen to provide accurate results for all time slices. 113

7.2 Errors are analyzed for pore pressure (A) and displacement (B) at various points in the parametric space, specifically for 81 combinations of parametric values. These combinations are selected from the minimum, maximum, and median values of four parametric ranges. The vertical axis of the plot represents the chosen parametric combinations, while the horizontal axis denotes time. The color bar represents the local error (Equation (5.21)) in each selected parametric combination versus time, which is the relative error of the PGD solution with respect to FEM for every time and parameter combination. 115

7.3 (A) Results of the vertical displacement versus time for a fixed coordinate in the backfill material ($r = 0.1048\,\mathrm{m}$ and $z = 23.8806\,\mathrm{m}$) for a particularized point in parametric space $\boldsymbol{\mu}^* = [5\,\frac{\mathrm{W}}{\mathrm{m}\,^\circ\mathrm{C}}, 3\times10^{-14}\,\frac{\mathrm{m}}{\mathrm{s}}, 55600\,\mathrm{MPa}, 3.5\,\mathrm{m}]$. (B) Vertical displacement distribution at time $t = 7\,\mathrm{year}$ for the same particularized point in parametric space. 116

7.4 The maximum relative error of pore pressure (A) and displacement (B) in the first time steps is compared to the base case, with compression tolerances of $\eta_{\mathrm{tol}}^{\mathrm{comp}} = 10^{-3}$ and $\eta_{\mathrm{tol}}^{\mathrm{comp}} = 10^{-4}$. 120

7.5 Maximum relative error on pore pressure (A) and displacement (B) in the first time steps for different cases (base case, $\eta_{\text{tol}}^{\text{comp}} = 10^{-3}$, and $\eta_{\text{tol}}^{\text{comp}} = 10^{-4}$). 122
7.6 Number of modes required for the final output of the generalized temperature solution for each time slice. The results demonstrate that the ΔT-solver requires only half the number of modes needed for the conventional T-solver. 123
7.7 (A) Mode amplitude decrease without an initial point. (B) Use of the previous time step. 124
7.8 After 63-time steps, which is equivalent to 1.8 year, the previous time step was utilized as the initial point for the current time step. As shown in (A), without using the previous time steps, the number of modes that need to be computed is much larger than the number with the usage of previous time steps (B). 125

List of Tables

2.1 Differential operator ($\boldsymbol{\nabla}$) descriptions for axisymmetric conditions. . . . 22
2.2 Properties description. 23
2.3 Symbols description. 27

3.1 Constants used for the solution of the problem (3.7). 43
3.2 Stopping criteria for PGD. 43

5.1 The solid phase properties. The asterisk (*) represents the range of material parameters treated as variables. The minimum and maximum bounds of the ranges were selected from the tables provided in the references. . . 66
5.2 Stopping criteria for PGD internal loops. 71

6.1 The solid phase properties. The asterisk (*) represents the range of material parameters treated as variables. The minimum and maximum bounds of the ranges were selected from the tables provided in the references. . . 84
6.2 Time constants and coefficients of exponential power expression. 85
6.3 Stopping criteria for PGD. 95
6.4 Stopping criteria for PGD. 100

7.1 Four different combinations of stopping criteria, including the maximum number of fixed-point iterations ($\text{iter}_{\max}$) and the enrichment tolerance of PGD (η_{tol}), have been selected for the PGD linear solver, along with the problem units. These selections are presented in Table. 112
7.2 Stopping criteria for PGD linear solver as based case. 119
7.3 Stopping criteria for PGD compression. 120

List of Symbols

- Table of fluid material properties notations:

Symbol	Units	Description
ρ_f	$\mathrm{kg\,m^{-3}}$	Density of the fluid phase
c_f	$\mathrm{J\,kg^{-1}\,{}^{\circ}C^{-1}}$	Specific heat of the fluid phase
α_f	$\mathrm{{}^{\circ}C^{-1}}$	Heat expansion coefficient of the fluid phase
K_f	Pa	Bulk modulus of the fluid phase

- Table of solid material properties notations:

Symbol	Units	Description
ρ_s	$\mathrm{kg\,m^{-3}}$	Density of the solid phase
K	$\mathrm{m\,s^{-1}}$	Hydraulic conductivity of the porous medium
κ	$\mathrm{W\,m^{-1}\,{}^{\circ}C^{-1}}$	Heat conductivity of the porous medium
c_s	$\mathrm{J\,kg^{-1}\,{}^{\circ}C^{-1}}$	Specific heat of the solid phase
α_s	$\mathrm{{}^{\circ}C^{-1}}$	Heat expansion coefficient of the solid phase
ϕ	-	Porosity
α	-	Biot's coefficient
K_D	Pa	Bulk modulus of the fully drained poroelastic body
K_s	Pa	Bulk modulus of the solid phase
E	Pa	Elastic modulus
ν	-	Poisson's ratio

- Table of notations for cylindrical coordinates (axisymmetric assumption):

Symbol	Units	Description
r	m	Radial coordinate (horizontal direction)
z	m	Axial coordinate (vertical direction)

- Table of description for the nabla ($\boldsymbol{\nabla}$) operator in axisymmetric conditions:

Thermal or Hydraulic part	Mechanical part
$\begin{bmatrix} \frac{\partial}{\partial r} \\ \frac{\partial}{\partial z} \end{bmatrix}$	$\begin{bmatrix} \frac{\partial}{\partial r} & 0 \\ 0 & \frac{\partial}{\partial z} \\ \frac{1}{r} & 0 \\ \frac{\partial}{\partial z} & \frac{\partial}{\partial r} \end{bmatrix}$

- Table of notations for unknown fields:

Symbol	Units	Description
T	°C	Temperature
p	Pa	Pore water pressure
u_r	m	Radial displacement
u_z	m	Axial displacement
$\mathbf{u}$	m	Vector of displacement

- Table of notations for sink, source, fluxes, and external forces:

Symbol	Units	Description
$\mathbf{g}$	$\mathrm{m\,s^{-2}}$	Vector of gravitational acceleration
g	$\mathrm{m\,s^{-2}}$	Gravity
$\mathbf{b}$	$\mathrm{N\,m^{-3}}$	Vector of body force
$\mathbf{b}_\mathrm{f}$	$\mathrm{N\,m^{-3}}$	Vector of body force of fluid
$\mathbf{t}_N$	$\mathrm{N\,m^{-2}}$	Traction force
q	$\mathrm{W\,m^{-3}}$	Heat source
$\mathbf{i}_c$	$\mathrm{W\,m^{-2}}$	Heat flux
$\mathbf{j}_w$	$\mathrm{m\,s^{-1}}$	Hydraulic flux

- Table of time parameters and operators descriptions:

Symbol	Units	Description
θ	–	Time integration parameter used in this study is 0.75
t	s	Time
Δt	s	Time step
i	–	Super-index as time slice
$\dot{T}$	$^{\circ}\mathrm{C\,s^{-1}}$	Derivative of temperature with respect to time
$\dot{p}$	$\mathrm{Pa\,s^{-1}}$	Derivative of pressure with respect to time
$\dot{\mathbf{u}}$	$\mathrm{m\,s^{-1}}$	Derivative of displacement with respect to time

- Table of descriptions of matrices and vectors after FEM discretizations:

Symbol	Description
$\mathbf{K}_{\mathrm{T}}$	Stiffness matrix for thermal part
$\mathbf{M}_{\mathrm{T}}$	Mass matrix for thermal part
$\mathbf{M}_{\mathrm{pT}}$	Coupling mass matrix of temperature in hydraulic part
$\mathbf{K}_{\mathrm{p}}$	Stiffness matrix for hydraulic part
$\mathbf{M}_{\mathrm{p}}$	Mass matrix for hydraulic part
$\mathbf{G}_{\mathrm{pd}}$	Coupling matrix of volumetric strain in hydraulic part
$\mathbf{K}_{\mathrm{d}}$	Stiffness matrix for mechanical part
$\mathbf{G}_{\mathrm{dT}}$	Coupling matrix of temperature in mechanical part
$\mathbf{G}_{\mathrm{dp}}$	Coupling mtrix of pressure in mechanical part
$\mathbf{f}_{\mathrm{q}}$	Force term generated by heat source
$\mathbf{f}_{\mathbf{b}_{\mathrm{f}}}$	Force term generated by gravity in hydraulic part
$\mathbf{f}_{\mathrm{d}}$	Force term generated by body force and traction force
$\mathbf{N}_{\mathrm{T}}$	Matrix of shape functions for temperature
$\mathbf{N}_{\mathrm{p}}$	Matrix of shape functions for pressure
$\mathbf{N}_{\mathrm{d}}$	Matrix of shape functions for displacement
$\mathbf{B}_{\mathrm{T}}$	B-operator matrix for temperature
$\mathbf{B}_{\mathrm{p}}$	B-operator matrix for pressure
$\mathbf{B}_{\mathrm{d}}$	B-operator matrix for displacement
$\mathbf{B}_{\mathrm{v}}$	B-operator matrix for volumetric displacement

- Table of PGD stopping criteria description:

Symbol	Description
η_{tol}	Enrichment Tolerance
M_{max}	Maximum number of Modes
ϵ_{tol}	Tolerance for Fixed-point iteration
iter_{max}	Maximum number of iteration for Fixed-point iteration

- Table of external dimensions definitions:

Symbol	Description
μ_κ	Heat conductivity of the host rock
μ_K	Hydraulic conductivity of the host rock
μ_E	Elastic modulus of the host rock
μ_L	Geometric parameter (spacing between canisters)

- Table of interval and domain descriptions:

Symbol	Description
I_{μ_κ}	Heat conductivity domain
I_{μ_K}	Hydraulic conductivity domain
I_{μ_E}	Elastic modulus domain
I_{μ_L}	Geometric parameter domain
$I_{\boldsymbol{\mu}}$	Parametric domain
I_t	Time domain
Ω	Spatial domain
Γ	Boundary domain
Γ_{N}	Neumann boundary domain
Γ_{D}	Dirichlet boundary domain

- Table of global separated input data definitions:

Symbol	Description
$\mathbf{K}^i_{\mathbf{GT}}(\boldsymbol{\mu})$	Separated global stiffness matrix thermal part in time slice i
$\mathbf{F}^i_{\mathbf{T}}(\boldsymbol{\mu})$	Separated global force vector thermal part in time slice i
$\mathbf{K}^i_{\mathbf{G}}(\boldsymbol{\mu})$	Separated global stiffness matrix hydro-mechanical part in time slice i
$\mathbf{F}^i_{\mathbf{G}}(\boldsymbol{\mu})$	Separated global force vector hydro-mechanical part in time slice i

- Table of global separated output data definitions:

Symbol	Description
$\mathbf{T}^i(\boldsymbol{\mu})$	Separated output for thermal part in time slice i
$\mathbf{U}^i(\boldsymbol{\mu})$	Separated output for hydro-mechanical part in time slice i

Chapter 1

Introduction

A Reduced Order Model (ROM) based on Proper Generalized Decomposition (PGD) is developed to address multi-physical processes in porous media inspired from deep geological repository applications (nuclear waste disposal). This study contributes to the development of a supplemental tool with respect to computational multi-physical models used in the subsurface of the earth. Features of the subsurface, like the physical coefficients governing mechanical and transport processes, are often based on various data, such as data obtained from mapping, drilling, or seismic studies, involving uncertainties [14]. We are considering a configuration in which we would need to solve problems efficiently and in a repetitive way for any value of the physical coefficients governing it. This supplementary tool will have to handle effectively and treat such needs. It should be emphasized that studying PGD on such multi-physical problems is new. Therefore, combining these different techniques requires simplifications concerning the scope of the thesis. The development will thus make use of simplifying assumptions to define the goals of this study, with a view toward the whole problem close to reality for future prospectives (outlook).

This chapter provides the foundation for this research by illustrating its originality based on a knowledge gap identified in the literature. Section 1.1 briefly outlines the history of multi-physical procedures in porous media and their terminology. It discusses why these models have been developed and mention their generic applications. Section 1.2 focuses on the application of multi-physical processes, specifically emphasizing their utilization in deep geological repositories. The investigation of these processes in this context has been the primary impetus for this research.

Section 1.3 pinpoints the objectives of the thesis in link with the simplifying assumptions introduced. Section 1.4 illustrates why such problems are computationally expensive and how researchers have dealt with them. Then, the need for research concerning ROM techniques will be discussed. More particularly, Reduced Basis (RB), Proper Orthogonal Decomposition (POD), and PGD will be outlined. Moreover, in this section, the recent application of RB and POD in multi-physical processes in porous media will be brought up. In the end, the impetus for applying PGD to multi-physical problems will be discussed briefly. Section 1.5 renders a short review of what PGD is and what has been researched.

Finally, Section 1.6 states the thesis's key objectives and presents its structure through its chapters.

1.1 Multi-physical processes in porous media

Many engineering problems are related to processes occurring within the earth's subsurface or surface, thus involving geomaterials, i.e. geological host rocks, or soils (solid phase). The pore space inside them is often filled with gaseous and liquid phases. These systems are denoted as saturated or partially saturated porous media respectively, depending on the presence of only a liquid phase or both a liquid and gaseous phases (Figure 1.1). Building anthropogenic engineering structures in such natural geomaterial media imposes extrinsic loads on such a system. Geomechanics and hydrogeology are the two main generic topics that have dealt with such engineering problems within the last decades.

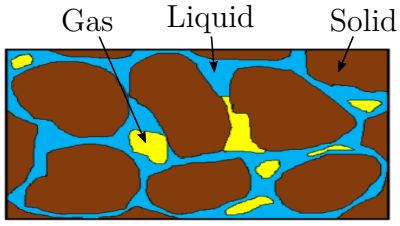

Figure 1.1: Schematic representation of porous medium with three phases.

Understanding the (coupled) response of a natural porous medium to the building of engineering structures is crucial to designing structures that can safely provide their purposes. As a result, the requirement for predicting the behavior of geomaterials subjected to various extrinsic loads has motivated investigating multi-physical processes

in a multiphase porous medium, leading to the development of prediction tools. The multi-physical processes at hand in geomaterials require considering the concurrent impacts of mechanical deformation, fluid flow, heat transfer, and chemical alterations in a multiphase porous medium where three phases are present (solid, liquid, and gas). However, taking into account all the possible multi-physical interactions between all the phases is out of reach for solving engineering scale problems. Therefore, simplifying assumptions will be introduced here. By disregarding the chemical aspects, these sorts of problems can be classified using a variety of terminologies, such as coupled Thermo-Mechanical (TM), Hydro-Mechanical (HM), Thermo-Hydro (TH), and Thermo-Hydro-Mechanical (THM) problems, depending on the incorporated physical processes.

The pioneering work of Karl Terzaghi [142] was the beginning of coupled problems research in the field of Geomechanics. He performed controlled laboratory studies to understand consolidation, which causes soils to settle under load. He dealt with a one-dimensional fluid-saturated porous medium problem which also can be called coupled HM problem, in a simplified version, which resulted in his consolidation theory. Afterward, Meinzer [90], in hydrogeology, was the first to study the elastic behavior of aquifers. In his work, he used Terzaghi's effective stress concept to connect pressure changes directly to increased stress levels. However, numerous other contributions should not be overlooked concerning the theory and application of porous media, such as the works of Pratt and Johnson [119], Theis [143], Fillunger [41], Muskat [93], Jacob [73], Boer [15, 16], and Ehler and Bluhm [39] to name a few.

Biot [12] expanded Terzaghi's theory to encompass three dimensions and entail a continuum formulation applicable to a porous medium. Assuming full saturation, he considered that the instantaneous load exerted on a porous medium is carried partly by the pore water and partly by the solid skeleton. Biot's approach to soil consolidation assumes Hookean elastic materials and Darcy's law for porous skeleton's mechanical and hydraulic behavior, respectively. The similarity of this theory with thermoelasticity was discussed by Biot [13], Geertsma [50], Rice and Cleary [124], and Norris [103], and the terminology of poroelasticity was first introduced by Geertsma [52]. Poroelasticity has been used for decades for instance in Geertsma [51], McNamee and Gibson [88], Cryer [32], Nur and Byerlee [105], Garg and Nur [48], Coussy [30], Bear and Corapcioglu [9], Jupp and Schultz [75], Wang [162], and Verrujit [156, 157].

In different engineering problems, depending on the application, it is sometimes compulsory to consider thermal effects in porous media. The research on the impact of heat flow (thermal part) on the pore pressures (hydraulic part) and the solid skeleton (mechanical part) and vice versa is, in this case, essential; these kinds of problems are called coupled THM problems. Paleciauskas and Domenico [112], by modifying the Biot theory to nonisothermal poroelasticity conditions (thermo-poroelasticity), presented the impact of heat conduction on a fluid-saturated rock, by deriving governing equations for thermo-poroelasticity problems. Many authors have contributed to this area by assuming heat conductivity as the only heat transfer mechanism, for instance, Bear and Corapcioglu [8], Noorishad et al. [102], McTigue [89], Coussy [31], Cheng [21], and Selvadurai and Suvorov [129]. These assumptions make the problems tractable. However, their validity depends on the applications and objectives of the study. For some applications, it is necessary to consider convection next to conduction as a transport mechanism for thermal aspects, making the coupled problem more intricate [115, 100].

The coupled THM problems can be partially saturated with elastoplastic behavior, [85, 53, 98, 44, 46] which makes them nonlinear. Also, such problems can introduce anisotropy [62, 154] and spatial heterogeneity [113, 166] or can even require considering chemical aspects [155, 28] which largely increase their complexity. For such problems, the necessities of in situ [11, 23], mock-up [139, 140], and laboratory tests [130, 133] for interpreting and calibrating material data are inevitable. It is well known that the complexity of natural systems, and in particular systems related to the Earth, is extremely large. Our goal in this work is to apply reduced-order methods and study their efficiency in the context of THM problems. Therefore, we will restrict the setup to a simple but meaningful case with which we can test the methods and set the basis for future extensions to more complex systems.

1.2 Application of multi-physical modeling in deep geological repositories

The application of THM models in geo-environmental problems has gained significant attention in recent decades, particularly in addressing engineering problems in geomechanics and hydrogeology. One of the most extensively studied and important applications of these models is the design of deep geological repositories. Nuclear

power plants generating electricity produce High-Level Radioactive Waste (HLW) that remains hazardous for 1000 years. Deep geological repositories are now one of the most promising alternatives for the long-term storage of HLW. Many Countries including Belgium, Canada, Finland, Germany, Japan, Spain, and the United States are developing these waste storage techniques [167], to isolate HLW from human and environmental interactions. Finland, at this stage, is the only country having a legally approved design, and the first deep geological disposal facility will start functioning in 2023 on the island of Olkiluoto [135]. Many authors have studied different aspects of deep geological repositories. For example, Olivella et al. [108], Nguyen and Selvadurai [97], Gens et al. [58], Nguyen et al. [98], Gens et al. [61], Selvadurai et al. [131], Toprak et al. [150]. The geotechnical group at UPC has had a large collaboration in the development of the Olkiluoute facility. The works led by Prof. Sebastia Olivella [152, 148, 150, 149, 151] were used in this thesis as a basis to produce a simplified model in which we can study and test the numerical methodologies we are proposing. The final goal of these methodologies is to produce an extremely fast solver tailored for many-query situations where a large family of similar problems needs to be tested. Some examples of many-query situations that are commonly found in practical engineering are inverse problems to estimate the value of some parameters; or optimization problems where an optimal value of some design variables needs to be determined. A numerical methodology, able to provide a fast solution to the forward problem, will largely accelerate or allow aiming for a larger accuracy in the solution of these problems.

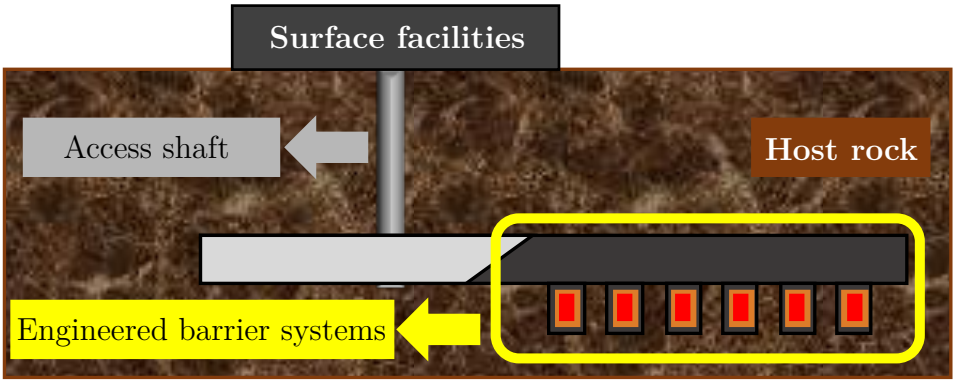

Figure 1.2: Schematic view of a multi-barrier system re-sketched from [129].

Figure 1.2 presents a multi-barrier system for the storage of HLW. It consists of two main barriers: the natural geological barrier made of the host rock and an

engineered barrier system. The host rock acts as the natural geological barrier for radioactivity and is where the vault system is built. Low permeability, geological stability, and chemical stability for the host rocks are required properties for HLW confinement [54]. Four categories of rocks–crystalline [40, 121], argillaceous [132, 153], rock salt [120, 10], and unsaturated tuff [109, 138]–are being investigated based on these properties.

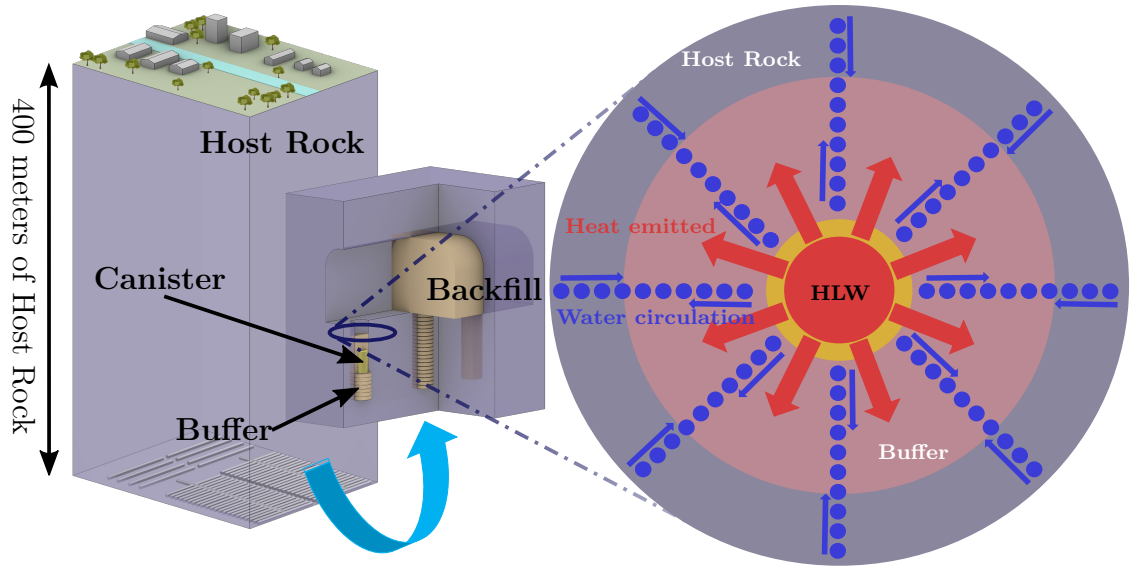

(A) (B)

Figure 1.3: (A) A deep geological repository re-sketched from [152], and (B) THM processes due to heat emitted from HLW and thermally induced stresses at the buffer and host rock and water circulation due to thermal expansion.

Figure 1.3-(A) illustrates a deep geological repository that relies on multi-barrier systems where the HLW is located around 400 meters underground [152]. The HLW is mechanically protected by a canister, mostly made of cast iron, with a copper shell added for corrosion prevention [76]. Highly compacted bentonite clay (buffer) is used to surround the canister. Thanks to its low hydraulic conductivity, microporous structure, excellent sorption capabilities, and swelling capacity, it is an effective barrier for shielding the canister. Shafts and boreholes are filled with the so-called backfill materials. These prevent access to the canisters. Several studies have been conducted about the materials to use as buffer/backfill; e.g. [59, 159, 160, 161, 171, 5, 1].

The numerical studies of the repositories need to reproduce the interaction between the main processes involved: the mechanics, the thermal transport, and the flow of water [60]. Figure 1.3-(B) shows a schematic view of these processes. An increase in the temperature due to the heat emitted by the waste produces two effects: i) thermally induced stresses at the buffer and host rock and ii) water circulation due to thermal expansion that might reach a change of state. The buffer is expected to accommodate a large part of these mechanical and thermal effects.

The THM model is complex to reflect the real physical concept. To encapsulate the HLW, an excavation procedure should be considered, after which heating starts. Excavation induces the presence of an Excavation Damaged Zone (EDZ), which affects not only the host rock's mechanical behavior but also its transfer properties (permeability) and the transfer boundary conditions (gallery ventilation) [107]. On the other hand, the buffer is only partially saturated and initially subjected to high suction (negative value of pore water pressure). For that, it is necessary to define the transmission of liquid to gas and gas to liquid phases. Many authors have studied the constitutive model for unsaturated cases; some examples are given in [2, 55, 86, 45]. However, it should be emphasized that such complexities (such as EDZ, the transmission of liquid to gas and gas to liquid phases, unsaturated cases, etc.) are outside the scope of this study. This is why simplified assumptions (Section 1.3) will be applied to such a model to concentrate on the objective of the thesis.

For such THM models, equilibrium equations for stresses and continuity equations for liquid water, gas, and energy should be solved simultaneously. This problem cannot be solved analytically, which requires defining computational approaches like Finite Element Method (FEM) techniques. Many works addressed this, for instance Gens et al. [58], Nguyen et al. [98], and Dupray et al. [35]. Accordingly, many commercial organizations, university researchers, industrial organizations, and research institutions have developed various codes, such as OpenGeoSys [163], FLAC [71], LAGAMINE [19, 29], UDEC and 3DEC [72], COMPASS [144], THAMES [106], ROCMAS [101], CODE-BRIGHT [108, 110], RDCA-THOUGH2 [113], and FRACON [96], most of them are based on FEM. However, as will be discussed in Section 1.4, these computational models are computationally costly, and it is of interest to find a way to deal with them more efficiently.

Multi-physical processes have also been investigated in various other applications. For instance, enhanced oil recovery (EOR) [80] benefits from THM processes that

increase the efficiency of oil recovery [83]. Geologic sequestration is another application that aims to reduce greenhouse gases in the atmosphere and has been studied by several authors [114, 158, 173]. Geothermal energy extraction is also an application requiring THM models, and various codes such as GEOCRACK [36], FRACTure [78], and HOTGRID [67] have been developed to study this problem. Many authors have used these codes, for example, Ghassemi et al. [63], Koh et al. [77], Simone et al. [33], and Pandey et al. [116]. Tunnel excavation, which typically involves a multi-stage tunneling technique, requires a coupled modeling effort considering the effects of inevitable seepage flow. Some contributions have addressed such applications through multi-physical investigation, e.g., [122, 118, 137]. Freezing action in soils is another configuration that many authors have studied using multi-physical modeling in porous media, e.g., [145, 65, 84]. Embankments and tailing dams are other engineering problems involving multi-physical processes. Tailings, which are peripheral products of mining ore and exploiting metals and minerals and are hazardous, have been the subject of multi-physical studies by many authors, including Gens et al. [56], Pinyol et al. [117], and Zandarin et al. [172].

1.3 THM modeling assumptions used in the thesis

The combination of the PGD technique with THM models is attractive because it can provide real-time solutions to coupled THM problems, replacing a costly Finite Element Method (FEM) traditional repetitive run with real-time integration. However, these models are complex and depend on various parameters. For example, in a deep geological repository, they rely on parameters such as heat and hydraulic conductivity, as well as the elastic modulus of the rock. Geometric parameters, such as the spacing between canisters, may also influence them for design purposes. To address this complexity and achieve a framework allowing real-time solution, we simplify the problem and render it linear. Consequently, the problem is fully saturated with quasi-static processes and thermo-poroelastic behavior inherited from the work of Selvaduri and Suvorov [129].

Another assumption made in this work is that heat conduction is the predominant mechanism of heat transport. This means that heat is transferred by activating solid and fluid particles through conduction while neglecting convection. The justification

for this assumption comes from the targeted application. In a poroelastic material, the heat convection that arises from the displacement of the solid can be ignored, and convective heat transmission is mainly caused by fluid flow. Since the problem deals with host rock with low porosity and low permeability properties, the fluid flow rate is low, and heat convection is disregarded [97]. This assumption results in a thermally one-way coupled problem.

Figure 1.4 illustrates the multi-physical processes occurring in a fully saturated porous medium. Under these assumptions, the medium can be viewed as a two-phase system, with the liquid phase depicted in blue and the solid phase in brown. In this system, heat transport occurs solely through conduction (Fourier's law), while water transport is driven exclusively by diffusion (Darcy's law). The mechanical response of the rock-solid skeleton is assumed to be linearly elastic (Hooke's law).

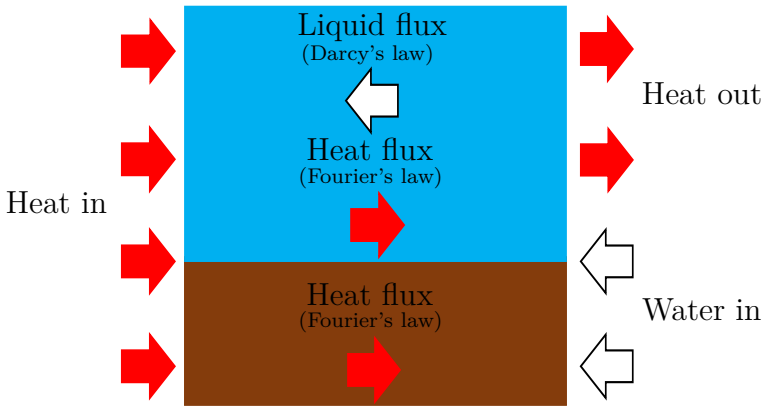

Figure 1.4: Multi-physical processes occurring in a fully saturated two-phase porous medium, presented here in a simplified form by using two colors; blue for the liquid phase and brown for the solid phase. Heat transport occurs solely through conduction (Fourier's law), while water transport is driven exclusively by diffusion (Darcy's law).

Figure 1.5 describes the couplings considered in the THM model in this thesis. The model is thermally one-way coupled, which means that the thermal aspect affects the hydraulic (diffusive fluid flow) and mechanical part (thermal strains). Conversely, the hydraulic and mechanical aspects do not affect the thermal part. Bi-directional coupling is included between the hydraulic and mechanical components, and Biot's law governs this coupling term. The overall governing equations are obtained by describing the continuity equations and the stress equilibrium with the corresponding constitutive laws (Fourier law, Darcy law, Hooke law, and Biot law). No phase change is thus considered in this work.

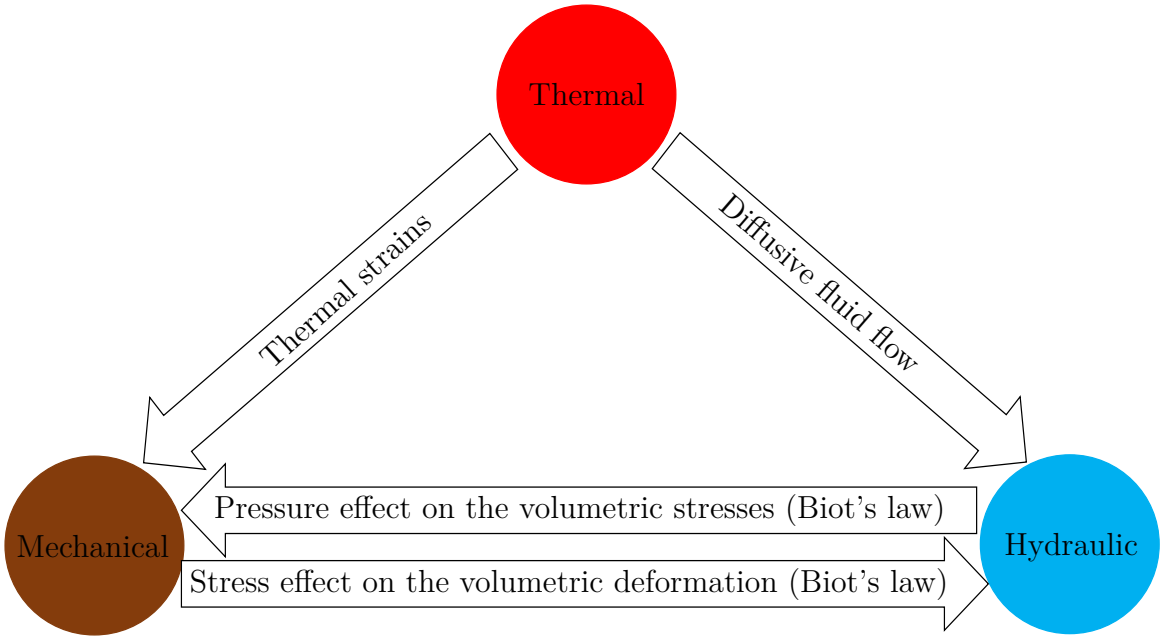

Figure 1.5: This illustration shows a thermally one-way coupled THM model, where thermal effects impact the hydraulic and mechanical parts, but not vice versa. Biot's concept defines the bi-directionality of hydraulic and mechanical parts, determining how much of the initial volumetric loading transfers between the solid skeleton and fluid.

The excavation procedure is also neglected in this study. This means that the rock is considered intact (no EDZ formulation) and that simulation starts from the heating emission from the HLW with a fully saturated medium. However, as will be discussed in the next Section 1.4, even these simplified problems are expensive, and in this project, a PGD technique (a ROM-based explained in Section 1.5) is used to tackle this difficulty.

1.4 Computational cost

The applications governed by a coupled Thermo-Hydro-Mechanical model described so far are computationally expensive. For spatial discretization, the coupled nature requires solving a large system of equations if a monolithic solver is used, while using a staggered scheme requires iterations. Furthermore, the time dimension needs to be integrated, multiplying the number of spatial problems by the number of time steps.

This represents a high but affordable computational cost. Several authors have proposed different alternatives to accelerate the solution to this problem. Some examples include HPC techniques and facilities that can be used to parallelize the computer load [146, 165, 170, 164, 147, 42], Multigrid [64] and Algebraic Multigrid methods [168, 169] to accelerate the solution of the systems of equations, and Staggered Newton schemes [125, 126, 104] to reduce the size of the systems.

The situation however becomes computationally extenuating when this forward problem is used in a multiple query situation, such as sensitivity analysis, e.g. [149], calibration, e.g. [22], parameter identification, e.g. [99], optimization, e.g. [148], uncertainty quantification, e.g. [123], or simply when a very fast solution close to real-time is needed for control, e.g. [27], In all these scenarios, many forward problems need to be solved and the computational cost increases accordingly.

In this work, we will use a different approach based on Model Order Reduction and more particularly Proper Generalized Decomposition methods. This technique will i) provide a real-time solution to a parametrized problem (after an initial offline computation phase) and ii) can be coupled with all the previous acceleration techniques to accelerate the offline phase.

1.4.1 Model Order Reduction

Model Order Reduction (MOR) techniques are a family of numerical techniques to deal with parametric problems. These are problems governed by a Partial Differential Equation (PDE) in which one or several parameters (e.g., physical properties, boundary conditions, geometry, etc.) are not known exactly, and it is of interest to compute the solution for any parameter value within a range.

The solution of the PDE, traditionally defined in terms of space and time, e.g., $u(\mathbf{x}, t)$, which in this subsection is a scalar function, although the method can deal with any scalar and vectorial function, is now recognized to depend on additional parameters $\boldsymbol{\mu} = [\mu_1, \mu_2, \ldots, \mu_{\mathrm{n_p}}]$, leading to the more general form $u(\mathbf{x}, t, \boldsymbol{\mu})$. As a result, the dimensionality of the problem increases significantly, with u living in a space consisting of three spatial dimensions, one time dimension, and $\mathrm{n_p}$ parametric dimensions, namely $u \in \mathrm{R}^{3+1+\mathrm{n_p}}$.

Standard discretization techniques cannot be used to seek a solution to the parametric problem, as the number of unknowns would increase exponentially with respect to the number of dimensions. For example, if the spatial mesh has 10^4 nodes (a con-

servative quantity), the number of times steps is 10^3, and we have four parametric dimensions, each one discretized with 10^2 points, the total number of unknowns becomes $10^{(4+3+4\times2)}$ unknowns, which is outside the current computer capacity. The goal of MOR techniques is to reduce that space.

Several MOR techniques have been successfully applied to science and engineering problems. For example, Sibileau et al. [134] used PGD as a MOR technique to provide explicit solutions to algebraic equations and simplify optimal design for architectured materials. Ortega-Gelabert et al. [111] developed an efficient simulation method for geophysical-geodynamic inverse problems using Reduced Basis (RB) and Markov chain Monte Carlo (MCMC) methods. They proposed a surrogate method that significantly reduces computational costs and demonstrated its effectiveness in various numerical examples. Garikapati et al. [49] used the PGD method and Griffith's global energy criterion to propose a reduced-order modeling framework for predicting crack propagation in brittle materials with random heterogeneities. Cavaliere et al. [18] used Inertia Relief and PGD to solve parametric structural problems with a nonintrusive reduced order model that provides all possible solutions for a range of parameters. The technique was validated through numerical tests and can be integrated with commercial Finite Element Method (FEM) packages, showing potential for multi-objective optimization. Schuler et al. [127] developed a PGD-based reduced model for the Thermo-Mechanical (TM) analysis of IGBT power modules, enabling a faster solution than classical FEMs. They used a strain-life law to compute power module lifetime and conducted a sensitivity analysis for selecting acceptable parameter values. A robust design study was also performed to demonstrate the effectiveness of the proposed approach.

Overall, the MOR approach consists of two stages: the offline stage and the online stage. All expensive computations are executed only once in the offline stage. In the offline stage, the so-called surrogate model will be provided, called the parametric solution (meaning a family of solutions), also called the generalized solution. The generalized solution is an output that contains all the possible solutions for independent parametric, space, and time dimensions. The next stage, the online stage, provides the post-process solution in real time. That means by particularizing a specific point in parametric, space, and time dimensions and putting it as input in the surrogate model, the output will emerge in a fraction of a second.

A-posteriori and a-priori methods are two classes used to categorize ROM methods. First, the a-posteriori concepts of Reduced Basis (RB) [87, 66] and Proper Orthogonal Decomposition (POD) [20] will be briefly described. If a problem requires N equations to be solved by FEM, a linear combination of m basis vectors extracted from solutions for specific values of the parameters (called snapshots), which is a small number compared to N, will be used as solution space. The new system of dimension m is thus a reduced version of the original system of dimension N (the full-order solution). The full-order system is converted into the reduced version by applying a projection matrix that complies with the m basis vectors. These m basis vectors are deduced from snapshots that consist of full-order system solutions at specific points in the parametric dimensions. These methods are denoted as a-posteriori since they rely on full-order solution snapshots to generate the basis. The critical component of these approaches (RB and POD) is the selection of parametric points as snapshots to deliver precise and effective output, which is where the idea of error estimate appears. The second class of ROM techniques is the a-priori concept which means that the generalized solution will be produced without computing any snapshots. These techniques deliver a blind prediction of the parametric solutions. The most well-known a-priori method is Proper Generalized Decomposition (PGD) [26], which will be explained in more detail in Section 1.5.

1.4.2 POD and RB in THM processes in porous media

Few research contributions combined POD and RB methodologies with computational approaches in the context of multi-physical processes in porous media in geomechanics or hydrogeology applications. The ROM techniques are often problem-dependent, meaning that for each problem statement, these techniques should be individually investigated. Moreover, multi-physical problems in porous media are time-dependent, coupled, and may be non-linear. This makes them even more complicated, which is also another reason why such topics have been so rarely tackled with ROM techniques.

In this area, Florez et al. [43], by applying the POD technique on coupled flow and geomechanics simulations (using thermo-poroelasticity), have decreased the computational costs. Degen et al. [34] studied the RB method applied to such problems in the context of geothermal applications. In the work by Nasika et al. [95], the RB technique was applied to the tailing dam problems as a coupled HM case with

an unsaturated and nonlinear geomechanical model. It is shown that their RB techniques achieve a speedup of 3 to 15 times in comparison with the full-order model. Another contribution by Nasika et al. [94] is using the Discrete Empirical Interpolation Method (DEIM), a hyper-reduction technique that is developed for solving fully coupled HM equations governing water flow through soil, resulting in significant computational time reduction. Larion et al. [82] developed a goal-oriented error estimator for an optional selection of snapshots in the RB technique to solve the coupled THM problem corresponding to the advance of a glacier on a host rock mass. In their work, they solve the problem for the far-field case (large-scale). Their models consider two and three-dimensional thermo-poroelastic relations. In a follow-up contribution by Larion et al. [81], the RB technique was applied to the coupled THM case for the near-field (small-scale) problem corresponding to an in-situ heating test in a host rock of a geological repository. The RB approximation was used within an efficient surrogate-based inverse identification tool to identify material properties based on actual temperature and pore pressure measurements, decreasing the computational cost by up to 800. Another work in the deep geological repository concept has been proposed by Iollo et al. [70], who studied the application of the POD-greedy method on coupled THM problems in a two-dimensional case.

1.4.3 Application of PGD on coupled THM models

To the knowledge of the author, PGD was not applied in geo-environmental studies involving THM coupling. This combination constitutes the originality of the work. ROM techniques are firmly problem-dependent, so their application to such problems should be individually studied and analyzed. When corresponding to PGD methods, PGD is an a-priori technique, which means that it deals with the problem as a blind prediction tool and does not rely on a priori snapshot solutions from the full-order problem. Afterward, in the online phase, PGD will provide a family of solutions that can be obtained in real-time.

1.5 Proper Generalized Decomposition (PGD)

The concept of PGD was introduced by Ammar et al. [3, 4]. This technique is a powerful method to deal with problems that are suffering from the curse of dimensionality. Its concept is based on separated representations of the unknown fields based

on independent variables [24]. For instance, for a conduction problem, an unknown temperature field depending on three parameters μ_1, μ_2, and μ_3 is approximated as:

$$T(\mathbf{x}, \mu_1, \mu_2, \mu_3) = \sum_{j=1}^{M} T^j(\mathbf{x}) G_1^j(\mu_1) G_2^j(\mu_2) G_3^j(\mu_3), \tag{1.1}$$

where each term, $j = 1, 2, \ldots, M$, is described by a temperature function T^j that depends only on space (and it does not depend on the parameters μ_i) and a set of parametric functions $G_1^j(\mu_1)$, $G_2^j(\mu_2)$, and $G_3^j(\mu_3)$, depending only on the parameters.

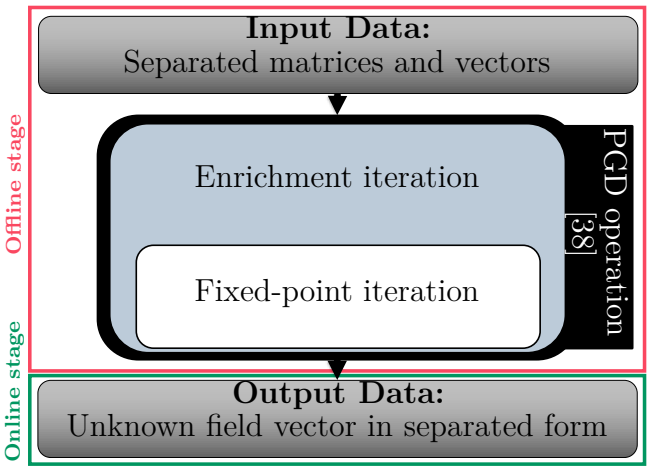

Figure 1.6: The Proper Generalized Decomposition (PGD) technique consists of two stages: offline and online. The offline stage requires a significant computational cost, while the online stage can be performed in real-time. The PGD solver employs two iterative procedures: enrichment iterations and fixed-point iterations. The enrichment iterations compute the mode successively, while the fixed-point iterations compute each mode iteratively. By providing input data to the encapsulated PGD solver as will be explained, we can perform these two iterative procedures within specified tolerances.

The Proper Generalized Decomposition will be applied here to the parametric PDEs of the coupled THM models by using FEM techniques as a base full-order computational approach. The matrices and vectors arising from FEM will be used as inputs for the PGD operations. This requires setting them in the appropriate separated form. PGD combines an enrichment iteration (to compute the method successively) with a fixed-point iteration (to compute each mode iteratively) [175, 37] (Figure 1.6) as will be explained in Chapter 3.

The Proper Generalized Decomposition will solve the problem once for life (offline). Then by particularizing the different points in the parametric space (online),

the output can be generated in real-time. The result, called the parametric solution, is also denoted as a computational vademecum [25].

1.6 Outline and objective of this work

This work thus deals with parametrized transient coupled THM problems using an encapsulated PGD technique [38]. The combination of PGD and THM is interesting due to its potential to provide real-time solutions for coupled THM problems, thereby eliminating the requirement for repetitive traditional FEM runs. This is achieved through real-time integration, which is facilitated by the methodology. The primary objective of this work is to study the combination of these two techniques in the context of deep geological repositories. The primary objective of this work is to study the combination of these two techniques in the context of deep geological repositories, namely,

- To apply PGD for the solution of THM problems parameterized with material properties.
- To extend the parameterization and include geometrical parameters.
- To obtain solutions of the parametric THM problem in real-time.

The outline of the thesis to achieve these goals is as follows:

- Chapter 2 presents the non-isothermal quasi-static thermo-poroelastic governing equations. The strong form of the problem with its general boundary and initial conditions will be given. This chapter also briefly discusses the discretization technique that has been used.
- Chapter 3 presents a simple parametric problem with one parameter to introduce the PGD concept. This chapter shows in detail how the PGD will apply to the parametric PDE problem.
- Chapter 4 shows the extension of the PGD method to the THM problem. One of the work's main contributions will be presented in this chapter. The details of the separated representation of matrices and vectors of the THM problem will be shown.

- Chapter 5 aims at validating the technique by using a problem for which an analytical solution is available, inspired by the work of Selvadurai and Suvorov [129]. This chapter's aim is to illustrate that the methodology (a combination of the PGD with coupled THM) is working properly.
- Chapter 6 extracts the application of PGD on transient coupled THM cases inspired by the engineered barrier systems. This chapter presents the problem statement and the results of such a combination that is beneficial for identifying and optimizing application prospects.
- Chapter 7 proposes a discussion concerning the computational methods for coupled problems by using the PGD methodology.
- Chapter 8 collect all the contributions, conclusions and the future outlooks.

Chapter 2

Governing equations and discretization

In this chapter, the strong form of the THM governing equations and the corresponding constitutive laws will be presented. However, the governing equations here will be presented by considering simplifying assumptions that were mentioned in the previous chapter (Section 1.3).

Section 2.1 briefly outlines the constitutive laws, and governing equations. Section 2.2 shows the weak form of the problem and its discretization. In this section, the Finite Element Method (FEM) [174] with an axisymmetric assumption has been used as computational method.

2.1 Governing equations

In this section, the corresponding constitutive laws for the thermal, hydraulic, and mechanical components, the governing equations and notation definitions, as well as their boundary and initial conditions, will be presented. The implementation assumption in this work is that all problems are axisymmetric, therefore coordinates are provided in cylindrical coordinates, resulting in computational efficiency since the two-dimensional setting can describe the three-dimensional nature of the problem. The spatial coordinates are r and z, which represent the radial coordinate (horizontal

direction) and the axial coordinate (vertical direction), respectively. They are denoted in the domain Ω, which is represented by the coordinates (r, z).

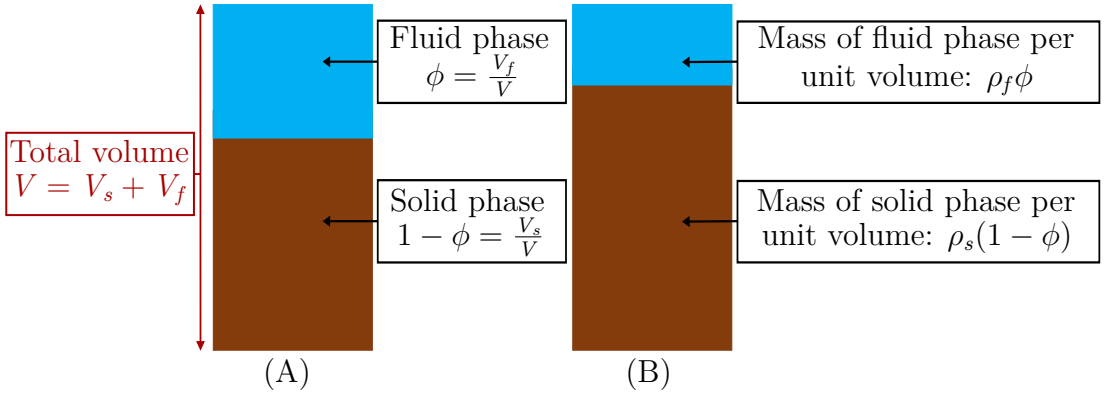

Figure 2.1: (A) Porosity (ϕ) in a fully saturated medium is determined by the proportion of fluid volume (V_f) to the overall volume (V). (B) shows the mass of each phase per unit volume.

Considering the problem to be fully saturated, the porous medium becomes a two-phase material. Therefore, porosity is defined here as the proportion of the fluid's volume (V_f) to the overall volume (V), which is represented by ϕ. Figure 2.1 illustrates the porosity and mass of each phase per unit volume in a fully saturated porous medium.

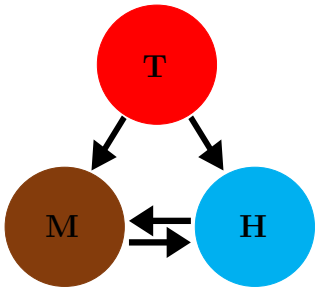

Figure 2.2: The THM process.

Figure 2.2 recalls that the THM model is thermally one-way coupled in this work. The main unknowns of the problem are temperature (T), pore water pressure (p), and the vector of displacement ($\mathbf{u}$).

2.1.1 Constitutive laws

The constitutive laws depend on the main unknowns of the THM problem. For the thermal part, Fourier's law (heat flux) and for the hydraulic part, Darcy's law

(hydraulic flux) have been used:

$$\mathbf{i}_c = -\kappa \boldsymbol{\nabla} T, \tag{2.1}$$

$$\mathbf{j}_w = -\frac{K}{\rho_f g}(\boldsymbol{\nabla} p - \rho_f \mathbf{g}), \tag{2.2}$$

where Equation (2.1) is Fourier's law [129], and κ is the heat conductivity in the saturated condition, and $\mathbf{i}_c$ is the heat flux. Equation (2.2) presents the hydraulic flux ($\mathbf{j}_w$) and is known as Darcy's law [47]. $g = 10\frac{\mathrm{m}}{\mathrm{s}^2}$ and $\mathbf{g} = [0, -g]$ are gravity and the vector of gravitational acceleration, respectively, and K is the hydraulic conductivity.

In the mechanical part, the definition of the stress tensor is necessary. It is a function of all the unknown variables. The constitutive relationships outlined in this thesis for the mechanical part consider only Hookean elastic materials [129]:

$$\boldsymbol{\sigma} = \mathbb{C} : \boldsymbol{\nabla}\mathbf{u} - \alpha p \boldsymbol{\delta} - 3K_D \alpha_s T \boldsymbol{\delta}, \tag{2.3}$$

where in Equation (2.3), $\mathbb{C}$ is the fourth-order tensor describing the stiffness of the material. It is isotropic and expressed in the axisymmetric form. In addition, α is the Biot coefficient, $\boldsymbol{\delta}$ is the identity matrix (Kronecker delta), K_D is the bulk modulus of the fully drained poroelastic body, and α_s is the heat expansion coefficient of the solid phase. By using Voigt notation, the fourth order tensor $\mathbb{C}$ is given as the material matrix $\mathbf{C}$ (for the axisymmetric case) [174]:

$$\mathbf{C} = \frac{E}{(1+\nu)(1-2\nu)} \begin{bmatrix} 1-\nu & \nu & \nu & 0 \\ \nu & 1-\nu & \nu & 0 \\ \nu & \nu & 1-\nu & 0 \\ 0 & 0 & 0 & \frac{1}{2}(1-2\nu) \end{bmatrix}. \tag{2.4}$$

In Equation (2.4), E and ν are elastic modulus and Poisson's ratio, from which K_D and α are defined by the following relations in Equation (2.3) [129]:

$$K_D = \frac{E}{1-2\nu}, \tag{2.5}$$

$$\alpha = 1 - \frac{K_D}{K_s}, \tag{2.6}$$

where in Equation (2.6), K_s is the bulk modulus of the solid phase. The concept of Biot's coefficient α tries to express how much of an initial instantaneous volumetric

loading is transferred onto the solid skeleton and how much it transfers to the fluid. For sloppy soils, usually, it is taken as unity (initially, any volumetric loading is fully obtained by the fluid phase). However, for rock like granite, it will be taken as $\alpha = 0.75$ [91].

Thermal or Hydraulic part	Mechanical part
$\begin{bmatrix} \frac{\partial}{\partial r} \\ \frac{\partial}{\partial z} \end{bmatrix}$	$\begin{bmatrix} \frac{\partial}{\partial r} & 0 \\ 0 & \frac{\partial}{\partial z} \\ \frac{1}{r} & 0 \\ \frac{\partial}{\partial z} & \frac{\partial}{\partial r} \end{bmatrix}$

Table 2.1: Differential operator ($\boldsymbol{\nabla}$) descriptions for axisymmetric conditions.

Table 2.1 defines the differential operator ($\boldsymbol{\nabla}$) [174], also known as the nabla operator in all the Equations (2.1), (2.2), and (2.3).

2.1.2 The field equations

The Thermal-Hydraulic-Mechanical (THM) coupled processes in porous media are described by partial differential equations (PDEs) that can be derived by inserting the constitutive laws (Equations (2.1), (2.2), and (2.3)) into the definitions of the continuity equations and stress equilibrium. All these fundamental theoretical bases for THM problems in this work can be found in Olivella et al. [108], Nguyen and Selvadurai [97], Wang [162], Verruijt [157], and Selvadurai and Suvorov [129]. The PDEs formulation is thermally one-way coupled, and the governing equations of our mathematical model to simulate the THM behavior are the following:

$$\begin{cases} ((1-\phi)\rho_s c_s + \phi\rho_f c_f)\,\dot{T} - \boldsymbol{\nabla}\cdot(\kappa\boldsymbol{\nabla}T) = q(t) & \text{in } \Omega \times I_t, \\ \\ (\dfrac{\phi}{K_f} + \dfrac{\alpha-\phi}{K_s})\dot{p} - \boldsymbol{\nabla}\cdot\Big(\dfrac{K}{\rho_f g}(\boldsymbol{\nabla}p - \rho_f \mathbf{g})\Big) & \\ \qquad + \alpha\boldsymbol{\nabla}\cdot\dot{\mathbf{u}} = (3\phi\alpha_f + 3(\alpha-\phi)\alpha_s)\,\dot{T} & \text{in } \Omega \times I_t, \\ \\ \alpha\boldsymbol{\nabla}p - \boldsymbol{\nabla}\cdot(\mathbb{C} : \boldsymbol{\nabla}\mathbf{u}) = \mathbf{b} - 3K_D\alpha_s\boldsymbol{\nabla}T & \text{in } \Omega \times I_t. \end{cases} \tag{2.7}$$

As already mentioned, the primary unknowns in these PDEs are the temperature (T), the pore pressure (p), and the vector of displacement ($\mathbf{u} = [u_r, u_z]$). $\dot{T}$, $\dot{p}$, and $\dot{\mathbf{u}}$ denote the derivatives of temperature, pressure, and vector of displacement with

respect to time. In Equation (2.7), $\mathbf{b}$ and $q(t)$ are the vectors of body force and the heat source respectively. Figure 2.3 presents a generic domain, where Γ_{t}, Γ_{r}, Γ_{b}, and Γ_{l} are the boundaries at the top, right, bottom, and left of Ω. In the governing equations, $\Omega \times I_t$ represents that the PDEs are valid in the spatial domain (Ω) and the interval of time (t). Table 2.2 describes all the material properties involved with their units.

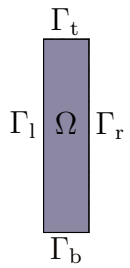

Figure 2.3: Boundaries and domain of a generic axisymmetric problem are presented. Here, Ω represents the spatial domain of the problem, while Γ_{t}, Γ_{r}, Γ_{b}, and Γ_{l} are the boundaries at the top, right, bottom, and left of Ω, respectively.

Symbol	Units	Description
ρ_s	$\mathrm{kg\,m^{-3}}$	Density of the solid phase
ρ_f	$\mathrm{kg\,m^{-3}}$	Density of the fluid phase
c_s	$\mathrm{J\,kg^{-1}\,{}^{\circ}C^{-1}}$	Specific heat of the solid phase
c_f	$\mathrm{J\,kg^{-1}\,{}^{\circ}C^{-1}}$	Specific heat of the fluid phase
κ	$\mathrm{W\,m^{-1}\,{}^{\circ}C^{-1}}$	Heat conductivity of the porous medium
α	-	Biot's coefficient
K_D	Pa	Bulk modulus of the fully drained poroelastic body
α_s	$\mathrm{{}^{\circ}C^{-1}}$	Heat expansion coefficient of the solid phase
α_f	$\mathrm{{}^{\circ}C^{-1}}$	Heat expansion coefficient of the fluid phase
K	$\frac{\mathrm{m}}{\mathrm{s}}$	Hydraulic conductivity of the porous medium
ϕ	-	Porosity
K_f	Pa	Bulk modulus of the fluid phase
K_s	Pa	Bulk modulus of the solid phase
E	Pa	Elastic modulus
ν	-	Poisson's ratio

Table 2.2: Properties description.

It is necessary to specify proper boundary and initial conditions for the solution of the governing PDEs. Γ represents the general format of the boundaries, which is the following:

$$\Gamma = \Gamma_{\mathrm{t}} \cup \Gamma_{\mathrm{r}} \cup \Gamma_{\mathrm{b}} \cup \Gamma_{\mathrm{l}}.$$

For the temperature field, the boundary conditions are defined to be either Dirichlet boundary conditions (prescribed temperature) on Γ_D^T or Neumann boundary conditions (prescribed heat flux) on Γ_N^T:

$$T(\mathbf{x}, t) = T_D(\mathbf{x}, t), \quad \mathbf{x} \in \Gamma_D^T, \tag{2.8}$$

$$\mathbf{i}_c \cdot \mathbf{n} = i_N(\mathbf{x}, t), \quad \mathbf{x} \in \Gamma_N^T. \tag{2.9}$$

Equation (2.8) presents the prescribed temperature on Γ_D^T, while Equation (2.9) presents the prescribed heat flux on Γ_N^T. $T_D(\mathbf{x}, t)$ and $i_N(\mathbf{x}, t)$ are given functions of position and time, with $\mathbf{n}$ the vector normal to the boundaries. The boundaries must satisfy:

$$\Gamma = \Gamma_D^T \cup \Gamma_N^T,$$

$$\Gamma_D^T \cap \Gamma_N^T = 0.$$

For the temperature, the initial condition is specified as follows:

$$T(\mathbf{x}, 0) = T_0(\mathbf{x}) \tag{2.10}$$

The boundary conditions for the pore water pressure field are presented in a similar manner as follows:

$$p(\mathbf{x}, t) = p_D(\mathbf{x}, t), \quad \mathbf{x} \in \Gamma_D^p, \tag{2.11}$$

$$\mathbf{j}_w \cdot \mathbf{n} = j_N(\mathbf{x}, t), \quad \mathbf{x} \in \Gamma_N^p. \tag{2.12}$$

Equation (2.11) presents the prescribed pore water pressure on Γ_D^p, while Equation (2.12) evaluates the prescribed hydraulic flux on Γ_N^p. $p_D(\mathbf{x}, t)$ and $j_N(\mathbf{x}, t)$ are given functions of position and time. The corresponding boundaries must satisfy:

$$\Gamma = \Gamma_D^p \cup \Gamma_N^p,$$

$$\Gamma_D^p \cap \Gamma_N^p = 0.$$

For the pore water pressure, the initial condition is specified as follows:

$$p(\mathbf{x}, 0) = p_0(\mathbf{x}) \tag{2.13}$$

The boundary conditions for the mechanical part of the problem are prescribed displacement on Γ_D^u and prescribed traction forces on Γ_N^u:

$$\mathbf{u}(\mathbf{x}, t) = \mathbf{u}_D(\mathbf{x}, t), \quad \mathbf{x} \in \Gamma_D^u, \tag{2.14}$$

$$\boldsymbol{\sigma} \cdot \mathbf{n} = \mathbf{t}_N(\mathbf{x}, t), \quad \mathbf{x} \in \Gamma_N^u. \tag{2.15}$$

Equation (2.14) presents the prescribed displacement on Γ_D^u, while Equation (2.15) shows the prescribed traction forces on Γ_N^u. $\mathbf{u}_D(\mathbf{x}, t)$ and $\mathbf{t}_N(\mathbf{x}, t)$ are given vector functions of position and time. The corresponding boundaries must satisfy:

$$\Gamma = \Gamma_D^u \cup \Gamma_N^u,$$

$$\Gamma_D^u \cap \Gamma_N^u = 0.$$

The initial conditions for the displacement field should be such that the different fields, especially pressure, stresses, and displacement, be balanced and at equilibrium. In this work, solving the steady-state version of the generic problem is applied based on the assumptions already mentioned in the previous section. By applying the initial condition of temperature (Equation (2.10)) and pressure (Equation (2.13)) in the third equation of governing Equations (2.7), the initial condition of displacement field is found:

$$\mathbf{u}(\mathbf{x}, 0) = \mathbf{u}_0(\mathbf{x}) \tag{2.16}$$

2.2 Weak form and discretization

This section states at first the weak form of the general form of the THM governing Equations (2.7). The vectors of unknowns will be defined. Later by using space (axisymmetric FEM [174]) and time discretization (θ-rule method [92]), the discretized matrices and vectors will be defined.

2.2.1 Weak form

It is essential to establish a set of weighting functions and test solutions for the temperature, pore water pressure, and displacement vector in order to build the weak form. However, this section presents only the weak form of the main governing Equations (2.7) for any v_{T}, v_{p}, and $\mathbf{v}_{\mathrm{d}}$ (test functions of temperature, pore water pressure, and displacements, respectively) satisfying homogeneous Dirichlet boundary

conditions on Γ_D^T, Γ_D^p, and Γ_D^u:

$$\begin{cases} \displaystyle\int_\Omega \boldsymbol{\nabla} v_{\mathrm{T}} \cdot (\kappa \boldsymbol{\nabla} T)\, rd\Omega + \int_\Omega v_{\mathrm{T}}\, ((1-\phi)\rho_s c_s + \phi\rho_f c_f)\, \dot{T}\, rd\Omega \\ \qquad\qquad = \displaystyle\int_\Gamma v_{\mathrm{T}}\, i_N\, rd\Gamma + \int_\Omega v_{\mathrm{T}}\, q(t)\, rd\Omega \end{cases} \quad \text{in} \quad \Omega \times I_t,$$

$$\begin{cases} \displaystyle\int_\Omega \boldsymbol{\nabla} v_{\mathrm{p}} \cdot (\frac{K}{\rho_f g} \boldsymbol{\nabla} p)\, rd\Omega + \int_\Omega v_{\mathrm{p}}\, (\frac{\phi}{K_f} + \frac{\alpha-\phi}{K_s}) \dot{p}\, rd\Omega \\ \qquad + \displaystyle\int_\Omega v_{\mathrm{p}}\, \alpha \boldsymbol{\nabla} \cdot \dot{\mathbf{u}}\, rd\Omega = \int_\Omega v_{\mathrm{p}}\, (3\phi\alpha_f + 3(\alpha-\phi)\alpha_s)\, \dot{T}\, rd\Omega \\ \qquad\qquad + \displaystyle\int_\Gamma v_{\mathrm{p}}\, j_N\, rd\Gamma + \int_\Omega \boldsymbol{\nabla} v_{\mathrm{p}}\, \frac{K}{\rho_f g} \rho_f \mathbf{g}\, rd\Omega \end{cases} \quad \text{in} \quad \Omega \times I_t, \tag{2.17}$$

$$\begin{cases} \displaystyle\int_\Omega \mathbf{v}_{\mathrm{d}}\, \alpha \boldsymbol{\nabla} p\, rd\Omega + \int_\Omega \boldsymbol{\nabla} \mathbf{v}_{\mathrm{d}}\, \cdot (\mathbb{C} : \boldsymbol{\nabla} \mathbf{u})\, rd\Omega = \\ \qquad - \displaystyle\int_\Omega \mathbf{v}_{\mathrm{d}}\, 3K_D \alpha_s \boldsymbol{\nabla} T\, rd\Omega + \int_\Omega \mathbf{v}_{\mathrm{d}}\, \mathbf{b}\, rd\Omega + \int_\Gamma \mathbf{v}_{\mathrm{d}}\, \mathbf{t}_N\, rd\Gamma \end{cases} \quad \text{in} \quad \Omega \times I_t.$$

In Equation (2.17), the terms i_N, j_N, and $\mathbf{t}_N$ are the heat and hydraulic fluxes and vector of traction forces, respectively. Their explicit dependence on $\mathbf{x}$ and t has been omitted for brevity. The main unknowns, T, p, and $\mathbf{u}$, are discretized as:

$$\begin{cases} T = \mathbf{N}_{\mathrm{T}} \mathbf{T}, \\ p = \mathbf{N}_{\mathrm{p}} \mathbf{p}, \\ \mathbf{u} = \mathbf{N}_{\mathrm{d}} \mathbf{d}. \end{cases} \tag{2.18}$$

In Equation (2.18), $\mathbf{T}$, $\mathbf{p}$, and $\mathbf{d}$ represent the nodal quantities of temperature, pressure, and displacement, respectively, while $\mathbf{N}_{\mathrm{T}}$, $\mathbf{N}_{\mathrm{p}}$, and $\mathbf{N}_{\mathrm{d}}$ correspond to the matrix of shape functions for temperature, pore water pressure, and displacement. The explanation of these matrices will be provided in the next section.

2.2.2 FEM formulation

This section presents the discrete equations for the THM model. The spatial domain is discretized using the axisymmetric FEM concept [174], while time is discretized using the θ-rule for the time discretization scheme. θ is a time-integration parameter determined based on the work of Nguyen and Selvadurai [97], who observed through their investigation that using $\theta = 0.75$ provides a reliable and stable solution. We can approximate time derivates by:

$$\dot{g} = f(g,t) \;\; \rightarrow \;\; g^{i+1} - g^i = \Delta t(1-\theta) f^i + \Delta t \theta f^{i+1}. \tag{2.19}$$

Where g and f are arbitrary functions in Equation (2.19), and Δt is the time step. The exponents $i+1$ and i represent the current and previous times, respectively.

The Galerkin-type weighted residual and θ-rule techniques are used to formulate the computational scheme used to solve the governing equations. The following discretized equations are obtained in the matrices and vector format by considering that the externally supplied heat and hydraulic fluxes are zero:

$$\left[\mathbf{M}_{\mathrm{T}} + \Delta t\theta \mathbf{K}_{\mathrm{T}}\right] \mathbf{T}^{i+1} = \Delta t \mathbf{f}_{\mathrm{q}} + \left[\mathbf{M}_{\mathrm{T}} + \Delta t(\theta - 1)\mathbf{K}_{\mathrm{T}}\right] \mathbf{T}^{i}, \tag{2.20}$$

$$\begin{aligned} \begin{bmatrix} \mathbf{M}_{\mathrm{p}} + \Delta t\theta \mathbf{K}_{\mathrm{p}} & \mathbf{G}_{\mathrm{pd}} \\ \theta \mathbf{G}_{\mathrm{dp}} & \theta \mathbf{K}_{\mathrm{d}} \end{bmatrix} \begin{bmatrix} \mathbf{p}^{i+1} \\ \mathbf{d}^{i+1} \end{bmatrix} = \begin{bmatrix} \Delta t \mathbf{f}_{\mathbf{b}_{\mathrm{f}}} \\ \mathbf{f}_{\mathrm{d}} \end{bmatrix} + \\ \begin{bmatrix} \mathbf{M}_{\mathrm{p}} + \Delta t(\theta - 1)\mathbf{K}_{\mathrm{p}} & \mathbf{G}_{\mathrm{pd}} \\ (\theta - 1)\mathbf{G}_{\mathrm{dp}} & (\theta - 1)\mathbf{K}_{\mathrm{d}} \end{bmatrix} \begin{bmatrix} \mathbf{p}^{i} \\ \mathbf{d}^{i} \end{bmatrix} + \\ \begin{bmatrix} \mathbf{M}_{\mathrm{pT}} & -\mathbf{M}_{\mathrm{pT}} \\ -\theta \mathbf{G}_{\mathrm{dT}} & (\theta - 1)\mathbf{G}_{\mathrm{dT}} \end{bmatrix} \begin{bmatrix} \mathbf{T}^{i+1} \\ \mathbf{T}^{i} \end{bmatrix}, \end{aligned} \tag{2.21}$$

where in Equations (2.20) and (2.21), $\mathbf{T}^{i+1}$, $\mathbf{p}^{i+1}$ and $\mathbf{d}^{i+1}$ are the unknowns for temperatures, pore water pressures, and displacements, with $\mathbf{T}^{i}$, $\mathbf{p}^{i}$ and $\mathbf{d}^{i}$ the known values for temperatures, pore water pressures, and displacements from the previous time. The descriptions of the symbols in Equations (2.20) and (2.21) are presented in Table 2.3.

Symbol	Description
$\mathbf{K}_{\mathrm{T}}$	Stiffness matrix for thermal part
$\mathbf{M}_{\mathrm{T}}$	Mass matrix for thermal part
$\mathbf{M}_{\mathrm{pT}}$	Coupling mass matrix of temperature in hydraulic part
$\mathbf{K}_{\mathrm{p}}$	Stiffness matrix for hydraulic part
$\mathbf{M}_{\mathrm{p}}$	Mass matrix for hydraulic part
$\mathbf{G}_{\mathrm{pd}}$	Coupling matrix of volumetric strain in hydraulic part
$\mathbf{K}_{\mathrm{d}}$	Stiffness matrix for mechanical part
$\mathbf{G}_{\mathrm{dT}}$	Coupling matrix of temperature in mechanical part
$\mathbf{G}_{\mathrm{dp}}$	Coupling mtrix of pressure in mechanical part
$\mathbf{f}_{\mathrm{q}}$	Force term generated by heat source
$\mathbf{f}_{\mathbf{b}_{\mathrm{f}}}$	Force term generated by gravity in hydraulic part
$\mathbf{f}_{\mathrm{d}}$	Force term generated by body force and traction force

Table 2.3: Symbols description.

The integration definitions for the components in Equations (2.20) and (2.21) can be found by referring to Equations (2.17) through (2.21). They are listed below:

$$\mathbf{K}_{\mathrm{T}} = \int_{\Omega} \mathbf{B}_{\mathrm{T}}^{\top} \kappa \mathbf{B}_{\mathrm{T}} \, r d\Omega, \tag{2.22}$$

$$\mathbf{M}_{\mathrm{T}} = \int_{\Omega} \mathbf{N}_{\mathrm{T}}^{\top} ((1-\phi)\rho_s c_s + \phi \rho_f c_f) \mathbf{N}_{\mathrm{T}} \, r d\Omega, \tag{2.23}$$

$$\mathbf{M}_{\mathrm{pT}} = \int_{\Omega} \mathbf{N}_{\mathrm{p}}^{\top} (3\phi\alpha_f + 3(\alpha-\phi)\alpha_s) \mathbf{N}_{\mathrm{T}} \, r d\Omega, \tag{2.24}$$

$$\mathbf{K}_{\mathrm{p}} = \int_{\Omega} \mathbf{B}_{\mathrm{p}}^{\top} \frac{K}{\rho_f g} \mathbf{B}_{\mathrm{p}} \, r d\Omega, \tag{2.25}$$

$$\mathbf{M}_{\mathrm{p}} = \int_{\Omega} \mathbf{N}_{\mathrm{p}}^{\top} (\frac{\phi}{K_f} + \frac{\alpha-\phi}{K_s}) \mathbf{N}_{\mathrm{p}} \, r d\Omega, \tag{2.26}$$

$$\mathbf{G}_{\mathrm{pd}} = \int_{\Omega} \mathbf{N}_{\mathrm{p}}^{\top} \alpha \mathbf{B}_{\mathrm{v}} \, r d\Omega, \tag{2.27}$$

$$\mathbf{K}_{\mathrm{d}} = \int_{\Omega} \mathbf{B}_{\mathrm{d}}^{\top} \mathbb{C} \mathbf{B}_{\mathrm{d}} \, r d\Omega, \tag{2.28}$$

$$\mathbf{G}_{\mathrm{dT}} = \int_{\Omega} \mathbf{N}_{\mathrm{d}}^{\top} 3K_D \alpha_s \mathbf{B}_{\mathrm{T}} \, r d\Omega, \tag{2.29}$$

$$\mathbf{G}_{\mathrm{dp}} = \int_{\Omega} \mathbf{N}_{\mathrm{d}}^{\top} \alpha \mathbf{B}_{\mathrm{p}} \, r d\Omega, \tag{2.30}$$

$$\mathbf{f}_{\mathrm{q}} = \int_{\Omega} \mathbf{N}_{\mathrm{T}}^{\top} q(t) \, r d\Omega, \tag{2.31}$$

$$\mathbf{f}_{\mathbf{b}_{\mathrm{f}}} = \int_{\Omega} \mathbf{N}_{\mathrm{p}}^{\top} \frac{K}{\rho_f g} \rho_f \mathbf{g} \, r d\Omega, \tag{2.32}$$

$$\mathbf{f}_{\mathrm{d}} = \int_{\Omega} \mathbf{N}_{\mathrm{d}}^{\top} \mathbf{b} \, r d\Omega + \int_{\Gamma} \mathbf{N}_{\mathrm{d}}^{\top} \mathbf{t}_N \, r d\Gamma. \tag{2.33}$$

In all the preceding equations, $\mathbf{N}_{\mathrm{T}}$, $\mathbf{N}_{\mathrm{p}}$, and $\mathbf{N}_{\mathrm{d}}$ are the matrices of shape functions for temperature, pressure, and displacements, respectively. These matrices, by using bilinear quadrilateral elements, are expressed as follows:

$$\mathbf{N}_{\mathrm{T}} = \mathbf{N}_{\mathrm{p}} = \begin{bmatrix} N_1 & N_2 & N_3 & N_4 \end{bmatrix}, \tag{2.34}$$

$$\mathbf{N}_{\mathrm{d}} = \begin{bmatrix} N_1 & 0 & N_2 & 0 & N_3 & 0 & N_4 & 0 \\ 0 & N_1 & 0 & N_2 & 0 & N_3 & 0 & N_4 \end{bmatrix}. \tag{2.35}$$

$\mathbf{B}_{\mathrm{T}}$, $\mathbf{B}_{\mathrm{p}}$, $\mathbf{B}_{\mathrm{v}}$, and $\mathbf{B}_{\mathrm{d}}$ are B-operator matrices for temperature, pressure, volumetric displacements, and displacement. They are defined as follows:

$$\begin{aligned}\mathbf{B}_{\mathrm{T}} = \mathbf{B}_{\mathrm{p}} &= \boldsymbol{\nabla}\mathbf{N}_{\mathrm{T}} \\ &= \begin{bmatrix} \frac{\partial}{\partial r} \\ \frac{\partial}{\partial z} \end{bmatrix} \mathbf{N}_{\mathrm{T}},\end{aligned} \tag{2.36}$$

$$\begin{aligned}\mathbf{B}_{\mathrm{v}} &= \boldsymbol{\nabla} \cdot \mathbf{N}_{\mathrm{d}} \\ &= \begin{bmatrix} \frac{\partial}{\partial r} + \frac{1}{r} & \frac{\partial}{\partial z} \end{bmatrix} \mathbf{N}_{\mathrm{d}},\end{aligned} \tag{2.37}$$

$$\begin{aligned}\mathbf{B}_{\mathrm{d}} &= \boldsymbol{\nabla}\mathbf{N}_{\mathrm{d}} \\ &= \begin{bmatrix} \frac{\partial}{\partial r} & 0 \\ 0 & \frac{\partial}{\partial z} \\ \frac{1}{r} & 0 \\ \frac{\partial}{\partial z} & \frac{\partial}{\partial r} \end{bmatrix} \mathbf{N}_{\mathrm{d}}.\end{aligned} \tag{2.38}$$

The rest of the descriptions of symbols in the Equations ((2.22) to (2.33)) are presented in Table 2.3.

Bi-linear quadrilateral shape functions are used in this work for temperature, pressure, and displacement. Reviewing the literature shows that the solution to such problems may contain a behavior with spurious oscillations or have some jumps. Such instability conditions can be tracked by the so-called inf-sup conditions (a.k.a Ladyzhenskaya-Babuska-Brezzi conditions) [6, 17, 7]. The use of bilinear quadrilateral elements has been observed in geotechnical applications involving coupled HM and THM problems. For example, Song et al. [136] employed a 2D axisymmetric numerical model with linear quadrilateral elements to analyze hydro-mechanical behavior in tunnels, introducing a novel excavation method in CODE-BRIGHT software. Similarly, Marcelo et al. [141] investigated the THM behavior of a Full-scale Engineered Barriers Experiment using a numerical model with bilinear quadrilateral elements, accurately predicting barrier state and evolution. It is noteworthy that CODE-BRIGHT, designed to solve coupled porous media problems (THM and HM), incorporates a generalized selective integration procedure that effectively addresses issues such as locking, mesh distortion, and hourglassing associated with linear quadrilateral elements [110].

In this work, no spurious oscillations have been observed. However, based on the literature review, it is recommended to check the inf-sup condition to ensure

stability. It should be noted that the main contribution of this work is not focused on FEM; rather, it lies in the combination of THM with the PGD technique. If spurious oscillations or jumps are encountered in the FEM solution, higher-order elements such as quadratic quadrilaterals or serendipity shape functions are recommended for the displacement field, as shown in the work by Nguyen and Selvadurai [97].

On the other hand, the PGD technique is an intrusive method that relies on separate tensors and vectors. These components, which will be explained in greater detail in the following chapters, are specifically tailored for bilinear quadrilateral elements. The code has been developed to accommodate these elements, and incorporating quadratic quadrilateral elements would require further modifications.

Chapter 3

Proper Generalized Decomposition for parametric problems

Decision-taking in practical engineering usually requires accounting and evaluating a large number of possible situations. In computational engineering, this is translated into solving many numerical models that usually are computationally extenuating. This is the case in design and parameter optimization, identification of parameters, and uncertainty quantification. These problems can usually be described by a main set of equations depending on some parameters. The family of solutions to evaluate arise from the range of values that the parameters might take. Naturally, the number of solutions to consider grows exponentially with the number of parameters that are considered, and so does the number of numerical models that need to be solved. Rapidly, the amount of computation required becomes unfeasible to be used in practice.

Model Order Reduction (MOR) is a family of techniques that allow dealing with parametric problems in a computationally efficient way. This work focuses on one technique called Proper Generalized Decomposition (PGD). It is based on two main ingredients: i) a separated representation of variables and operators and ii) a greedy enrichment strategy that computes the solution of the parametric problem iteratively.

In this chapter, the principles of the PGD method are presented, and its use is exemplified by a simple parametric steady-state thermal problem. Section 3.1 presents the statement of the parametric problem, Section 3.2 introduces the main

ideas of the PGD technique in the context of the simple problem that is shown in the first section, and Section 3.3 shows and discusses some results obtained by PGD. For a deeper discussion on the PGD method, the reader is referred to [175, 134].

3.1 Steady-state thermal problem

The simple problem under consideration in this section serves for the purpose of presenting the reduced order methodology and also to validate the implementation. It is governed by a pure diffusion equation in a cylinder with axisymmetric geometry, and therefore the 3D problem is described in a 2D domain. Moreover, the problem is built such that the solution is constant along the z-axis and only depends on r (Figure 3.1), and therefore, the solution is in practice 1D.

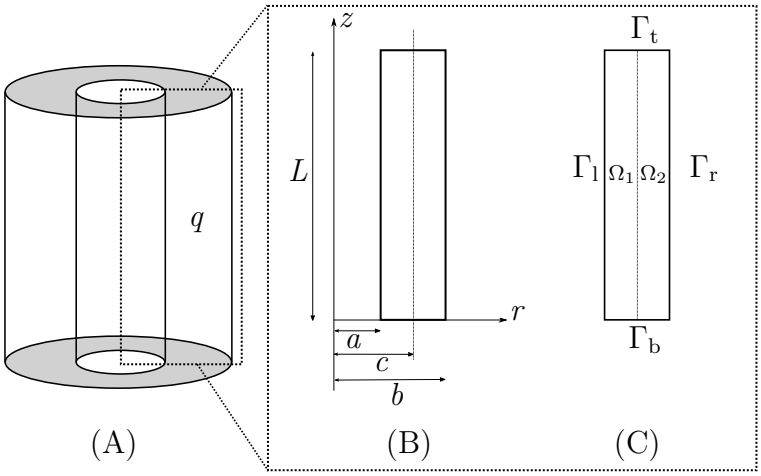

Figure 3.1: (A) Axisymmetric cylinder, (B) geometry, and (C) boundaries and domain.

The problem is governed by a Poisson equation,

$$-\boldsymbol{\nabla} \cdot (\kappa(\mathbf{x}) \boldsymbol{\nabla} T(\mathbf{x})) = q \quad \text{in } \Omega, \tag{3.1}$$

and closed with the proper boundary conditions described below. Using the axisymmetric symmetry, we name the spatial axis as r in the radial direction and z along the rotational axis. The vector $\mathbf{x}$ has coordinates (r, z). The domain $\Omega = \Omega_1 \cup \Omega_2$, as presented in Figure 3.1-C, is divided into two parts, Ω_1 and Ω_2, having different material properties,

$$\kappa(\mathbf{x}) = \begin{cases} \kappa_1 & \text{for } \mathbf{x} \in \Omega_1, \\ \kappa_2 & \text{for } \mathbf{x} \in \Omega_2. \end{cases} \tag{3.2}$$

The boundaries of Ω are Γ_{t}, Γ_{r}, Γ_{b}, and Γ_{l} at the top, right, bottom, and left, respectively. The boundary conditions are,

$$\begin{cases} T(\mathbf{x}) = T_l & \text{on } \Gamma_{\mathrm{l}}, \\ T(\mathbf{x}) = T_r & \text{on } \Gamma_{\mathrm{r}}, \\ (-\kappa \boldsymbol{\nabla} T) \cdot \mathbf{n} = 0 & \text{on } \Gamma_{\mathrm{t}} \cup \Gamma_{\mathrm{b}}, \end{cases} \tag{3.3}$$

where T_r and T_l are constant temperatures.

3.1.1 Discretization

By applying Finite Element Method (FEM) as a high-fidelity technique to discretize the problem, the standard algebraic system is obtained;

$$\mathbf{K}_{\mathrm{T}}\mathbf{T} = \mathbf{f}_{\mathrm{q}}, \tag{3.4}$$

where $\mathbf{T}$ contains the nodal temperature values and $\mathbf{K}_{\mathrm{T}}$ and $\mathbf{f}_{\mathrm{q}}$ are defined as,

$$\mathbf{K}_{\mathrm{T}} = \int_{\Omega} \mathbf{B}_{\mathrm{T}}^{\top} \kappa(\mathbf{x}) \mathbf{B}_{\mathrm{T}} \, r \, d\Omega, \quad \mathbf{f}_{\mathrm{q}} = \int_{\Omega} \mathbf{N}_{\mathrm{T}}^{\top} q \, r \, d\Omega. \tag{3.5}$$

The definitions of the matrices $\mathbf{B}_{\mathrm{T}}$ and $\mathbf{N}_{\mathrm{T}}$ are in Equations (2.34) and (2.36).

3.1.2 Parametric problem

We aim to solve the aforementioned problem for a range of κ_2, having κ_1 fixed. In this situation, we call κ_2 a parameter of the problem. In this thesis, all parameters will be noted with the letter μ. The thermal diffusivity κ therefore becomes,

$$\kappa(\mathbf{x}, \mu) = \begin{cases} \kappa_1 & \text{in } \Omega_1 \times I_\mu, \\ \mu & \text{in } \Omega_2 \times I_\mu, \end{cases} \tag{3.6}$$

where $\mu \in I_\mu = [\mu^{\min}, \mu^{\max}]$, and I_μ is the interval domain of the parameter. The parametric problem then becomes: find $T(\mathbf{x}, \mu)$ such as,

$$\begin{cases} -\boldsymbol{\nabla} \cdot (\kappa(\mathbf{x}, \mu) \boldsymbol{\nabla} T(\mathbf{x}, \mu)) = q & \text{in } \Omega \times I_\mu, \\ (-\kappa \boldsymbol{\nabla} T) \cdot \mathbf{n} = 0 & \text{on } (\Gamma_{\mathrm{t}} \cup \Gamma_{\mathrm{b}}) \times I_\mu, \\ T(\mathbf{x}, \mu) = T_l & \text{on } \Gamma_{\mathrm{l}} \times I_\mu, \\ T(\mathbf{x}, \mu) = T_r & \text{on } \Gamma_{\mathrm{r}} \times I_\mu, \end{cases} \tag{3.7}$$

Following the usual discretization procedure, the parametric problem is written in the algebraic form, and it results in a linear system of equations in which the matrix depends on the parameter,

$$\mathbf{K}_{\mathrm{T}}(\mu)\mathbf{T}(\mu) = \mathbf{f}_{\mathrm{q}}. \tag{3.8}$$

The solution vector, $\mathbf{T}(\mu)$, naturally inherits the dependence on the parameter. In this particular parametrization, the right-hand side $\mathbf{f}_{\mathrm{q}}$ is constant, but in a general case, it can also be dependent on μ. To solve the Equation (3.8), the boundary conditions should be applied. So, by moving the known values of boundaries to the right-hand side, the problem is going to be rewritten as follows:

$$\mathbf{K}_{\mathrm{T}}(\mu)\mathbf{T}(\mu) = \underbrace{\mathbf{f}_{\mathrm{q}} - \mathbf{K}_{\mathrm{T}}(\mu)\, T_D}_{\mathbf{F}(\mu)}. \tag{3.9}$$

T_D in Equation (3.9) represents all the Dirichlet boundary conditions values in Equation (3.7). The residual of Equation (3.9) is introduced as,

$$\mathbf{R}(\mathbf{T}(\mu)) := \mathbf{F}(\mu) - \mathbf{K}_{\mathrm{T}}(\mu)\mathbf{T}(\mu) = \mathbf{0}. \tag{3.10}$$

Equation (3.9) is expressed in integral form as well. Initially, Equation (3.10) introduces the residual form of Equation (3.9). Consequently, by employing the concept of weighted residuals, $\mathbf{T}(\mu)$ is searched as the solution of Equation (3.11) that is required to hold true for all $\delta\mathbf{T}(\mu)$, considering test functions analogous to virtual temperatures:

$$\int_{I_\mu} \delta\mathbf{T}(\mu)^{\top}\mathbf{R}(\mathbf{T}(\mu))\, d\mu = 0. \tag{3.11}$$

Importantly, integration in (3.11) is solely performed over the parametric space I_μ, with no involvement in the physical space. This characteristic stems from the algebraic nature of Equation (3.9), which is already discretized in space. Thus, in this context, the scalar product of the residual (forces) and the test function (virtual temperatures) assumes the role of space integration. Using the FEM model to solve it, let us denote $\mathbb{R}^n_\Omega$ as the number of degrees of freedom in the spatial mesh, and $\mathbb{R}^n_\mu$ as the number of gridding points used to discretize the extra dimension of μ. The total number of unknowns to determine becomes $\mathrm{n}_\Omega \mathrm{n}_\mu$. This product grows fast with the number of parameters, producing the so-called curse of dimensionality.

Such PDE is parametric due to its dependency on the parameter. Considering the parameter as an extra dimension is the way of looking at the problem in this work. One technique to deal with such a problem is using Model Order Reduction (MOR) technique, in which Proper Generalized Decomposition (PGD) is used here.

3.2 Encapsulated PGD methodology

To study the parametric steady-state thermal problem discussed in the previous section, the Proper Generalized Decomposition (PGD) is used as a Model Order Reduction (MOR) technique specifically designed to address parametric problems based on Partial Differential Equations (PDEs). An algebraic implementation of PGD by Díez and coauthors [37, 38] enables us to solve a parametric system of equations similar to Equation (3.9). When discretizing the dimension μ, the parametric matrix $\mathbf{K}_{\mathrm{T}}(\mu)$ is treated as a high-order tensor with additional dimensions representing variations with respect to the parameters. The PGD technique utilizes separate representations for all entities involved, such as operators like $\mathbf{K}_{\mathrm{T}}(\mu)$ and $\mathbf{F}_{\mathrm{T}}(\mu)$, as well as unknown solutions like $\mathbf{T}(\mu)$, where the temperature is treated as an unknown variable. Consequently, all objects are constructed as sums of terms, where each term corresponds to a product of one-dimensional functions. We delve deeper into this concept in the subsequent subsections. The algebraic implementation of PGD offers a straightforward approach to solving parametric problems, encompassing all necessary operations of the PGD algorithm, including high-dimensional tensor multiplication, linear solvers, and summations. However, it still requires constructing the operators $\mathbf{K}_{\mathrm{T}}(\mu)$ and $\mathbf{F}(\mu)$ as separate high-order tensors. In certain cases, the construction is exact (e.g., when parameters control material properties), while in other scenarios (e.g., when parameters influence geometry), it becomes more intricate and necessitates approximations. In the following subsections, we introduce the key components of the PGD method and utilize the problem described in Section 3.1 as an example to illustrate the separated operators and solutions.

The implementation of the algebraic PGD used here was proposed by Díez et al [37] and it is available at `https://git.lacan.upc.edu/zlotnik/algebraicPGDtools`.

3.2.1 Proper Generalized Decomposition work in principle

The high-dimensional problems suffer from the so-called curse of dimensionality. Here, by applying the PGD technique, such a bottleneck is circumvented. Using separated representations is at the heart of the PGD. Consequently, in such a concept, high-dimensional functions are presented in separable formats.

The high-dimensional function F is said to be separable if, for some integer value M, and for $i = 1, 2, \ldots, \mathrm{n_d}$ ($\mathrm{n_d}$ is the number of dimensions), and $m = 1, 2, \ldots, M$,

there exists a set of functions f_i^m that take values from a one-dimensional (1D) domain $I_i = [a_i, b_i]$ such that,

$$F(x_1, x_2, \ldots, x_{\mathrm{d}}) = \sum_{m=1}^{M} f_1^m(x_1) f_2^m(x_2) \ldots f_{\mathrm{n_d}}^m(x_{\mathrm{n_d}}). \tag{3.12}$$

Each coordinate corresponds to a distinct dimension, while F spans $\mathrm{n_d}$ dimensions. To enhance comprehension, we decompose the function F into $\mathrm{n_d}$ one-dimensional functions (f_i^m). Each one-dimensional sectional domain ($[a_i, b_i]$) is discretized with a variable number of nodes. Assuming that each one-dimensional sectional domain has been discretized into n_i nodes denoted by $x_i^{k_i}$, where $k_i = 1, 2, \ldots, n_i$, the coordinates of these nodes can be obtained using the equation $x_i^{k_i} = a_i + \frac{b_i - a_i}{n_i - 1}(k_i - 1)$ for $i = 1, 2, \ldots, \mathrm{n_d}$ and $k_i = 1, 2, \ldots, n_i$. Each scalar data coordinate (x_i) is transformed into vector data ($\mathbf{x}_i$),

$$\mathbf{x}_i = [a_i, a_i + \frac{b_i - a_i}{n_i - 1}, a_i + 2\frac{b_i - a_i}{n_i - 1}, \ldots, a_i + \frac{b_i - a_i}{n_i - 1}(n_i - 2), b_i].$$

Then, the high-dimensional function F is readily represented by the tensor of its nodal values $\mathbb{F} \in \mathbb{R}^{n_1 \times n_2 \times \ldots \times n_{\mathrm{n_d}}}$, such that,

$$\mathbb{F} = F(\mathbf{x}_1, \mathbf{x}_2, \ldots, \mathbf{x}_{\mathrm{n_d}})$$

After the discretization of each dimension (means each x_i), the function F can be seen as a high-order tensor,

$$\mathbb{F} = \sum_{m=1}^{M} \mathbf{f}_1^m \otimes \mathbf{f}_2^m \otimes \ldots \otimes \mathbf{f}_{\mathrm{n_d}}^m, \tag{3.13}$$

where $\otimes$ is the tensor product. Note that Equations (3.12) and (3.13) are equivalent in the sense that vectors $\mathbf{f}_i^m$ contain the nodal values of $f_i^m(x_i)$.

Dealing with a parametric problem with the Encapsulated PGD methodology requires separately expressing all the discretized parametric operators in Equation (3.9). Thus, $\mathbf{K}_{\mathrm{T}}(\mu)$ and $\mathbf{F}(\mu)$, the known components of the discretized system, should be defined in the separable format,

$$\begin{aligned} \mathbf{K}_{\mathrm{T}}(\mu) &= \underbrace{\int_{\Omega_1} \mathbf{B}_{\mathrm{T}}^{\top} \kappa_1 \mathbf{B}_{\mathrm{T}} \, r d\Omega}_{\mathbf{K}_{\mathrm{T}}^1} \underbrace{1}_{\phi_\mu^1} + \underbrace{\int_{\Omega_2} \mathbf{B}_{\mathrm{T}}^{\top} \mathbf{B}_{\mathrm{T}} \, r d\Omega}_{\mathbf{K}_{\mathrm{T}}^2} \underbrace{\mu}_{\phi_\mu^2} \\ &= \mathbf{K}_{\mathrm{T}}^1 \, \phi_\mu^1 + \mathbf{K}_{\mathrm{T}}^2 \, \phi_\mu^2, \end{aligned} \tag{3.14}$$

$$\begin{aligned}\mathbf{F}(\mu) &= \underbrace{(\int_\Omega \mathbf{N}_\mathrm{T}^\top q \; r d\Omega - \mathbf{K}_\mathrm{T}^1 T_D)}_{\mathbf{f}^1} \underbrace{1}_{\phi_\mu^1} + \underbrace{(-\mathbf{K}_\mathrm{T}^2 T_D)}_{\mathbf{f}^2} \underbrace{\mu}_{\phi_\mu^2} \\ &= \mathbf{f}^1 \, \phi_\mu^1 + \mathbf{f}^2 \, \phi_\mu^2.\end{aligned} \tag{3.15}$$

Note that $\mathbf{K}_\mathrm{T}(\mu)$ is written separately as the sum of two terms, each term being the product of a part depending only on space, $\mathbf{K}_\mathrm{T}^1$ and $\mathbf{K}_\mathrm{T}^2$, and a part depending only on the parameter μ, $\phi_\mu^1(\mu) = 1$, and $\phi_\mu^2(\mu) = \mu$.

Note also that the form of the right-hand side $\mathbf{F}(\mu)$ has a similar structure. In this case, the parametric functions $\phi_\mu^i(\mu)$ are the same in $\mathbf{K}_\mathrm{T}(\mu)$, and as $\mathbf{F}(\mu)$. This is particular to this example, and it is a consequence of how boundary conditions are handled, but, generally, the number of terms of $\mathbf{F}(\mu)$ and the parametric functions involved can be different from these of $\mathbf{K}_\mathrm{T}(\mu)$. The discrete version of the stiffness matrix and force vector written as separated tensors are for the present case,

$$\mathbb{K} = \sum_{\hat{m}=1}^{2} \mathbf{K}_\mathrm{T}^{\hat{m}} \otimes \mathbf{\Phi}_\mu^{\hat{m}}, \tag{3.16}$$

$$\mathbb{F} = \sum_{\tilde{m}=1}^{2} \mathbf{f}^{\tilde{m}} \otimes \mathbf{\Phi}_\mu^{\tilde{m}}. \tag{3.17}$$

$\mathbf{\Phi}_\mu^{\hat{m}}$ and $\mathbf{\Phi}_\mu^{\tilde{m}}$ are the vectors representing the discretized versions of the parametric function when the parameter is discretized.

A separable approximation $\mathbb{T}^M$ is used to approximate the solution $\mathbf{T}(\mu)$ from Equation (3.9),

$$\mathbf{T}(\mu) \approx \mathbb{T}^M = \sum_{m=1}^{M} \mathbf{T}^m \otimes \mathbf{G}_\mu^m. \tag{3.18}$$

Note that the vectors $\mathbf{T}^m$ and $\mathbf{G}_\mu^m$ are unknowns that need to be determined, along with the number of terms M (referred to as the final number of modes required to obtain accurate results). Each term of Equation (3.18)represents a mode. These terms are determined by a spatial-dependent component, $\mathbf{T}^m$, and a parametric component, $\mathbf{G}_\mu^m$. It should be noted that the vectors in each mode are normalized as follows:

$$\tilde{\mathbf{T}}^m = \frac{\mathbf{T}^m}{\|\mathbf{T}^m\|}, \; \tilde{\mathbf{G}}_\mu^m = \frac{\mathbf{G}_\mu^m}{\|\mathbf{G}_\mu^m\|}, \tag{3.19}$$

in order to have a unique representation. The normalized version then becomes $\mathbb{T}^M = \sum_{m=1}^{M} \sigma_m \tilde{\mathbf{T}}^m \otimes \tilde{\mathbf{G}}_\mu^m$, where σ_m is a scalar representing the amplitude of the term

$\sigma_m = \|\mathbf{T}^m\|\|\mathbf{G}_\mu^m\|$. Note that σ_m provides information on the relative importance of the modes in the separable approximation and therefore it will be used as one of the criteria to decide whether the number of terms, M, is sufficient to obtain the desired accuracy. It is useful to introduce the notation as,

$$\mathbb{T}^M = \mathbb{T}^{M-1} + \mathbf{T}^M \otimes \mathbf{G}_\mu^M, \tag{3.20}$$

where the super-index M indicates the number of terms of the approximation.

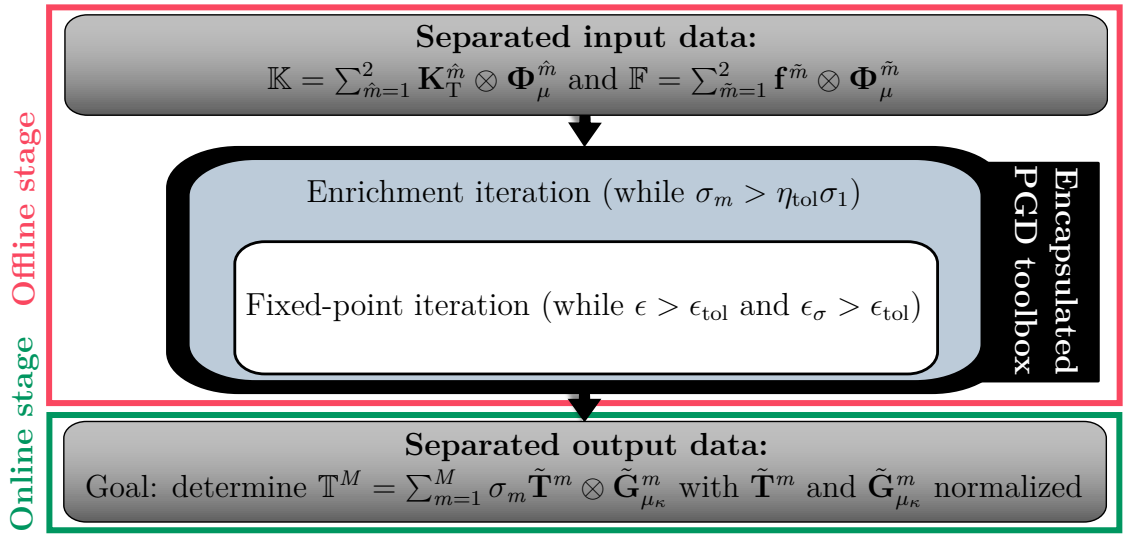

Figure 3.2: Scheme of the three main ingredients of the PGD methodology for the solution of parametric linear systems of equations. Inputs and outputs (gray boxes) are given in separated formats (ingredient 1). An enrichment iteration (ingredient 2) sequentially adds terms to the approximated unknown function $\mathbf{T}(\mu)$. A simple fixed-point method (ingredient 3) is used to deal with the nonlinearities introduced by the separated unknown function. In the figure, σ_m corresponds to the amplitude of the m term of $\mathbf{T}(\mu)$, η_{tol} is the tolerance used to stop the enrichment iteration, ϵ and ϵ_σ are the errors estimates for the fixed-point iterations (defined in Equations (3.36) and (3.37)), and ϵ_{tol} is the tolerance of the fixed-point.

The solution to the parametric problem (3.11) using PGD is described next. The starting point is the description of the inputs and the outputs of the PGD solver, represented in the Figure 3.2. All inputs and outputs will be given in separated forms. The encapsulated PGD library provides an easy-to-use implementation of the PGD algorithm to obtain the generalized (parametric) solution of a linear system such as (3.11). The three main ingredients of the PGD algorithm are: 1) separated representations, 2) an enrichment technique that will improve the solution by adding

one term at a time, and 3) a simple fixed-point scheme that deals with the nonlinearities introduced by the separated representation of the unknown function. The main ideas of these three ingredients will be briefly presented next.

3.2.2 Enrichment iteration

The PGD approach aims to solve Equation (3.11) using an approximation of the solution in the form indicated in Equation (3.20). A greedy scheme computes sequentially the terms in Equation (3.20). Each step of the enrichment iteration, or updating $\mathbb{T}^{M-1}$ into $\mathbb{T}^M$, entails solving the new rank-one term based on all the known prior terms. Assuming that $\mathbb{T}^{M-1}$ is the sum of the known prior terms, the remaining terms for $\mathbb{T}^M$ are $\mathbf{T}^M$ and $\mathbf{G}_\mu^M$, based on Equation (3.20). $\mathbf{T}^M$ and $\mathbf{G}_\mu^M$ are unknowns; from now on, the superscripts M in $\mathbf{T}^M$ and $\mathbf{G}_\mu^M$ will be omitted to simplify the notation. The unknowns ($\mathbf{T}$ and $\mathbf{G}_\mu$) should be found to minimize the residual of Equation (3.11). They are multiplying each other, which causes the problem to be nonlinear.

By defining an unknown high-dimensional tensor $\mathbb{T} = \mathbf{T} \otimes \mathbf{G}_\mu$ consisting of all the unknowns, Equation (3.20) is rewritten as,

$$\mathbb{T}^M = \mathbb{T}^{M-1} + \mathbb{T}. \tag{3.21}$$

Due to the incremental character of Equation (3.21), the expression of the residual in Equation (3.10) is written as,

$$\begin{aligned} \mathbf{R}(\mathbb{T}^M) &:= \mathbb{F} - \mathbb{K}\mathbb{T}^M = 0 \\ &:= \mathbb{F} - \mathbb{K}\mathbb{T}^{M-1} - \mathbb{K}\mathbb{T} = 0 \\ &:= \mathbf{R}(\mathbb{T}^{M-1}) - \mathbb{K}\mathbb{T} = 0. \end{aligned} \tag{3.22}$$

By using Equation (3.16) and the definition of $\mathbb{T} = \mathbf{T} \otimes \mathbf{G}_\mu$, it becomes,

$$\mathbf{R}(\mathbb{T}^{M-1}) - (\sum_{\hat{m}=1}^{2} \mathbf{K}_{\mathrm{T}}^{\hat{m}} \otimes \mathbf{\Phi}_\mu^{\hat{m}}) \cdot (\mathbf{T} \otimes \mathbf{G}_\mu) = 0 \tag{3.23}$$

The test function $\delta\mathbf{T}(\mu)$ in Equation (3.11) has to be selected now in accordance with the unknown of the rank-one problem consisting in introducing in Equation (3.11) the residual as defined in Equations (3.22) and (3.23),

$$\delta\mathbf{T}(\mu) = \delta\mathbb{T} = \delta\mathbf{T} \otimes \mathbf{G}_\mu + \mathbf{T} \otimes \delta\mathbf{G}_\mu. \tag{3.24}$$

By inserting Equations (3.24) and (3.23) in Equation (3.11), a nonlinear problem is obtained. The numerical approach to deal with the nonlinearity of this problem is based on the fixed-point iteration, which is explained next.

3.2.3 Fixed-point iteration

In the fixed-point iteration method, each unknown is solved independently, presuming that the other components are known. With the use of this concept, the nonlinear problem for the problem (3.7) is split into two consecutive linear equations:

- The **first** problem reads: given $\mathbf{G}_\mu$, compute $\mathbf{T}$ (in encapsulated PGD, the starting guess is a vector with all components set to the value of one, and it is subsequently normalized).
- The **second** problem reads: given $\mathbf{T}$, compute $\mathbf{G}_\mu$.

Note that the proposed method iterates two linear equations to reach a stationary solution based on the stopping criterion for one achievement term.

For the first problem (computing $\mathbf{T}$), by assuming that $\mathbf{G}_\mu$ is known, the test function is expressed as,

$$\delta\mathbb{T} = \delta\mathbf{T} \otimes \mathbf{G}_\mu. \tag{3.25}$$

By inserting Equations (3.25) and (3.23) in Equation (3.11), and applying algebraic manipulation for all $\delta\mathbf{T} \in \mathbb{R}^{\mathrm{n}_\Omega}$, the following linear system of equations for $\mathbf{T}$ is obtained,

$$\left[\sum_{\hat{m}=1}^{2} \mathbf{K}_{\mathrm{T}}^{\hat{m}} c^{\hat{m}}\right]\mathbf{T} = \sum_{\tilde{m}=1}^{2} \mathbf{f}^{\tilde{m}} \hat{c}^{\tilde{m}} - \sum_{m=1}^{M-1}\left[\sum_{\hat{m}=1}^{2} \mathbf{K}_{\mathrm{T}}^{\hat{m}} c^{\hat{m},m}\right]\mathbf{T}^{m}, \tag{3.26}$$

where $\hat{m}$, $\tilde{m}$, and m represent the number of terms for the stiffness matrix, force vector, and temperature unknown fields, respectively. The scalars $c^{\hat{m}}$, $\hat{c}^{\tilde{m}}$, and $c^{\hat{m},m}$ are computable terms defined by the following expressions:

$$c^{\hat{m}} = \left((\mathbf{\Phi}_\mu^{\hat{m}} \odot \mathbf{G}_\mu)^{\mathrm{T}} \mathbf{G}_\mu\right), \tag{3.27}$$

$$\hat{c}^{\tilde{m}} = \left(\mathbf{\Phi}_\mu^{\tilde{m}^{\mathrm{T}}}\, \mathbf{G}_\mu\right), \tag{3.28}$$

$$c^{\hat{m},m} = \left((\mathbf{\Phi}_\mu^{\hat{m}} \odot \mathbf{G}_\mu^{m})^{\mathrm{T}} \mathbf{G}_\mu\right). \tag{3.29}$$

In Equations (3.27) and (3.29), $\odot$ is the Hadamard product (component by component product corresponding to the command " .* " in MATLAB).

For the second problem (computing $\mathbf{G}_\mu$), $\mathbf{T}$ has to be taken as a known value from the previous computation, and the test function is the following,

$$\delta\mathbb{T} = \mathbf{T} \otimes \delta\mathbf{G}_\mu. \tag{3.30}$$

By inserting Equations (3.30) and (3.23) in Equation (3.11) and applying algebraic manipulations for all $\delta\mathbf{G}_\mu \in \mathbb{R}^{n_\mu}$, the following linear system for $\mathbf{G}_\mu$ is obtained,

$$\mathbf{G}_\mu \odot \left[\sum_{\hat{m}=1}^{2} (\mathbf{T}^{\mathrm{T}} \mathbf{K}_{\mathrm{T}}^{\hat{m}} \mathbf{T}) \mathbf{d}_\mu^{\hat{m}} \right] = \sum_{\tilde{m}=1}^{2} (\mathbf{T}^{\mathrm{T}} \mathbf{f}^{\tilde{m}}) \hat{\mathbf{d}}_\mu^{\tilde{m}} - \sum_{m=1}^{M-1} \sum_{\hat{m}=1}^{2} (\mathbf{T}^{\mathrm{T}} \mathbf{K}_{\mathrm{T}}^{\hat{m}} \mathbf{T}^m) \mathbf{d}_\mu^{\hat{m},m}, \tag{3.31}$$

where vectors $\mathbf{d}_\mu^{\hat{m}}$, $\hat{\mathbf{d}}_\mu^{\tilde{m}}$ and $\mathbf{d}_\mu^{\hat{m},m}$ are computable terms defined as

$$\mathbf{d}_\mu^{\hat{m}} = \mathbf{\Phi}_\mu^{\hat{m}}, \tag{3.32}$$

$$\hat{\mathbf{d}}_\mu^{\tilde{m}} = \mathbf{\Phi}_\mu^{\tilde{m}}, \tag{3.33}$$

$$\mathbf{d}_\mu^{\hat{m},m} = \left(\mathbf{\Phi}_\mu^{\hat{m}} \odot \mathbf{G}_\mu^m \right). \tag{3.34}$$

After one iteration, new $\mathbf{T}$, and $\mathbf{G}_\mu$ are obtained, but, for being sure if they reach a stationary solution, the new results must be controled with the old results with some stopping criteria. Then, if it is not converged, the procedure is restarted by changing the old values with amount of the new values and obtained the next new values. The stopping criterion is discussed in the following subsection.

3.2.4 Convergence control and stopping criteria

As it has been illustrated in Figure 3.2, PGD requires two iterations. The outer iteration is an enrichment iteration adding new terms in Equation (3.20), while the inner iteration consists of the fixed-point iteration process to deal with the nonlinearity character of the problem defined by the PGD operations.

In the enrichment iteration based on Equation (3.20), we first need to normalize the vectors ($\mathbf{T}^m$ and $\mathbf{G}_\mu^m$) in each mode. Then $\sigma_m = \|\mathbf{T}^m\|\|\mathbf{G}_\mu^m\|$, the amplitude of each mode, is calculated. By comparing the amplitude of the last computed mode with the amplitude of the first one, the following stopping criterion for the enrichment iteration is defined;

$$\frac{\sigma_m}{\sigma_1} < \eta_{\mathrm{tol}}, \tag{3.35}$$

where η_{tol} is a given tolerance.

The fixed-point iterative scheme requires a stopping criterion to decide whether the current approximation for $\mathbf{T}$ and $\mathbf{G}_\mu$ is acceptable or not. The stopping criterion is based on the stationary of the solution: the iteration is stopped if the modification from the previous iteration is small enough. Thus, assume that $\tilde{\mathbf{T}}^{\text{old}}$ and $\tilde{\mathbf{G}}_\mu^{\text{old}}$ characterize the normalized values at the previous iteration and σ^{old} is the amplitude of the previous iteration. After the fixed-point iteration loop, the new normalized approximation by $\tilde{\mathbf{T}}^{\text{new}}$ and $\tilde{\mathbf{G}}_\mu^{\text{new}}$ and the amplitude of the new iteration is σ^{new}. For this iterative scheme, two errors, ϵ and ϵ_σ, are defined as,

$$\epsilon = \|\tilde{\mathbf{T}}^{\text{new}} - \tilde{\mathbf{T}}^{\text{old}}\| \|\tilde{\mathbf{G}}_\mu^{\text{new}} - \tilde{\mathbf{G}}_\mu^{\text{old}}\|, \tag{3.36}$$

$$\epsilon_\sigma = \frac{|\sigma^{\text{new}} - \sigma^{\text{old}}|}{\sigma^{\text{old}}}. \tag{3.37}$$

By defining an error tolerance ϵ_{tol}, the following stopping criterion is defined for the fixed-point iteration procedure;

$$\epsilon < \epsilon_{\text{tol}} \text{ and } \epsilon_\sigma < \epsilon_{\text{tol}}, \tag{3.38}$$

and for this scheme, both stopping criteria must be satisfied.

3.3 An example of a PGD solution

This section presents the result of the parametric problem (3.7) obtained using the PGD methodology described in the previous section. The main goal is to make the reader familiar with the particular shape and properties of the separated functions.

Note that PGD as, most reduced order techniques, can be divided into two phases: first, the construction of the reduced basis, and second the use of the basis to obtain a particular solution. The first step, so-called the offline phase, was described in Section 3.2, and it is usually expensive but is done only once. The second step, the online phase, in the case of PGD, is particularly inexpensive as obtaining a new solution does not involve solving any linear system of equations.

Table 3.1 displays the constants pertaining to problem (3.7) and is illustrated in Figure 3.1. It is important to note that the heat source (q) is uniformly distributed across the entire domain.

Symbol	Units	Value	Definition
a	m	2	Inner radius
c	m	3	Middle radius
b	m	4	Outer radius
L	m	10	Length
T_{l}	°C	10	Prescribed temperature at Γ_{l}
T_{r}	°C	10	Prescribed temperature at Γ_{r}
κ_1	W m^{-1} °C^{-1}	10	Heat conductivity of subdomain Ω_1
q	W m^{-3}	13.5282	Heat source

Table 3.1: Constants used for the solution of the problem (3.7).

As previously discussed, the heat conductivity of subdomain Ω_2 is considered to be a parameter taking values in, $\mu \in \left[1.5\ \frac{\mathrm{W}}{\mathrm{m°C}}, 5\ \frac{\mathrm{W}}{\mathrm{m°C}}\right]$.

Symbol	Amount	Definition
η_{tol}	10^{-2}	Modes Tolerance
M_{max}	50	Maximum number of Modes
ϵ_{tol}	10^{-6}	Tolerance for Fixed-point iteration
$\mathrm{iter}_{\mathrm{max}}$	50	Maximum number of iteration for Fixed-point iteration

Table 3.2: Stopping criteria for PGD.

Using the tolerances of Table 3.2, a solution with three terms ($M = 3$) is obtained, namely,

$$\begin{aligned}\mathbf{T}(\mathbf{x},\mu) &= \sum_{m=1}^{3} \sigma_m \tilde{\mathbf{T}}^m(\mathbf{x}) \otimes \tilde{\mathbf{G}}_\mu^m(\mu) \\ &= \sigma_1 \tilde{\mathbf{T}}^1(\mathbf{x}) \otimes \tilde{\mathbf{G}}_\mu^1(\mu) + \sigma_2 \tilde{\mathbf{T}}^2(\mathbf{x}) \otimes \tilde{\mathbf{G}}_\mu^2(\mu) + \sigma_3 \tilde{\mathbf{T}}^3(\mathbf{x}) \otimes \tilde{\mathbf{G}}_\mu^3(\mu).\end{aligned} \tag{3.39}$$

Note that $\mathbf{T}(\mathbf{x},\mu)$ is a generalized solution that includes the dependence on space and on the parameter (in this case, the thermal conductivity). The solution at any point in the spatial and the parametric domains can be obtained by interpolation operations.

It is usual that the amplitude of the terms in the solution decreases. This is shown in Figure 3.3, which presents the relative amplitude of the terms with respect to the first one. In this case, the amplitude decreases fast and monotonically. This is desirable, but unfortunately, it is not guaranteed by the algorithm, and it is common to obtain a non-monotonous decrease of the amplitudes.

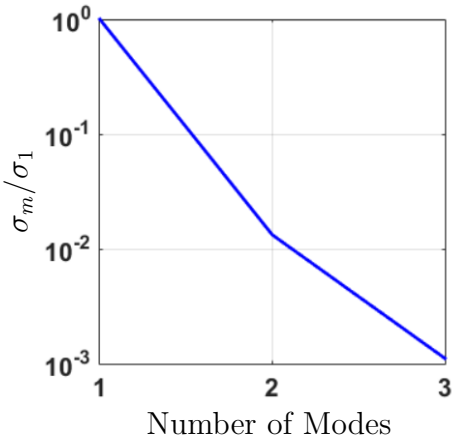

Figure 3.3: Relative amplitude versus modes.

Figure 3.4 presents all the spatial and parametric functions that compose the generalized solution, $\mathbf{T}(\mathbf{x}, \mu)$.

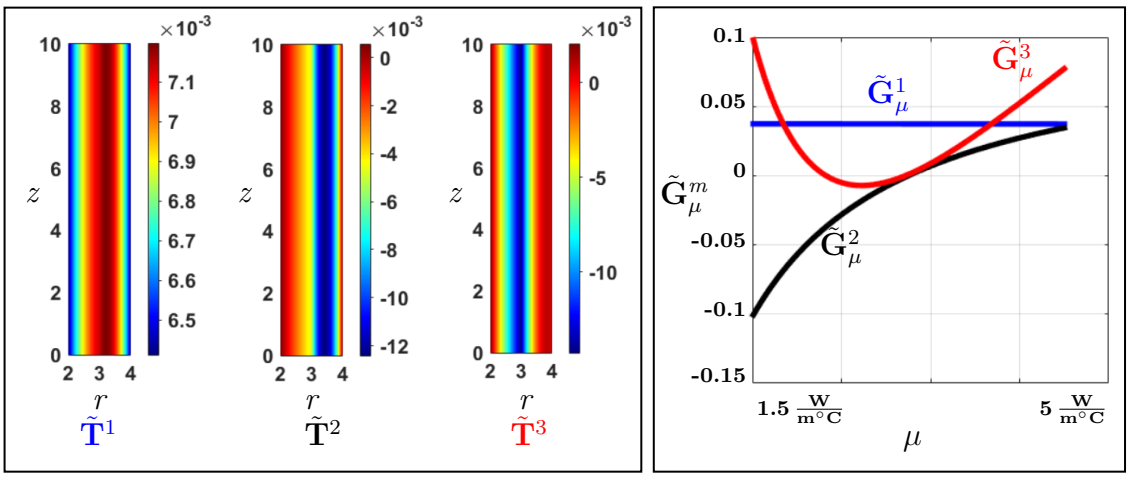

(A) (B)

Figure 3.4: (A) Three modes of normalized spatial functions, and (B) three modes of normalized parametric functions.

When the offline computation of the PGD parametric solution is complete, its particularization at some given parameter values is very inexpensive. By particularizing arbitrary parameter value in the range of its variations, for instance $\mu = 1.5\,\frac{\mathrm{W}}{\mathrm{m°C}}$, the PGD approximation is directly computed in real-time by,

$$\mathbf{T}(\mathbf{x}, 1.5) = \sigma_1 \tilde{\mathbf{T}}^1(\mathbf{x}) \otimes \tilde{\mathbf{G}}^1_\mu(1.5) + \sigma_2 \tilde{\mathbf{T}}^2(\mathbf{x}) \otimes \tilde{\mathbf{G}}^2_\mu(1.5) + \sigma_3 \tilde{\mathbf{T}}^3(\mathbf{x}) \otimes \tilde{\mathbf{G}}^3_\mu(1.5). \quad (3.40)$$

The field results and their relative error are computed and illustrated in Figure 3.5 for $\mu = 1.5\ \frac{\mathrm{W}}{\mathrm{m°C}}$. The relative error ($\epsilon^{1.5}_{\mathrm{RE}}(\mathbf{x})$) is defined as,

$$\epsilon^{1.5}_{\mathrm{RE}}(\mathbf{x}) = \frac{\|\mathbf{T}^{1.5}_{\mathrm{FEM}}(\mathbf{x}) - \mathbf{T}(\mathbf{x}, 1.5)\|}{\|\max\left(\mathbf{T}^{1.5}_{\mathrm{FEM}}(\mathbf{x})\right)\|}. \tag{3.41}$$

In Equation (3.41), $\mathbf{T}^{1.5}_{\mathrm{FEM}}(\mathbf{x})$ means the solution of FEM for $\mu = 1.5\ \frac{\mathrm{W}}{\mathrm{m°C}}$.

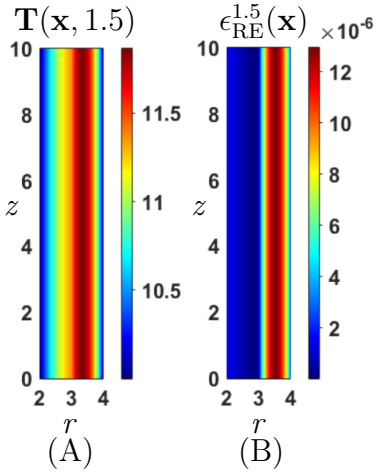

Figure 3.5: Temperature field result (A) and relative error (B) of PGD at $\mu = 1.5\ \frac{\mathrm{W}}{\mathrm{m°C}}$.

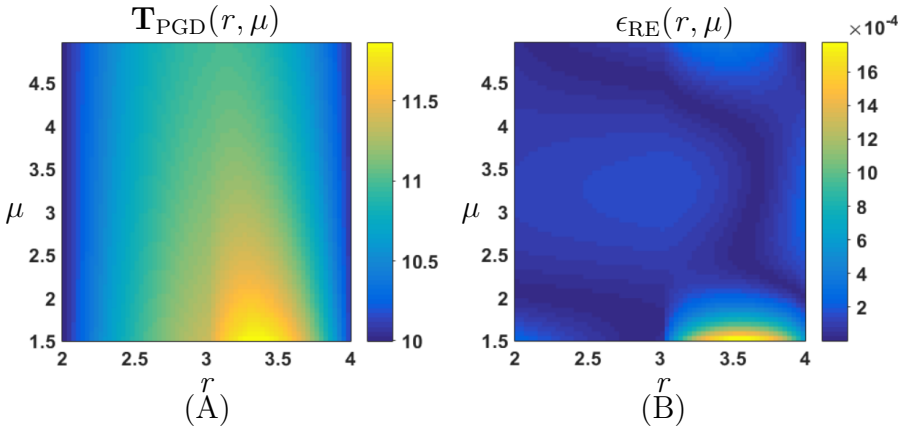

Figure 3.6: (A) The generalized solution of temperature as a function of space and parameter, and (B) relative error of the whole domain (spatial and parametric).

Taking into account the symmetry of the problem 3.1, it is easy to see that the solution depends only on one spatial axis (it is actually 1D). This is clearly shown in Figure 3.5-A. Therefore, by considering the space solution as a one-dimensional function, for this simple problem, it is possible to plot the complete solution depending on space and the parameter in a 2D space. This is shown in Figure 3.6, together with

an error map showing that the generalized solution, with only three terms, provides a very accurate result with a maximum error of 16×10^{-4}. The relative error, in this case, is computed as a function of space and parameter,

$$\epsilon_{\mathrm{RE}}(r,\mu) = \frac{\|\mathbf{T}^{\mu}_{\mathrm{FEM}}(r) - \mathbf{T}_{\mathrm{PGD}}(r,\mu)\|}{\|\mathbf{T}^{\mu}_{\mathrm{FEM}}(r)\|}. \tag{3.42}$$

In Equation (3.42), $\mathbf{T}^{\mu}_{\mathrm{FEM}}(r)$ means the solution of FEM for a specific value of μ.

Chapter 4

Application of PGD to THM problems

This Chapter presents the application of the PGD methodology for the solution of parametric THM problems. The novelties introduced here (with respect to Chapter 3) are:

- the problem is transient,
- the coupled character of THM must be considered,
- the problem is parameterized on three materials and one geometrical parameter.

The material parameters considered as extra dimensions (in addition to space and time) are the heat conductivity, the hydraulic conductivity, and the elastic modulus. A geometrical parameter consisting of the radial dimension of the geometric domain is considered as well, as will be explained in more detail.

This chapter is divided into three sections. Section 4.1 presents the parameters that have been considered, how they affect the field equations, and their discretization. Section 4.2 explains how time integration is performed, and illustrates the form of the discretized parametric matrices and vectors for the discrete problem. Finally, Section 4.3 outlines the separated input and output data required for the use of the PGD formulation.

4.1 Parametric problem

The main governing equations of the THM problem were presented in Chapter 2 (Equation (2.7)). This work focuses on model order reduction for THM problems with applications inspired by deep geological repositories. In that context, we defined the parameters as the physical properties of the host rock, as these are usually poorly constrained and might vary. Therefore three materials are defined:

- the hydraulic conductivity, denoted as $K(\mathbf{x}, \mu_K)$, where μ_K controls the hydraulic conductivity of the host rock,
- the heat conductivity, denoted as $\kappa(\mathbf{x}, \mu_\kappa)$, where μ_κ controls the heat conductivity of the host rock and
- the elastic modulus, denoted as $E(\mathbf{x}, \mu_E)$, where μ_E controls the elastic modulus of the host rock.

Additionally, we included one geometrical parameter that controls the "distance between canisters" and could be used for the design of the repository.

As explained in Chapter 3, PGD treats the parameters as extra dimensions of the problem. In the models presented next, we have 2 spatial dimensions, 1 time dimension, and 4 parametric dimensions. Computing a general solution in this 7-dimensional space using standard discretization techniques is unfeasible.

The material properties are defined as functions depending on space and the parameters. For example, the heat conductivity $\kappa(\mathbf{x}, \mu_\kappa)$ takes values for all $\mathbf{x} \in \Omega$ and for any $\mu_\kappa \in [\mu_\kappa^{\min}, \mu_\kappa^{\max}]$. The actual functions and the actual range of the parameters will be defined next for every example problem. Similarly, the hydraulic conductivity and the elastic modulus are set as $K(\mathbf{x}, \mu_K)$ and $E(\mathbf{x}, \mu_E)$, respectively. Note that in the following sections, the dependence of these functions on space will be omitted to simplify the notation.

The geometrical parameter is of a different kind, and it is more complex to deal with. First, it does not appear on the partial differential equations (PDEs) (Equation (2.7)) but on the definition of the domain in which the PDEs are being solved. The computational domain $\Omega(\mu_L)$ changes when the parameter μ_L varies. Introducing the effect of geometrical parameters is, in general, not easy. In the following examples, we will restrict to a simple but meaningful parameterization where the model is extended laterally to control the distance between the canisters in a periodic repository. The

left half of the model representing the canister is fixed (Ω_1), while the right half representing the host rock between the canisters (Ω_2), is controlled by the parameter. Figure 4.1 shows the two parts of the domain and presents the family of geometries that are obtained by varying μ_L.

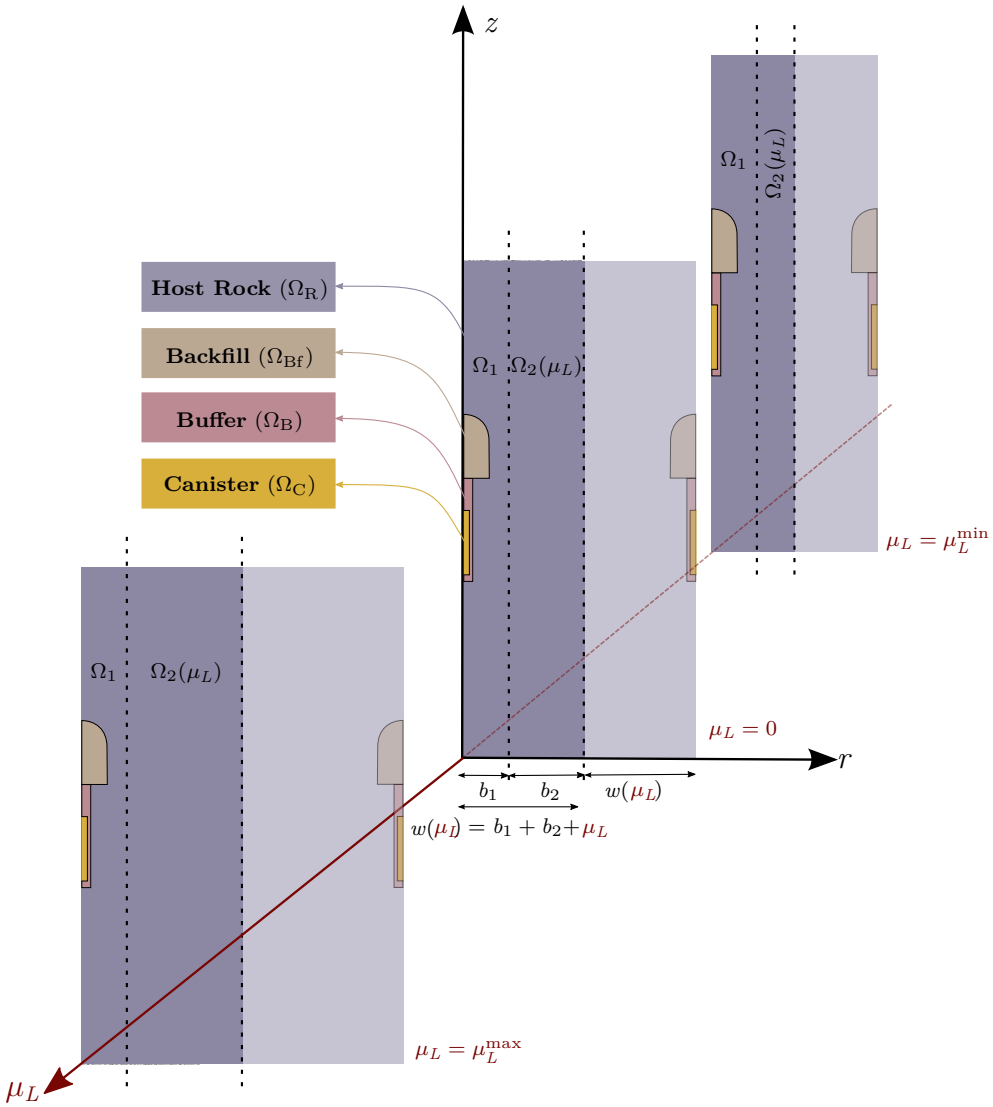

Figure 4.1: The entire spatial domain ($\Omega(\mu_L) = \Omega_1 \cup \Omega_2(\mu_L)$) is divided into two subdomains. The left half of the model, which includes the canister, buffer, backfill, and some part of the host rock, is fixed (Ω_1). The right half of the model, which represents the host rock between canisters ($\Omega_2(\mu_L)$), is controlled by the geometric parameter (μ_L). This parameter affects the $\Omega_2(\mu_L)$ domain only by shortening or elongating the radial direction.

The full parametric domain is defined by the cross-product of the domains of each one of the parameters, $I_{\boldsymbol{\mu}} = I_{\mu_\kappa} \times I_{\mu_K} \times I_{\mu_E} \times I_{\mu_L}$. A point in the parametric space $\boldsymbol{\mu} = [\mu_\kappa, \mu_K, \mu_E, \mu_L]$ is a vector with the coordinates of the 4 parametric dimensions.

The main governing equations, outlined in Chapter 2, will now be formulated in the parametric form in the domain $\Omega(\mu_L) \times I_t \times I_{\boldsymbol{\mu}}$. Note that the domain definition implies that the parameters serve as new coordinates for the problem domain. The interval $I_t = [0, t_{\text{final}}]$ is used as the time domain. The THM governing equations presented in Chapter 2 (Equation (2.7)) are reformulated in parametric form as,

$$\begin{cases} ((1-\phi)\rho_s c_s + \phi\rho_f c_f)\dot{T}(\mu_\kappa, \mu_L) \\ \qquad\qquad - \boldsymbol{\nabla}\cdot(\kappa(\mu_\kappa)\boldsymbol{\nabla} T(\mu_\kappa, \mu_L)) = q(t) & \text{in } \Omega(\mu_L)\times I_t \times I_{\boldsymbol{\mu}}, \\ \left(\dfrac{\phi}{K_f} + \dfrac{\alpha-\phi}{K_s(\mu_E)}\right)\dot{p}(\boldsymbol{\mu}) - \boldsymbol{\nabla}\cdot\left(\dfrac{K(\mu_K)}{\rho_f g}(\boldsymbol{\nabla} p(\boldsymbol{\mu}) - \rho_f \mathbf{g})\right) & \text{in } \Omega(\mu_L)\times I_t \times I_{\boldsymbol{\mu}}, \\ \quad + \alpha\boldsymbol{\nabla}\cdot\dot{\mathbf{u}}(\boldsymbol{\mu}) = (3\phi\alpha_f + 3(\alpha-\phi)\alpha_s)\dot{T}(\mu_\kappa, \mu_L) & \\ \alpha\boldsymbol{\nabla} p(\boldsymbol{\mu}) - \boldsymbol{\nabla}\cdot(\mathbb{C}(E(\mu_E), \nu) : \boldsymbol{\nabla}\mathbf{u}(\boldsymbol{\mu})) = & \\ \qquad\qquad \mathbf{b} - 3K_D(\mu_E)\alpha_s\boldsymbol{\nabla} T(\mu_\kappa, \mu_L) & \text{in } \Omega(\mu_L)\times I_t \times I_{\boldsymbol{\mu}}. \end{cases} \tag{4.1}$$

The solution to the thermal part only depends on two parameters which are heat conductivity (μ_κ) and the geometric parameter (μ_L). On the other hand, the solution of the hydro-mechanical part depends on all the parameters ($\boldsymbol{\mu}$). The material properties, $\kappa(\mu_\kappa)$, $K(\mu_K)$, $K_s(\mu_E)$, $E(\mu_E)$, and $K_D(\mu_E)$, depend on a single parameter. Note that all the space dependencies were omitted to shorten the notation. All the symbols concerning the main governing parametric PDEs have been explained in Chapter 2 (Table 2.2).

The boundary conditions for the parametric governing PDEs are divided into Dirichlet and Neumann boundary conditions. For all the problems presented in this work, the Neumann boundary conditions for thermal and hydraulic aspects are homogeneous, meaning that their fluxes are zero. The reason is that all the problems in this thesis are symmetrical.

The temperature boundary conditions are,

$$\begin{cases} T(\mathbf{x}, \mu_\kappa, \mu_L, t) = T_D(\mathbf{x}, \mu_\kappa, \mu_L, t) & \text{on } \Gamma_D^T(\mu_L)\times I_t \times I_{\boldsymbol{\mu}}, \\ -\kappa(\mu_\kappa)\boldsymbol{\nabla} T(\mathbf{x}, \mu_\kappa, \mu_L, t)\cdot\mathbf{n} = 0 & \text{on } \Gamma_N^T(\mu_L)\times I_t \times I_{\boldsymbol{\mu}}. \end{cases} \tag{4.2}$$

Prescribed temperature boundary conditions are described by a known function $T_D(\mathbf{x}, \mu_\kappa, \mu_L, t)$ that, as shown in (4.2), might depend on space, time, and parameters. This function will be described in the following chapters for the particular cases being modeled.

Boundary conditions for the hydraulic field are,

$$\begin{cases} p(\mathbf{x}, \boldsymbol{\mu}, t) = p_D(\mathbf{x}, \boldsymbol{\mu}, t) & \text{on } \Gamma_D^p(\mu_L) \times I_t \times I_{\boldsymbol{\mu}}, \\ -\dfrac{K(\mu_K)}{\rho_f g}(\boldsymbol{\nabla} p(\mathbf{x}, \boldsymbol{\mu}, t) - \rho_f \mathbf{g}) \cdot \mathbf{n} = 0 & \text{on } \Gamma_N^p(\mu_L) \times I_t \times I_{\boldsymbol{\mu}}, \end{cases} \tag{4.3}$$

where $p_D(\mathbf{x}, \boldsymbol{\mu}, t)$ is a given function.

The mechanical field Equation (4.4) presents the Dirichlet and Neumann boundary conditions, where $\mathbf{u}_D(\mathbf{x}, \boldsymbol{\mu}, t)$ and $\mathbf{t}_N(\mathbf{x}, \boldsymbol{\mu}, t)$ are given functions for prescribed displacement and traction forces, respectively,

$$\begin{cases} \mathbf{u}(\mathbf{x}, \boldsymbol{\mu}, t) = \mathbf{u}_D(\mathbf{x}, \boldsymbol{\mu}, t) & \text{on } \Gamma_D^u(\mu_L) \times I_t \times I_{\boldsymbol{\mu}}, \\ \boldsymbol{\sigma} \cdot \mathbf{n} = \mathbf{t}_N(\mathbf{x}, \boldsymbol{\mu}, t) & \text{on } \Gamma_N^u(\mu_L) \times I_t \times I_{\boldsymbol{\mu}}. \end{cases} \tag{4.4}$$

The initial conditions for the problem should be such that all the fields be balanced and at equilibrium. The definition of initial conditions for the parametric THM problem is as,

$$\begin{cases} T(\mathbf{x}, \mu_\kappa, \mu_L, 0) = T_0(\mathbf{x}, \mu_\kappa, \mu_L) & \text{in } \Omega(\mu_L) \times I_{\boldsymbol{\mu}}, \\ p(\mathbf{x}, \boldsymbol{\mu}, 0) = p_0(\mathbf{x}, \boldsymbol{\mu}) & \text{in } \Omega(\mu_L) \times I_{\boldsymbol{\mu}}, \\ \mathbf{u}(\mathbf{x}, \boldsymbol{\mu}, 0) = \mathbf{u}_0(\mathbf{x}, \boldsymbol{\mu}) & \text{in } \Omega(\mu_L) \times I_{\boldsymbol{\mu}}, \end{cases} \tag{4.5}$$

where $T_0(\mathbf{x}, \mu_\kappa, \mu_L)$ and $p_0(\mathbf{x}, \boldsymbol{\mu})$ are given functions based on the problem statement of the examples. In the upcoming chapters, we will determine the initial conditions of the displacement field ($\mathbf{u}_0(\mathbf{x}, \boldsymbol{\mu})$) by inserting the functions $T_0(\mathbf{x}, \mu_\kappa, \mu_L)$ and $p_0(\mathbf{x}, \boldsymbol{\mu})$ into the mechanical aspect and solving the steady-state version of the parametric problem.

4.2 Space-time discretization of parametric THM

The numerical solution to the parametric THM problem requires discretizing space, time, and parametric dimensions. The space discretization is done using standard

FE, similar to what is presented in Chapter 2. In transient problems, it is usual to discretize time using a marching scheme. We are going to use exactly the same approach here. The time integration in standard FE requires solving one linear system of equations at every time step. Similarly, here every step involves the solution of one linear parametric system. Note that this idea is not the most common approach in reduced-order methods, where taking time as an extra parametric dimension is commonplace. Here we will not try to reduce the time dimension. The parametric character of the problem, although, makes the discrete operators arising from the space discretization dependent on the parameters.

By employing Equations (2.20) and (2.21) from Chapter 2, the parametric matrix problem for advancing one-time step is derived as follows:

$$\underbrace{\left[\mathbf{M}_{\mathrm{T}}(\boldsymbol{\mu})+\Delta t^{i}\theta\mathbf{K}_{\mathrm{T}}(\boldsymbol{\mu})\right]}_{\mathbf{K}^{i}_{\mathbf{GT}}(\boldsymbol{\mu})}\mathbf{T}^{i+1}(\boldsymbol{\mu})=\Delta t^{i}\mathbf{f}_{\mathrm{q}}+\underbrace{\left[\mathbf{M}_{\mathrm{T}}(\boldsymbol{\mu})+\Delta t^{i}(\theta-1)\mathbf{K}_{\mathrm{T}}(\boldsymbol{\mu})\right]}_{\mathbf{K}^{i*}_{\mathbf{GT}}(\boldsymbol{\mu})}\mathbf{T}^{i}(\boldsymbol{\mu}), \tag{4.6}$$

for the thermal problem and,

$$\begin{aligned}\underbrace{\begin{bmatrix}\mathbf{M}_{\mathrm{p}}(\boldsymbol{\mu})+\Delta t^{i}\theta\mathbf{K}_{\mathrm{p}}(\boldsymbol{\mu}) & \mathbf{G}_{\mathrm{pd}}(\boldsymbol{\mu})\\ \theta\mathbf{G}_{\mathrm{dp}}(\boldsymbol{\mu}) & \theta\mathbf{K}_{\mathrm{d}}(\boldsymbol{\mu})\end{bmatrix}}_{\mathbf{K}^{i}_{\mathbf{G}}(\boldsymbol{\mu})}\underbrace{\begin{bmatrix}\mathbf{p}^{i+1}(\boldsymbol{\mu})\\ \mathbf{d}^{i+1}(\boldsymbol{\mu})\end{bmatrix}}_{\mathbf{U}^{i+1}(\boldsymbol{\mu})}&=\underbrace{\begin{bmatrix}\Delta t^{i}\mathbf{f}_{\mathbf{b}_{\mathrm{f}}}(\boldsymbol{\mu})\\ \mathbf{f}_{\mathrm{d}}(\boldsymbol{\mu})\end{bmatrix}}_{\mathbf{F}^{i}_{*}(\boldsymbol{\mu})}+\\ \underbrace{\begin{bmatrix}\mathbf{M}_{\mathrm{p}}(\boldsymbol{\mu})+\Delta t^{i}(\theta-1)\mathbf{K}_{\mathrm{p}}(\boldsymbol{\mu}) & \mathbf{G}_{\mathrm{pd}}(\boldsymbol{\mu})\\ (\theta-1)\mathbf{G}_{\mathrm{dp}}(\boldsymbol{\mu}) & (\theta-1)\mathbf{K}_{\mathrm{d}}(\boldsymbol{\mu})\end{bmatrix}}_{\mathbf{K}^{i*}_{\mathbf{G}}(\boldsymbol{\mu})}&\underbrace{\begin{bmatrix}\mathbf{p}^{i}(\boldsymbol{\mu})\\ \mathbf{d}^{i}(\boldsymbol{\mu})\end{bmatrix}}_{\mathbf{U}^{i}(\boldsymbol{\mu})}+\\ \underbrace{\begin{bmatrix}\mathbf{M}_{\mathrm{pT}}(\boldsymbol{\mu}) & -\mathbf{M}_{\mathrm{pT}}(\boldsymbol{\mu})\\ -\theta\mathbf{G}_{\mathrm{dT}}(\boldsymbol{\mu}) & (\theta-1)\mathbf{G}_{\mathrm{dT}}(\boldsymbol{\mu})\end{bmatrix}}_{\mathbf{G}_{\mathbf{T}}(\boldsymbol{\mu})}&\underbrace{\begin{bmatrix}\mathbf{T}^{i+1}(\boldsymbol{\mu})\\ \mathbf{T}^{i}(\boldsymbol{\mu})\end{bmatrix}}_{\mathbf{T}(\boldsymbol{\mu})},\end{aligned} \tag{4.7}$$

for the Hydro-Mechanical (HM) problem. In Equations (4.6) and (4.7), i represents the time slice, which varies from $i = 1$ to $\mathrm{n_t}$, where $\mathrm{n_t}$ denotes the number of time steps.

All the definitions of the FEM discretized matrices and vectors in (4.6) and (4.7) are provided in Chapter 2 (Subsection 2.2.2). It should be emphasized that Equations (4.6) and (4.7) are stated prior to the application of any Dirichlet-prescribed boundary condition. Now, with the utilization of these definitions, the Dirichlet boundary conditions are transferred to the right-hand side, as shown in,

$$\mathbf{F}^{i}_{\mathbf{T}}(\boldsymbol{\mu})=\Delta t^{i}\mathbf{f}^{i}_{\mathrm{q}}+\mathbf{K}^{i*}_{\mathbf{GT}}(\boldsymbol{\mu})\mathbf{T}^{i}(\boldsymbol{\mu})+\mathbf{f}_{\mathbf{DT}}(\boldsymbol{\mu}), \tag{4.8}$$

$$\mathbf{F}^i_{\mathbf{G}}(\boldsymbol{\mu}) = \mathbf{F}^i_*(\boldsymbol{\mu}) + \mathbf{K}^{i*}_{\mathbf{G}}(\boldsymbol{\mu})\mathbf{U}^i(\boldsymbol{\mu}) + \mathbf{G}_{\mathbf{T}}(\boldsymbol{\mu})\mathbf{T}(\boldsymbol{\mu}) + \mathbf{f}_{\mathbf{DU}}(\boldsymbol{\mu}), \tag{4.9}$$

In Equation (4.8), $\mathbf{f}_{\mathbf{DT}}(\boldsymbol{\mu})$ is a parametric force term that comes from prescribed temperatures. In Equation (4.9), $\mathbf{f}_{\mathbf{DU}}(\boldsymbol{\mu})$ is a parametric force term that arises from prescribed pressure and displacements. The systems of Equations (4.6) and (4.7) are written as,

$$\mathbf{K}^i_{\mathbf{GT}}(\boldsymbol{\mu})\mathbf{T}^{i+1}(\boldsymbol{\mu}) = \mathbf{F}^i_{\mathbf{T}}(\boldsymbol{\mu}), \tag{4.10}$$

$$\mathbf{K}^i_{\mathbf{G}}(\boldsymbol{\mu})\mathbf{U}^{i+1}(\boldsymbol{\mu}) = \mathbf{F}^i_{\mathbf{G}}(\boldsymbol{\mu}). \tag{4.11}$$

Note that the unknown $\mathbf{U}^{i+1}(\boldsymbol{\mu}) = [\mathbf{p}^{i+1}(\boldsymbol{\mu})\ \mathbf{d}^{i+1}(\boldsymbol{\mu})]^{\mathrm{T}}$ includes the displacement and the pressure fields, while the temperature has its own equation. This is a consequence of the uncoupling between the field equations that is possible in the case of a fully saturated medium. The method proposed here naturally exploits this by solving first the temperature problem and the HM problem.

The parametric domain also requires to be discretized. This arises from the requirement for all variables and operators to be maintained in a separated format. As a result, discretization is carried out independently for each individual parametric dimension.

Recalling that a separated function takes the form (Equation (3.12)),

$$F(\mu_1, \mu_2, \mu_3, \mu_4) = \sum_{m=1}^{M} f_1^m(\mu_1) f_2^m(\mu_2) f_3^m(\mu_3) f_4^m(\mu_4).$$

The one-dimensional (1D) mesh for μ_1 represents the range of values that might take μ_1 and is used for the representation of the functions $f_1^m(\mu_1)$. Similarly, for all the parametric dimensions.

4.3 PGD applied to parametric THM problem

The PGD methodology is based on the separated representation of unknowns and operators, as described in Chapter 3. Therefore, we need to obtain separable versions of all the matrices and vectors in (4.6) and (4.7). Each of those matrices depends on the parameters, and the variation of each matrix with the parameters requires to be expressed in a separable format. Note that providing a separated form for each of the blocks of the systems (4.6) and (4.7) is enough, as the composition of the separated blocks will produce a full system that is also separable and has at most as many terms as the sum of the terms of all the blocks. Although, finding separable expressions for

all the matrices is not trivial in most cases. Next, we will show that most matrices involved in our problem admit an exact analytical separated form, while some are approximate.

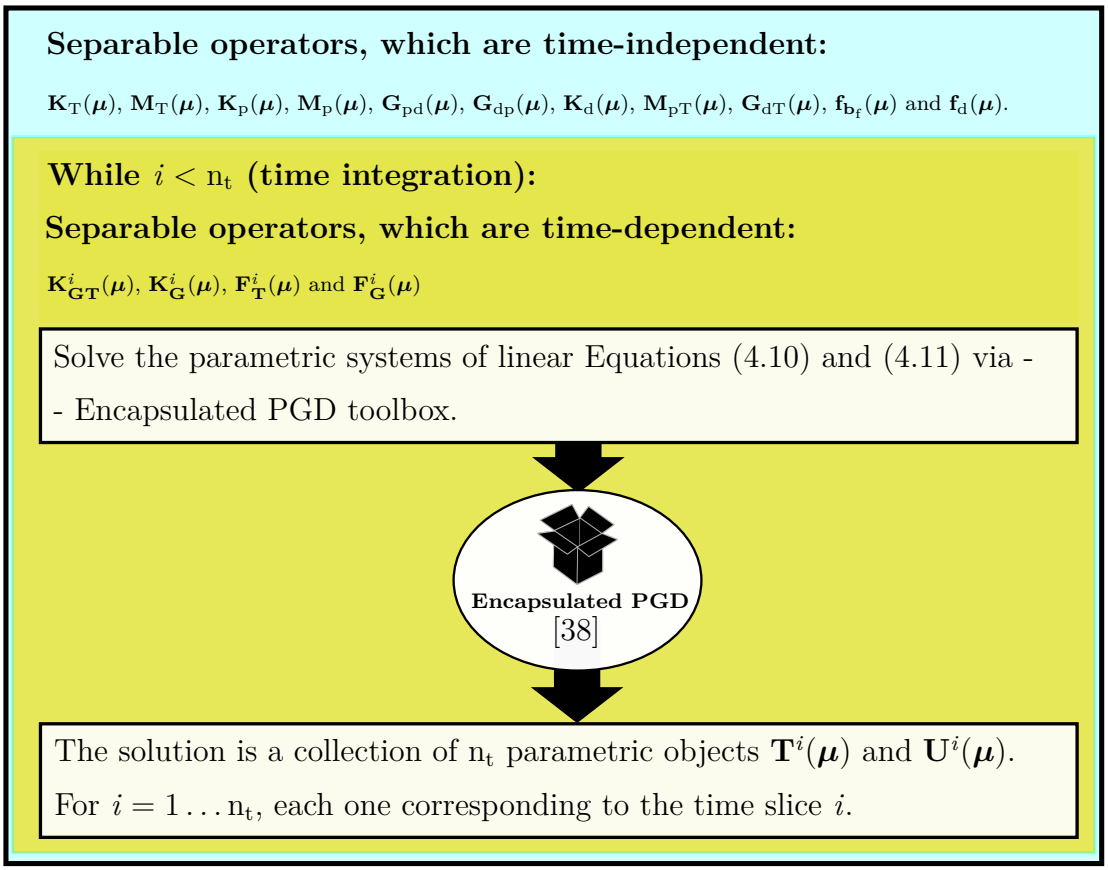

Figure 4.2: The systematic procedure of seeking a generalized solution of parametric THM. It presents that for solving this problem by Encapsulated PGD toolbox, it is necessary to define the input data in separated formats. The generalized solutions are the separated unknowns, a collection of $\mathrm{n_t}$ parametric objects of $\mathbf{T}^i(\boldsymbol{\mu})$ and $\mathbf{U}^i(\boldsymbol{\mu})$.

Figure 4.2 illustrates the discrete unknown vectors at time step t, denoted as $\mathbf{T}^t(\boldsymbol{\mu})$ and $\mathbf{U}^t(\boldsymbol{\mu})$. These vectors are determined by solving (4.10) and (4.11) at each time step. It is important to note that the components of the matrix operators in these equations remain fixed over time. However, the global structure of these matrices ($\mathbf{K}^i_{\mathbf{GT}}$ and $\mathbf{K}^i_{\mathbf{G}}$) needs to be determined for each time slice based on the time step within that slice. Conversely, the right-hand sides of the equations change at each time slice since they involve the solutions from the previous time step. Therefore, all the components within the global matrices are constructed before the time integration procedure begins. However, the global structure of these matrices, along with the

right-hand side, needs to be reconstructed at every time step to match the time-step requirements for each slice. The solution at each time slice involves solving a parametric linear system, which is accomplished using the encapsulated PGD [38].

4.3.1 Separable operators for material parameters

As mentioned previously, all matrices in Equations (4.6) and (4.7) require to be expressed in a separate format. The methodology for obtaining these separate representations for parameters that control material properties was discussed in Chapter 3, Subsection 3.2.1. For the general problem, we will adopt the same approach. The domain Ω is subdivided into several subdomains that represent the various materials involved, such as the canister (Ω_{C}), buffer (Ω_{B}), backfill (Ω_{Bf}), and host rock (Ω_{R}). In the following examples, only the host rock materials are parametric. Therefore, the thermal conductivity $\kappa(\mathbf{x}, \mu_\kappa)$ takes the value of the parameter in the host rock spatial domain (Ω_{R}), while it takes a fixed value (that might change from material to material) otherwise,

$$\kappa(\mathbf{x}, \mu_\kappa) = \begin{cases} \mu_\kappa & \text{if } \mathbf{x} \in \Omega_{\mathrm{R}} \text{ with } \mu_\kappa \in I_{\mu_\kappa}, \\ 1.4\,\frac{\mathrm{w}}{\mathrm{m}\,^\circ\mathrm{C}} & \text{if } \mathbf{x} \in \Omega_{\mathrm{B}}, \\ 1.4\,\frac{\mathrm{w}}{\mathrm{m}\,^\circ\mathrm{C}} & \text{if } \mathbf{x} \in \Omega_{\mathrm{Bf}}, \\ 390\,\frac{\mathrm{w}}{\mathrm{m}\,^\circ\mathrm{C}} & \text{if } \mathbf{x} \in \Omega_{\mathrm{C}}, \end{cases} \tag{4.12}$$

with this definition and following the exact same procedure as described in Subsection 3.2.1, a separated representation for $\mathbf{K}^i_{\mathbf{GT}}(\mu_\kappa)$ is obtained (see underbrace in (4.6)),

$$\mathbf{K}^i_{\mathbf{GT}}(\mu_\kappa) = \mathbf{M}_{\mathrm{T}} + \Delta t^i \theta (\mathbf{K}^0_{\mathrm{T}} + \mathbf{K}^1_{\mathrm{T}} \mu_\kappa). \tag{4.13}$$

The previous expression can be separated into three matrices: $\mathbf{M}_{\mathrm{T}}$, $\mathbf{K}^0_{\mathrm{T}}$, and $\mathbf{K}^1_{\mathrm{T}}$. These matrices represent the mass and stiffness components for the thermal part, and their definitions can be found in equations (2.22) and (2.23) of Chapter 2. Regarding the parametric part, it is relatively straightforward. The functions involved either take a value of one (and therefore are not explicitly written) or follow the identity function $f(\mu_\kappa) = \mu_\kappa$.

Similarly, the right-hand side is built as,

$$\mathbf{F}^i_{\mathbf{T}}(\mu_\kappa) = \Delta t^i \mathbf{f}^i_{\mathrm{q}} + \left[\mathbf{M}_{\mathrm{T}} + \Delta t^i (\theta - 1) \mathbf{K}_{\mathrm{T}}(\mu_\kappa)\right] \mathbf{T}^i(\mu_\kappa) - \mathbf{K}^i_{\mathbf{GT}}(\mu_\kappa) \mathbf{T}_{\mathrm{D}}(\mu_\kappa), \tag{4.14}$$

where $\mathbf{f}_{\mathrm{q}}$ is defined in (2.31) and $\mathbf{T}^i(\mu_\kappa)$ is the temperature solution at the previous time step i, and $\mathbf{T}_{\mathrm{D}}(\mu_\kappa)$ is vector generated by the Dirichlet boundary conditions

that are computed separately as described in (4.2). Note that because all the objects are separated, their sum and product are also separable.

As mentioned before, the problem allows for solving the thermal part first, and then, once the (parametric) thermal field is known, a Hydro-Mechanical (HM) problem is solved. Next, the operators involved in the HM part will be presented in a separate form. All the matrix operators from (4.7) require to be separated. Following the notation introduced in (4.7), we call $\mathbf{K}^i_{\mathbf{G}}(\boldsymbol{\mu})$ to the left-hand side of the equation, and $\mathbf{K}^{i*}_{\mathbf{G}}(\boldsymbol{\mu})$ and $\mathbf{G}_{\mathbf{T}}(\boldsymbol{\mu})$ to the matrices involved in the right-hand side. Their separated expressions are,

$$\mathbf{K}^i_{\mathbf{G}}(\mu_K,\mu_E) = \mathbf{K}^{i\ 0}_{\mathbf{G}} + \mathbf{K}^{i\ 1}_{\mathbf{G}}\,\mu_K + \mathbf{K}^{i\ 2}_{\mathbf{G}}\,\mu_E + \mathbf{K}^{i\ 3}_{\mathbf{G}}\,\frac{1}{\mu_E}, \tag{4.15}$$

$$\mathbf{K}^{i*}_{\mathbf{G}}(\mu_K,\mu_E) = \mathbf{K}^{i*0}_{\mathbf{G}} + \mathbf{K}^{i*1}_{\mathbf{G}}\,\mu_K + \mathbf{K}^{i*2}_{\mathbf{G}}\,\mu_E + \mathbf{K}^{i*3}_{\mathbf{G}}\frac{1}{\mu_E}, \tag{4.16}$$

$$\mathbf{F}^i_*(\mu_K) = \mathbf{F}^{i\ 0}_* + \mathbf{F}^{i\ 1}_*\mu_K, \tag{4.17}$$

$$\mathbf{G}_{\mathbf{T}}(\mu_E) = \mathbf{G}^0_{\mathbf{T}} + \mathbf{G}^1_{\mathbf{T}}\mu_E. \tag{4.18}$$

All the components in Equations (4.15) to (4.18) are presented in Appendix A.1. To close the HM problem, pressure and displacement boundary conditions must be applied. The Dirichlet-type conditions are imposed by passing to the right-hand side the corresponding vector $\mathbf{f}_{\mathbf{DU}}$, as

$$\mathbf{f}_{\mathbf{DU}}(\mu_\kappa,\mu_K,\mu_E) = -\mathbf{K}_{\mathbf{G}}(\mu_K,\mu_E)\mathbf{U}_{\mathrm{D}}(\mu_\kappa,\mu_K,\mu_E),$$

where $\mathbf{U}_{\mathrm{D}}(\mu_\kappa,\mu_K,\mu_E)$ is a vector with the values imposed to the Dirichlet boundary conditions that, in a general case, could depend on the parameters. As any other operator, $\mathbf{U}_{\mathrm{D}}(\mu_\kappa,\mu_K,\mu_E)$ is in separated format as,

$$\mathbf{U}_{\mathrm{D}}(\mu_\kappa,\mu_K,\mu_E) = \sum_{\check{m}}^{\check{M}} \mathbf{U}^{\check{m}}_{\mathrm{D}}\, W^{\check{m}}_{\mu_\kappa}(\mu_\kappa)\, W^{\check{m}}_{\mu_K}(\mu_K)\, W^{\check{m}}_{\mu_E}(\mu_E). \tag{4.19}$$

In Equation (4.19), $\mathbf{U}^{\check{m}}_{\mathrm{D}}$ represents a spatial function, while $W^{\check{m}}_{\mu_\kappa}(\mu_\kappa)$, $W^{\check{m}}_{\mu_K}(\mu_K)$, and $W^{\check{m}}_{\mu_E}(\mu_E)$ represent parametric functions related to heat conductivity, hydraulic conductivity, and elastic modulus, respectively. The particular definition of $\mathbf{U}_{\mathrm{D}}(\mu_\kappa,\mu_K,\mu_E)$ is problem dependent and will be set accordingly to the Dirichlet boundary conditions imposed.

4.3.2 Separable operators for geometric parameter

The separable expressions arising from the geometrical parameters are always more complex than those from material parameters. The matrices and vectors involved have a dependence on geometry that is rarely linear and usually require approximations. The geometry parameter defined for this example is simple as it only affects the r coordinate. Although, its effect in the matrices does not admit an exact, separable representation. The procedure to obtain the separated matrices is described next.

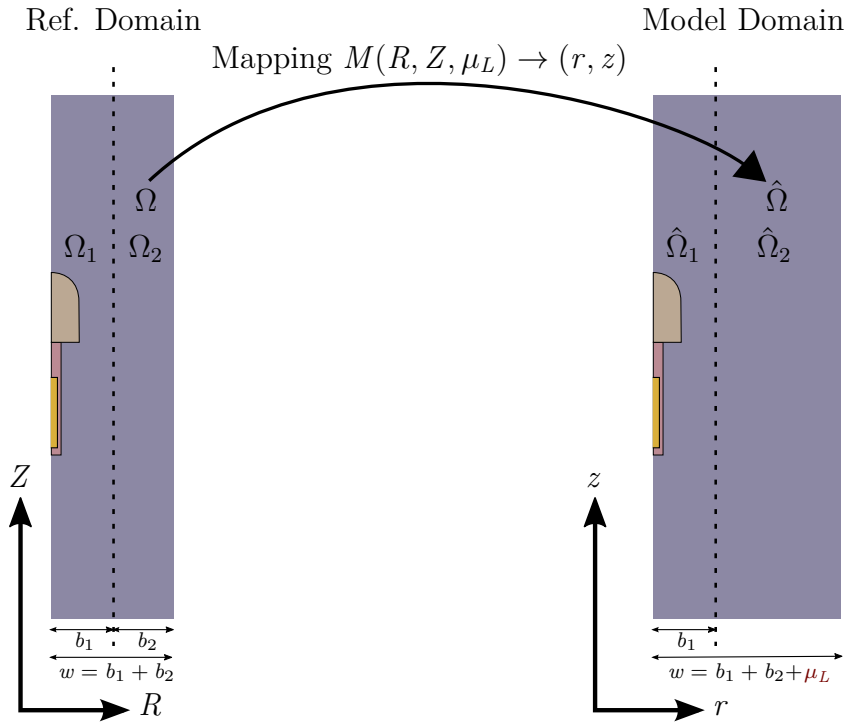

Figure 4.3: Mapping of the domain problem from the reference domain to the model domain is accomplished using the mapping function $M(R, Z, \mu_L)$. This function explicitly affects the Ω_2 domain, while Ω_1 remains fixed. The figure illustrates the generic concept of reference domain geometry and demonstrates how the geometric parameter μ_L influences it through the mapping function.

A fixed reference domain Ω with coordinates R and Z is defined as in Figure 4.3. A mapping function $M(R, Z, \mu_L)$ depending on the parameter, is defined such as it "deforms" Ω into the model domain $\hat{\Omega}$ that you want to simulate. This mapping allows introduction into the equations of the variations in the geometry produced by the parameter. In this particular case, the mapping affects only the right half of the

domain, Ω_2, and it is defined as,

$$M(R,Z,\mu_L) = \begin{cases} z = Z \\ r = \begin{cases} R & \text{if } \mathbf{x} \in \Omega_1, \\ \gamma_1(\mu_L)R + \gamma_2(\mu_L) & \text{if } \mathbf{x} \in \Omega_2, \end{cases} \end{cases} \tag{4.20}$$

where $\gamma_1(\mu_L)$ and $\gamma_2(\mu_L)$ are,

$$\gamma_1(\mu_L) = (\frac{\mu_L}{b_2} + 1), \text{ and } \gamma_2(\mu_L) = (-\frac{b_1}{b_2}\mu_L). \tag{4.21}$$

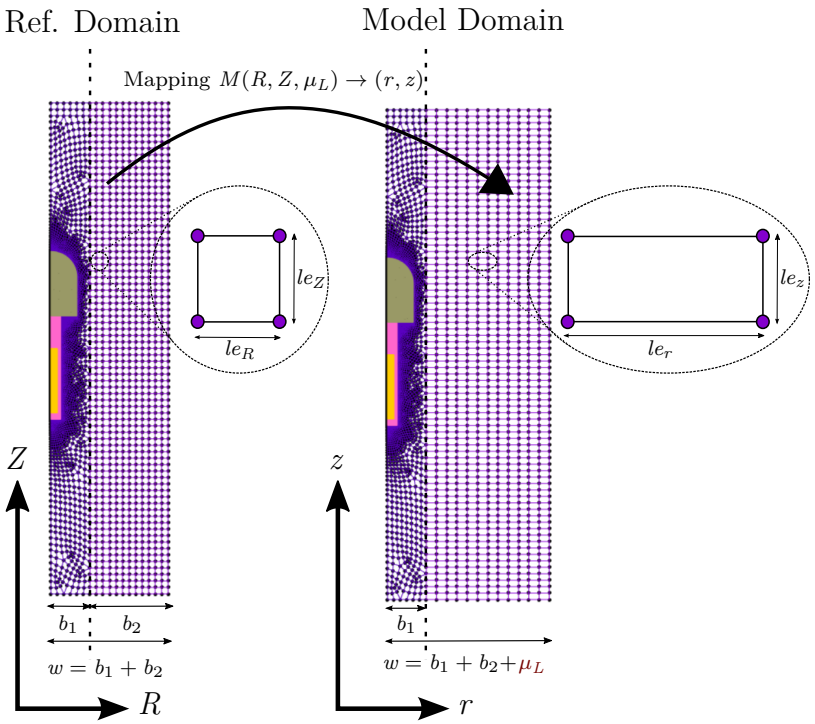

Figure 4.4: Mapping of the domain problem affects the element. So, the size of bilinear quadrilateral elements will be changed from the reference domain (le_R and le_Z) to the model domain (le_r and le_z).

For all the problems in this thesis that will be discussed in the following chapters, the spatial discretization (quadrilateral elements) in Ω_2 is regular and parallel to the space coordinates (similar to Figure 4.4). This simplifies the mapping function as all the elements in Ω_2 are identical, and the effect of the parameter in them is the same.

Therefore it is enough to analyze the effect of the mapping in one single element. Same as with the integration in standard finite elements, the mapping will be introduced via the inverse of the Jacobian to transform the gradients from the reference to the model domains. Actually, both mappings will be present, the standard isoparametric mapping going from the FE reference element to the corresponding element in the Reference domain Ω, and then the geometrical mapping going from the Reference domain to the model domain. This is shown in Figure 4.5.

The Jacobian of the isoparametric mapping is denoted as $\mathbf{J}$, and the Jacobian of the geometrical mapping is $\hat{\mathbf{J}}$,

$$\hat{\mathbf{J}} = \begin{cases} \mathbf{J} & \text{if } \mathbf{x} \in \Omega_1, \\ \begin{bmatrix} \gamma_1(\mu_L) & 0 \\ 0 & 1 \end{bmatrix} \mathbf{J} & \text{if } \mathbf{x} \in \Omega_2. \end{cases} \tag{4.22}$$

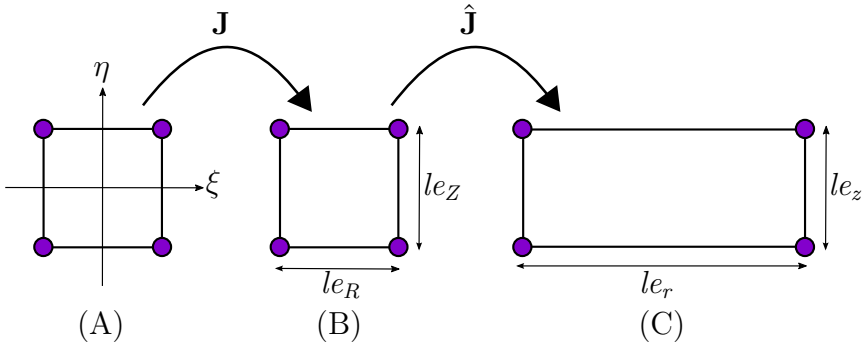

Figure 4.5: (A) The parental element is mapped by $\mathbf{J}$ to the reference element, (B) it is the reference element, $\hat{\mathbf{J}}$ maps it to the model element, and (C) it is the model element.

An exactly separated format can be defined for most of the matrices in (4.6) and (4.7) through these mappings. First, a detailed presentation will be given on how to find the separated matrix for a specific case. For instance, when $\mathbf{K}_{\mathrm{T}}$ is considered, the main definition presented in Chapter 2 (Equation (2.22)) will be employed. However, in order to ensure an accurate representation of the separated geometric representation, let us take a moment to recall the definition by incorporating a new definition of the B-operator within it. Thus, we have:

$$\mathbf{K}_{\mathrm{T}} = \int_{\Omega} \mathbf{B}_{\mathrm{T_{NEW}}}^{\top} \kappa \mathbf{B}_{\mathrm{T_{NEW}}} \, r d\Omega. \tag{4.23}$$

In Equation (4.23), $\mathbf{B}_{\mathrm{T}_{\mathrm{NEW}}}$ represents the new definition of the B-operator within this geometric parameter concept. It inherits the definition concept of the B-operator from Chapter 2 (Equation (2.36)) due to its dependence on the radial direction. Therefore, $\mathbf{B}_{\mathrm{T}_{\mathrm{NEW}}}$ is defined as follows:

$$\mathbf{B}_{\mathrm{T}_{\mathrm{NEW}}} = \begin{cases} \mathbf{B}_{\mathrm{T}} & \text{if } \mathbf{x} \in \Omega_1, \\ \begin{bmatrix} \frac{1}{\gamma_1(\mu_L)} & 0 \\ 0 & 1 \end{bmatrix} \mathbf{B}_{\mathrm{T}} & \text{if } \mathbf{x} \in \Omega_2, \end{cases} \tag{4.24}$$

In Equation (4.24), $\mathbf{B}_{\mathrm{T}}$ represents the B-operator that was previously defined in Chapter 2, specifically in Equation (2.36). Furthermore, in Equation (4.23), the integration part $rd\Omega$ is defined differently in two distinct domains due to the influence of the isoparametric and geometrical mapping (Equation (4.22)), as well as the definition of the mapping (Equation (4.20)). The specific definitions of the integration part $rd\Omega$ are as follows:

$$rd\Omega = \begin{cases} Rd\Omega & \text{if } \mathbf{x} \in \Omega_1, \\ (\gamma_1(\mu_L)R + \gamma_2(\mu_L))\gamma_1(\mu_L)d\Omega & \text{if } \mathbf{x} \in \Omega_2, \end{cases} \tag{4.25}$$

The following separated equation is derived by substituting Equations (4.24) and (4.25) into Equation (4.23):

$$\begin{aligned} \mathbf{K}_{\mathrm{T}} = & \underbrace{\left(\int_{\Omega_1} \mathbf{B}_{\mathrm{T}}^{\top}\kappa\mathbf{B}_{\mathrm{T}} Rd\Omega + \int_{\Omega_2} \mathbf{B}_{\mathrm{T}}^{\top}\kappa \begin{bmatrix} 1 & 0 \\ 0 & 0 \end{bmatrix} \mathbf{B}_{\mathrm{T}} Rd\Omega\right)}_{\mathbf{K}_{\mathrm{T}}^0} + \\ & \underbrace{\left(\int_{\Omega_2} \mathbf{B}_{\mathrm{T}}^{\top}\kappa \begin{bmatrix} 0 & 0 \\ 0 & 1 \end{bmatrix} \mathbf{B}_{\mathrm{T}} Rd\Omega\right)}_{\mathbf{K}_{\mathrm{T}}^1} \gamma_1^2(\mu_L) + \underbrace{\left(\int_{\Omega_2} \mathbf{B}_{\mathrm{T}}^{\top}\kappa \begin{bmatrix} 1 & 0 \\ 0 & 0 \end{bmatrix} \mathbf{B}_{\mathrm{T}} d\Omega\right)}_{\mathbf{K}_{\mathrm{T}}^2} \frac{\gamma_2(\mu_L)}{\gamma_1(\mu_L)} + \\ & \underbrace{\left(\int_{\Omega_2} \mathbf{B}_{\mathrm{T}}^{\top}\kappa \begin{bmatrix} 0 & 0 \\ 0 & 1 \end{bmatrix} \mathbf{B}_{\mathrm{T}} d\Omega\right)}_{\mathbf{K}_{\mathrm{T}}^3} \gamma_1(\mu_L)\gamma_2(\mu_L). \end{aligned} \tag{4.26}$$

For the remaining components in Equations (4.6) and (4.7), such as $\mathbf{M}_{\mathrm{T}}$, $\mathbf{M}_{\mathrm{pT}}$, $\mathbf{M}_{\mathrm{p}}$, $\mathbf{K}_{\mathrm{p}}$, $\mathbf{G}_{\mathrm{dT}}$, and $\mathbf{G}_{\mathrm{dp}}$, the separated representation with respect to the geometrical parameter is presented for both the thermal and HM problems as,

$$\mathbf{M}_{\mathrm{T}}(\mu_L) = \mathbf{M}_{\mathrm{T}}^0 + \mathbf{M}_{\mathrm{T}}^1\gamma_1^2(\mu_L) + \mathbf{M}_{\mathrm{T}}^2\gamma_1(\mu_L)\gamma_2(\mu_L), \tag{4.27}$$

$$\mathbf{M}_{\mathrm{pT}} = \mathbf{M}^0_{\mathrm{pT}} + \mathbf{M}^1_{\mathrm{pT}}\gamma_1^2(\mu_L) + \mathbf{M}^2_{\mathrm{pT}}\gamma_1(\mu_L)\gamma_2(\mu_L), \tag{4.28}$$

$$\mathbf{M}_{\mathrm{p}} = \mathbf{M}^0_{\mathrm{p}} + \mathbf{M}^1_{\mathrm{p}}\gamma_1^2(\mu_L) + \mathbf{M}^2_{\mathrm{p}}\gamma_1(\mu_L)\gamma_2(\mu_L), \tag{4.29}$$

$$\mathbf{K}_{\mathrm{p}} = \mathbf{K}^0_{\mathrm{p}} + \mathbf{K}^1_{\mathrm{p}}\gamma_1^2(\mu_L) + \mathbf{K}^2_{\mathrm{p}}\frac{\gamma_2(\mu_L)}{\gamma_1(\mu_L)} + \mathbf{K}^3_{\mathrm{p}}\gamma_1(\mu_L)\gamma_2(\mu_L), \tag{4.30}$$

$$\mathbf{G}_{\mathrm{dT}} = \mathbf{G}^0_{\mathrm{dT}} + \mathbf{G}^1_{\mathrm{dT}}\gamma_1(\mu_L) + \mathbf{G}^2_{\mathrm{dT}}\gamma_1^2(\mu_L) + \mathbf{G}^3_{\mathrm{dT}}\gamma_2(\mu_L) + \mathbf{G}^4_{\mathrm{dT}}\gamma_1(\mu_L)\gamma_2(\mu_L), \tag{4.31}$$

$$\mathbf{G}_{\mathrm{dp}} = \mathbf{G}^0_{\mathrm{dp}} + \mathbf{G}^1_{\mathrm{dp}}\gamma_1(\mu_L) + \mathbf{G}^2_{\mathrm{dp}}\gamma_1^2(\mu_L) + \mathbf{G}^3_{\mathrm{dp}}\gamma_2(\mu_L) + \mathbf{G}^4_{\mathrm{dp}}\gamma_1(\mu_L)\gamma_2(\mu_L), \tag{4.32}$$

$$\mathbf{G}_{\mathrm{pd}} = \mathbf{G}^0_{\mathrm{pd}} + \mathbf{G}^1_{\mathrm{pd}}\gamma_1(\mu_L) + \mathbf{G}^2_{\mathrm{pd}}\gamma_2(\mu_L) + \mathbf{G}^3_{\mathrm{pd}}\gamma_1^2(\mu_L) + \mathbf{G}^4_{\mathrm{pd}}\gamma_1(\mu_L)\gamma_2(\mu_L). \tag{4.33}$$

The matrices in the previous expressions are all standard matrices. All are defined in Appendix A.2.

The matrix that remains to be separated, the stiffness matrix of the mechanical problem, $\mathbf{K}_{\mathrm{d}}$, does not admit an exact separated expression. The procedure to find an approximated $\mathbf{K}_{\mathrm{d}}$ follows. Using (4.20) and (4.22) the matrix $\mathbf{K}_{\mathrm{d}}$ is written as,

$$\begin{aligned}\mathbf{K}_{\mathrm{d}} =& \mathbf{K}^0_{\mathrm{d}} + \mathbf{K}^1_{\mathrm{d}}\gamma_1(\mu_L) + \mathbf{K}^2_{\mathrm{d}}\gamma_2(\mu_L) + \mathbf{K}^3_{\mathrm{d}}\gamma_1^2(\mu_L) + \\ & \mathbf{K}^4_{\mathrm{d}}\gamma_1(\mu_L)\gamma_2(\mu_L) + \mathbf{K}^5_{\mathrm{d}}\frac{\gamma_2(\mu_L)}{\gamma_1(\mu_L)} + \\ & \mathbf{K}^6_{\mathrm{d}}(\mu_L).\end{aligned} \tag{4.34}$$

Note that the first five terms in (4.34) are already in separated format, although the last term $\mathbf{K}^6_{\mathrm{d}}(\mu_L)$ is not, and its expression is,

$$\mathbf{K}^6_{\mathrm{d}}(\mu_L) = \int_{\Omega_2} \mathbf{N}^{\mathrm{T}}_{\mathrm{d}} \frac{E}{(1+\nu)(1-2\nu)} \begin{bmatrix} 1-\nu & 0 \\ 0 & 0 \end{bmatrix} \mathbf{N}_{\mathrm{d}} \frac{\gamma_1(\mu_L)}{\gamma_1(\mu_L)R + \gamma_2(\mu_L)} d\Omega, \tag{4.35}$$

that this is not separable as the functions of the parameters $\gamma_1(\mu_L)$ and $\gamma_2(\mu_L)$ are dividing. The parametric part is then approximated using the following series,

$$\frac{\gamma_1(\mu_L)}{\gamma_1(\mu_L)R + \gamma_2(\mu_L)} \approx \frac{1}{R}\gamma_1(\mu_L) + \sum_{n=0}^{\infty}(-1)^{n+1}\frac{(R-b_1)^{n+1}}{(R)^{n+2}}(\frac{\mu_L}{b_2})^{n+1}\gamma_1(\mu_L). \tag{4.36}$$

By substituting (4.36) in (4.35) and then all in (4.34), the following separated stiffness matrix is obtained,

$$\begin{aligned}\mathbf{K}_{\mathrm{d}} =&\mathbf{K}_{\mathrm{d}}^{0}+\mathbf{K}_{\mathrm{d}}^{1}\gamma_1(\mu_L)+\mathbf{K}_{\mathrm{d}}^{2}\gamma_2(\mu_L)+\mathbf{K}_{\mathrm{d}}^{3}\gamma_1^2(\mu_L)+\\ &\mathbf{K}_{\mathrm{d}}^{4}\gamma_1(\mu_L)\gamma_2(\mu_L)+\mathbf{K}_{\mathrm{d}}^{5}\frac{\gamma_2(\mu_L)}{\gamma_1(\mu_L)}+\\ &\sum_{n=0}^{\mathrm{N}_\infty}\mathbf{K}_{\mathrm{d}}^{6+n}(\frac{\mu_L}{b_2})^{n+1}\gamma_1(\mu_L).\end{aligned} \tag{4.37}$$

Again, all the matrices in (4.37) are standard numeric matrices and are detailed in Appendix A.2.

The force vector, including the body and traction forces and Dirichlet boundary conditions, admits an exact separation as,

$$\mathbf{f}_{\mathbf{b}_f}=\mathbf{f}_{\mathbf{b}_f}^{0}+\mathbf{f}_{\mathbf{b}_f}^{1}\gamma_1(\mu_L)+\mathbf{f}_{\mathbf{b}_f}^{2}\gamma_1^2(\mu_L)+\mathbf{f}_{\mathbf{b}_f}^{3}\gamma_2(\mu_L)+\mathbf{f}_{\mathbf{b}_f}^{4}\gamma_1(\mu_L)\gamma_2(\mu_L), \tag{4.38}$$

$$\mathbf{f}_{\mathrm{d}}=\mathbf{f}_{\mathrm{d}}^{0}+\mathbf{f}_{\mathrm{d}}^{1}\gamma_1^2(\mu_L)+\mathbf{f}_{\mathrm{d}}^{1}\gamma_1(\mu_L)\gamma_2(\mu_L). \tag{4.39}$$

All the blocks required for the separated version of the HM problem have been presented. This parametric linear system of equations will be solved to advance one time slice.

Having explained all the relevant concepts, we can now discuss the selection of bilinear quadrilateral elements and the decision to avoid transitioning to quadratic elements. In Chapter 2, the intrusive nature of choosing between linear and quadratic elements is discussed. Should there be a need to switch from bilinear to quadratic elements, additional contributions would be required to incorporate the geometric parameter. This can be observed in Equations (A.46) to (A.57) in Appendix A.2, where new terms involving operators such as $\frac{\partial \mathbf{N}_{\mathrm{d}}}{\partial R}$ and $\frac{\partial \mathbf{N}_{\mathrm{d}}}{\partial Z}$ are introduced. Modifying the code from linear to quadratic elements would involve making corresponding adjustments to their implementation.

Finally, now that the material parametrization has been presented and all the separated operators are defined, and similarly has been done for the geometrical parameter, the combination of both types of parameters is involved but trivial to obtain. All the operator for the 4-parameter case are presented in Appendix A.3.

Chapter 5

Methodology validation

The goal of this chapter is to validate the methodology that was outlined in the previous chapter. To this end, PGD is applied to a transient coupled THM academic problem with known solutions [129].

This chapter is divided into two sections. Section 5.1 provides the problem statement of the academic problem used for validation. Further, this section will present the analytical solutions and the corresponding Finite Element Method (FEM) formulation and its convergence plots, as well as the choice of parameters of the problem. Section 5.2 presents the results obtained from the academic problem, while Section 5.3 focuses on the analysis and discussion of these results, including the definition and use of various errors for analysis.

5.1 Problem statement

This section will explore an academic problem involving an axisymmetric cylindrical geometry to validate the methodology. The 3D axisymmetric problem is formulated on a 2D domain taking benefit from the symmetry. Additionally, as shown in Figure 5.1, the academic problem under investigation involves the constraints imposed on the lateral surface of the symmetric cylinder due to radial motion, heat flux, and fluid flux. Using such boundary conditions, the problem solution along the r-axis is constant and only depends on the z-coordinate, which means it is a 1D problem, see Figure 5.1. Under these conditions, it is possible to develop an analytical solution.

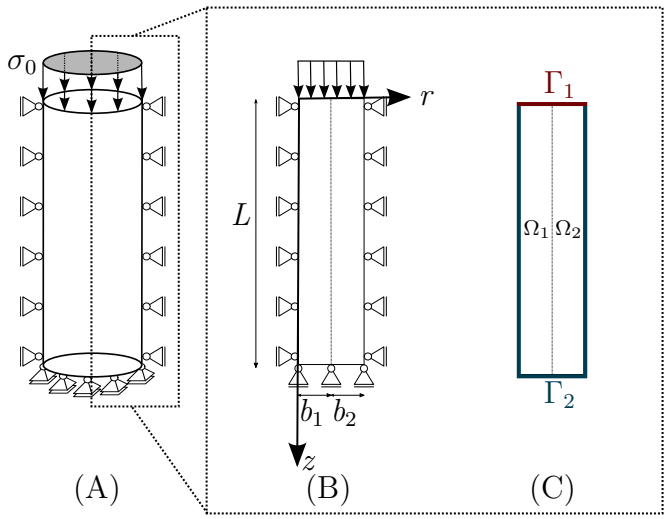

Figure 5.1: (A) Axisymmetric cylinder under uniform stress, (B) geometry, and (C) boundaries and domain.

In Chapter 2, the three main governing equations are presented (Equation (2.7)). Note that in this problem, gravity forces and heat sources are neglected. The main governing equations are therefore simplified as,

$$\begin{cases} ((1-\phi)\rho_s c_s + \phi\rho_f c_f)\,\dot{T} - \boldsymbol{\nabla}\cdot(\kappa\boldsymbol{\nabla}T) = 0 & \text{in } \Omega\times I_t, \\ (\dfrac{\phi}{K_f} + \dfrac{\alpha-\phi}{K_s})\dot{p} - \boldsymbol{\nabla}\cdot(\dfrac{K}{\rho_f g}\boldsymbol{\nabla}p) \\ \qquad + \alpha\boldsymbol{\nabla}\cdot\dot{\mathbf{u}} = (3\phi\alpha_f + 3(\alpha-\phi)\alpha_s)\,\dot{T} & \text{in } \Omega\times I_t, \\ \alpha\boldsymbol{\nabla}p - \boldsymbol{\nabla}\cdot(\mathbb{C}:\boldsymbol{\nabla}\mathbf{u}) = -3K_D\alpha_s\boldsymbol{\nabla}T & \text{in } \Omega\times I_t. \end{cases} \tag{5.1}$$

The dependencies of the unknowns on $\mathbf{x}$ and t are omitted for brevity. We use spatial coordinates r and z to represent the radial and downward directions, respectively, with $\mathbf{x}$ as a vector having coordinates (r, z). All the material properties mentioned in Equation (5.1) are described in Table 2.2.

As shown in Figure 5.1-C, the domain $\Omega = \Omega_1 \cup \Omega_2$ is split into two subdomains, the boundaries of Ω are Γ_1 and Γ_2 at the top and remaining parts of the domain, respectively. For the thermal field, the boundary conditions are,

$$\begin{cases} T(\mathbf{x},t) = 0 & \text{on } \Gamma_1\times I_t, \\ (-\kappa\boldsymbol{\nabla}T)\cdot\mathbf{n} = 0 & \text{on } \Gamma_2\times I_t. \end{cases} \tag{5.2}$$

The boundary conditions for the hydraulic field are,

$$\begin{cases} p(\mathbf{x},t) = 0 & \text{on } \Gamma_1 \times I_t, \\ (-\dfrac{K}{\rho_f g}\boldsymbol{\nabla} p)\cdot \mathbf{n} = 0 & \text{on } \Gamma_2 \times I_t. \end{cases} \tag{5.3}$$

A uniform load per unit surface (σ_0) is applied on the top boundary of the domain, and the lateral displacement is constrained to be zero, which translates in the mechanical boundary conditions,

$$\begin{cases} \boldsymbol{\sigma}\cdot\mathbf{n} = \sigma_0 & \text{on } \Gamma_1 \times I_t, \\ \mathbf{u}(\mathbf{x},t) = 0 & \text{on } \Gamma_2 \times I_t. \end{cases} \tag{5.4}$$

The initial conditions are defined as,

$$\begin{cases} T(\mathbf{x},0) = T_0 & \text{in } \Omega, \\ p(\mathbf{x},0) = p_0 & \text{in } \Omega, \\ \mathbf{u}(\mathbf{x},0) = \mathbf{u}_0(\mathbf{x}) & \text{in } \Omega, \end{cases} \tag{5.5}$$

where T_0 and p_0 are spatially uniform.

The value of p_0 is defined as in Selvadurai and Suvorov [129],

$$\begin{aligned} p_0 = &- \frac{\alpha\sigma_0}{\alpha^2 + \left(\frac{\phi}{K_f} + \frac{\alpha-\phi}{K_s}\right)\left(\frac{E(1-\nu)}{(1-2\nu)(1+\nu)}\right)} \\ &+ \frac{\left(\frac{E(1-\nu)}{(1-2\nu)(1+\nu)}\right)\Big[(\alpha-\phi)3\alpha_s T_0 + \phi 3\alpha_f T_0\Big] - K_D 3\alpha_s T_0 \alpha}{\alpha^2 + \left(\frac{\phi}{K_f} + \frac{\alpha-\phi}{K_s}\right)\left(\frac{E(1-\nu)}{(1-2\nu)(1+\nu)}\right)}. \end{aligned} \tag{5.6}$$

The initial condition of the mechanical field ($\mathbf{u}_0(\mathbf{x})$) is not spatially uniform. It is found as the solution of a steady-state equation for the mechanical field by inserting the constant T_0 and p_0. For the problem at hand, T_0 and σ_0 are set to 50 °C and 10.9 MPa, respectively. For the geometry, L, b_1, and b_2 are set to 10 m, 0.5 m, and 0.5 m, respectively.

The application problem is inspired by [149] and involves an engineered barrier system located underground and surrounded by granitic rocks. For the input data in this closed-form case, the properties of the solid phase are assumed to be similar to those of granitic rocks, as presented in Table 5.1. As for the input properties of the fluid phase, the values for density, specific heat, heat expansion coefficient, and bulk modulus for fluids ρ_f, c_f, α_f and K_f are considered to be $1000\frac{\text{kg}}{\text{m}^3}$, $4180\frac{\text{j}}{\text{kg°C}}$, $6.9\times10^{-5}\frac{1}{\text{°C}}$ and 2200MPa, respectively.

Symbol	Units	Description	Solid properties	Reference
ρ_s	$\frac{\text{Kg}}{\text{m}^3}$	Density	2743	[149]
ϕ	–	Porosity	0.005	[149]
c_s	$\frac{\text{J}}{\text{Kg }^\circ\text{C}}$	Specific heat	764	[149]
α_s	$\frac{1}{^\circ\text{C}}$	Heat expansion	0.85×10^{-5}	[149]
α	–	Biot's coefficient	0.75	[91]
ν	–	Poisson's ratio	0.25	[149]
κ	$\frac{\text{W}}{\text{m }^\circ\text{C}}$	Heat conductivity	$I_{\mu_\kappa} = [1.5, 5]^{(*)}$	[79]
K	$\frac{\text{m}}{\text{s}}$	Hydraulic conductivity	$I_{\mu_K} = [3 \times 10^{-14}, 3 \times 10^{-12}]^{(*)}$	[149]
E	MPa	Elastic modulus	$I_{\mu_E} = [55600, 68000]^{(*)}$	[74]

Table 5.1: The solid phase properties. The asterisk (*) represents the range of material parameters treated as variables. The minimum and maximum bounds of the ranges were selected from the tables provided in the references.

5.1.1 Analytical solution

Using the symmetry of the problem and the boundary conditions, the main Partial Differential Equations (PDEs) admit an equivalent 1D formulation,

$$\begin{cases} ((1-\phi)\rho_s c_s + \phi\rho_f c_f)\,\dot{T} - \kappa\dfrac{\partial^2 T}{\partial z^2} = 0 & \text{in } \ I_z \times I_t, \\ (\dfrac{\phi}{K_f} + \dfrac{\alpha-\phi}{K_s})\dot{p} - \dfrac{K}{\rho_f g}\dfrac{\partial^2 p}{\partial z^2} + \alpha\dfrac{\partial \dot{u}_z}{\partial z} = (3\phi\alpha_f + 3(\alpha-\phi)\alpha_s)\,\dot{T} & \text{in } \ I_z \times I_t, \\ \alpha\dfrac{\partial p}{\partial z} - \dfrac{E(1-\nu)}{(1-2\nu)(1+\nu)}\dfrac{\partial^2 u_z}{\partial z^2} = -3K_D\alpha_s\dfrac{\partial T}{\partial z} & \text{in } \ I_z \times I_t, \end{cases} \tag{5.7}$$

where $I_z = [0, L]$ is the interval of one-dimensional space in the axial direction (z-axis).

The PDEs (5.7) have closed-form solutions [129]. The analytical solution for temperature (T) and pressure (p) are,

$$T(z,t) = T_0 \sum_{m=1,3,5,\ldots} \frac{4}{m\pi} \sin\Big(\frac{m\pi}{2L}z\Big) \exp\Big(-\frac{m^2\pi^2}{4L^2}kt\Big). \tag{5.8}$$

$$\begin{aligned} p(z,t) = p_0 \sum_{m=1,3,5,\ldots} \frac{4}{m\pi} \sin\Big(\frac{m\pi}{2L}z\Big) \exp\Big(-\frac{m^2\pi^2}{4L^2}ct\Big) - \\ \sum_{m=1,3,5,\ldots} A\frac{4}{m\pi} \sin\Big(\frac{m\pi}{2L}z\Big) \exp\Big(-\frac{m^2\pi^2}{4L^2}ct\Big) + \\ \sum_{m=1,3,5,\ldots} A\frac{4}{m\pi} \sin\Big(\frac{m\pi}{2L}z\Big) \exp\Big(-\frac{m^2\pi^2}{4L^2}kt\Big). \end{aligned} \tag{5.9}$$

Where in Equations (5.8) and (5.9), k, c, and A are,

$$k = \frac{\kappa}{(1-\phi)\rho_s c_s + \phi\rho_f c_f},$$

$$c = \frac{\frac{K}{\rho_f g}}{\frac{\alpha^2(1-2\nu)(1+\nu)}{E(1-\nu)} + (\frac{\phi}{K_f} + \frac{\alpha-\phi}{K_s})},$$

$$A = -T_0 \frac{(\phi\alpha_f + (\alpha-\phi)\alpha_s - \frac{\alpha K_D(1-2\nu)(1+\nu)}{E(1-\nu)}\alpha_s)}{\frac{1}{k}\frac{K}{\rho_f g} - (\frac{\phi}{K_f} + \frac{\alpha-\phi}{K_s} + \frac{\alpha^2(1-2\nu)(1+\nu)}{E(1-\nu)})}.$$

The analytical solution for axial displacement (u_z) is as [129],

$$\begin{aligned} u_z(z,t) = \frac{(1-2\nu)(1+\nu)}{E(1-\nu)} \\ \Big[- \sum_{m=1,3,5,\ldots} (3K_D\alpha_s T_0 + \alpha A)\frac{8L}{m^2\pi^2} \cos\Big(\frac{m\pi}{2L}z\Big) \exp\Big(-\frac{m^2\pi^2}{4L^2}kt\Big) \\ + \sum_{m=1,3,5,\ldots} \alpha(A-p_0)\frac{8L}{m^2\pi^2} \cos\Big(\frac{m\pi}{2L}z\Big) \exp\Big(-\frac{m^2\pi^2}{4L^2}ct\Big) + \sigma_0(z-L)\Big]. \end{aligned} \tag{5.10}$$

These analytical solutions are used to check the FEM implementation by controlling their convergence plots, which are discussed in the following subsection.

5.1.2 Finite Element Method validation

The first step for validating the overall methodology is to validate the FEM implementation. The following convergence curves (Figure 5.2) are produced to show that the FEM model is behaving as expected.

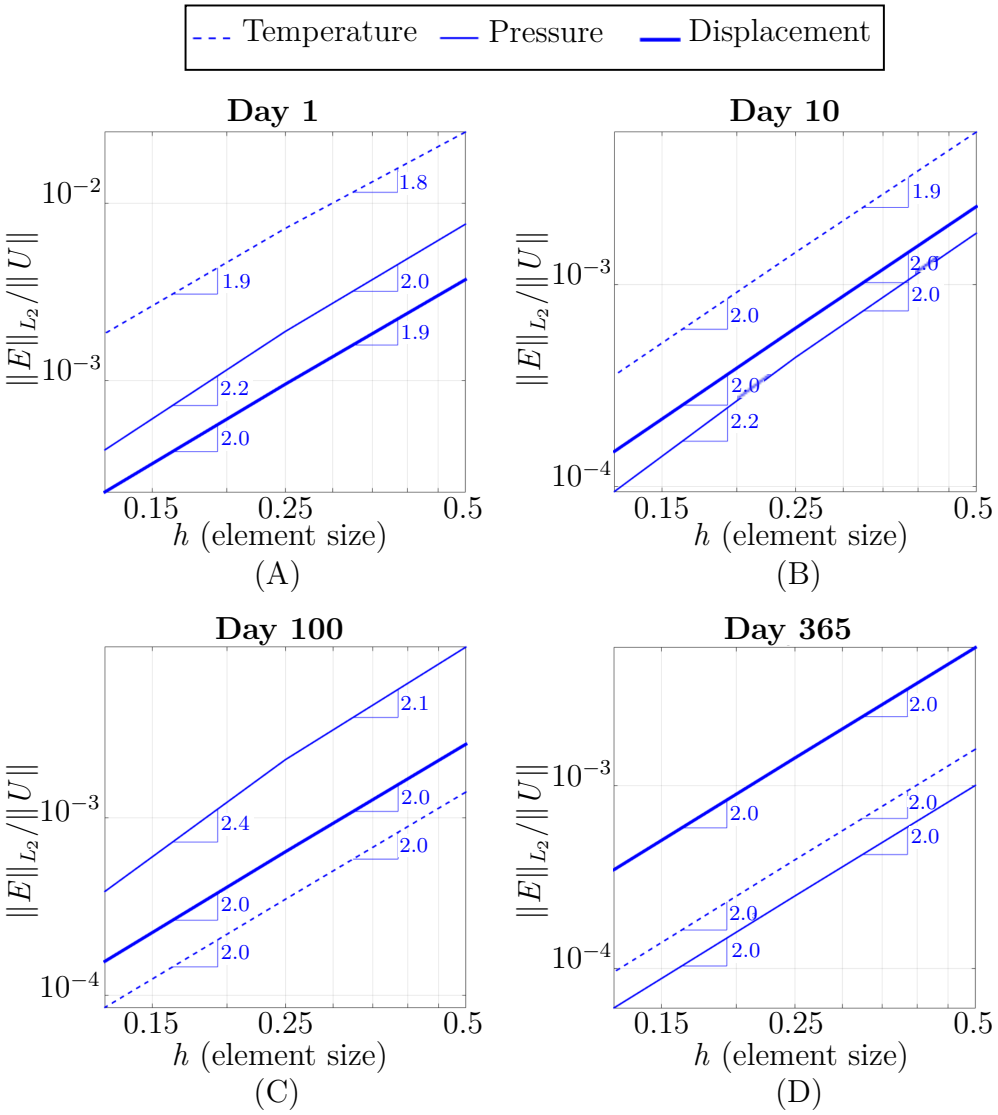

Figure 5.2: Convergence plots at (A) day 1, (B) day 10, (C) day 100, and (D) day 356 demonstrate that reducing the element size (h) results in a decreasing L_2 norm of the error. The observed convergence order of two aligns with the expected behavior for the linear elements utilized in this study.

The error in the FEM approximation is a function $E(r, z)$ defined as the difference between the analytical and the FEM solutions,

$$E(r, z) = U(r, z) - U_{\text{FEM}}(r, z), \tag{5.11}$$

where $U(r, z)$ and $U_{\text{FEM}}(r, z)$ represent the analytical and FEM solution for temperature or pressure, or displacement. The error varies over the solution domain. To

measure how the global error decreases as the mesh is refined, the norm of the error,

$$\|E\|_{L_2} = \sqrt{\int_\Omega E(r,z)^2 d\Omega}, \tag{5.12}$$

is used. Figure 5.2 provides the convergence plots, based on the L_2 norm of the error in space. The expected order of convergence for linear elements is two [68], and Figure 5.2 shows our implementation provides the correct orders.

In Chapter 2 (end of Subsection 2.2.2), it was mentioned that the bi-linear quadrilateral had been used for the in-house code developed for this study, and the possibility of the existence of oscillations and jumps due to instability had been discussed. The convergence plots in Figure 5.2 suggest that no such issues are observed for the present problem, as will also be illustrated in Section 5.2. It should be emphasized that no such issues are also observed in the application problem, which will be presented in Chapter 6.

5.1.3 Parametric problem

Let us assume now that we are interested in finding a solution to the prior problem for ranges of values of the heat conductivity (μ_κ), the hydraulic conductivity (μ_K), the elastic modulus (μ_E), and a geometrical parameter (μ_L). Homogeneous material parameters (μ_κ, μ_K, and μ_E) in the whole domain are considered in this academic problem, with the ranges (I_{μ_κ}, I_{μ_K}, and I_{μ_E}) that are presented in Table 5.1. The geometric parameter is similar to that of Subsection 4.3.2; where its interval is defined as,

$$\Omega(\mu_L) = \Omega_1 \cup \Omega_2(\mu_L), \text{ where } \mu_L \in I_{\mu_L} = [-0.1\,\mathrm{m}, 0.5\mathrm{m}]\,. \tag{5.13}$$

The results presented here show that the implementation is working correctly for the four-parameter case. The parametric PDEs is same as Equation (4.1).

In this case, all Dirichlet and Neumann boundary conditions concerning thermal and hydraulic problems are zero and therefore, they do not depend on the parameters. Same happens with the Dirichlet boundary conditions of the mechanical equilibrium equation (Equation (5.4)). Conversely, the Neumann boundary conditions of the mechanical part are not homogeneous (Equation (5.4)), and they are affected by the geometric parameter. The mechanical boundary conditions are,

$$\begin{cases} \boldsymbol{\sigma} \cdot \mathbf{n} = \sigma_0 & \text{on } \Gamma_1(\mu_L) \times I_{\boldsymbol{\mu}} \times I_t, \\ \mathbf{u}(\mathbf{x}, t) = 0 & \text{on } \Gamma_2(\mu_L) \times I_{\boldsymbol{\mu}} \times I_t, \end{cases} \tag{5.14}$$

where $\boldsymbol{\mu} = [\mu_\kappa, \mu_K, \mu_E, \mu_L]$ is a vector with the coordinates of the four parametric dimensions.

It is necessary to define the initial conditions for the parametric problem. The initial pressure depends on the elastic modulus. Equation (5.5) is reformulated as,

$$\begin{cases} T(\mathbf{x}, \boldsymbol{\mu}, 0) = T_0 & \text{in } \Omega(\mu_L) \times I_{\boldsymbol{\mu}}, \\ p(\mathbf{x}, \boldsymbol{\mu}, 0) = \Lambda_{\mu_E}(\mu_E) & \text{in } \Omega(\mu_L) \times I_{\boldsymbol{\mu}}, \\ \mathbf{u}(\mathbf{x}, \boldsymbol{\mu}, 0) = \mathbf{u}_0(\mathbf{x}, \boldsymbol{\mu}) & \text{in } \Omega(\mu_L) \times I_{\boldsymbol{\mu}}, \end{cases} \tag{5.15}$$

where $\Lambda_{\mu_E}(\mu_E)$ is defined as,

$$\begin{aligned} \Lambda_{\mu_E}(\mu_E) = &- \frac{\alpha\sigma_0}{\alpha^2 + \left(\frac{\phi}{K_f} + \frac{(\alpha-\phi)(1-2\nu)(1-\alpha)}{\mu_E}\right)\left(\mu_E \frac{(1-\nu)}{(1-2\nu)(1+\nu)}\right)} \\ &+ \frac{\left(\mu_E \frac{(1-\nu)}{(1-2\nu)(1+\nu)}\right)\left[(\alpha-\phi)3\alpha_s T_0 + \phi 3\alpha_f T_0\right] - \frac{3\alpha_s T_0 \alpha}{(1-2\nu)}\mu_E}{\alpha^2 + \left(\frac{\phi}{K_f} + \frac{(\alpha-\phi)(1-2\nu)(1-\alpha)}{\mu_E}\right)\left(\mu_E \frac{(1-\nu)}{(1-2\nu)(1+\nu)}\right)}. \end{aligned} \tag{5.16}$$

The parametric initial displacement in Equation (5.15) ($\mathbf{u}_0(\mathbf{x}, \boldsymbol{\mu})$) will be sought for by solving the parametric steady-state solution of the mechanical equilibrium equation.

The discretization of space and time is done as usual in numerical methods (Section 2.2). The parametric nature of this problem also requires the discretization of the parametric domains. The separated representation adopted by PGD allows for the independent discretization of each parametric dimension. The grids used in this application are as follows:

- The dimension controlling the heat conductivity (μ_κ), is discretized linearly with 701 nodes.
- The dimension controlling the hydraulic conductivity (μ_K), is discretized with 1501 nodes distributed logarithmically, as this quantity spans over several orders of magnitude.
- The dimension controlling the elastic modulus (μ_E), is discretized linearly with 249 nodes.
- The dimension controlling the geometry (μ_L), is discretized linearly with 601 nodes.

5.2 Results of the academic problem

By specifying all the individual input data for the Encapsulated PGD methodology [38], the separate unknowns are determined as solutions for each time slice. For every time slice (t), the unknown fields are,

$$\mathbf{T}^t(\mathbf{x}, \mu_\kappa, \mu_L) = \sum_{\hat{m}=1}^{\hat{M}^t} \mathbf{T}^{\hat{m}}(\mathbf{x}) B^{\hat{m}}_{\mu_\kappa}(\mu_\kappa) B^{\hat{m}}_{\mu_L}(\mu_L), \tag{5.17}$$

$$\mathbf{U}^t(\mathbf{x}, \mu_\kappa, \mu_K, \mu_E, \mu_L) = \sum_{m=1}^{M^t} \mathbf{U}^m(\mathbf{x}) G^m_{\mu_\kappa}(\mu_\kappa) G^m_{\mu_K}(\mu_K) G^m_{\mu_E}(\mu_E) G^m_{\mu_L}(\mu_L). \tag{5.18}$$

In Equations (5.17) and (5.18), $\hat{M}^t$ and M^t are the numbers of modes used in the thermal and hydro-mechanical separated output, respectively. Functions B and G represent the parametric dependence.

The PGD method utilizes two nested loops: the enrichment and the fixed-point iteration. Both are iterative procedures that employ a tolerance for the stopping criterion. The tolerance for the enrichment is denoted as η_{tol}, while the tolerance for the fixed point is referred to as ϵ_{tol}. Additionally, a maximum number of iterations is defined. In certain applications, it is advantageous to set a predetermined number of iterations for the inner fixed-point loop instead of checking for convergence. In the specific case of PGD, this approach can be employed without compromising the overall solution accuracy as will be shown later. For this problem, a total of five fixed-point iterations has been found to be sufficient, with the primary stopping criterion being the enrichment tolerance. Striking a balance between the number of fixed-point iterations and the enrichment tolerance is crucial to achieve accurate and efficient results for each individual problem.

Symbol	Amount	Definition
η_{tol}	10^{-3},10^{-4},10^{-5},10^{-6}	Enrichment Tolerance
iter_{max}	5	Maximum number of iteration for Fixed-point iteration

Table 5.2: Stopping criteria for PGD internal loops.

Next, we will focus on the effect of the tolerance used for enrichment (η_{tol}). Naturally, the smaller the tolerance, the larger the number of terms in the solution and the higher the expected accuracy. This will be demonstrated through examples solved

using four different tolerances, as presented in Table 5.2. The aim is to show that by decreasing the enrichment tolerance, the accuracy of the problem will increase.

The parametric problem discussed in Section 5.1.3 was solved over a one-year time domain, with a time step of one day. To demonstrate the shape and behavior of the solution, the three primary fields (pressure, temperature, and displacement) are presented for a specific point in time and a set of parameters. Given $\boldsymbol{\mu}^* = [5, \frac{\mathrm{W}}{\mathrm{m},^\circ\mathrm{C}}, 3 \times 10^{-12}, \frac{\mathrm{m}}{\mathrm{s}}, 55600, \mathrm{MPa}, -0.1, \mathrm{m}]$ and $t = 185$ days, Figure 5.3 displays the spatial solution for temperature, pressure, and displacement versus depth (represented by the z-axis, also presented in Figure 5.1), obtained with different enrichment tolerances. The Finite Element (FE) solution is included as a reference. The figure illustrates how the PGD solution approximates the FE solution as the tolerance is reduced. For this academic problem, a tolerance of $\eta_{\mathrm{tol}} = 10^{-6}$ provides the most accurate result compared to the others.

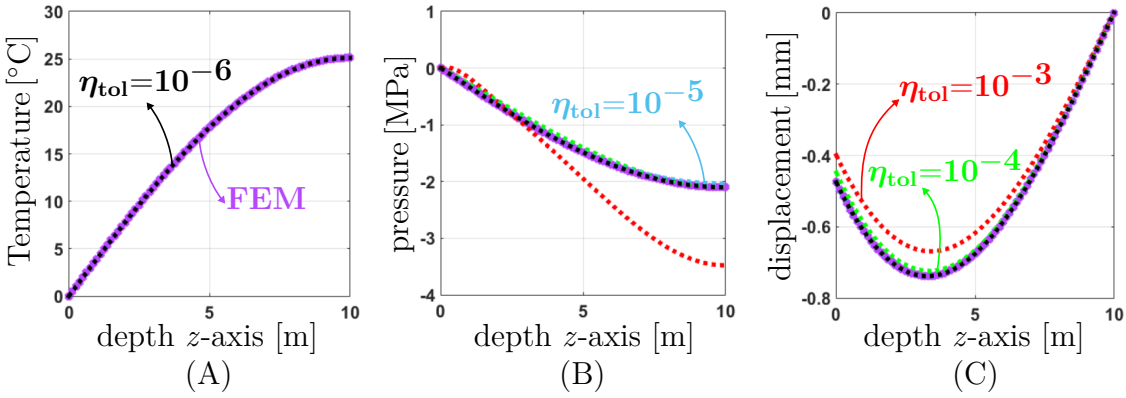

Figure 5.3: Space solution of the validation problem for time = 185 days and parameters $\boldsymbol{\mu}^* = [5\,\frac{\mathrm{W}}{\mathrm{m}\,^\circ\mathrm{C}}, 3 \times 10^{-12}\,\frac{\mathrm{m}}{\mathrm{s}}, 55600\,\mathrm{MPa}, -0.1\,\mathrm{m}]$. Several PGD solutions computed for different PGD-enrichment tolerances (η_{tol}) are displayed alongside the FE solution. As the tolerance is reduced, the error of PGD in comparison to FE diminishes. It is worth noting that in the case of the thermal field, the solutions for all tolerances are on top of the FE.

Figure 5.4 shows temperature, pressure, and displacement results over time for a fixed space coordinate ($z = 9.75\,\mathrm{m}$) and a specific point in parametric space $\boldsymbol{\mu}^* = [1.5\,\frac{\mathrm{W}}{\mathrm{m}\,^\circ\mathrm{C}}, 3 \times 10^{-12}\,\frac{\mathrm{m}}{\mathrm{s}}, 55600\,\mathrm{MPa}, -0.1\,\mathrm{m}]$. The graph also includes the FE solution for comparison. As the enrichment tolerance is reduced, the PGD solution converges towards the FE solution.

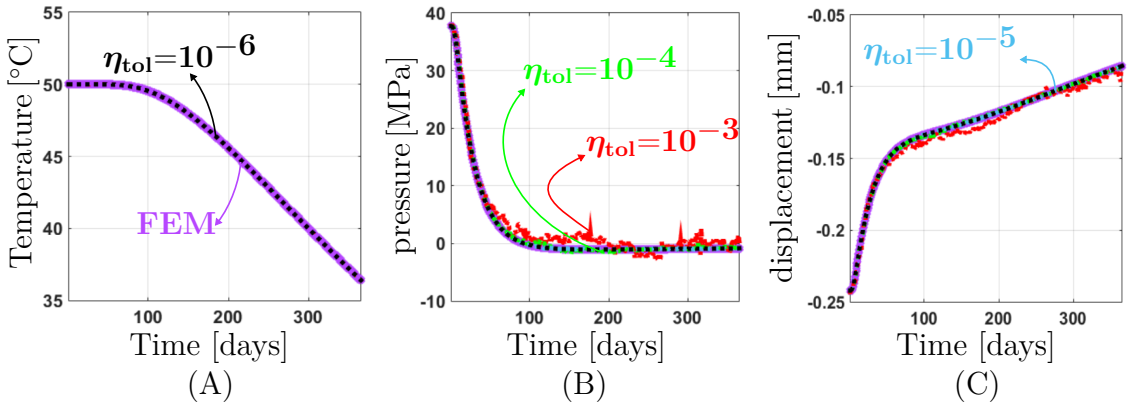

Figure 5.4: Time solution of the validation problem for $z = 9.75\,\text{m}$ and parameters $\boldsymbol{\mu}^* = [1.5\,\frac{\text{W}}{\text{m}\,^\circ\text{C}}, 3\times10^{-12}\,\frac{\text{m}}{\text{s}}, 55600\,\text{MPa}, -0.1\,\text{m}]$. Several PGD solutions computed for different PGD-enrichment tolerances (η_{tol}) are shown together with the FE solution. When the tolerance is being reduced, the error of PGD with respect to FE vanishes. Note that in the case of the thermal field, the solution for all tolerances are on top of the FE.

5.3 Discussion and analysis of the results

The solution at each time step is stored in two separate tensors: one for the thermal problem and one for the hydro-mechanical problem. Although the solution is stored as separate tensors, it can be conceptually expressed as a 6th-order tensor (space + time + 4 parameters). Computing the global error involves integrating over the complete 6-dimensional hypercube, which is computationally demanding. In this study, we present an approximation of the global error and examine several sections or slices of the hypercube. For example, fixing all the parametric dimensions (i.e., assigning a particular value to each parameter) transforms the solution into a standard FE output, enabling the measurement of errors in space and time. Additionally, computing a norm in the space-time dimension allows for the computation of a scalar error for every parameter combination. The error is then displayed in several meaningful slices of the complete solution, and various error definitions are presented for this purpose. The first error definition is a global scalar error of a field f, denoted as ϵ_G^f, which involves integration across all dimensions,

$$\epsilon_G^f = \frac{\|f_{\text{FE}} - f_{\text{PGD}}\|_{\Omega\times I_t\times I_{\boldsymbol{\mu}}}}{\|f_{\text{FE}}\|_{\Omega\times I_t\times I_{\boldsymbol{\mu}}}}. \tag{5.19}$$

This error is applied to the temperature, pressure, and displacement fields arising from the problem. If the integration is not done in all dimensions, other error measures

are defined. For example, the error in time is a one-dimensional function defined as,

$$\epsilon_t^f(t) = \frac{\|f_{\text{FE}}(t) - f_{\text{PGD}}(t)\|_{\Omega \times I_{\boldsymbol{\mu}}}}{\|f_{\text{FE}}(t)\|_{\Omega \times I_{\boldsymbol{\mu}}}}, \tag{5.20}$$

and if the integration is only taken in space, the following five-dimensional local error is defined,

$$\epsilon_{\boldsymbol{\mu}}^f(t, \boldsymbol{\mu}) = \frac{\|f_{\text{FE}}^{\boldsymbol{\mu}}(t) - f_{\text{PGD}}(t, \boldsymbol{\mu})\|_{\Omega}}{\|f_{\text{FE}}^{\boldsymbol{\mu}}(t)\|_{\Omega}}. \tag{5.21}$$

With the equipment of these errors definitions, some results are presented next.

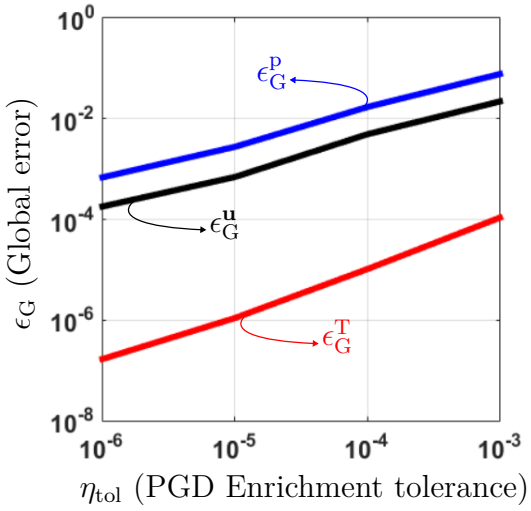

Figure 5.5: Effect of a decrease of the enrichment tolerance, the accuracy of global error for temperature ($\epsilon_{\text{G}}^{\text{T}}$), pressure ($\epsilon_{\text{G}}^{\text{p}}$), and displacement ($\epsilon_{\text{G}}^{\mathbf{u}}$) increases.

The convergence of the global error (integrating in all dimensions) is presented in Figure 5.5. The error of all the fields is reduced when the PGD-enrichment tolerance decreases. As explained before, the computation of this global error, ϵ_G, is very demanding computationally, so it is approximated using a simple quadrature having only 3 points at each parametric dimension. Nevertheless, the stable decrease in the convergence curve shows that this approximation is enough to get its trend. Based on the convergence curves, the following results are presented for the enrichment tolerance $\eta_{\text{tol}} = 10^{-6}$.

After demonstrating the global convergence of the solution, we now focus on specific slices to show the accuracy and behavior of local solutions. The evolution of the error over time is measured using ϵ_t defined in Equation (5.20). Figure 5.6 illustrates the error distribution over time. As previously observed, the temperature field demonstrates higher accuracy compared to the pressure and displacement fields.

This disparity can be attributed to the inherent simplicity of the thermal problem, which involves only two relevant parameters and is not coupled to other variables. In a fully coupled problem, the accuracy of the temperature field is expected to be affected by errors in pressure and displacement, leading to a decrease in overall accuracy. However, in this case, where the thermal aspect is decoupled, the temperature field exhibits significantly higher accuracy than the hydro-mechanical aspect. In this study, several trials were conducted using a monolithic solver, revealing that when solving the THM problem, even with the thermal aspect decoupled from the hydro-mechanical aspect and employing a monolithic approach, the efficiency is noticeably reduced, impacting the overall parametric solution. However, when the thermal problem is solved separately, the solution becomes faster and more accurate compared to the coupled approach. In any case, the worst error (from the pressure) is below 10^{-3}, showing that the PGD solution is accurate enough for most practical engineering purposes.

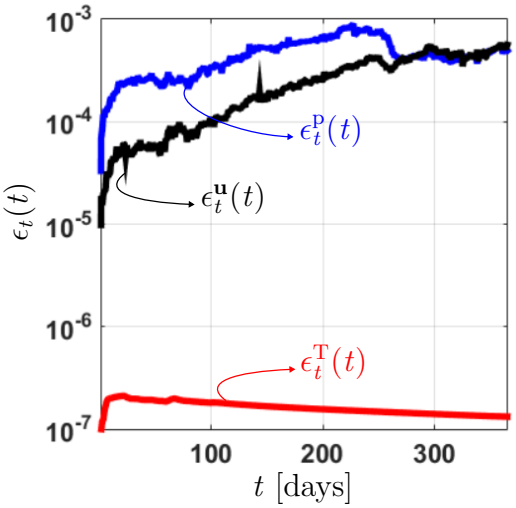

Figure 5.6: The global errors in each time slice by assigning $\eta_{\text{tol}} = 10^{-6}$, for all the fields output are less than 10^{-3}; however, for temperature $\epsilon_t^{\mathrm{T}}(t)$, the global errors are 10^4 more accurate than the pressure $\epsilon_t^{\mathrm{p}}(t)$ and displacement $\epsilon_t^{\mathbf{u}}(t)$.

It is interesting to verify whether all the points of the parametric space results have the same level of accuracy. To achieve this, one can choose different combinations of parameters and compute local error based on Equation (5.21). For the temperature, such an error will not be sought since it is more accurate compared to the rest by several orders of magnitude. For every parameter, the minimum, maximum, and middle points have been taken. This led to a selection of a total of 81 parameter

value combinations for further analysis. The error plot used to study these 81 selected combinations of parameter values will be organized line by line as illustrated in Figure 5.7. Figure 5.7 is structured by nested blocks of three values of parameters. It is split into three blocks corresponding to the minimum median and maximum values of the first parameter. Each of these three blocks is subsequently recursively divided into three blocks for the three values of the other parameters. The most "inner" parameter of heat conductivity undergoes the most frequent changes by blocks of three lines, followed by the elastic modulus (blocks of 9 lines) and geometric parameter (blocks of 27 lines), while hydraulic conductivity serves as the outer parameter (three blocks of 27 lines).

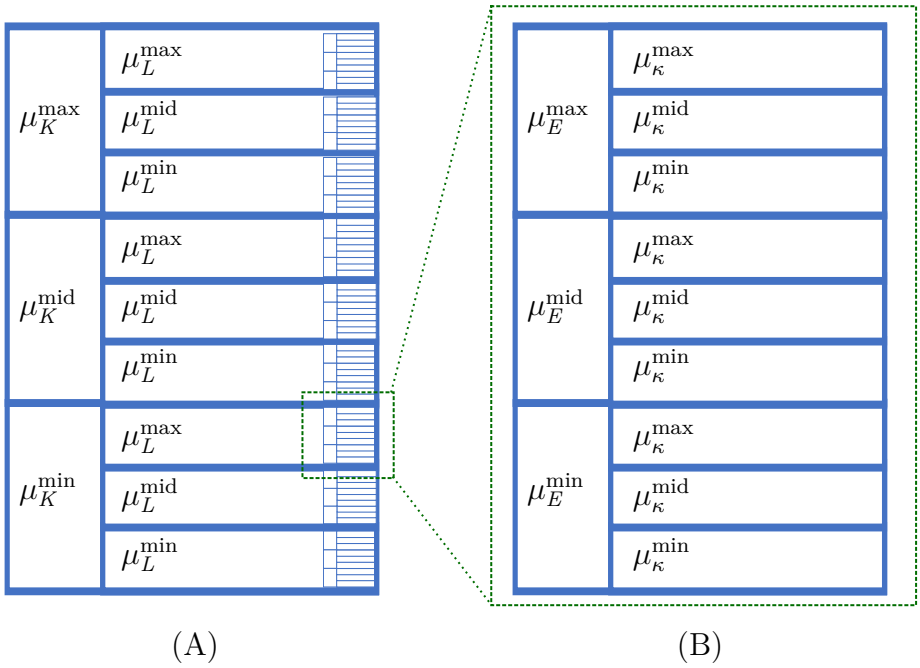

Figure 5.7: The representation structure of the error explaining the parametric space comprises two blocks: (A) blocks corresponding to the values of the "outer" parameters, namely hydraulic conductivity and geometric parameter, and (B) blocks matching the variations of the "inner" parameters, namely elastic modulus and thermal conductivity.

The vertical axis of Figure 5.8 (lines) employs the same combinations of definitions as those presented in Figure 5.7. Furthermore, Figure 5.8 plots the error as a color code against time on the horizontal axis. After computing the error for each combination using the definition in Equation (5.21), the results are reported in Figure 5.8. The color bar in Figure 5.8 denotes the level of local error, which remains below

2 percent for all values. It is worth emphasizing that most of the plot surface is blue, indicating high accuracy and values of local errors close to zero.

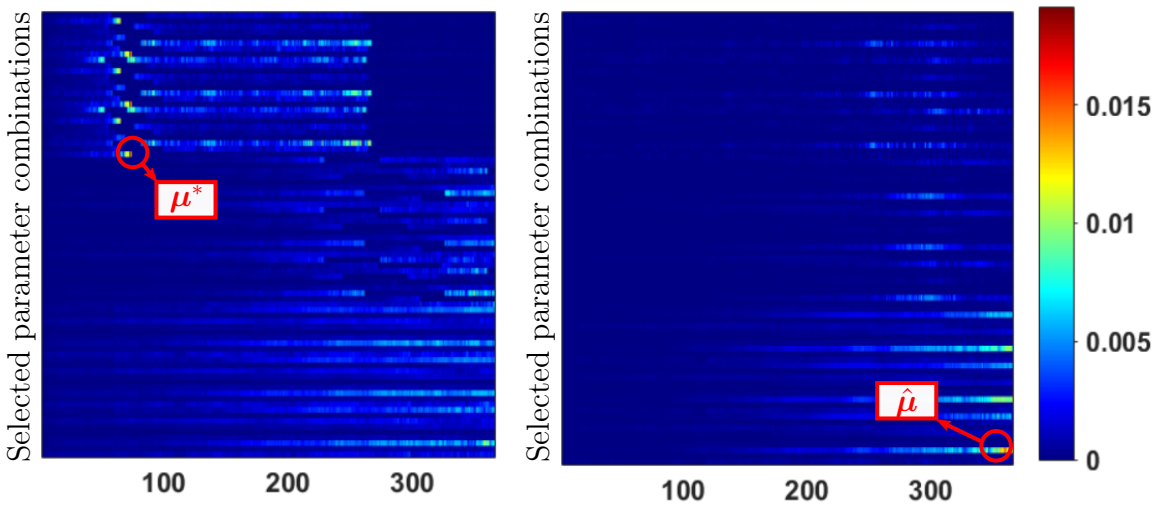

Figure 5.8: The vertical axis represents the selected parametric combinations, and the horizontal axis is the time. This figure presents the local error for pressure (A) and displacement (B) for 81 various parametric combinations, which have been taken from the minimum, maximum, and middle points of the four parametric ranges. The color bar represents the local error (Equation (5.21)) in each selected parametric combination versus time, which is the relative error of the PGD solution with respect to FEM for every time and parameter combination

For some parameter value combinations, a lower accuracy is obtained than the rest of the selected parameter value combinations. For instance, the pressure for the selected parametric combination $\boldsymbol{\mu}^* = [1.5\,\frac{\mathrm{W}}{\mathrm{m}\,^\circ\mathrm{C}}, 3\times10^{-12}\,\frac{\mathrm{m}}{\mathrm{s}}, 55600\,\mathrm{MPa}, -0.1\,\mathrm{m}]$ the same as that for Figure 5.4. As shown in Figure 5.4-B, the pressure decreases fast, reaching a very small value after the day 73. For such a combination, the day 73 is the starting point of pressure to close to zero values compared with initial pressure. That is why for that specific point, to converge to more accurate results is harder than the rest. So, finding a more accurate solution requires a smaller enrichment tolerance (η_{tol}) for that specific time slice. The same conclusion can be drawn for the displacement. For the selected parametric combination $\hat{\boldsymbol{\mu}} = [5\,\frac{\mathrm{W}}{\mathrm{m}\,^\circ\mathrm{C}}, 3\times10^{-14}\,\frac{\mathrm{m}}{\mathrm{s}}, 55600\,\mathrm{MPa}, -0.1\,\mathrm{m}]$, the value of displacement for some spots is much smaller than for others, which explains why it is hard to find very accurate results in relative terms. However, as presented in Figure 5.6, the change of global error, which is the

average of the selected parameter combinations in each time slice, is less than 10^{-3}, which is accurate.

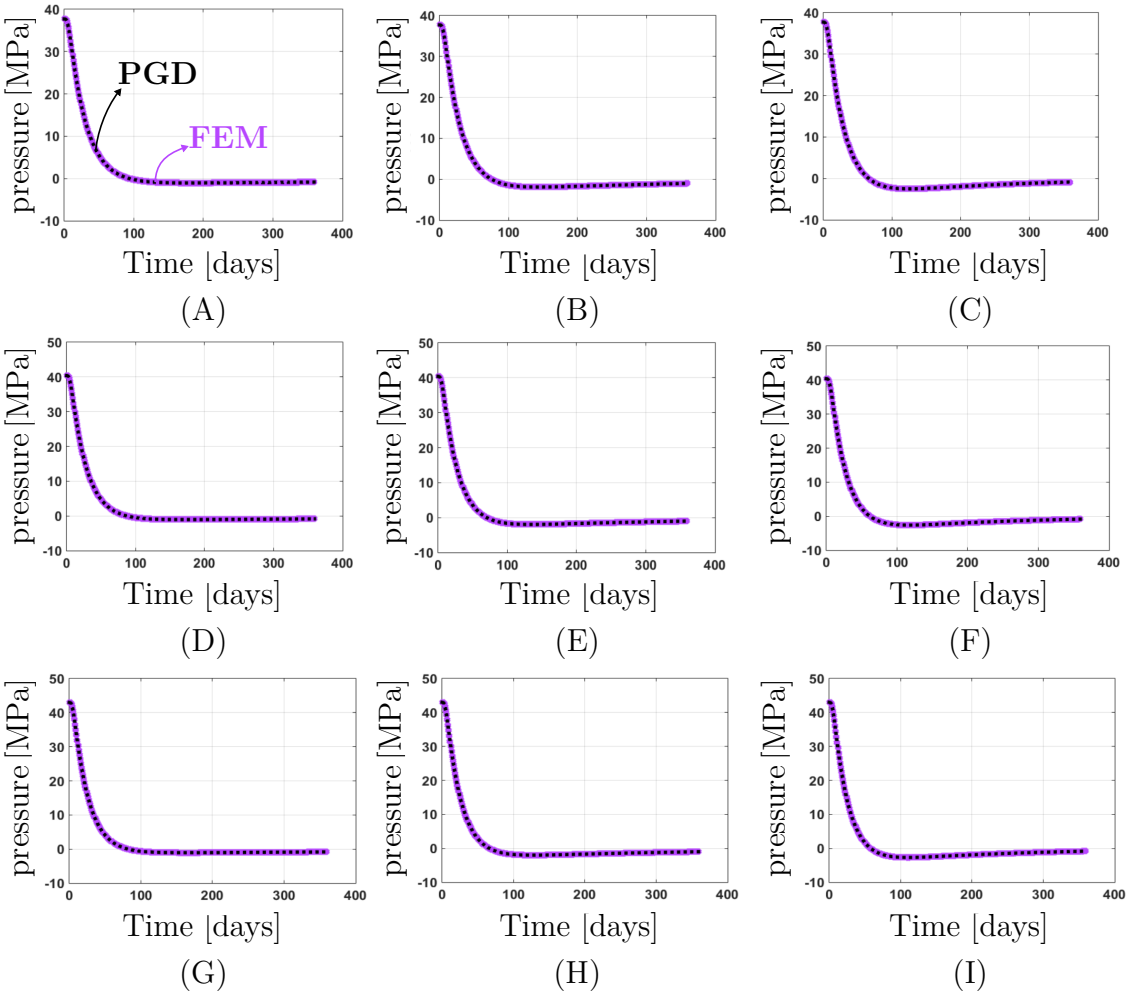

Figure 5.9: This figure aims to explain the presence of a distinct blue square in the upper right corner of Figure 5.8-A, which represents a specific combination. This particular combination achieves a faster attainment of steady-state compared to the other combinations in Figure 5.8-A, resulting in significantly improved accuracy. The figure consists of nine plots illustrating the evolution of pressure over time for different parametric combinations. The maximum hydraulic conductivity ($\mu_\kappa^{\max}$) is held constant, while the geometric parameter ($\mu_L^{\min}$) remains unchanged. The plots are grouped based on variations in heat conductivity and elastic modulus values.

In Figure 5.8-A, the presence of a distinct blue square in the upper right region indicates highly accurate results compared to the rest of the plot. For a physical understanding of this region, refer to Figure 5.9. The plots in Figure 5.9 demonstrate that the blue square is attributed to faster attainment of steady state compared

to other combinations. This specific region corresponds to a combination where all hydraulic conductivities (μ_K) are at their maximum values ($\mu_K^{\max}$).

Analyzing the evolution of pressure versus time for nine selected points within this region reveals that in certain cases (Figure 5.9-C, F, and I), the results reach steady state after approximately 250 days. In Figure 5.9, the geometric parameter (μ_L) remains constant at its minimum value ($\mu_L^{\min}$). Figures 5.9-A, D, and G have the heat conductivity (μ_κ) set to its minimum value ($\mu_\kappa^{\min}$), while the elastic modulus (μ_E) varies as $\mu_E^{\min}$, μ_E^{mid}, and $\mu_E^{\max}$, respectively. Similarly, Figures 5.9-B, E, and H have the heat conductivity set to its middle value (μ_κ^{mid}), and the elastic modulus varies as $\mu_E^{\min}$, μ_E^{mid}, and $\mu_E^{\max}$, respectively. Finally, Figures 5.9-C, F, and I have the heat conductivity set to its maximum value ($\mu_\kappa^{\max}$), and the elastic modulus varies as $\mu_E^{\min}$, μ_E^{mid}, and $\mu_E^{\max}$, respectively.

Therefore, it can be concluded that the pressure response, influenced by the maximum hydraulic conductivity, rapidly drops and reaches a steady state within approximately 50 days for some cases and 250 days for others. On average, the results suggest that once the system reaches a steady state, further application of PGD for those specific parameter combinations is unnecessary, as the results converge and become similar.

Chapter 6

Application to a simplified model of engineered barrier system

This chapter shows the application of the Proper Generalized Decomposition (PGD) methodology to simplified engineered barrier systems, which are governed by Thermo-Hydro-Mechanical (THM) problems. To the author's knowledge, this combination of methodologies has not been studied yet. The main objective is to illustrate that building a generalized (parametric) solution with PGD for such a problem is possible. The accuracy and efficiency of the approach for such problems will be assessed. The possible exploitations of the generalized solutions in the context of a deep geological repository will also be outlined.

This chapter is divided into three sections. Section 6.1 presents all the common features and concepts of the two version of the problem that will be discussed in the other sections. Section 6.2 illustrates the problem with three material parameters (heat conductivity, hydraulic conductivity, and elastic modulus of the host rock) as extra dimensions. Section 6.3 particularizes the approach to the problem as dependent on a geometric parameter (distance between canisters).

6.1 Common features and concepts of problems

In Chapter 1 (Section 1.2), the concept of engineered barrier systems was discussed as the typical model problem in this study. Figure 6.1 serves as a visual reminder

of this concept. It illustrates a deep geological repository with two primary barriers: the geological barrier, represented by the host rock (granite in this case), and the engineered barrier, which includes a canister encapsulating the High-Level Waste (HLW), along with the buffer and backfill materials.

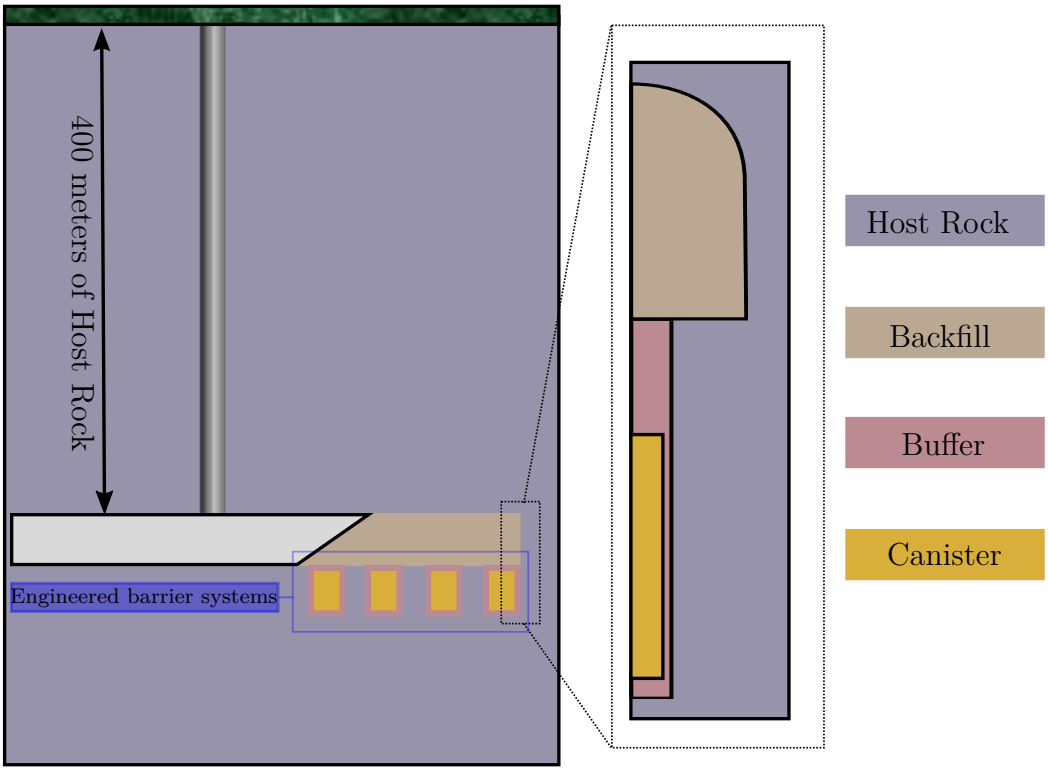

Figure 6.1: The deep geological repository is divided into two main barriers: one is the low permeability host rock as a natural barrier, and the other one is the engineered barrier system. The engineered barrier system consists of three main components, which are a canister (which contains the HLW), buffer, and backfill materials.

Figure 6.2 depicts the model problem, including its geometry and materials, that will be examined in this study. As a reminder, the model assumes axisymmetry, which is why it is presented in a two-dimensional axisymmetric representation. The remaining assumptions of this model are presented in Chapter 1 (Subsection 1.3). The domain ($\Omega = \Omega_{\mathrm{R}} \cup \Omega_{\mathrm{Bf}} \cup \Omega_{\mathrm{B}} \cup \Omega_{\mathrm{C}}$) is divided into four subdomains: Ω_{R} represents the host rock, Ω_{Bf} represents the backfill, Ω_{B} represents the buffer, and Ω_{C} represents the canister domains. The boundaries are labeled as Γ_{t}, Γ_{r}, Γ_{b}, and Γ_{l} at the top, right, bottom, and left of Ω, respectively. The objective of this study is to investigate the impact of heat released by the High-Level Waste (HLW) in the system, which is modeled by introducing a heat source in Ω_{C}.

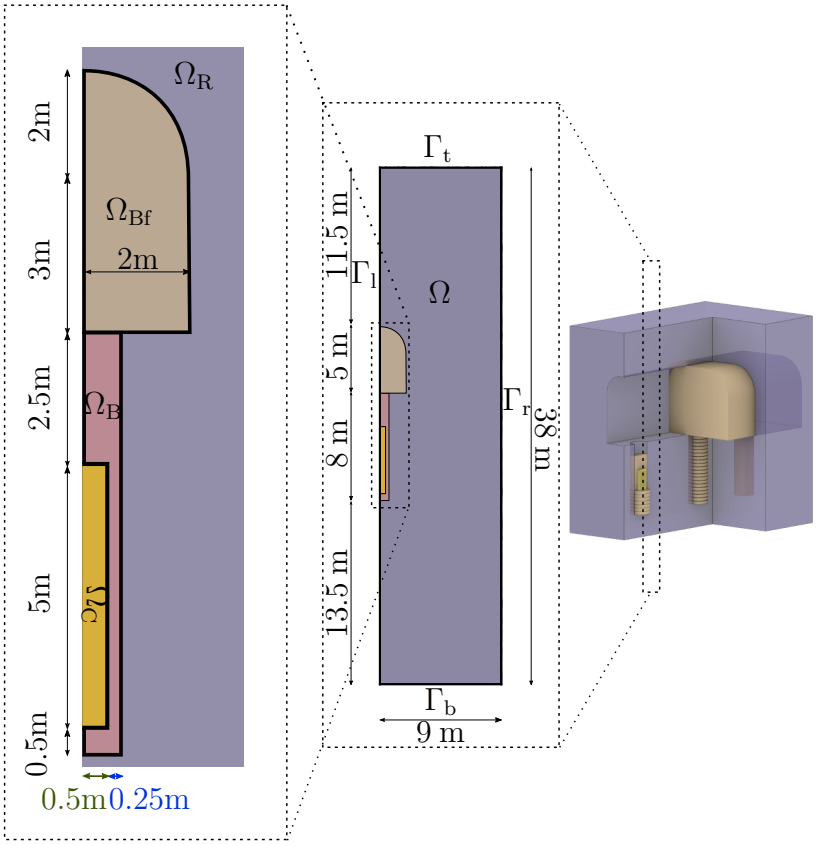

Figure 6.2: The model problem and its geometry are re-sketched from [149].

Figure 6.3 illustrates the top view of the engineering barrier system, revealing the continuous backfill area. Since the problem assumes axisymmetry, the backfill domain is approximated as a ring, similar to the left figure in Figure 6.2. Based on these assumptions, all three primary governing equations of a THM model are presented by Equation (2.7) in Chapter 2.

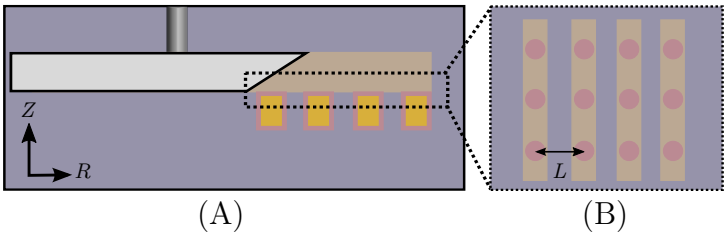

Figure 6.3: Side view of the engineered barrier system in the deep geological repository (A). The top view of the repository (B) illustrates the continuous backfill, which is approximated using an axisymmetric geometry. Additionally, it depicts the inter-distance between canisters (L), which will be investigated as a geometrical parameter in this context.

Table 6.1 presents the solid phase properties for the various components, namely the host rock (granite), canister, backfill, and buffer. The subscripts f and s represent the fluid and solid phases, respectively. The fluid properties include the density (ρ_f), specific heat (c_f), heat expansion coefficient (α_f), and bulk modulus (K_f), which are given by the following values: 1000, $\frac{\text{kg}}{\text{m}^3}$, 4180 $\frac{\text{J}}{\text{kg·K}}$, 6.9×10^{-5} $\frac{1}{^\circ\text{C}}$, and 2200 MPa, respectively.

Symbol	Units	Description	Rock	Canister	Backfill	Buffer	Reference
ρ_s	$\frac{\text{Kg}}{\text{m}^3}$	Density	2743	8930	2780	2780	[149]
ϕ	–	Porosity	0.005	–	0.27	0.37	[149]
c_s	$\frac{\text{J}}{\text{Kg }^\circ\text{C}}$	Specific heat	764	390	800	830	[149]
α_s	$\frac{1}{^\circ\text{C}}$	Heat expansion	0.85×10^{-5}	10^{-5}	9×10^{-4}	9×10^{-4}	[149]
α	–	Biot's coefficient	0.75	–	1	1	[91]
ν	–	Poisson's ratio	0.25	0.3	0.3	0.3	[149]
κ	$\frac{\text{W}}{\text{m }^\circ\text{C}}$	Heat conductivity	$I_{\mu_\kappa} = [1.5, 5]^{(*)}$	390	1.4	1.4	[79]
K	$\frac{\text{m}}{\text{s}}$	Hydraulic conductivity	$I_K = [3 \times 10^{-14}, 3 \times 10^{-12}]^{(*)}$	–	7.6×10^{-13}	5.6×10^{-14}	[149]
E	MPa	Elastic modulus	$I_E = [55600, 68000]^{(*)}$	210000	65.8	42.4	[74]

Table 6.1: The solid phase properties. The asterisk (*) represents the range of material parameters treated as variables. The minimum and maximum bounds of the ranges were selected from the tables provided in the references.

In the first equation (conservation of energy) of the three main governing equations in (2.7), the heat source is added on the right-hand side based on the properties of the HLW at Ω_{C}. In the following subsection, the time dependency of the power supplied by the HLW will be explained in detail. In this thesis, before going through the other discussions, it should be reminded that Finite Element Method (FEM) is used as a (high fidelity) discretization technique, as explained in detail in Chapter 2 (Subsection 2.2.2)

6.1.1 Heat source

The heat source ($q(t)$) is defined as follows:

$$q(t) = \frac{P(t)}{V_c}. \tag{6.1}$$

In Equation (6.1), V_c is the volume of the canister, and $P(t)$ is the power evolution. The power evolution of each canister is calculated by Equation (6.2), which depends on two parameters, the residual power at the time of deposition (t_i) and the decay rate (a_i) [69]. The power function that is used in this work is,

$$P(t) = P(0) \sum_{i=1}^{7} a_i \exp(-t/t_i). \tag{6.2}$$

In Equation (6.2), $P(0) = 1700\,\mathrm{W}$ is the canister power at the time of deposition, and a_i and t_i are the parameters, which are given in Table 6.2.

i	t_i [years]	a_i [-]
1	20	0.060147
2	50	0.705024
3	200	-0.054753
4	500	0.249767
5	2000	0.025407
6	5000	-0.009227
7	20000	0.023877

Table 6.2: Time constants and coefficients of exponential power expression.

Figure 6.4 illustrates the power evolution versus time. This function is applied in the model (Equation (2.7)) to simulate the heat generated by the HLW (Equation (6.1)).

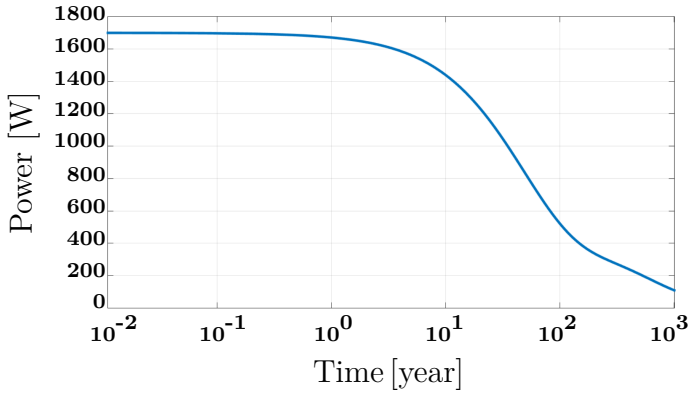

Figure 6.4: Power evolution versus time in the year to simulate the HLW as the heat source.

6.1.2 Boundary conditions

The boundary conditions are either Dirichlet boundary conditions (prescribed unknown values) or Neumann boundary conditions (prescribed fluxes or traction forces). Figure 6.5 illustrates the generic concept of boundary conditions for the model problem. Here, the hydraulic and mechanical boundary conditions are constant with respect to time. The prescribed temperatures at the top and bottom boundaries are not constant with respect to time due to the close proximity of boundaries to the heat source.

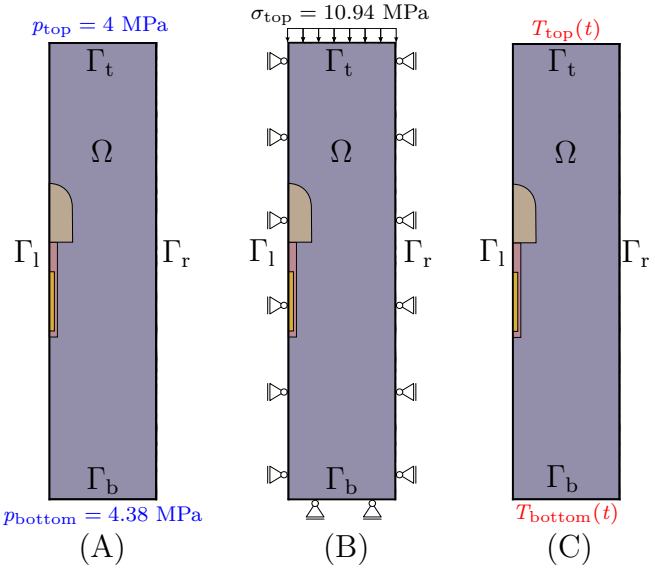

Figure 6.5: Hydraulic (A) mechanical (B) and thermal (C) boundary conditions.

Figure 6.5-A illustrates the boundary conditions for the hydraulic field. Hydrostatic water pressure is applied as Dirichlet boundary conditions on the upper and lower boundaries, i.e., $p_{\text{top}} = \rho_f g\, h_{\text{top}}$ and $p_{\text{bottom}} = \rho_f g\, h_{\text{bottom}}$, where $h_{\text{top}} = 400\,\text{m}$ and $h_{\text{bottom}} = 438\,\text{m}$. Along the vertical boundaries, Neumann boundary conditions are applied due to the symmetry of the problem. These boundary conditions are homogeneous, meaning that hydraulic fluxes are zero [150]. Thus, the boundary conditions for the hydraulic field are as,

$$\begin{cases} p(\mathbf{x}, t) = 4\,\text{MPa} & \text{on } \Gamma_{\text{t}} \times I_t, \\ p(\mathbf{x}, t) = 4.38\,\text{MPa} & \text{on } \Gamma_{\text{b}} \times I_t, \\ -\dfrac{K}{\rho_f g}(\boldsymbol{\nabla} p - \rho_f \mathbf{g}) \cdot \mathbf{n} = 0 & \text{on } (\Gamma_{\text{l}} \cup \Gamma_{\text{r}}) \times I_t. \end{cases} \tag{6.3}$$

As has been presented in Figure 6.5-B, a uniform load per unit surface ($\sigma_{\text{top}} = 10.94\,\text{MPa}$) is applied on the top boundary. This load comes from the gravity weight of the host rock mass at 400 m. The lateral displacement is constrained to be zero, which is translated in the mechanical boundary conditions [150] as,

$$\begin{cases} \boldsymbol{\sigma} \cdot \mathbf{n} = 10.94\,\text{MPa} & \text{on } \Gamma_{\text{t}} \times I_t, \\ u_z(\mathbf{x}, t) = 0 & \text{on } \Gamma_{\text{b}} \times I_t, \\ u_r(\mathbf{x}, t) = 0 & \text{on } (\Gamma_{\text{l}} \cup \Gamma_{\text{r}}) \times I_t. \end{cases} \tag{6.4}$$

Figure 6.5-C depicts the generic format of the thermal boundary conditions. Since the problem exhibits an axial symmetry, Neumann boundary conditions are applied along the vertical boundaries, being homogeneous, meaning the heat fluxes are zero. In the confined area, the prescribed temperatures at the top ($T_{\text{top}}(t)$) and bottom ($T_{\text{bottom}}(t)$) are not constant, and they are functions of time due to their proximity with the heat source as follows:

$$\begin{cases} T(\mathbf{x}, t) = T_{\text{top}}(t) & \text{on } \Gamma_{\text{t}} \times I_t, \\ T(\mathbf{x}, t) = T_{\text{bottom}}(t) & \text{on } \Gamma_{\text{b}} \times I_t, \\ (-\kappa \boldsymbol{\nabla} T) \cdot \mathbf{n} = 0 & \text{on } (\Gamma_{\text{l}} \cup \Gamma_{\text{r}}) \times I_t. \end{cases} \tag{6.5}$$

In order to determine the dependencies $T_{\text{top}}(t)$ and $T_{\text{bottom}}(t)$, a side model (large model) should be solved only for the thermal aspect (Poisson's equation). The following subsection explains the detail of the computation of time-dependent thermal boundary conditions.

Before delving into the computation of thermal boundary conditions, it is important to emphasize that the selection of boundary conditions in this study is based on the same setup as Toprak et al. [150] for the purpose of comparison. However, from a fundamental standpoint, the methodology used for temperature can also be extended to the pressure field.

6.1.3 The computation of time-dependent thermal boundary conditions

The domain of the confined area (small model) should not be too large to execute THM computations cheaply. Nevertheless, its top and bottom thermal Dirichlet boundary conditions are too close, and therefore boundaries cannot have a constant temperature versus time. For finding the time dependency of the temperature on

the top and bottom boundaries of the small model (Figure 6.6-C), a thermal analysis will be conducted on a larger scale with a boundary far from the heat source (Figure 6.6-B). However, it is important to emphasize that the explanation provided in Figure 6.6 applies to both problems addressed in this chapter. The intention here is to present the concept rather than the specific parametric details. Therefore, the thermal boundary conditions, represented by $T_{\text{top}}(t, \mu_\kappa, \mu_L)$ and $T_{\text{bottom}}(t, \mu_\kappa, \mu_L)$, which depend on material and geometric parameters, have not been illustrated in Figure 6.6-C.

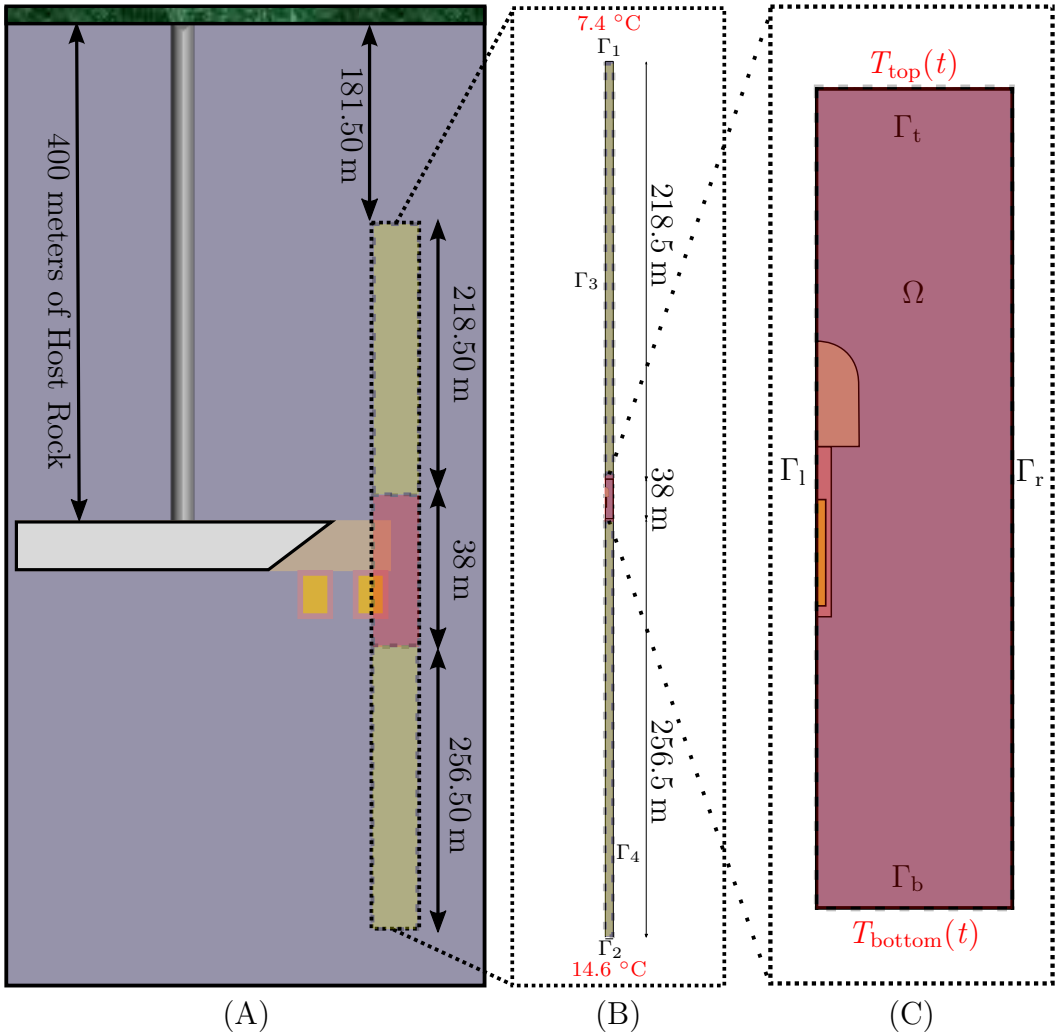

Figure 6.6: Based on the global deep geological repository model (A), a large scale model (B) is extracted to solve and find the temperatures to prescribe as a function of time on the top and bottom boundaries of the smaller model (C).

The decision to utilize a large model depth is based on Toprak's work [148]. He specifically extracted a depth of 513 m from Figure 6.6-A to investigate the thermal behavior of that particular section. Toprak employed a confined domain (small domain) to conduct computationally efficient THM calculations. However, he observed that domains located close to boundaries cannot maintain a constant temperature. To determine suitable boundary conditions for the top and bottom, a thermal analysis was performed on larger geometries. Two large models and one reference model (with fixed prescribed temperature values on the top and bottom of the small domain throughout the entire time interval) were evaluated. Among these computations, the model utilized in this study represents the closest approximation to reality and serves as an appropriate larger domain for determining the thermal boundary conditions within the confined area. The problem statement corresponding to this large model should be defined. The main governing equation of such a problem is the first equation of Equation (2.7). To close this problem statement, the boundary conditions should be defined. Since the model is symmetry, homogeneous Neumann boundary conditions on the lateral boundaries are considered, with vanishing heat fluxes. For the top and bottom boundaries of the large-scale model, the prescribed temperatures are derived from the following definition from [128],

$$T = 0.014h + 4.9, \tag{6.6}$$

where $0.014\ \frac{^\circ\mathrm{C}}{\mathrm{m}}$ is the geothermal gradient, h represents the depth, and $4.9\,^\circ\mathrm{C}$ is the surface temperature. The depth for the top and bottom boundaries for the large-scale model are taken as 181.5 m and 694.5 m (Figure 6.6-A). By inserting these values as the depth for the top and bottom boundary of the large model (Figure 6.6-B) in Equation (6.6), $7.4\,^\circ\mathrm{C}$ and $14.6\,^\circ\mathrm{C}$ are found as the prescribed temperature on the top and bottom for the large model, respectively.

The problem statement of the large-scale model is defined as follows:

$$\begin{cases} -\boldsymbol{\nabla} \cdot (\kappa(\mathbf{x}) \boldsymbol{\nabla} T(\mathbf{x}, t)) = q(t) & \text{in } \Omega_{\text{large-model}} \times I_t, \\ T(\mathbf{x}, t) = 7.4\,^\circ\mathrm{C} & \text{on } \Gamma_1 \times I_t, \\ T(\mathbf{x}, t) = 14.6\,^\circ\mathrm{C} & \text{on } \Gamma_2 \times I_t, \\ (-\kappa \boldsymbol{\nabla} T) \cdot \mathbf{n} = 0 & \text{on } (\Gamma_3 \cup \Gamma_4) \times I_t, \end{cases} \tag{6.7}$$

where $\Omega_{\text{large-model}}$ is the spatial domain of the large-scale model and Γ_1, Γ_2, Γ_3, and Γ_4 are the top, bottom, left, and right boundaries of $\Omega_{\text{large-model}}$, respectively.

By solving Equation (6.7), one can extract the averaged temperature values obtained along the top and bottom boundaries of the confined model (small model). Two scalar functions of time will be obtained to be applied as Dirichlet boundary conditions of the small model. It should also be mentioned that to ease this extraction, the time discretizations of the large and small scale models is taken the same. The results concerning this part with details will be presented for the three material parameters parametric problem in Section 6.2.

6.1.4 Initial conditions

The initial conditions are defined as follows:

$$\begin{cases} T(\mathbf{x},0) = T_0(\mathbf{x}) & \text{in } \Omega, \\ p(\mathbf{x},0) = p_0(\mathbf{x}) & \text{in } \Omega, \\ \mathbf{u}(\mathbf{x},0) = \mathbf{u}_0(\mathbf{x}) & \text{in } \Omega. \end{cases} \tag{6.8}$$

In Equation (6.8), $T_0(\mathbf{x})$ is the initial temperature equal to the geothermal temperature, which is not spatially uniform and matches the geothermal gradient. $p_0(\mathbf{x})$ is the initial pressure and is equivalent to the hydrostatic pressure in the confined area. It is thus not spatially uniform either. $\mathbf{u}_0(\mathbf{x})$ is the initial displacement which will be found as the solution of a steady-state equation for the mechanical field by inserting the $T_0(\mathbf{x})$ and $p_0(\mathbf{x})$.

6.1.5 Parametric definition

Here two classes parametric THM problems will be investigated. For the first one, three material parameters concerning the host rock regions are considered as extra dimensions: the heat conductivity (μ_κ), the hydraulic conductivity (μ_K), and the elastic modulus (μ_E). For the second problem, these rock material properties are considered known, but the distance between canisters is considered as the (only) geometric parameter (μ_L) and thus as an extra dimension. All the parametric field equations are the same as Equation (4.1) with respectively three and one parameters for each problem.

As illustrated in Figure 6.2, the three material parameters in the Ω domain are non-homogeneous, and the exact definition of parameters are as follows:

$$\kappa(\mathbf{x}, \mu_\kappa) = \begin{cases} \mu_\kappa & \text{if } \mathbf{x} \in \Omega_{\mathrm{R}} \text{ with } \mu_\kappa \in I_{\mu_\kappa}, \\ 1.4\,\frac{\mathrm{w}}{\mathrm{m}\,^\circ\mathrm{C}} & \text{if } \mathbf{x} \in \Omega_{\mathrm{B}}, \\ 1.4\,\frac{\mathrm{w}}{\mathrm{m}\,^\circ\mathrm{C}} & \text{if } \mathbf{x} \in \Omega_{\mathrm{Bf}}, \\ 390\,\frac{\mathrm{w}}{\mathrm{m}\,^\circ\mathrm{C}} & \text{if } \mathbf{x} \in \Omega_{\mathrm{C}}, \end{cases} \tag{6.9}$$

$$K(\mathbf{x}, \mu_K) = \begin{cases} \mu_K & \text{if } \mathbf{x} \in \Omega_{\mathrm{R}} \text{ with } \mu_K \in I_{\mu_K}, \\ 5.6 \times 10^{-14}\,\frac{\mathrm{m}}{\mathrm{s}} & \text{if } \mathbf{x} \in \Omega_{\mathrm{B}}, \\ 7.6 \times 10^{-13}\,\frac{\mathrm{m}}{\mathrm{s}} & \text{if } \mathbf{x} \in \Omega_{\mathrm{Bf}}, \\ 1.0 \times 10^{-20}\,\frac{\mathrm{m}}{\mathrm{s}} & \text{if } \mathbf{x} \in \Omega_{\mathrm{C}}, \end{cases} \tag{6.10}$$

$$E(\mathbf{x}, \mu_E) = \begin{cases} \mu_E & \text{if } \mathbf{x} \in \Omega_{\mathrm{R}} \text{ with } \mu_E \in I_{\mu_E}, \\ 42.4\,\mathrm{MPa} & \text{if } \mathbf{x} \in \Omega_{\mathrm{B}}, \\ 65.8\,\mathrm{MPa} & \text{if } \mathbf{x} \in \Omega_{\mathrm{Bf}}, \\ 210000\,\mathrm{MPa} & \text{if } \mathbf{x} \in \Omega_{\mathrm{C}}. \end{cases} \tag{6.11}$$

In Equations (6.9) to (6.11), I_{μ_κ}, I_{μ_K}, and I_{μ_E} represent the ranges of material parameters for heat conductivity, hydraulic conductivity, and elastic modulus of the rock, respectively. The bounds of these ranges are presented in Table 6.1.

In Chapter 4, the implementation of the geometric parameter for the second class of problems was given in Figure 4.1. Here, the following definition of the parameter is used,

$$w(\mu_L) = b_1 + B_2(\mu_L), \text{ where } \mu_L \in I_L = [-0.5\,\mathrm{m}, 3.5\mathrm{m}]\,. \tag{6.12}$$

The idea behind Equation (6.12) was illustrated in Chapter 4 (Figure 4.1). Here in this problem, b_1 is the fixed width which contains the canister, the buffer, the backfill, and some part of the host rock domains over a width of 3 m. The second part of the domain, made variable by the geometrical parameter $B_2(\mu_L)$, is defined as follows:

$$B_2(\mu_L) = b_2 + \mu_L. \tag{6.13}$$

In Equation (6.13), b_2 represents the value of the variable width ($B_2(\mu_L)$) when $\mu_L = 0$, which is 6 m. The parameter μ_L allows for the consideration of different distances between canisters in the repository. It should be emphasized that using this definition

enables the use of the same mesh topology for the entire range of μ_L, simplifying the problem. This idea of using the same mesh topology was also presented in Chapter 4, in Figure 4.4.

As discussed in Chapter 5 (Subsection 5.1.3), each individual parameter, as an additional dimension, needs to undergo discretization. The discretization process for all material parameters follows a similar approach to that used in the previous chapter. However, for geometric parameters, a regular discretization technique utilizing 801 nodes is employed in this particular case.

6.2 Results for a three material parameters problem

In this section, we seek the PGD solution by considering the three material parameters as additional dimensions. Figure 6.7 illustrates the two preprocessing steps employed to address this problem. As depicted, the initial conditions are separated (Figure 6.7-A), and the thermal boundary conditions are also separated (Figure 6.7-B) as the first extraction steps. These preprocessing steps, referred to as ICs PGD BOX and BCs PGD BOX in this work, generate separate input data for the THM problem at hand. Matrices and vectors are defined separately based on these ICs PGD BOX and BCs PGD BOX (as discussed in Chapter 4), leading to the sought generalized solution depicted in Figure 6.8.

The purpose of providing ICs PGD BOX and BCs PGD BOX is to utilize their computationally inexpensive offline solutions with PGD. Once solved, these solutions can be saved and used online for the transient THM concept. The ICs PGD BOX represents the initial separated values required to initiate the transient simulation, while the BCs PGD BOX represents the separated thermal boundary conditions applied during the transient simulation. This online approach offers a fast and efficient solution, as it involves simply loading the precomputed solutions without the need for additional computations.

It is important to emphasize that BCs PGD BOX only includes the separated boundary conditions for temperature. These conditions are implemented on each time slice as known values on the boundary, ensuring that the PGD solution on that boundary is homogeneous and represents the known separated temperature values. On the other hand, it should be noted that the prescribed Dirichlet boundary conditions

for pressure and displacement are applied using a function called "deleteRowsDBC" in encapsulated PGD [38]. This function enforces Dirichlet boundary conditions by shifting columns to the right-hand side and introducing zeros in the matrix rows and columns (with a one on the diagonal). By using the homogeneous PGD solution on the boundary, the consistency of the Dirichlet boundary conditions is maintained throughout the entire time interval. However, in encapsulated PGD, the Dirichlet boundary conditions should be constant values independent of parameters. Hence, BCs PGD BOX was developed to handle the thermal aspect separately, taking into account the dependency of thermal boundary conditions on parameters.

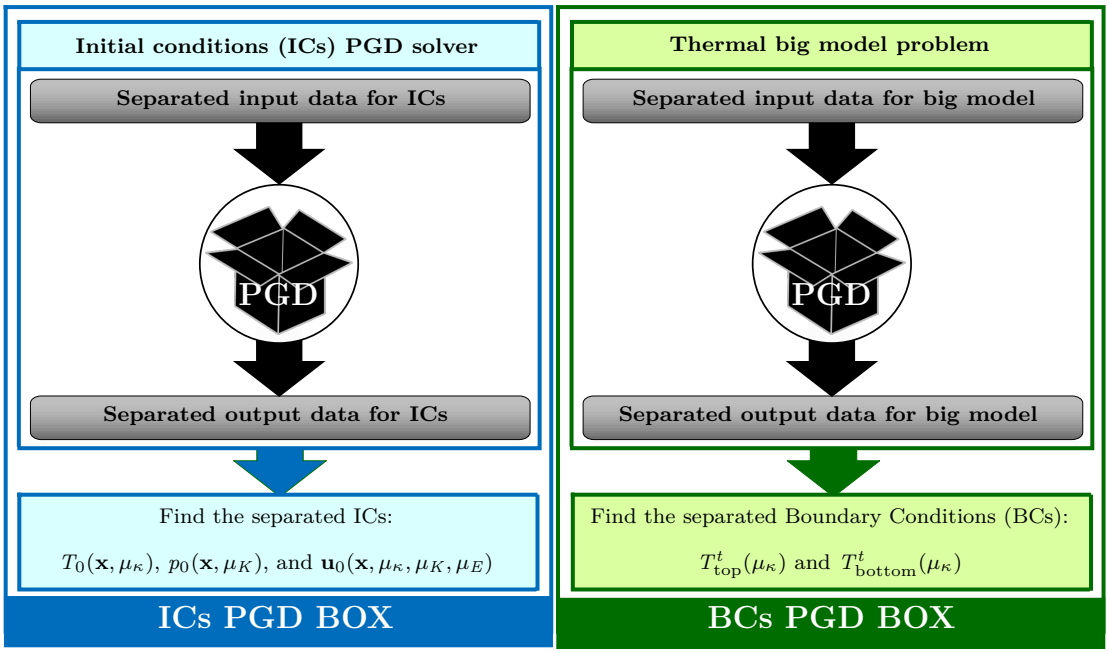

(A) (B)

Figure 6.7: In this problem, the first pre-processing step consists of solving the steady-state problem to define the initial conditions (Equation (6.8)) and extracting the output in separated forms (A). The second pre-processing step involves solving the parametric thermal problem of the auxiliary large-scale model (Equation (6.7)) and extracting the average separated thermal values for the top and bottom boundaries of the small model (B). In BCs PGD BOX, T^t_{top} and T^t_{bottom} represent the separated thermal boundary conditions for the time slice t for the top and bottom boundaries of the smaller model, respectively.

[38] Figure 6.8 illustrates that one PGD problem is solved at each time slice t by having all the separated input data. The final output is a collection of all the time slices of $\mathbf{T}^t(\mathbf{x}, \mu_\kappa)$ and $\mathbf{U}^t(\mathbf{x}, \mu_\kappa, \mu_K, \mu_E)$. The separated output data for the problem

at hand for a given time slice are as follows:

$$\mathbf{T}^t(\mathbf{x}, \mu_\kappa) = \sum_{\hat{m}=1}^{\hat{M}^t} \mathbf{T}^{\hat{m}}(\mathbf{x}) B^{\hat{m}}_{\mu_\kappa}(\mu_\kappa), \tag{6.14}$$

$$\mathbf{U}^t(\mathbf{x}, \mu_\kappa, \mu_K, \mu_E) = \sum_{m=1}^{M^t} \mathbf{U}^m(\mathbf{x}) G^m_{\mu_\kappa}(\mu_\kappa) G^m_{\mu_K}(\mu_K) G^m_{\mu_E}(\mu_E), \tag{6.15}$$

Equations (6.14) and (6.15) involve two quantities, $\hat{M}^t$ and M^t, which respectively correspond to the number of modes used in the thermal and hydro-mechanical separated outputs. Functions B and G are used to denote the parametric dependence.

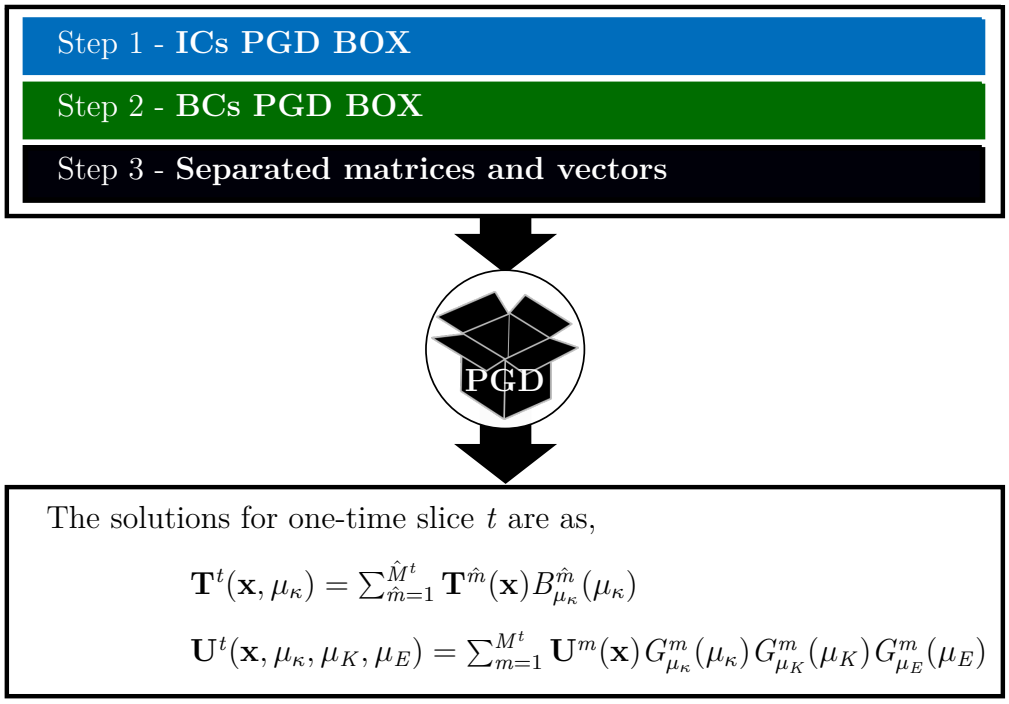

Figure 6.8: Generalized solution to the parametric coupled THM problem at hand. It shows that the separated unknowns for each time slice will be found by providing the ICs PGD BOX, BCs PGD BOX, and all the separated matrices and vectors.

The present section will first show the generalized solution of the thermal boundary conditions at the top and bottom boundaries of the small domain and its accuracy. Then the accuracy of the final output data will be analyzed in relation to the computation gain and the efficiency of the methodology. Finally, a small discussion will be outlined concerning the possible exploitation of the generalized solution. The geometry for the domain is fixed to study this first parametric problem (material

parameters only). Therefore, the worst-case scenario from a thermal viewpoint has been considered for this three-material parameter case study (the closest distance between canisters, which means $\mu_L = -0.5\,\mathrm{m}$).

6.2.1 Generalized solutions for thermal boundary conditions

Figure 6.7-B presents the concept of providing a generalized solution for the temperature to be prescribed on the top and bottom boundaries of the small domain. Such separated prescribed boundary conditions are as follows:

$$T^t_{\mathrm{top}}(\mu_\kappa) = \sum_{\tilde{m}=1}^{\tilde{M}^t} Q^{\tilde{m}}_{\mu_\kappa}(\mu_\kappa), \tag{6.16}$$

$$T^t_{\mathrm{bottom}}(\mu_\kappa) = \sum_{\breve{m}=1}^{\breve{M}^t} \Upsilon^{\breve{m}}_{\mu_\kappa}(\mu_\kappa). \tag{6.17}$$

In Equations (6.16) and (6.17), $\tilde{M}^t$ and $\breve{M}^t$ are the numbers of modes used in a given time slice used in the prescribed temperature on top and the prescribed temperature on the bottom boundaries of the small scale model. $Q^{\tilde{m}}_{\mu_\kappa}(\mu_\kappa)$ and $\Upsilon^{\breve{m}}_{\mu_\kappa}(\mu_\kappa)$ are the parametric functions that depend on the heat conductivity of host rock considered as a parameter for the thermal problem.

Symbol	Amount	Definition
η_{tol}	10^{-5}	Enrichment Tolerance
$\mathrm{iter}_{\mathrm{max}}$	5	Maximum number of iteration for Fixed-point iteration

Table 6.3: Stopping criteria for PGD.

The separated prescribed boundary conditions are found by solving the large-scale parametric thermal model (the parametric form of Equation (6.7)) using the PGD numerical parameters as presented in Table 6.3 and taking out the separated output data in the top and bottom boundaries of the small domain.

For a value of the heat conductivity of the rock within the interval of variation of this parameter, $\mu_\kappa = 1.5\,\frac{\mathrm{W}}{\mathrm{m}\,^\circ\mathrm{C}}$, the comparison between the FEM and the PGD solution is given in Figure 6.9. This figure shows that the PGD solution for this particularized point of the parametric space is in agreement with the FEM solution.

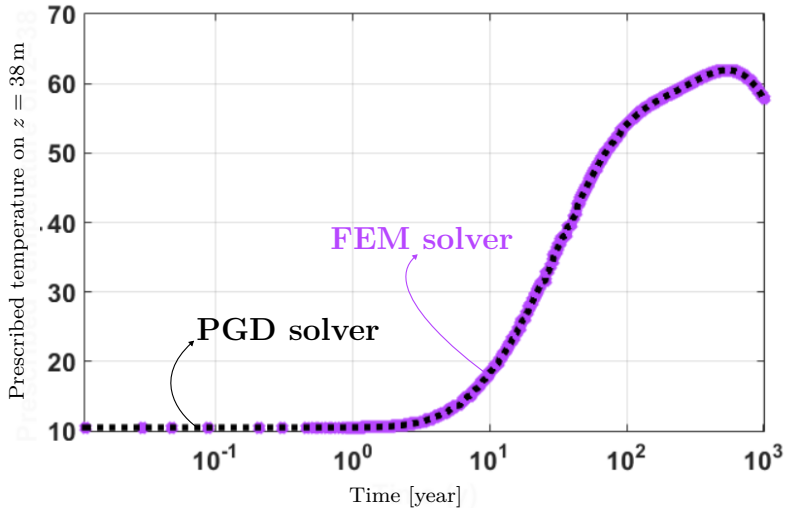

(A)

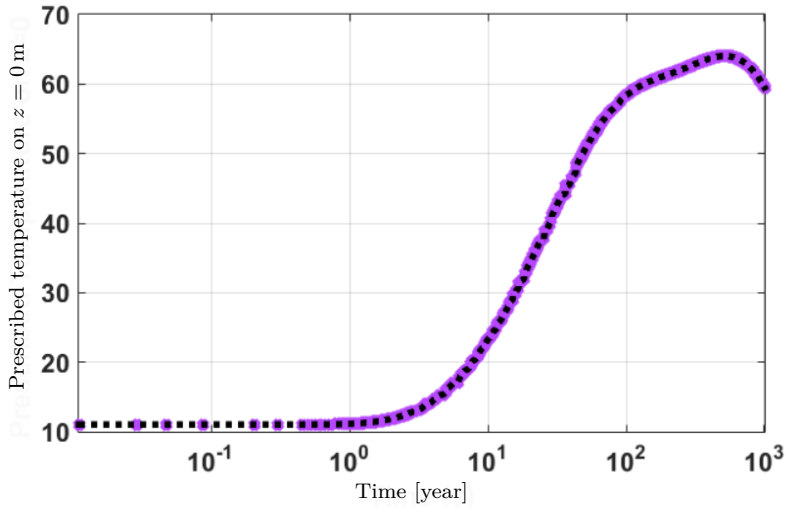

(B)

Figure 6.9: Figures (A) and (B) present the prescribed temperature versus time for the top and bottom boundaries of the small-scale model, respectively. They show that the results of the PGD solver are in agreement with the FEM for $\mu_\kappa = 1.5 \frac{\mathrm{W}}{\mathrm{m}\,^\circ\mathrm{C}}$.

Taking into account that the top and bottom prescribed boundary conditions are scalar functions of time and of the heat conductivity of the rock, it is easy to plot the error associated with the PGD solution with respect to the FEM as a function of time and heat conductivity of the rock, see Figure 6.10. The error is computed as in Equations (6.18) and (6.19):

$$\epsilon_{\mathrm{top}}(\mu_\kappa, t) = \frac{\| T^{\mu_\kappa}_{\mathrm{top}}(t) - T^{t}_{\mathrm{top}}(\mu_\kappa) \|}{\| T^{\mu_\kappa}_{\mathrm{top}}(t) \|}, \tag{6.18}$$

$$\epsilon_{\text{bottom}}(\mu_\kappa, t) = \frac{\| T^{\mu_\kappa}_{\text{bottom}}(t) - T^{t}_{\text{bottom}}(\mu_\kappa) \|}{\| T^{\mu_\kappa}_{\text{bottom}}(t) \|}, \tag{6.19}$$

where, $T^{\mu_\kappa}_{\text{top}}(t)$ and $T^{\mu_\kappa}_{\text{bottom}}(t)$ are an output of FEM for a specific μ_κ, which gives the prescribed temperatures on top and bottom boundaries of the small scale model, respectively. On the other hand, $T^{t}_{\text{top}}(\mu_\kappa)$ and $T^{t}_{\text{bottom}}(\mu_\kappa)$ are the generalized solutions for time slice t.

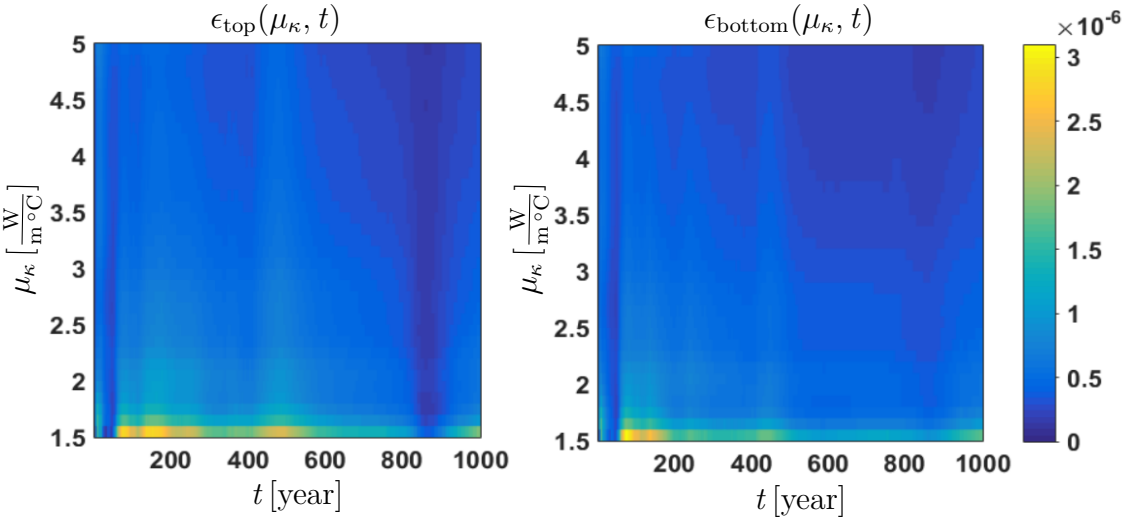

(A) (B)

Figure 6.10: Relative error of the whole domain (time and heat conductivity of the rock) for prescribed temperature on top (A) and bottom (B).

Figure 6.10 illustrates the high accuracy achieved by the PGD implementation for both the top and bottom boundary conditions across the entire domain of time and the heat conductivity of the rock as an extra dimension.

6.2.2 Accuracy of the generalized solution

This thesis explores two methods for solving the THM problem: the conventional solver and the Δ-solver. To understand the differences between these two implementation concepts, the thermal aspect is presented in detail. For the thermal part, there are two solvers: the T-solver (conventional solver) and the ΔT-solver (Δ-solver). The T-solver requires solving one PGD linear problem per time step, as outlined below:

$$\mathbf{K}^{i}_{\mathbf{GT}} \mathbf{T}^{i+1}(\mathbf{x}, \mu_\kappa) = \mathbf{f}_{\text{q}} + \mathbf{K}^{i*}_{\mathbf{GT}} \mathbf{T}^{i}(\mathbf{x}, \mu_\kappa). \tag{6.20}$$

The final generalized solution of the T-solver will be the collection of parametric objects $\mathbf{T}^t$ for each time slice t. There is another implementation method that has

been explored and tested, called the ΔT-solver. This method involves seeking the solution to the thermal aspect by first defining the unknown temperature at the current time as follows:

$$\mathbf{T}^{i+1} = \mathbf{T}^{i} + \Delta\mathbf{T}^{i}, \tag{6.21}$$

By substituting Equation (6.21) for $\mathbf{T}^{i+1}$ in Equation (6.20), the following ΔT-solver arises:

$$\begin{aligned}\mathbf{K}^{i}_{\mathbf{GT}}(\mathbf{x},\mu_\kappa)\Delta\mathbf{T}^{i}(\mathbf{x},\mu_\kappa) =& \mathbf{f}_{\mathrm{q}}(\mathbf{x}) + \mathbf{K}^{i*}_{\mathbf{GT}}(\mathbf{x},\mu_\kappa)\mathbf{T}^{i}(\mathbf{x},\mu_\kappa) - \\ & \mathbf{K}^{i}_{\mathbf{GT}}(\mathbf{x},\mu_\kappa)\mathbf{T}^{i}(\mathbf{x},\mu_\kappa).\end{aligned} \tag{6.22}$$

The unknown for this solver is $\Delta\mathbf{T}^{i}(\mathbf{x},\mu_\kappa)$ for each time slice t, and the solution for the current result is obtained by adding the variation $\Delta\mathbf{T}^{i}(\mathbf{x},\mu_\kappa)$ to the previous temperature field, $\mathbf{T}^{i}(\mathbf{x},\mu_\kappa)$. This means that an increased number of modes is accumulated from previous results (i.e., from previous time slices). A method to limit the number of modes is thus compulsory. In Chapter 3, PGD was used to solve linear systems. However, in this section, a different operation will be performed using PGD, which involves decreasing the number of modes accumulated by summing the solution of ΔT-solver with the previous temperature field using PGD, a process known as compression. One of the goals of PGD compression is to compress the parametric solution obtained as separated output data from the PGD linear solver. However, achieving this objective can be challenging, especially in the case of coupled HM problem, as investigated in this work, due to difficulties in terms of efficiency and accuracy. It has been observed that in the coupled HM case, the compression goal cannot be achieved. The principles of PGD compression are explained in detail in these studies [134, 37, 38]. Upon observing the outcomes of applying the Δ-solver to the thermal case, it has been noted that it offers both efficiency and accuracy. This choice is driven by the fact that the Δ-solver delivers precise results while employing fewer modes compared to the conventional solver for the thermal part. By specifically utilizing the Δ-solver for the thermal aspect, the research strives to achieve a harmonious blend of accuracy and computational efficiency.

To obtain the generalized solution for the thermal aspect, both the enrichment tolerance for the PGD linear solver (η_{tol}) and the enrichment tolerance for PGD compression ($\eta^{\mathrm{comp}}_{\mathrm{tol}}$) are set to 10^{-3}. The PGD linear solver is executed for 5 fixed-point iterations, while the PGD compression requires a larger number of iterations, such as 200 fixed-point iterations, with a fixed point tolerance of $\epsilon_{\mathrm{tol}} = 10^{-3}$. Increasing the

number of iterations is crucial for PGD compression in order to reduce the number of modes. By doing so, the number of modes decreases accordingly. On the other hand, for the PGD linear solver, a tradeoff between the enrichment tolerance and the number of fixed-point iterations needs to be determined for each problem. In this case, the chosen tradeoff is 5 fixed-point iterations and an enrichment tolerance of $\eta_{\text{tol}} = 10^{-3}$ to ensure efficient and accurate results.

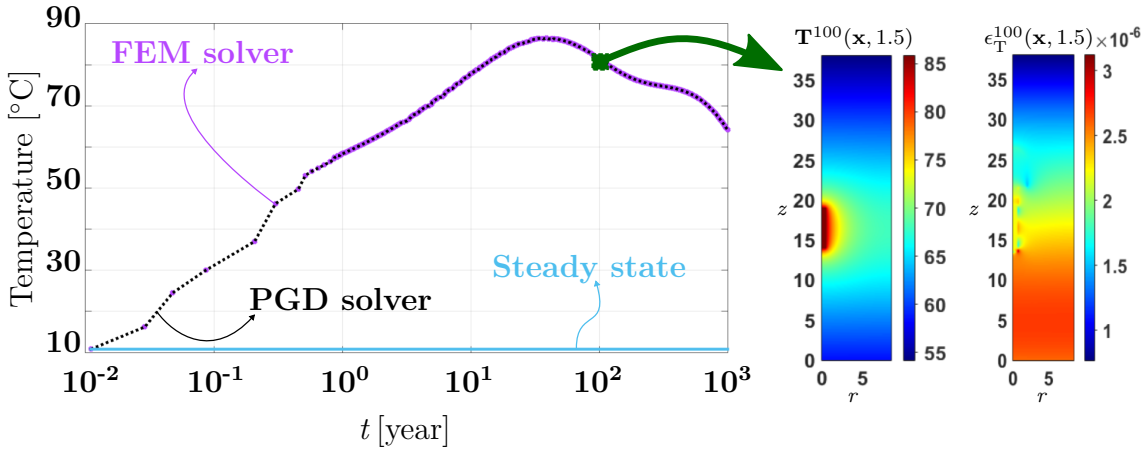

Figure 6.11: (A) Result of temperature versus time for a fixed coordinate in space ($r = 0.8\,\text{m}$ and $z = 17.5\,\text{m}$) in the rock material with a particularized point in parametric space $\mu_\kappa = 1.5\,\frac{\text{W}}{\text{m}\,^\circ\text{C}}$, and (B) Temperature field output at $t = 100\,\text{year}$ for the same particularized point in parametric space.

Figure 6.11-A illustrates the solution of temperature versus time for one particular point in the parametric space ($\mu_\kappa = 1.5\,\frac{\text{W}}{\text{m}\,^\circ\text{C}}$) at a fixed coordinate located on the rock next to the buffer ($r = 0.8\,\text{m}$ and $z = 17.5\,\text{m}$). It shows good accuracy with respect to the FEM solution. On the other hand, Figure 6.11-B presents the temperature field result and its total relative error map after 100 years for the same point in the parametric space. The relative error for temperature field ($\epsilon_{\text{T}}^{100}(\mathbf{x}, 1.5)$) is defined as,

$$\epsilon_{\text{T}}^{100}(\mathbf{x}, 1.5) = \frac{\|\mathbf{T}_{\text{FEM}}^{1.5}(\mathbf{x}, 100) - \mathbf{T}^{100}(\mathbf{x}, 1.5)\|}{\|\max\left(\mathbf{T}_{\text{FEM}}^{1.5}(\mathbf{x}, 100)\right)\|}. \tag{6.23}$$

In Equation (6.23), $\mathbf{T}_{\text{FEM}}^{1.5}(\mathbf{x}, 100)$ denotes the solution of FEM for $\mu_\kappa = 1.5\,\frac{\text{W}}{\text{m}\,^\circ\text{C}}$ at $t = 100\,\text{year.}$, while $\mathbf{T}^{100}(\mathbf{x}, 1.5)$ is the solution of PGD for the time slice $t = 100\,\text{year}$ for a specific parametric space $\mu_\kappa = 1.5\,\frac{\text{W}}{\text{m}\,^\circ\text{C}}$.

To assess the generalized solution of temperature more globally, global error per time slice, as explained in Chapter 5 in Equation 5.20, can be computed. Figure 6.12

presents this global error versus the time slice which is varying from the year zero to the year 1000, showing that the generalized solution of the thermal part is accurate.

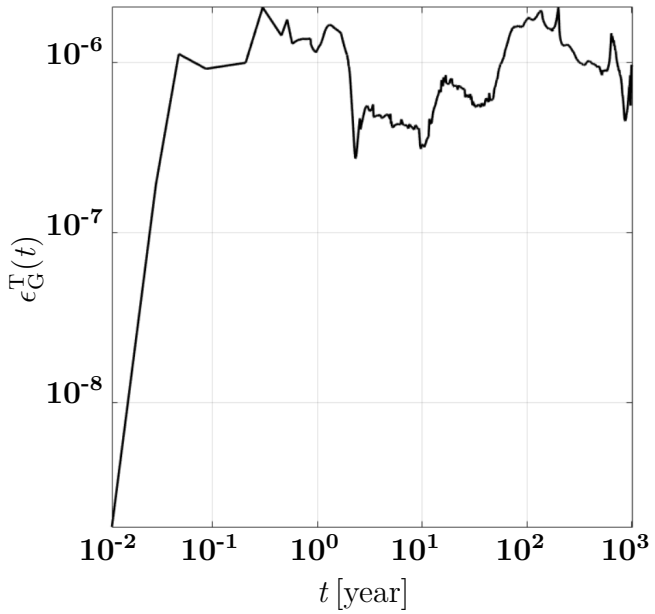

Figure 6.12: Global errors of the thermal solution in each time slice are less than 10^{-5}, quantifying the accuracy of the generalized solutions in the whole domain of time, spatial and parametric space.

Now, the generalized solution of the transient coupled Hydro-Mechanical (HM) aspects will be sought by using the generalized solution of the thermal part as input data. First, the choice of the enrichment tolerance (η_{tol}) is studied as a starting point for this investigation. Then, by having an accurate generalized solution, the study of the outputs versus times and their field results will be investigated.

Symbol	Amount	Definition
η_{tol}	10^{-5},10^{-6}	Enrichment Tolerance
iter_{max}	5	Maximum number of iteration for Fixed-point iteration

Table 6.4: Stopping criteria for PGD.

The global behavior of the generalized solution of the Hydro-Mechanical (HM) part (Equation (6.15)) will be investigated using global error definitions versus time for two different enrichment tolerances, as outlined in Table 6.4. The global error versus time, as previously mentioned for the thermal case, is a one-dimensional function defined in Equation (5.20) in Chapter 5.

Figure 6.13 shows that it is necessary to use $\eta_{\text{tol}} = 10^{-6}$ to have a sufficient accuracy (on the order of 10^{-3}) for the generalized solution of the coupled HM part. Therefore, from now on, for the present three-parameter problem, the study of the output versus time and their field results will be discussed by considering $\eta_{\text{tol}} = 10^{-6}$.

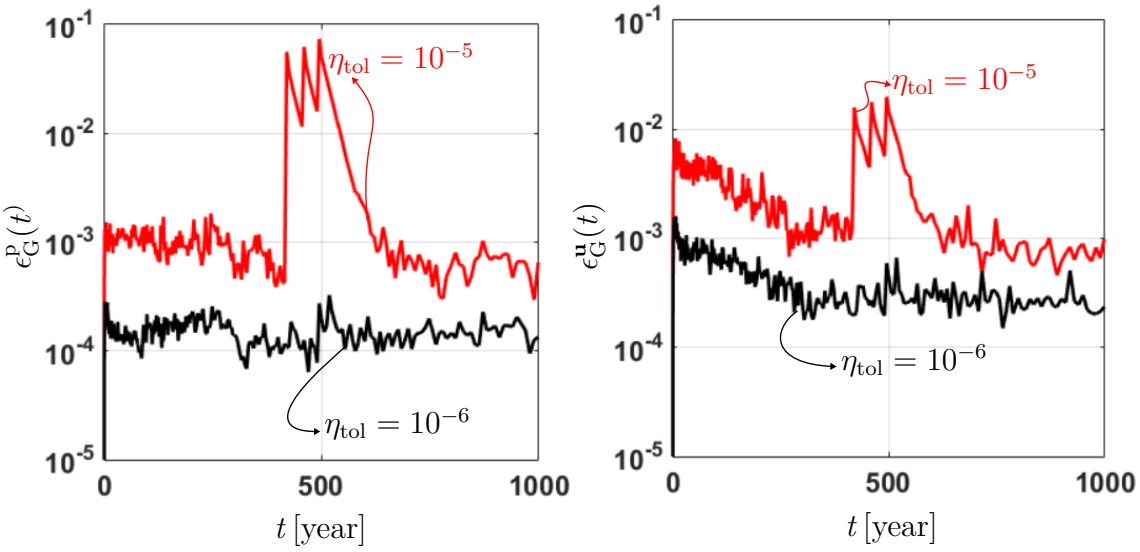

(A) (B)

Figure 6.13: (A) Behavior of the global error for pressure versus time, (B) Global error of displacement versus time. For both cases, the effect of a smaller enrichment tolerance $\eta_{\text{tol}} = 10^{-6}$ is illustrated. For $\eta_{\text{tol}} = 10^{-6}$, the accuracy for the whole domain of time for both cases is almost less than 10^{-3}.

Now, with the generalized solution, it is possible to explore various combinations of outputs in just a fraction of a second. All one needs to do is specify points in spatial space, parametric space, and time domain. For example, by specifying the parametric point at $\boldsymbol{\mu}^* = [1.5\,\frac{\text{W}}{\text{m}\,^\circ\text{C}}, 3 \times 10^{-14}\,, \frac{\text{m}}{\text{s}}\,68000\,\text{MPa}]$, one can explore the solutions for pressure, radial and vertical displacements versus time at a spatial coordinate of $r = 0.8\,\text{m}$ and $z = 17.5\,\text{m}$ (which is located in the rock material close to the buffer). Additionally, one can also explore the output field results for a specific year, such as $t = 10\,\text{years}$, for the same particularized point in the parametric space. The results are presented in Figures 6.14.

Figures 6.14-A, C, and E show the accuracy of the PGD solution compared to the FEM solution over time. On the other hand, Figures 6.14-B, D, and F present the results of pressure, radial, and vertical displacements, along with their relative

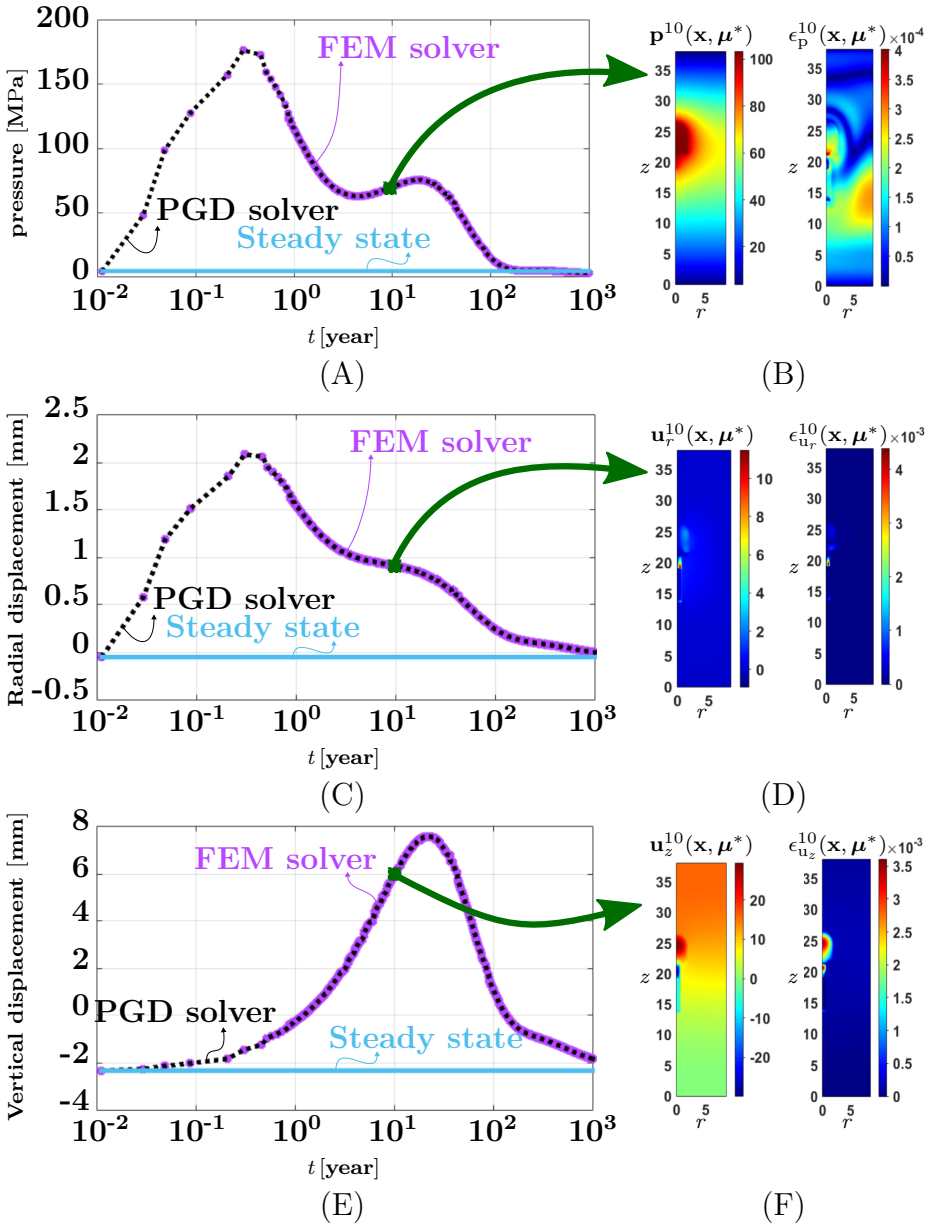

Figure 6.14: (A), (C) and (E) illustrate the results for pressure, radial displacement, and vertical displacement versus time, respectively. These results correspond to a specific point in the parametric space, $\boldsymbol{\mu}^* = [1.5\,\frac{\mathrm{W}}{\mathrm{m\,°C}}, 3\times10^{-14}\,\frac{\mathrm{m}}{\mathrm{s}}, 68000\,\mathrm{MPa}]$, and a fixed coordinate in space ($r = 0.8\,\mathrm{m}$ and $z = 17.5\,\mathrm{m}$) , which is located in the rock material close to the buffer. The results demonstrate agreement with the FEM solutions over time. (B), (D) and (F) display the field results for the same specific point in the parametric space at a time slice of $t = 10\,\mathrm{years}$ for pressure, radial displacement, and vertical displacement, respectively. These results further confirm the accuracy of the methodology.

errors, at a specific time slice of $t = 10$ years for the same particularized point in the parametric space. The relative errors for each field are defined as follows:

$$\epsilon_{\mathrm{p}}^{10}(\mathbf{x}, \boldsymbol{\mu}^*) = \frac{\|\mathbf{p}_{\mathrm{FEM}}^{\boldsymbol{\mu}^*}(\mathbf{x}, 10) - \mathbf{p}^{10}(\mathbf{x}, \boldsymbol{\mu}^*)\|}{\|\max\left(\mathbf{p}_{\mathrm{FEM}}^{\boldsymbol{\mu}^*}(\mathbf{x}, 10)\right)\|}. \tag{6.24}$$

$$\epsilon_{\mathrm{u}_r}^{10}(\mathbf{x}, \boldsymbol{\mu}^*) = \frac{\|\mathbf{u}_r{}_{\mathrm{FEM}}^{\boldsymbol{\mu}^*}(\mathbf{x}, 10) - \mathbf{u}_r{}^{10}(\mathbf{x}, \boldsymbol{\mu}^*)\|}{\|\max\left(\mathbf{u}_r{}_{\mathrm{FEM}}^{\boldsymbol{\mu}^*}(\mathbf{x}, 10)\right)\|}. \tag{6.25}$$

$$\epsilon_{\mathrm{u}_z}^{10}(\mathbf{x}, \boldsymbol{\mu}^*) = \frac{\|\mathbf{u}_z{}_{\mathrm{FEM}}^{\boldsymbol{\mu}^*}(\mathbf{x}, 10) - \mathbf{u}_z{}^{10}(\mathbf{x}, \boldsymbol{\mu}^*)\|}{\|\max\left(\mathbf{u}_z{}_{\mathrm{FEM}}^{\boldsymbol{\mu}^*}(\mathbf{x}, 10)\right)\|}. \tag{6.26}$$

In Equations (6.24), (6.25), and (6.26), $\mathbf{p}_{\mathrm{FEM}}^{\boldsymbol{\mu}^*}(\mathbf{x}, 10)$, $\mathbf{u}_r{}_{\mathrm{FEM}}^{\boldsymbol{\mu}^*}(\mathbf{x}, 10)$, and $\mathbf{u}_z{}_{\mathrm{FEM}}^{\boldsymbol{\mu}^*}(\mathbf{x}, 10)$ denote the solution of pressure, radial, and vertical displacement with FEM solver for particularized parametric point $\boldsymbol{\mu}^*$. The notations $\mathbf{p}^{10}(\mathbf{x}, \boldsymbol{\mu}^*)$, $\mathbf{u}_r{}^{10}(\mathbf{x}, \boldsymbol{\mu}^*)$, and $\mathbf{u}_z{}^{10}(\mathbf{x}, \boldsymbol{\mu}^*)$ refer to the output of online solver of PGD for one specific parametric point ($\boldsymbol{\mu}^*$) and time slice ($t = 10$ year) for pressure, radial and vertical displacement, respectively. Figure 6.14 shows that the PGD solution for the pressure, the radial, and the vertical displacements is in agreement with the FEM solution.

Figures 6.11, 6.12, 6.13, and 6.14 present that the methodology is accurate in the context of a simplified model of a engineering barrier system. In the following subsections, the efficiency and the possible exploitation of such generalized solutions will be discussed.

6.2.3 The efficiency of the generalized solution

As discussed in previous chapters, the PGD methodology is divided in two stages: the offline stage, which is computationally costly but only computed once, and the online stage, which costs a fraction of a second; therefore, its cost is negligible. The offline stage is a collection of PGD solutions per time slice. This means that each time slice has a different number of enrichment modes to reach the enrichment tolerance. Figure 6.15-A depicts the requirement of a number of modes (M^t) for each time slice (t) to build (6.15) for enrichment tolerance of 10^{-6}. For instance, Figure 6.15-B illustrates that for a time slice of ten years ($t = 10$ years), achieving an enrichment tolerance of $\eta_{\mathrm{tol}} = 10^{-6}$ requires 361 modes ($M^{10} = 361$). Figure 6.15 shows that the integration scheme does not cause the number of modes to explode with time,

but rather it remains bounded. On the contrary, after some time, the number of modes starts decreasing because the solution reaches a steady state. This confirms the efficiency of the time discretization implementation in this work.

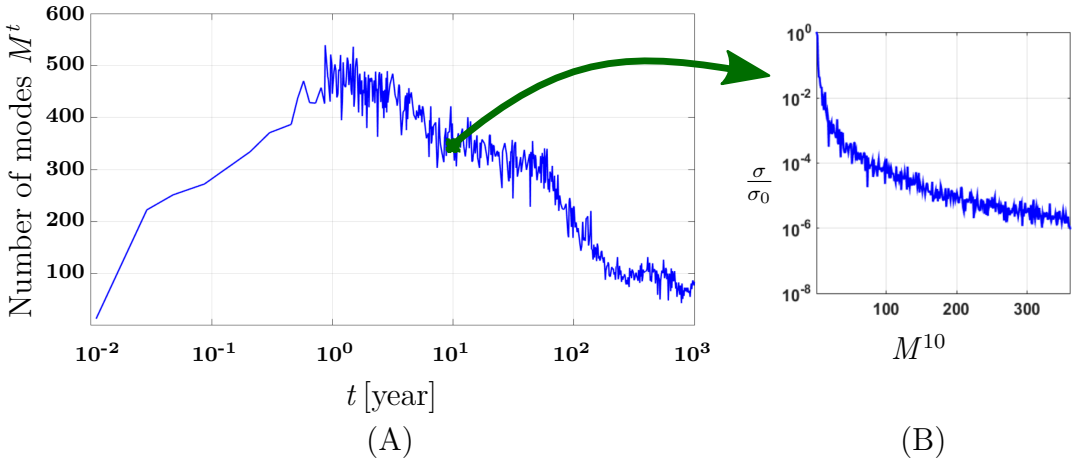

(A) (B)

Figure 6.15: Number of modes (M^t) versus time slice (t) for finding the solution of Equation (6.15) as an offline stage procedure: (A), number of modes as a function of time. (B) illustration of the enrichment procedure for the time slice year $t = 10\,\text{year}$, for which 361 Modes are required to reach the enrichment tolerance ($\eta_{\text{tol}} = 10^{-6}$).

Figure 6.16 shows that performing PGD is computationally expensive initially, taking almost 12 days to complete. However, once the offline stage is completed, the online stage becomes a matter of simply specifying points in the parametric space and receiving the output in a fraction of a second. In terms of computational cost, the Break-Even Point (BEP) is the number of forward problems (FEM) solutions at which the total computational cost of the forward FEM models becomes lower than the computational cost of the PGD solver. As shown in Figure 6.16, for the parametric problem at hand, this BEP corresponds to the solution of 802 forward problems. Beyond this point, the computational cost of additional FEM simulations continues to increase.

In a previous study by Larion et al. [81], the ATLAS experiment for repository characterization was addressed using a reduced basis approximation as a surrogate-based model for solving inverse problems in THM parametric identification. The study revealed that solving 13050 forward problems with a FEM solver would take approximately 200 days of computational time, significantly exceeding the time required for 802 FEM solutions. This highlights the inefficiency of classical repetitive FEM solutions and emphasizes the advantages of utilizing a PGD solver. The PGD

solver provides an online solution with an offline computational cost of only 12 days, making it a more efficient choice.

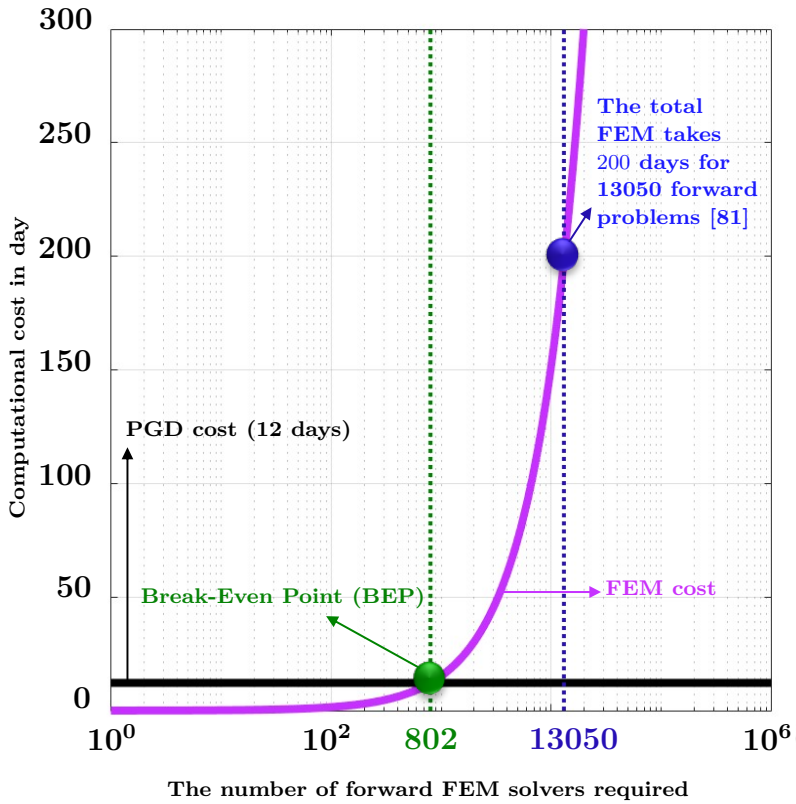

Figure 6.16: The computational cost of the PGD solver depends on building the generalized solution (offline stage), while for FEM solvers, the cost increases beyond the Break-Even Point (BEP) of solving 802 models. In cases where a large number of models are required, such as in parametric identification problems needing 13,050 models, classical FEM models can take up to 200 days, while the PGD solver takes only 12 days, making it 16.67 times faster. Thus, using the PGD solver is more advantageous, depending on the problem's objective.

The literature example demonstrates the necessity of solving a larger number of forward FEM solvers to achieve accurate results beyond the mentioned Break-Even Point (BEP) of 802 forward solutions. Furthermore, the generalized solution obtained from PGD proves effective in solving various inverse problems, including those with scattering measurements or sensitivity analysis across parameter landscapes. Notably, PGD's ability to provide online solutions without requiring the full-order model sets it apart from other reduced-order modeling techniques. Unlike these methods, PGD does not rely on error estimators for point selection and interpolation, instead relying solely on separated input and output data. In summary, the literature example and

the intrinsic characteristics of PGD reveal its advantages in terms of both efficiency and accuracy, making it a favorable approach.

6.2.4 Possible exploitations of the generalized solution

One of the main reasons for computing repetitive solutions to such parametric problems is doing the sensitivity analysis. Sensitivity analysis is a crucial aspect of parametric Partial Differential Equations (PDEs). Understanding how these variations impact the solution is essential for gaining insight into the behavior of PDEs and for making informed decisions in numerous scientific and engineering fields.

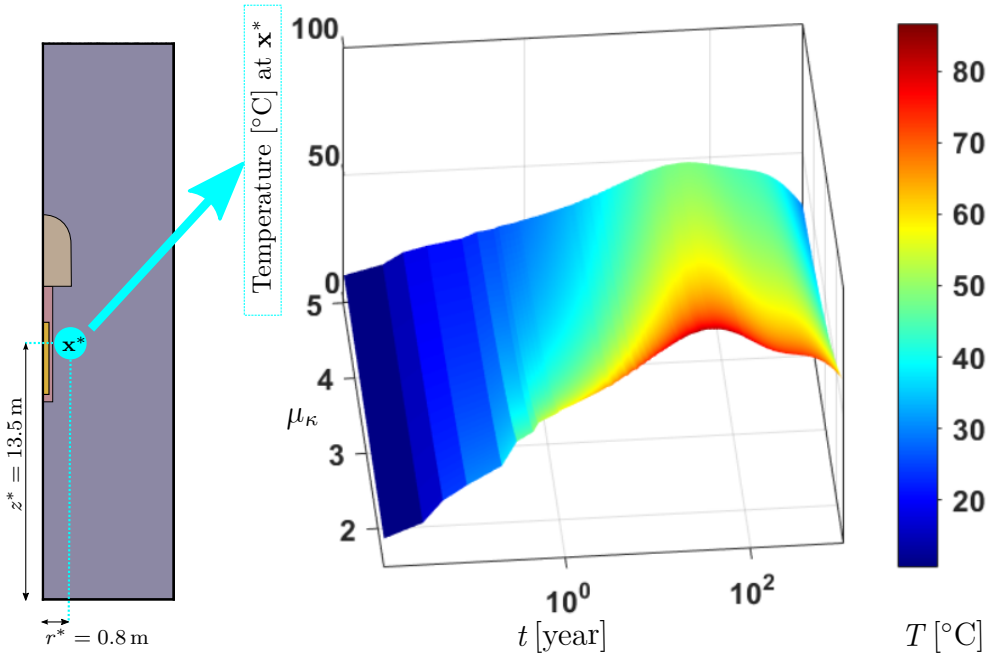

Figure 6.17: A generalized solution enables the investigation of the output sensitivity of the problem by making slight changes to the values of the input parameters within their specified range. Specifically, (A) focuses on a specific coordinate ($\mathbf{x}^*$) where temperature monitoring is required as the heat conductivity of the rock changes over time. In (B), a three-dimensional plot illustrates the variation of temperature over time and the heat conductivity at that particular spatial coordinate ($\mathbf{x}^*$). The color bar indicates the corresponding temperature values.

This thesis presents generalized solutions for parametric PDEs, which enables the rapid evaluation of the sensitivity of the solution to change in the input parameters. The solution can be analyzed in a fraction of a second by perturbing the parameters,

providing valuable insights into the system behavior. Figure 6.17 illustrates this concept at a specific spatial coordinate ($\mathbf{x}^*$), which shows how the temperature at a given spatial position changes versus time when the rock heat conductivity is modified. The presented solution is an excellent tool for sensitivity analysis of parametric PDEs, enabling also efficient optimization of the input parameters to achieve desired outputs. It can thus also be used for inverse analysis for parametric identification purposes.

6.3 Results for a geometrically parametrized problem

The second problem is similar to the previous one, only with the exception that the parameter is now geometric. From an application perspective, this problem could be used after the previous one in a context in which, after a material parameter identification, the repository would need to be optimized by solving the problem as dependent on the geometric parameter (optimization of the distance between canisters).

For this section, the problem depends on only one extra dimension: a geometric parameter (μ_L). The generalized solution is similar to Equations (5.17) and (5.18), with the material parameter functions deleted from the separated unknowns. We have assumed fixed values for the material properties for this problem, which are the minimum values of the material parameters in their intervals in Table 6.1. Since there is only one extra dimension, it is easy to calculate the error for the entire parametric domain versus time. The definitions of errors for the temperature, pressure, and displacement fields are as follows:

$$\epsilon_{\mathrm{G}}^{\mathrm{T}}(t,\mu_L) = \frac{\|\mathbf{T}_{\mathrm{FEM}}^{\mu_L}(t) - \mathbf{T}_{\mathrm{PGD}}^{t}(\mu_L)\|_{\Omega}}{\|\mathbf{T}_{\mathrm{FEM}}^{\mu_L}(t)\|_{\Omega}}, \tag{6.27}$$

$$\epsilon_{\mathrm{G}}^{\mathrm{p}}(t,\mu_L) = \frac{\|\mathbf{p}_{\mathrm{FEM}}^{\mu_L}(t) - \mathbf{p}_{\mathrm{PGD}}^{t}(\mu_L)\|_{\Omega}}{\|\mathbf{p}_{\mathrm{FEM}}^{\mu_L}(t)\|_{\Omega}}, \tag{6.28}$$

$$\epsilon_{\mathrm{G}}^{\mathbf{u}}(t,\mu_L) = \frac{\|\mathbf{u}_{\mathrm{FEM}}^{\mu_L}(t) - \mathbf{u}_{\mathrm{PGD}}^{t}(\mu_L)\|_{\Omega}}{\|\mathbf{u}_{\mathrm{FEM}}^{\mu_L}(t)\|_{\Omega}}. \tag{6.29}$$

The generalized solution to this problem has been generated with an enrichment tolerance of $\eta_{\mathrm{tol}} = 10^{-5}$. Figure 6.18 presents the error in the whole domain of the

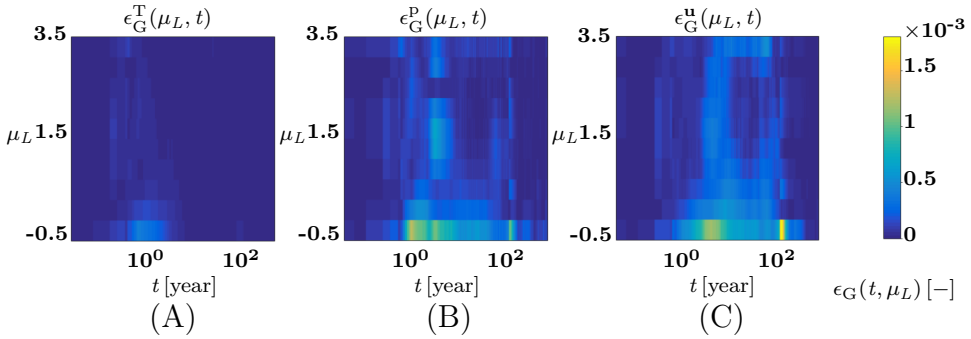

Figure 6.18: The variation of temperature error (A), pressure error (B), and displacement error (C) is observed across the entire domain of the geometric parameter and time. The color bar represents the corresponding relative errors ($\epsilon_G(t, \mu_L)$).

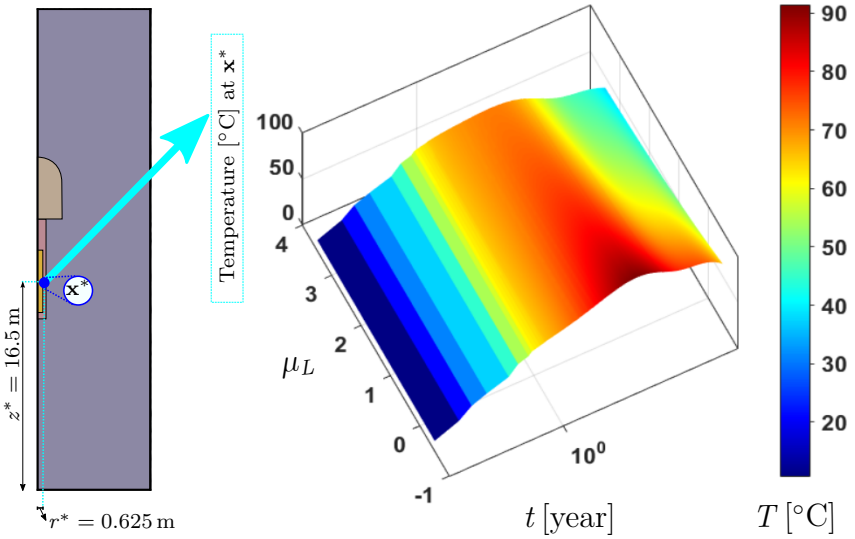

Figure 6.19: The parametric response of temperature with respect to the geometric parameter (μ_L) and time (t) was evaluated for the buffer adjacent to the canister (B). In some studies, the maximum temperature of the buffer has been analyzed as part of the design criteria for a repository. Thus, this coordinate ($\mathbf{x}^*$) holds significance in determining the optimal spacing between canisters to ensure that the maximum allowable temperature in the buffer is not exceeded (A). The color bar represents the corresponding temperature values.

geometric parameter and time. This figure shows that the generalized solution is accurate enough (the errors are almost less than 10^{-3} for all the fields.)

One crucial factor to consider in the design of a deep geological repository is the spacing between canisters. Figure 6.19 demonstrates that obtaining a fast and feasible generalized solution for temperature at a specific coordinate on the buffer adjacent

to the canister is possible. Such results can greatly contribute to determining the optimal and safest spacing between canisters. This analysis can be efficiently conducted as part of the overall solution package for repository design. In general, most repository concepts have a design criterion of 100 °C for the maximum temperature in the bentonite buffer [57], which serves as a basis for making decisions regarding the most cost-effective and secure spacing between canisters. Furthermore, the current online solution would allow for the exploration of design factors, such as partial saturation, by extending the current work to nonlinear aspects. This would enable the examination of how different parameters impact the time required to reach saturation [150]. Additionally, by considering the partial saturation case and developing the current linear-to-nonlinear approach, the swelling pressure could be studied as a design factor for the bentonite material [149].

Chapter 7

Discussion on the development of the numerical methodology

This chapter presents a detailed discussion of some specific parameters associated with the Proper Generalized Decomposition (PGD) methodology in the context of its use for coupled problems inspired by deep geological repositories. This chapter focuses on the four-parameters case and aims to investigate how the numerical parameters of the stopping criteria for the PGD linear solver impact both the global error of the generalized solution as well as more specific (local) errors for every combination of parameter values in the parametric space. Furthermore, the chapter presents an additional result for the four-parameters case, which demonstrates that the methodology works properly for almost every point of the parametric and spatial spaces in the whole domain of time.

The chapter also discusses the number of iterations required for the inner loop of the PGD solver (fixed-point iteration). It details the reasons why this number of iterations is kept limited to small and fixed. Additionally, the performance of the numerical methodology is studied in relation to the use of PGD compression and other possible features of the solver, such as the use of Δ-solver, or using such as the solution of the last time step, as potential starters for the PGD linear solver for the current time step. All the definitions and values for the coupled THM problems are taken from Chapter 6. It is important to emphasize that only the four-parameters case will be considered for the present discussion.

This chapter is divided into four sections. Section 7.1 outlines the effects of the parameters reading the stopping criteria of the PGD linear solver (for the four-parameters case). Additionally, it explains why choosing a small fixed number of iterations for the involved fixed point scheme makes sense. Section 7.2 discusses the use of PGD compression and its performance. Section 7.3 presents the idea of the Δ-solver and its effect on thermal and coupled Hydro-Mechanical (HM) aspects. Finally, Section 7.4 discusses using the previous time step as a starting point for the PGD linear solver.

7.1 Effects of PGD solver stopping criteria on accuracy and efficiency

In this section, the focus is solely on the coupled HM case due to the high accuracy achieved for the thermal aspect in all previous chapters. The maximum temperature error across the entire domain of time and the entire parametric space is only 0.0037. Therefore, particular emphasis is placed on the coupled HM aspect of the problem. Consequently, four stopping criteria and units for the output fields have been investigated for this methodology, and they are presented in Table 7.1.

Symbol	Unit of p	Unit of $\mathbf{u}$	η_{tol}	iter_{max}
Υ_1	Pa	m	10^{-5}	5
Υ_2	Pa	m	10^{-5}	25
Υ_3	Pa	m	5.5×10^{-6}	10
Υ_4	MPa	mm	10^{-5}	5

Table 7.1: Four different combinations of stopping criteria, including the maximum number of fixed-point iterations (iter_{max}) and the enrichment tolerance of PGD (η_{tol}), have been selected for the PGD linear solver, along with the problem units. These selections are presented in Table.

To study the behavior of each combination (Υ_1, Υ_2, Υ_3, and Υ_4), we will evaluate their accuracy by examining the global error of the corresponding generalized solution obtained as a function of time. The computation of different types of error has been discussed in Chapter 5, Section 5.2. In this section, we will study the error as a one-dimensional function, similar to the one in Equation (5.20).

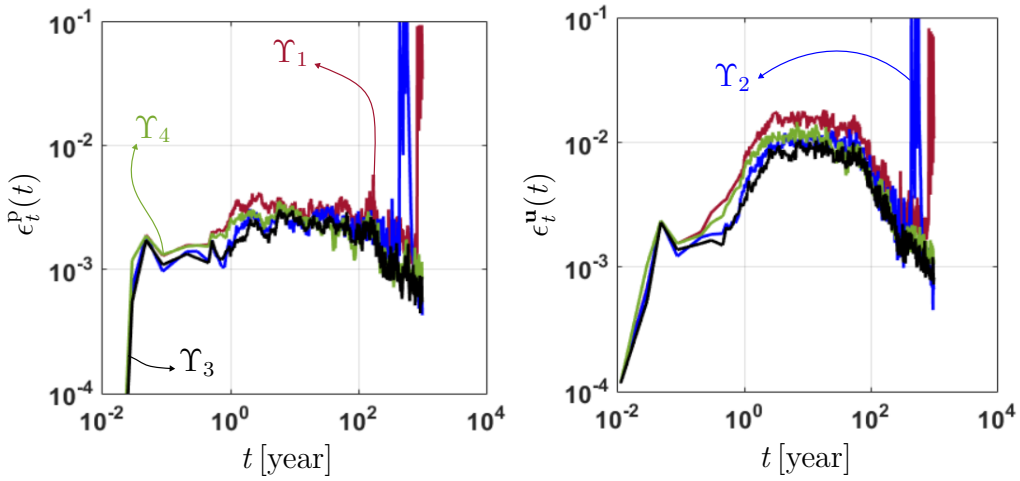

Figure 7.1: Global errors in each time slice for a different combination of stopping criteria for the pore pressure (A) and the displacement (B) fields. Combinations of Υ_3 and Υ_4 are seen to provide accurate results for all time slices.

Figure 7.1 demonstrates, corresponding Υ_1 and Υ_2, that increasing the number of iterations in fixed-point iterations from five to 25 does not improve global accuracy. Consequently, increasing the number of iterations in the inner loop of the PGD linear solver only results in a more computationally expensive procedure without any benefit. Therefore, this inner loop can be relaxed with a low number of iterations similar to five in favor of efficiency. The tradeoff of choosing a fixed number of iterations for this inner loop should be investigated for each problem. Here it is observed that choosing five or ten iterations provides accurate solutions by selecting proper enrichment tolerance. For instance, for Υ_1, with 5 iterations, the total computational cost for the PGD offline stage is 61 days, while for Υ_2, with 25 fixed iterations, the computational cost rises to almost 185 days. On the other hand, for Υ_3, a fixed number of ten iterations with a smaller enrichment tolerance results in an accurate global error behavior versus time and an even more efficient solution, requiring almost 35 days less than Υ_2 (with a computational cost of 150 days for this case).

Generally, the iterative procedure is chosen to converge to a certain tolerance by considering a number of iterations that are not fixed but determined by a level of accuracy to read. However, in the present case, a different approach is taken. To apply PGD to the problem at hand, it is computationally more efficient to use a smaller number of iterations for the inner loop of PGD. This can be understood as

follows. The PGD algorithm consists of two iterative procedures: an enrichment iteration (outer loop) and a fixed-point iteration (inner loop). Therefore, fixing the number of iterations for the fixed-point loop in the PGD context makes sense. The reason for this approach is that if proper convergence is not achieved in the fixed-point loop because of the (low) fixed number of iterations, it will introduce an error in the term. To fix this, the (outer) enrichment loop will try to correct the global residual when determining the subsequent term. Increasing the number of modes will make the PGD algorithm more accurate, further improving its effectiveness. Therefore, it is more appropriate, depending on the engineering problem under investigation, to find the best tradeoff between the enrichment tolerance and the number of fixed-point iterations to obtain the most efficient and accurate output from the PGD linear solver.

Figure 7.1 demonstrates that both combinations Υ_3 and Υ_4 yield accurate global error results. Notably, the key difference between Υ_3 and Υ_4 is their offline computational costs, with Υ_3 requiring almost 150 days and Υ_4 requiring nearly 100 days. Moreover, due to the nonhomogeneous units of the output fields causing the coupled HM aspect, the PGD algorithm necessitates a stronger enrichment tolerance, similar to Υ_3. Alternatively, before using PGD, the algorithm could choose output field units so that quantities watch similar order of magnitude to ensure accurate results similar to Υ_4. The reason for the decrease in accuracy from a global perspective when units result in quantities with a number order of magnitude is that the convergence of only one of the output fields will dominate the convergence check in the enrichment tolerance. As such, it is necessary to identify this and address this issue by either using a smaller enrichment tolerance or preparing all separated input data in a format that the PGD linear solver can handle, ensuring that output fields are on the same scale. By taking either of these steps, it is possible to avoid such an effect in the convergence check and ensure that accurate results are obtained.

The study conducted by Marcelo et al. [141] demonstrates an acceptable 5 % error threshold, widely recognized as excellent in the application of THM models within deep geological repositories. Their research primarily focuses on the numerical investigation of the THM behavior in Full-scale Engineered Barrier Experiments. This comprehensive approach combines both numerical and experimental investigations.

By considering this 5 % threshold as an indicator in this thesis, it can be observed that if the global error is the key factor for decision-making from a designer's per-

spective, then, based on Figure 7.1, everything is satisfactory, particularly for the Υ_3 and Υ_4 combinations. However, if specific combinations of parameters and their relative errors are important, a more comprehensive understanding of this effect can be gained by investigating local errors, such as those for the Υ_3 combination. To perform a thorough analysis, local errors were determined for various parameter combinations, including the minimum, median, and maximum values for each parameter dimension. This resulted in the selection of 81 parameter value combinations for further analysis. The error plot presented in Figure 7.2, organized similarly to Figure 5.7 in Chapter 5, displays the vertical axis representing the same combination definitions as Figure 5.7, while the horizontal axis represents time. The color-coded plot in Figure 7.2 illustrates the computed error for each combination, using the definition presented in Chapter 5 and Equation (5.21), for the Υ_3 case.

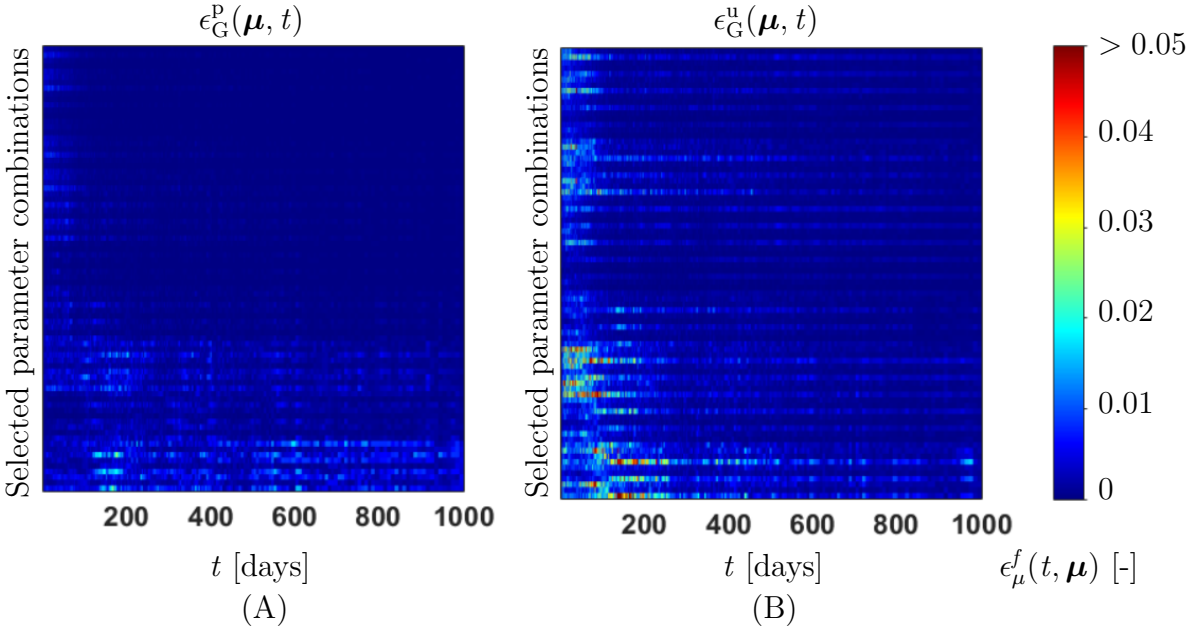

Figure 7.2: Errors are analyzed for pore pressure (A) and displacement (B) at various points in the parametric space, specifically for 81 combinations of parametric values. These combinations are selected from the minimum, maximum, and median values of four parametric ranges. The vertical axis of the plot represents the chosen parametric combinations, while the horizontal axis denotes time. The color bar represents the local error (Equation (5.21)) in each selected parametric combination versus time, which is the relative error of the PGD solution with respect to FEM for every time and parameter combination.

Figure 7.2 illustrates the error across the entire parametric space over time for combination Υ_3 in the PGD parameters. The error analysis reveals that nearly 100 %

of the pore pressure field and approximately 99.7 % of the displacement field have error levels below 0.05. These findings align with the study conducted by Marcelo et al. [141], which also indicates acceptable error levels for the displacement fields. Notably, the color-coded error plot in Figure 7.2 indicates specific localized errors exceeding 0.05, which comprise only approximately 0.3 % of the selected parametric space. To highlight these localized errors, specific points in spatial coordinates with errors exceeding 0.05 are provided. For example, at the particular parametric point $\boldsymbol{\mu}^* = [5\,\frac{\mathrm{W}}{\mathrm{m\,°C}}, 3\times10^{-14}, \frac{\mathrm{m}}{\mathrm{s}}, 55600\,\mathrm{MPa}, 3.5\,\mathrm{m}]$ located in the backfill at spatial coordinate ($r = 0.1048\,\mathrm{m}$, and, $z = 23.8806\,\mathrm{m}$), the vertical displacement versus time exhibits a local error of approximately 9 % in the backfill region during year 7. Figure 7.3 depicts this information through two components: the left graph illustrates the change in vertical displacement versus time at the specific point in the backfill, while the figure on the right showcases the spatial distribution with the specific large local error at the corresponding time of year 7. Although the overall accuracy is good, there are certain areas, similar to those depicted in Figure 7.3, where accuracy is reduced. It should be emphasized, however, that the PGD methodology is robust and capable of correcting such errors as time progresses (in the case of Figure 7.3, the error decreases again after year 10).

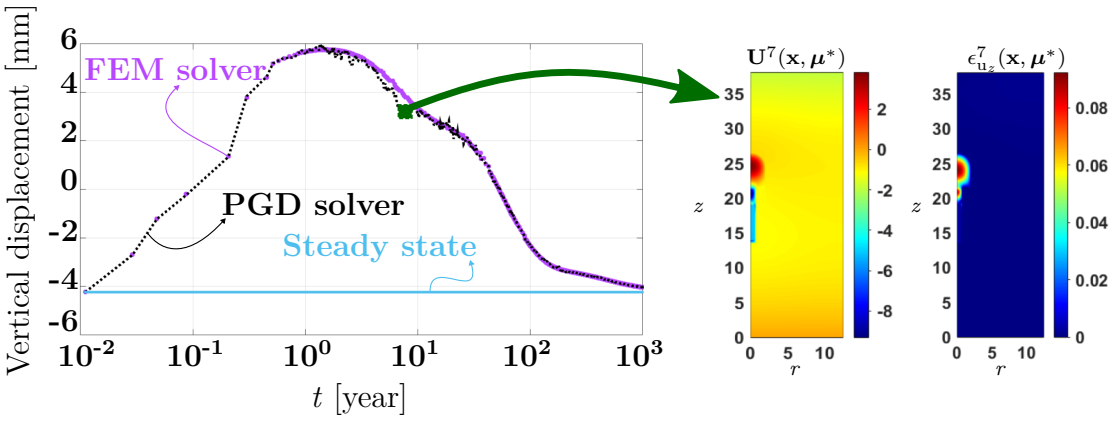

(A) (B)

Figure 7.3: (A) Results of the vertical displacement versus time for a fixed coordinate in the backfill material ($r = 0.1048\,\mathrm{m}$ and $z = 23.8806\,\mathrm{m}$) for a particularized point in parametric space $\boldsymbol{\mu}^* = [5\,\frac{\mathrm{W}}{\mathrm{m\,°C}}, 3\times10^{-14}\,\frac{\mathrm{m}}{\mathrm{s}}, 55600\,\mathrm{MPa}, 3.5\,\mathrm{m}]$. (B) Vertical displacement distribution at time $t = 7\,\mathrm{year}$ for the same particularized point in parametric space.

From an application standpoint, the focus should be directed towards Figure 7.2, which reveals the presence of localized errors, given that the maximum temperature

occurs within the first 100 years. It is important to note that the region in the selected parametric space, where the color-coded error plot exceeds the threshold of 0.05 (as depicted in Figure 7.2), corresponds to specific localized errors, as demonstrated in Figure 7.3. These errors exhibit a high level of localization in spatial, temporal, and parametric dimensions.

Furthermore, Figure 7.2 indicates that the majority of localized errors occur in rows associated with the extreme values of the parameters. If such error levels pose challenges for the designers' application objectives, a smaller enrichment tolerance would be necessary. However, reducing the enrichment tolerance might adversely impact computational efficiency for the current problem. It is worth mentioning that the computation of these results used the current four-parameter THM model, with the offline stage requiring approximately 150 days. Achieving higher accuracy would demand computational resources exceeding 150 days, which is not deemed efficient.

Hence, the subsequent sections investigate the potential of PGD compression, the Δ-solver, and the previous solution as a starting point for the PGD linear solver to assess whether they can enhance computational efficiency. Nevertheless, it is essential to emphasize that the existing methodology remains accurate and efficient for problems with three material parameters as an additional dimension, as well as for problems involving only one geometric parameter as an additional dimension. Two examples illustrating these scenarios were presented in Chapter 6. Section 6.2 demonstrated the effectiveness of the methodology for a problem with three material parameters, while Section 6.3 established its accuracy and efficiency for a problem with only one geometric parameter.

7.2 Effect of PGD compression

To reduce the number of terms in high-dimensional functions, an effective approach is to employ PGD compression. However, it is crucial to note that PGD compression must not be confused with the PGD linear solver previously discussed in Chapter 3. PGD compression primarily aims to reduce the number of terms and complexity of high-dimensional functions. This method relies on combining two key concepts: least-squares projection and the PGD strategy. By integrating these two approaches, it becomes possible to select a subset of significant terms from each dimension and

reconstruct the high-dimensional function with a smaller number of terms while still achieving a high level of accuracy in representing the overall function [134, 37, 38].

Before delving into the analysis of the potential benefit of an application of PGD compression on the four-parameters case, an overview of the concept of PGD compression in relation to the thermal aspect of the problem is given here to explain its principle. This will serve as an introduction to the topic and help to better understand the subsequent discussion. To illustrate this concept, let us consider the output of a temperature simulation for a specific time t, which is represented by separated matrices as follows:

$$\mathbf{T}^t(\mathbf{x}, \mu_\kappa, \mu_L) = \sum_{m=1}^{M^t} \mathbf{T}^m(\mathbf{x}) B^m_{\mu_\kappa}(\mu_\kappa) B^m_{\mu_L}(\mu_L). \tag{7.1}$$

To mitigate the effects of a large number of terms M^t in $\mathbf{T}^t(\mathbf{x}, \mu_\kappa, \mu_L)$, PGD compression can be employed. It consists of the following operations:

1. Least-squares projection:

$$\jmath(\mathbf{T}_{\text{com}}) = \|\mathbf{T}_{\text{com}} - \mathbf{T}^t(\mathbf{x}, \mu_\kappa, \mu_L)\| \tag{7.2}$$

2. The aim is to compute a separable approximation, where $N \ll M^t$:

$$\mathbf{T}_{\text{com}} = \sum_{n=1}^{N} \hat{\mathbf{T}}^n(\mathbf{x}) \hat{B}^n_{\mu_\kappa}(\mu_\kappa) \hat{B}^n_{\mu_L}(\mu_L). \tag{7.3}$$

3. The primary objective of using the PGD strategy in this context is to formulate a rank-one approximation of the minimization problem of $\jmath(\mathbf{T}_{\text{com}})$.

Note that the proposed method involves iterating three linear equations to reach a stationary solution based on a stopping criterion for a single achievement term. It is worth noting that the last procedure entirely relies on the PGD strategy, which was previously discussed in detail in Chapter 3.

To achieve even more accurate results in the four-parameters case, it is necessary to run the PGD linear solver with a stronger stopping criterion, as mentioned in the previous section. Such stronger stopping criteria for the PGD linear solver are presented in Table 7.2 as the base case for comparison with the results of PGD compression. It should be emphasized that this concept is only studied in detail for the coupled HM aspect of the four-parameter case, as the thermal aspect is already

accurate and efficient enough. By implementing the stopping criteria mentioned in Table 7.2, the PGD has been run for almost 190 days, and it only provides results for two years out of 1000 years of simulation (73 time steps out of 497 time steps). While the results are accurate for the entire domain of time, spatial and parametric space, they are not efficient.

Symbol	Amount	Definition
η_{tol}	10^{-6}	Modes Tolerance
M_{max}	2000	Maximum number of Modes
ϵ_{tol}	10^{-6}	Tolerance for Fixed-point iteration
iter_{max}	15	Maximum number of iteration for Fixed-point iteration

Table 7.2: Stopping criteria for PGD linear solver as based case.

The results of the base case will now be studied to investigate whether PGD compression can increase the efficiency of the problem for the first half of a year. To study this four-parameters case with PGD compression, the input data that was previously presented (Chapter 4) in a discretized and separated format for the PGD linear solver will be utilized. This input data includes the following categories:

$$\mathbf{K}_{\mathbf{G}}^{i}(\boldsymbol{\mu})\mathbf{U}^{i+1}(\boldsymbol{\mu}) = \mathbf{F}_{\mathbf{G}}^{i}(\boldsymbol{\mu}). \tag{7.4}$$

This equation has already been discussed in detail in Chapter 4 (Equation (4.11)). To remind the reader, $\mathbf{U}^{i+1}(\boldsymbol{\mu})$ comprises the separated forms of pore pressure and displacement as unknowns for the current time step. Before applying the Dirichlet boundary conditions, we will discuss $\mathbf{F}_{\mathbf{G}}^{i}(\boldsymbol{\mu})$, which is repeated here as a reminder:

$$\mathbf{F}_{\mathbf{G}}^{i}(\boldsymbol{\mu}) = \mathbf{F}_{*}^{i}(\boldsymbol{\mu}) + \mathbf{K}_{\mathbf{G}}^{i*}(\boldsymbol{\mu})\mathbf{U}^{i}(\boldsymbol{\mu}) + \mathbf{G}_{\mathbf{T}}(\boldsymbol{\mu})\mathbf{T}(\boldsymbol{\mu}). \tag{7.5}$$

The number of modes is higher for the smaller enrichment tolerance. For instance, in this case, for the second time step (0.03 year), there are 445 modes. To find the unknown $\mathbf{U}^3$ while having $\mathbf{U}^2$ as 445 separated terms and multiplying it with $\mathbf{K}_{\mathbf{G}}^{i*}(\boldsymbol{\mu})$, the total number of terms for the right-hand side will be $10,832$. The large number of terms produced by smaller enrichment tolerances causes the PGD linear solver to run slower. Therefore, PGD compression has been studied and applied to the right-hand side using different criteria presented in Table 7.3.

The reason for choosing a large maximum iteration in PGD compression is to reduce the number of modes, which would enable the PGD compression to reach the

tolerance using the fixed-point iteration process. The PGD compression is applied separately for each part of the field, meaning that the right-hand side related to the pore water pressure is compressed separately, followed by the right-hand side related to the displacement, and then all the parts are joined together as a large, separated right-hand side force vector. By implementing this method with $\eta_{\text{tol}}^{\text{comp}} = 10^{-3}$ and $\eta_{\text{tol}}^{\text{comp}} = 10^{-4}$, the right-hand side for the third time step was reduced from 10832 to 19 and 10832 to 38, respectively. However, the PGD compression itself has an offline computational cost, which, for each case, is 27 and 36 minutes, respectively, for this time step.

Symbol	Amount	Definition
$\eta_{\text{tol}}^{\text{comp}}$	10^{-3},10^{-4}	Modes Tolerance
$M_{\text{max}}^{\text{comp}}$	5000	Maximum number of Modes
$\epsilon_{\text{tol}}^{\text{comp}}$	10^{-6}	Tolerance for Fixed-point iteration
$\text{iter}_{\text{max}}^{\text{comp}}$	200	Maximum number of iteration for Fixed-point iteration

Table 7.3: Stopping criteria for PGD compression.

Firstly, the problem needs to maintain its accuracy, and secondly, it needs to be significantly more efficient than the base case. Thus, to evaluate the effect of the enrichment tolerances of the PGD compression process on the accuracy, the maximum error in the output fields will be presented as a function of time for the first half year.

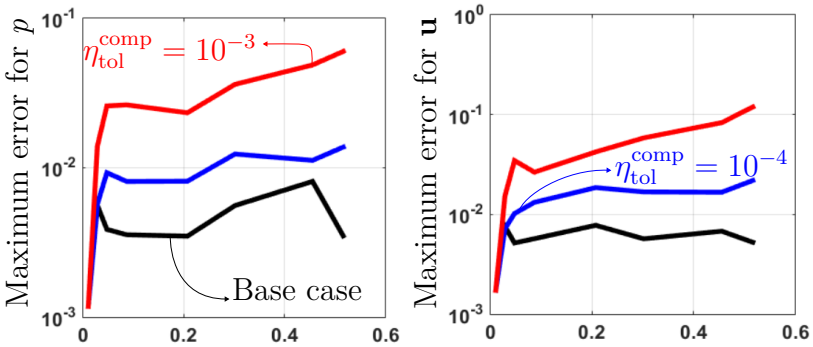

Figure 7.4: The maximum relative error of pore pressure (A) and displacement (B) in the first time steps is compared to the base case, with compression tolerances of $\eta_{\text{tol}}^{\text{comp}} = 10^{-3}$ and $\eta_{\text{tol}}^{\text{comp}} = 10^{-4}$.

Figure 7.4 illustrates that the accuracy of the base case decreases when PGD compression is applied, especially when $\eta_{\text{tol}}^{\text{comp}} = 10^{-3}$, which shows significant inaccuracies. Although the results for the $\eta_{\text{tol}}^{\text{comp}} = 10^{-4}$ seem fine, a closer analysis of the problem reveals that the error in the "shock" conditions (the most transient part of the problem) increases to more than two percent, which is not desirable. Such an error will be inherited by the next generation of computations, making the generalized solution of the next results inaccurate. Therefore, it is crucial to address this issue to ensure the accuracy of future computations. It is important to keep the maximum error consistency, at least during the shock procedure. The total computational cost for the computed time steps for the base case is almost 6.8 days. For $\eta_{\text{tol}}^{\text{comp}} = 10^{-4}$, the total computational cost is 6.5 days. It should be emphasized through that the total computational cost of the offline stage for the PGD linear solver actually decreases. However, the offline computational cost of PGD compression is also expensive. For instance, for $\eta_{\text{tol}}^{\text{comp}} = 10^{-4}$, the computational cost of PGD compression is almost one and a half days, and the computational cost of the PGD linear solver is 5 days. In total, the overall cost is thus not significantly improved for this case study.

To solve the problem, Equation (7.5) serves as the right-hand side, which should be provided as separated input data. During the solution process, the solution from the previous time step propagates to the right-hand side due to the separated functions $\mathbf{U}^i$, leading to the generation of a large, separated, high-dimensional tensor. However, as previously seen with this problem, compressing the entire right-hand side is not an efficient solution. To improve efficiency, only the preceding $\mathbf{U}^i$ is compressed and subsequently used for the right-hand side. This approach is examined to evaluate its efficacy in addressing the issue. The criterion used for PGD compression is similar to that in Table 7.3.

In Figure 7.5, it is observed that using $\eta_{\text{tol}}^{\text{comp}} = 10^{-3}$ is not accurate at all, while $\eta_{\text{tol}}^{\text{comp}} = 10^{-4}$ accumulates errors at the start of the "shock" (the most transient part of the solution). It seems that the error will increase as the solution progresses. The total computational cost for $\eta_{\text{tol}}^{\text{comp}} = 10^{-4}$ is 7.5 days, while for the base case, it is 9 days. Although this approach is a bit faster, the observation shows that when the error accumulates significantly during the transient phase, it affects the rest of the problem.

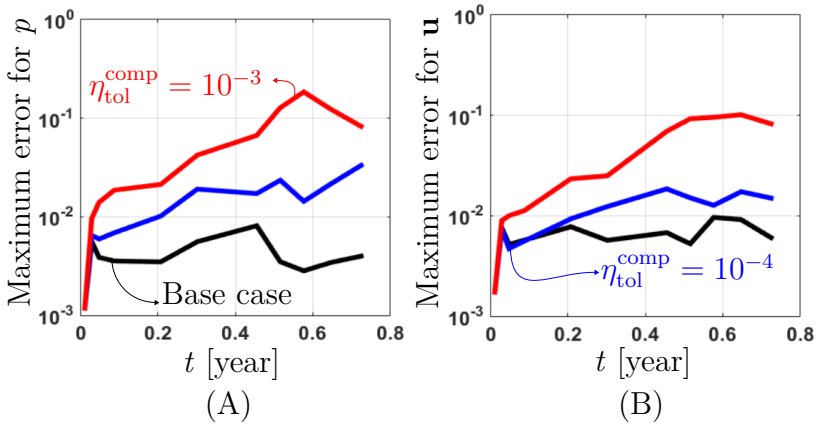

Figure 7.5: Maximum relative error on pore pressure (A) and displacement (B) in the first time steps for different cases (base case, $\eta_{\text{tol}}^{\text{comp}} = 10^{-3}$, and $\eta_{\text{tol}}^{\text{comp}} = 10^{-4}$).

In conclusion, after testing various configurations, we were unable to identify a scenario in which the compressed versions were faster, more efficient, or more accurate than the uncompressed base case.

7.3 Use of a Δ-solver methodology

In this thesis, the thermal aspect of the THM problem has been tackled using the ΔT-solver for PGD linear solver in all cases. This choice is explained in detail in this section, and before discussing numerical considerations, the ΔT-solver concept is briefly presented and compared to the conventional T-solver. It will also be noted that this technique has been implemented for the coupled HM case, but it did not improve its efficiency; rather, it is only beneficial for the thermal part.

To explain the concept of ΔT-solver, the parametric thermal equation of the problem inspired by the deep geological repository will be discussed, taking into consideration both the heat conductivity of the rock and the geometric parameter as additional dimensions. The PGD linear solver in a conventional way, also denoted as the T-solver, solves the following equation:

$$\mathbf{K}_{\mathbf{GT}}^{i}(\mathbf{x}, \mu_\kappa, \mu_L)\mathbf{T}^{i+1}(\mathbf{x}, \mu_\kappa, \mu_L) = \Delta t^i \mathbf{f}_{\text{q}}^{i}(\mathbf{x}) + \mathbf{K}_{\mathbf{GT}}^{i*}(\mathbf{x}, \mu_\kappa, \mu_L)\mathbf{T}^{i}(\mathbf{x}, \mu_\kappa, \mu_L). \quad (7.6)$$

This means that by providing the separated input data of Equation (7.6) for the PGD linear solver, the collection of generalized solutions obtained by the T-solver for each time step is considered the solution. Discussion concerning the separated input data has been given in Chapter 4.

Now, the ΔT-solver is defined using the following equation:

$$\mathbf{T}^{i+1}(\mathbf{x}, \mu_\kappa, \mu_L) = \Delta\mathbf{T}^{i}(\mathbf{x}, \mu_\kappa, \mu_L) + \mathbf{T}^{i}(\mathbf{x}, \mu_\kappa, \mu_L). \tag{7.7}$$

By inserting Equation (7.7) into Equation (7.6), the ΔT-solver is defined as follows:

$$\begin{aligned}\mathbf{K}^{i}_{\mathbf{GT}}(\mathbf{x}, \mu_\kappa, \mu_L)\Delta\mathbf{T}^{i}(\mathbf{x}, \mu_\kappa, \mu_L) =& \Delta t^{i}\mathbf{f}^{i}_{\mathrm{q}}(\mathbf{x}) + \\ & \mathbf{K}^{i*}_{\mathbf{GT}}(\mathbf{x}, \mu_\kappa, \mu_L)\mathbf{T}^{i}(\mathbf{x}, \mu_\kappa, \mu_L) - \\ & \mathbf{K}^{i}_{\mathbf{GT}}(\mathbf{x}, \mu_\kappa, \mu_L)\mathbf{T}^{i}(\mathbf{x}, \mu_\kappa, \mu_L)\end{aligned} \tag{7.8}$$

The separated input data for the ΔT-solver are obtained from Equation (7.8). The PGD linear solver solution for Equation (7.8) produces a separated $\Delta\mathbf{T}^{i}(\mathbf{x}, \mu_\kappa, \mu_L)$. To obtain the current temperature ($\mathbf{T}^{i+1}$) based on Equation (7.7), the solution of Equation (7.8) is summed with the previous time step temperature solution. As the number of terms accumulates and increases, PGD compression is necessary to decrease the number of terms for each time step. Since this technique works accurately and efficiently for the thermal aspect, it is more efficient to apply it to the thermal part and then move it to the right-hand side.

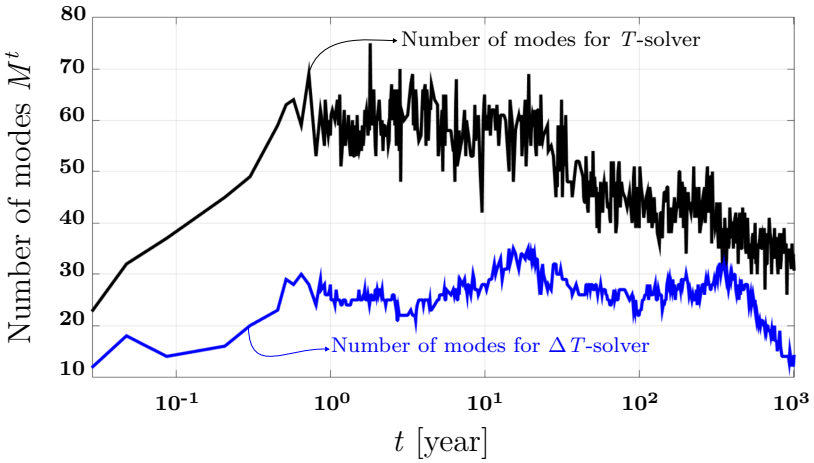

Figure 7.6: Number of modes required for the final output of the generalized temperature solution for each time slice. The results demonstrate that the ΔT-solver requires only half the number of modes needed for the conventional T-solver.

Figure 7.6 presents the reason for the superiority of the ΔT-solver. Both cases have the same global error accuracy, less than 10^{-4}. However, for the ΔT-solver, the final generalized temperature solution includes half the number of modes for each time step compared to the conventional T-solver. This is advantageous because the generalized temperature solution will move to the right-hand side for the coupled HM

case and will be multiplied by some separated tensor. Therefore, having fewer modes for the generalized temperature solution and the same accuracy makes it logical to use this technique as a solution for the thermal aspect.

For the case of the coupled HM equations, the Δ-solver was tried, which resulted in a rapid increase in the number of modes. It took almost five days to solve a single time step. It is challenging to capture the first shock in the transient case for the coupled HM aspects, and a more robust method is required to deal with it effectively. However, even for the time step, which is equivalent to 2 year, the Δ-solver implemented and did not show any efficiency concerning the coupled HM case.

7.4 Previous time step as starting point for PGD linear solver

The PGD toolbox provides a valuable capability to restart a solution by utilizing a separated tensor as an initial point. In the context of the coupled HM aspect, the separated output data in time has been employed as a starting point for the PGD linear solver. However, utilizing this initial point proves to be inefficient during the early time steps due to the presence of abrupt changes in the transient part, commonly referred to as "shock". Moreover, utilizing such an initial point may even lead to an increase in the number of modes required to accurately represent the problem.

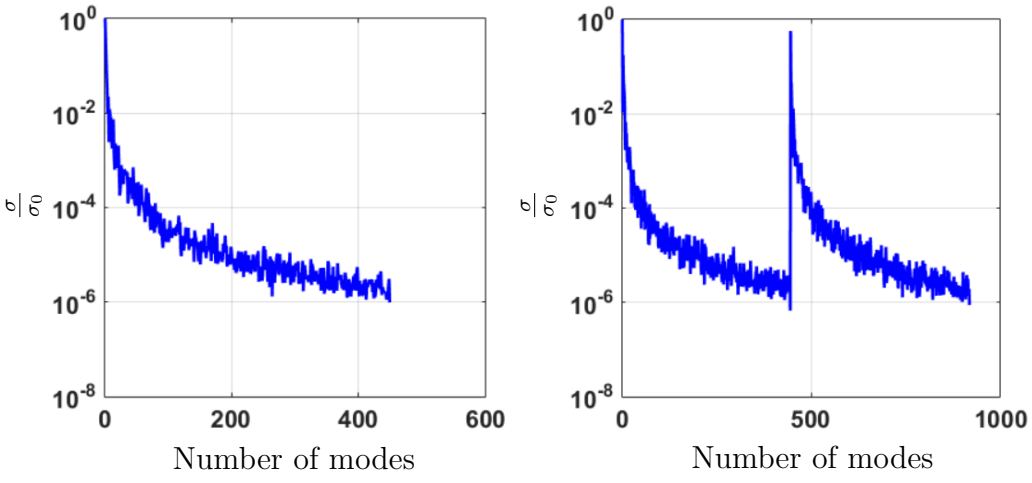

Figure 7.7: (A) Mode amplitude decrease without an initial point. (B) Use of the previous time step.

During a transient "shock", the previous time steps were employed, as shown in Figure 7.7. At the third time step, we utilized the second time step as the initial point. It is evident that the solution starts from zero and experiences multiplication by the number of modes. However, this approach proves to be ineffective, resulting in the same computational cost. The substantial increase in the number of modes significantly impacts the PGD calculation as it progresses to the subsequent time step on the right-hand side. This effect stems from the multiplication of terms between the known fields and separated stiffness matrices.

To illustrate this point, Figure 7.7 showcases two different cases. The left plot demonstrates the decrease in enrichment tolerance versus the number of modes for the third time step (0.05 year) without utilizing any information from the previous time step (no initial point). Conversely, the right plot represents the utilization of information from the previous time step (i.e., the solution of time step number two (0.03 year)) as an initial point for time step number three. This comparison highlights the inefficiency of employing the previous time step as an initial point, leading to an increase in computational cost by at least two times for the initial part of the problem.

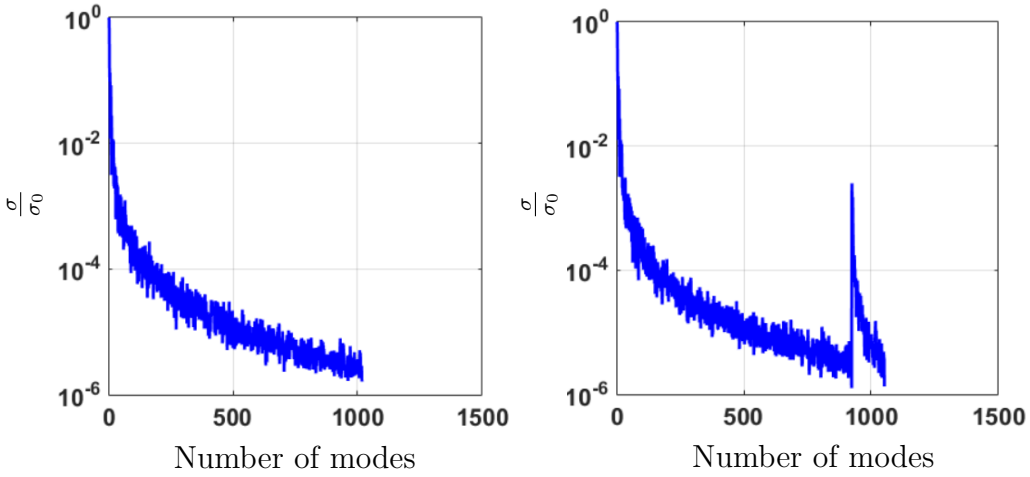

(A) (B)

Figure 7.8: After 63-time steps, which is equivalent to 1.8 year, the previous time step was utilized as the initial point for the current time step. As shown in (A), without using the previous time steps, the number of modes that need to be computed is much larger than the number with the usage of previous time steps (B).

Figure 7.8 presents the relationship between amplitude and the number of modes after 63 time steps, equivalent to an elapsed time of 1.8 years. Achieving high accuracy

requires a fine enrichment tolerance of 10^{-6} for the four parameters, resulting in a substantial computational time. The results extend up to time step 63, utilizing information from the previous time steps, particularly time step 62. Notably, Figure 7.8-B demonstrates that adding just a few terms can achieve the desired accuracy, reducing computational time to approximately four days. However, incorporating the previous solution as an initial point after a shock introduces the accumulation of modes, necessitating PGD compression. Unfortunately, the current functionality of PGD compression proves to be suboptimal and inefficient, as discussed in Section 7.2, with no significant improvements in efficiency observed when applied to the accumulated results.

The main reason for the presence of jumps in Figures 7.7 and 7.8 is that, in the first case, the results undergo abrupt changes, and the initial values are not suitable for the PGD method. Consequently, the solution starts from zero and accumulates all the initial guesses. In the second case, although it is still in a transient "shock" process, it shows a slightly improved behavior compared to the first figure, resulting in a smaller jump.

Chapter 8

Conclusions and future work

The Proper Generalized Decomposition (PGD) is a mathematical framework belonging to the class of Model Order Reduction (MOR) techniques. Despite its proven efficiency, there is a research gap in exploring its application to transient coupled Thermo-Hydro-Mechanical (THM) problems in porous media. This thesis seeks to address this gap by investigating the application of PGD in THM problems, with a focus on providing real-time solutions. Drawing inspiration from the concept of deep geological repositories, this work studies the potential of the PGD methodology in solving THM problems in a simplified deep geological repository. In this chapter, a summary of the contributions made throughout this work will be presented, followed by a summary of the conclusions and recommendations, all in bullet points. Additionally, future work related to this topic will be discussed at the end.

8.1 Summary of the contributions

The methodology for defining separated operators required for THM problems was thoroughly investigated and applied as input for the PGD methodology. The effectiveness of this concept was confirmed through a benchmark problem. The PGD methodology was then applied to a simplified model of an engineered barrier system, followed by an investigation of the impact of various parameters on the quality of results. This investigation explored the application of PGD to problems involving three material parameters and one geometric parameter, which were considered extra

dimensions in this work. The main contributions of this work can be classified into three principal aspects.

8.1.1 Separable operators and time integration of THM for PGD

As discussed in this thesis, the use of separated representations is the fundamental concept behind the PGD technique. One of the significant contributions of this work, presented in Chapter 4, is the introduction of separable operators for THM problems. This approach is novel in that it considers the transient and coupled nature of the THM problem and parametrizes it based on three material parameters, namely heat and hydraulic conductivity, elastic modulus, and one geometrical parameter, which represents a variation of the spatial domain size in the radial direction.

This thesis presents the separated exact representations of high-dimensional tensors and vectors for the three material parameters in THM. Furthermore, it provides an explanation of how the geometrical parameter has been dealt with by demonstrating the use of the Jacobian and the approximated representation through an approximation series as defined in Equation (4.34). All the detailed information about the separated tensors and vectors for problems involving the three material parameters only, the geometrical parameter only, and all four parameters can be found in Appendix A. This comprehensive analysis and demonstration of the separated representations will contribute significantly to the parametrization of THM problems and their solutions.

In Chapter 4, the approach for achieving the time integration within the PGD methodology is presented. Rather than considering time as an extra dimension, the PGD problem is solved at each time step. The systematic procedure of seeking the generalized solution of parametric THM is illustrated in Figure 4.2.

8.1.2 The validation of methodology

In Chapter 5, validation has been conducted for applying the PGD methodology to the transient THM problem. To validate this methodology, an analytical solution from the work of Selvadurai and Suvorov [129] was used as a benchmark. In this benchmark, all four parameters were considered as extra dimensions, and the solution was stored at each time step in two separated tensors, one for the thermal problem

and one for the hydro-mechanical problem, taking benefit from the one-way coupling in the problem. Although the solution was stored as separate tensors, it can be conceptually expressed as a 6th-order tensor (space + time + 4 parameters).

To validate the results, three quantifications of errors were defined. The first concept was the global error, defined in Equation (5.19), which involved local errors integrating over the complete 6-dimensional hypercube, making it computationally demanding. An approximation of the global error was presented to overcome this challenge. The second error assessed for validation was the integration of error only over spatial and parametric space, with the error in time being a one-dimensional function, as defined in Equation (5.20). Finally, the third error was the integration of error over space only, as defined in Equation (5.21). This error allowed for observing the behavior of the methodology in the entire parametric space and time interval.

The results presented show that the separable operators and time integration applied for the methodology are working correctly. The validation confirms the reliability and accuracy of the PGD methodology, demonstrating its applicability.

8.1.3 Exploring PGD on a simplified model of engineered barrier system

In Chapter 6, two problems were examined through the presentation of a simplified model of an engineered barrier system. The first problem considered three material parameters, heat and hydraulic conductivity of the rock and the elastic modulus of the rock, as extra dimensions. The second problem considered only a geometric parameter, allowing for varying the distance between two canisters as an extra dimension. The accuracy and efficiency of these problems were evaluated and presented.

The results showed that the generalized solutions to these problems were accurate, and a discussion about the efficiency of the PGD implementation was initiated by presenting the break-even point as from which PGD becomes beneficial for repeated solutions of parametric problems. The discussion also explored the potential applications of the generalized solution, which enables rapid evaluations (real-time solution), making it possible for users to perform tasks systematically in the frame of inverse identification procedures.

In Chapter 7, a discussion was provided to assess the effect of different PGD methodology parameters. Four different stopping criteria for the PGD methodology have been studied and investigated. It is presented that for the four-parameters case,

if the accuracy in the whole parametric, spatial, and time spaces are required (small local errors), stronger enrichment tolerance is necessary. However, it is also shown that the code can be modified based on the choice of a proper system of units enforcing that the output fields of the PGD linear solver are scaled in a way that their value has the same or close orders of magnitude. These studies arise from the fact that the problem is coupled, and for the PGD linear solver to deal with the difference in the order of magnitude of the output, it should have smaller enrichment tolerances or similar or close orders of magnitude for the considered quantities.

It was shown that by considering $\eta_{\text{tol}} = 5.5 \times 10^{-6}$ and a fixed number of iterations in the fixed point iteration process, which is 10 for fixed-point iteration, an accurate result is obtained. This result shows that if the designer is looking for global error, this problem for the four-parameter case is very accurate. However, some spots in the output are detected where the errors are localized in some spatial, time, or parametric space. For this reason, to have a more comprehensive perspective, color-coded error map plots were presented in Figure 7.2, based on the definition of the error in Chapter 5, in Equation 5.21.

These plots show that the pressure is accurate in the whole domain of time and parametric space. However, in 95 percent of the whole parametric space and time interval, the displacement is very accurate, while for 5 percent of this space, the error level exceeds 2 percent. As discussed previously, this problem may be considered accurate because it is very localized depending on the envisioned application.

In Chapter 7, various discussions concerning the four-parameter case have been presented to boost efficiency. However, after testing various configurations for PGD compression and also using information from the previous time steps in the time integration, it has been observed that currently, they do not help solving the problem faster and provide more accurate results efficiently.

Nevertheless, the Δ-solver technique has been found to be beneficial for the thermal part of the problem, even if not suitable for the hydro-mechanical part.

8.2 Conclusions and recommendations

This section serves as a reflective overview, offering insights into the significant findings and experiences acquired during this research endeavor. It encompasses both achievements and failures encountered along the way, providing lessons for future

prospects. Additionally, recommendations for further exploration and potential avenues of improvement will be discussed:

- In the context of multiphysical problems like coupled THM, it is advisable to use units that ensure the output fields are of similar orders of magnitude. This allows PGD to determine the appropriate enrichment tolerance for all the fields collectively, resulting in a more efficient and accurate process.

- In the context of the PGD technique, the application of which is problem-dependent, it is recommended to explore adjustments in tolerance settings, including the PGD enrichment tolerance and the fixed number of fixed-point iterations. This research revealed that reducing the fixed number of fixed-point iterations from 200 to 5 maintained the same level of accuracy while significantly improving efficiency and reducing computation time from one month to three days.

- The study of the four-parameter case in a simplified engineered barrier system highlighted the increased complexity introduced by the inclusion of intrusive parameters, such as the geometric parameter. It became evident that addressing this parameter was not as straightforward as in other cases, posing additional challenges in the analysis.

- During the research, it was observed that adding an extra dimension to the problem significantly increased the computational cost. On average, for one parameter, the computation time was approximately half day to 3 days, for two parameters (different parameter combinations) it extended to one week, for three parameters (different parameter combinations) it ranged from 12 to 30 days, and for the four-parameter case, obtaining accurate results from a global perspective required at least 100 days. This demonstrates the substantial impact of increasing dimensionality on the efficiency of the PGD technique.

8.3 Future work

In future work, it is recommended to further investigate the main assumptions presented in this thesis as a reference for analyzing THM problems in the context of

deep geological repositories. The current study encompasses several assumptions, including full saturation, consideration of quasi-static processes, and assuming thermo-poroelastic behavior. Furthermore, the model assumes axisymmetry and disregards excavation effects, assuming intact rock.

To begin, building upon the current study, it is advisable to progress from linear to nonlinear analysis, incorporating material nonlinearity and partial saturation. Subsequently, exploring the implementation of excavation concepts would be valuable. However, to develop a model that better represents a deep geological repository, more complex concepts and investigations are necessary.

Additionally, based on recommendations from the literature review, utilizing bilinear quadrilateral elements for temperature and pressure fields, and quadratic quadrilateral elements for displacement, would ensure compliance with inf-sup conditions. Therefore, modifying the current work to incorporate these aspects is also recommended.

In summary, the following future works are suggested as the next steps for further research and outlooks:

- The first step towards the modification is to improve the meshing by transitioning from bilinear quadrilateral elements to quadratic quadrilateral elements for the mechanical field. This transition ensures that the inf-sup conditions are satisfied for all the problems where this concept is applied.

- The deep geological repository problem is phased and involves an excavation before the stage of HLW. Obviously, to consider a more realistic scenario, the effect of the excavation damage zone should be considered. Therefore, studying the excavation damage zone can be viewed as another outlook to improve the reference of the analysis.

- To extend the applicability of the analysis to repository applications, studying the problem in a nonlinear format by incorporating partial saturation and material nonlinearity, including accounting for the swelling aspect of bentonite, would be necessary.

- The next step is to extend the spatial dimensionality from 2D axisymmetric to 3D, which brings us closer to reality. By considering the real geometry of the backfill, we can capture the intricacies and complexities of the current system.

This enhancement allows for a more accurate representation of the physical processes and interactions occurring within the system.

Appendix A

Separated operators for PGD

It is important to note that the separated tensors and vectors discussed in this appendix pertain to the more general case presented in the thesis. The thesis focuses on a simplified engineered barrier system, with its corresponding equations, as well as the separated tensors and vectors, briefly introduced in Chapter 4. Three specific problems related to this system have been analyzed and discussed in Chapter 6 and Chapter 7. The first problem involves three material parameters serving as external dimensions: heat conductivity (μ_κ), hydraulic conductivity (μ_K), and elastic modulus (μ_E). The second problem considers a single geometric parameter as an extra dimension, which is the spacing between canisters. Finally, the third problem involves all four parameters as additional dimensions. This appendix provides a detailed presentation of the separated tensors and vectors used as input data for the encapsulated PGD in three sections: Section A.1 presents the details for the three material parameters only, Section A.2 focuses on the geometric parameter only, and Section A.3 covers the separated tensors and vectors for all four parameters as extra dimensions.

A.1 Material parameters

In Chapter 4, Subsection 4.3.1, the separable operators for material parameters are briefly introduced. The details of Equations (4.15) to 4.18 are provided here. It is important to emphasize that in Equations (4.15) to (4.17), the superscript i represents the time slice i. For example, for time slice $i = 571$, the separated tensor for the

global stiffness matrix, denoted as Equation (4.15), is as follows:

$$\mathbf{K}_{\mathbf{G}}^{571}(\mu_K, \mu_E) = \mathbf{K}_{\mathbf{G}}^{571\,0} + \mathbf{K}_{\mathbf{G}}^{571\,1}\,\mu_K + \mathbf{K}_{\mathbf{G}}^{571\,2}\,\mu_E + \mathbf{K}_{\mathbf{G}}^{571\,3}\,\frac{1}{\mu_E}.$$

Therefore, the global stiffness matrix for time slice 571, denoted as $\mathbf{K}_{\mathbf{G}}^{571}(\mu_K, \mu_E)$, is separated into four terms. Now, in a more general aspect which also is presented in Equation (4.15) defines it as follows:

$$\mathbf{K}_{\mathbf{G}}^{i}(\mu_K, \mu_E) = \mathbf{K}_{\mathbf{G}}^{i\ 0} + \mathbf{K}_{\mathbf{G}}^{i\ 1}\,\mu_K + \mathbf{K}_{\mathbf{G}}^{i\ 2}\,\mu_E + \mathbf{K}_{\mathbf{G}}^{i\ 3}\,\frac{1}{\mu_E},$$

the definition of the components are as follows:

$$\mathbf{K}_{\mathbf{G}}^{i\ 0} = \begin{bmatrix} \mathbf{M}_{\mathrm{p}}^{0} + \theta\Delta t^{i}\,\mathbf{K}_{\mathrm{p}}^{0} & \mathbf{G}_{\mathrm{pd}} \\ \theta\mathbf{G}_{\mathrm{dp}} & \theta\mathbf{K}_{\mathrm{d}}^{0} \end{bmatrix}, \tag{A.1}$$

$$\mathbf{K}_{\mathbf{G}}^{i\ 1} = \begin{bmatrix} \theta\Delta t^{i}\,\mathbf{K}_{\mathrm{p}}^{1} & \mathbf{0} \\ \mathbf{0} & \mathbf{0} \end{bmatrix}, \tag{A.2}$$

$$\mathbf{K}_{\mathbf{G}}^{i\ 2} = \begin{bmatrix} \mathbf{0} & \mathbf{0} \\ \mathbf{0} & \theta\mathbf{K}_{\mathrm{d}}^{1} \end{bmatrix}, \tag{A.3}$$

$$\mathbf{K}_{\mathbf{G}}^{i\ 3} = \begin{bmatrix} \mathbf{M}_{\mathrm{p}}^{1} & \mathbf{0} \\ \mathbf{0} & \mathbf{0} \end{bmatrix}. \tag{A.4}$$

Just a reminder, in all the equations mentioned above and throughout the thesis, it should be noted that Δt^i represents the time step for time slice i. For $\mathbf{K}_{\mathbf{G}}^{i*}$ in Equation (4.16), it exhibits similarity to Equations (A.1) to (A.4). However, for pedagogical purposes, let us present it here once more. Instead of using *thera* in Equations (A.1) to (A.4), we should employ $(\theta - 1)$. Therefore, the separated components are as follows:

$$\mathbf{K}_{\mathbf{G}}^{i*0} = \begin{bmatrix} \mathbf{M}_{\mathrm{p}}^{0} + (\theta-1)\Delta t^{i}\,\mathbf{K}_{\mathrm{p}}^{0} & \mathbf{G}_{\mathrm{pd}} \\ (\theta-1)\mathbf{G}_{\mathrm{dp}} & (\theta-1)\mathbf{K}_{\mathrm{d}}^{0} \end{bmatrix}, \tag{A.5}$$

$$\mathbf{K}_{\mathbf{G}}^{i*1} = \begin{bmatrix} (\theta-1)\Delta t^{i}\,\mathbf{K}_{\mathrm{p}}^{1} & \mathbf{0} \\ \mathbf{0} & \mathbf{0} \end{bmatrix}, \tag{A.6}$$

$$\mathbf{K}_{\mathbf{G}}^{i*2} = \begin{bmatrix} \mathbf{0} & \mathbf{0} \\ \mathbf{0} & (\theta-1)\mathbf{K}_{\mathrm{d}}^{1} \end{bmatrix}, \tag{A.7}$$

$$\mathbf{K}_{\mathbf{G}}^{i*^3} = \begin{bmatrix} \mathbf{M}_{\mathrm{p}}^1 & \mathbf{0} \\ \mathbf{0} & \mathbf{0} \end{bmatrix}. \tag{A.8}$$

The components of the separated vectors for Equation (4.17) are as follows:

$$\mathbf{F}_*^{i\ 0} = \begin{bmatrix} \Delta t^i\, \mathbf{f}_{\mathbf{b}_{\mathrm{f}}}^0 \\ \mathbf{f}_{\mathrm{d}} \end{bmatrix}, \tag{A.9}$$

$$\mathbf{F}_*^{i\ 1} = \begin{bmatrix} \Delta t^i\, \mathbf{f}_{\mathbf{b}_{\mathrm{f}}}^1 \\ \mathbf{0} \end{bmatrix}. \tag{A.10}$$

Finally, the components of the separated tensor corresponding to Equation (4.18) are as follows:

$$\mathbf{G}_{\mathbf{T}}^0 = \begin{bmatrix} \mathbf{M}_{\mathrm{pT}} & -\mathbf{M}_{\mathrm{pT}} \\ -\theta\mathbf{G}_{\mathrm{dT}}^0 & (\theta-1)\mathbf{G}_{\mathrm{dT}}^0 \end{bmatrix}, \tag{A.11}$$

$$\mathbf{G}_{\mathbf{T}}^1 = \begin{bmatrix} \mathbf{0} & \mathbf{0} \\ -\theta\mathbf{G}_{\mathrm{dT}}^1 & (\theta-1)\mathbf{G}_{\mathrm{dT}}^1 \end{bmatrix}. \tag{A.12}$$

In Equations (A.1) to (A.12), the definitions of $\mathbf{M}_{\mathrm{pT}}$, $\mathbf{G}_{\mathrm{pd}}$, $\mathbf{G}_{\mathrm{dp}}$, and $\mathbf{f}_{\mathrm{d}}$ are similar to the ones in Chapter 2, which are Equations (2.24), (2.27), (2.30), and (2.33), respectively. The remaining components are defined as follows:

$$\mathbf{K}_{\mathrm{p}}^0 = \int_{\Omega\setminus\Omega_{\mathrm{R}}} \mathbf{B}_{\mathrm{p}}^\top \frac{K}{\rho_f g}\mathbf{B}_{\mathrm{p}}\, rd\Omega, \tag{A.13}$$

$$\mathbf{K}_{\mathrm{p}}^1 = \int_{\Omega_{\mathrm{R}}} \mathbf{B}_{\mathrm{p}}^\top \frac{1}{\rho_f g}\mathbf{B}_{\mathrm{p}}\, rd\Omega, \tag{A.14}$$

$$\mathbf{K}_{\mathrm{d}}^0 = \int_{\Omega\setminus\Omega_{\mathrm{R}}} \mathbf{B}_{\mathrm{d}}^\top \mathbb{C}(E,\nu)\mathbf{B}_{\mathrm{d}}\, rd\Omega, \tag{A.15}$$

$$\mathbf{K}_{\mathrm{d}}^1 = \int_{\Omega_{\mathrm{R}}} \mathbf{B}_{\mathrm{d}}^\top \mathbb{C}(1,\nu)\mathbf{B}_{\mathrm{d}}\, rd\Omega, \tag{A.16}$$

$$\mathbf{M}_{\mathrm{p}}^0 = \int_{\Omega\setminus\Omega_{\mathrm{R}}} \mathbf{N}_{\mathrm{p}}^\top \frac{(\alpha-\phi)(1-\alpha)(1-2\nu)}{E}\mathbf{N}_{\mathrm{p}}\, rd\Omega + \int_{\Omega} \mathbf{N}_{\mathrm{p}}^\top \frac{\phi}{K_f}\mathbf{N}_{\mathrm{p}}\, rd\Omega, \tag{A.17}$$

$$\mathbf{M}_{\mathrm{p}}^1 = \int_{\Omega_{\mathrm{R}}} \mathbf{N}_{\mathrm{p}}^\top (\alpha-\phi)(1-\alpha)(1-2\nu)\mathbf{N}_{\mathrm{p}}\, rd\Omega, \tag{A.18}$$

$$\mathbf{f}_{\mathbf{b}_{\mathrm{f}}}^0 = \int_{\Omega\setminus\Omega_{\mathrm{R}}} \mathbf{N}_{\mathrm{p}}^\top \frac{K}{\rho_f g}\rho_f \mathbf{g}\, rd\Omega, \tag{A.19}$$

$$\mathbf{f}_{\mathbf{b}_{\mathrm{f}}}^1 = \int_{\Omega_{\mathrm{R}}} \mathbf{N}_{\mathrm{p}}^\top \frac{1}{\rho_f g}\rho_f \mathbf{g}\, rd\Omega, \tag{A.20}$$

$$\mathbf{G}^0_{\mathrm{dT}} = \int_{\Omega\setminus\Omega_{\mathrm{R}}} \mathbf{N}^\top_{\mathrm{d}} \frac{E}{1-2\nu}\alpha_s \mathbf{B}_{\mathrm{T}}\, r d\Omega, \tag{A.21}$$

$$\mathbf{G}^1_{\mathrm{dT}} = \int_{\Omega_{\mathrm{R}}} \mathbf{N}^\top_{\mathrm{d}} \frac{1}{1-2\nu}\alpha_s \mathbf{B}_{\mathrm{T}}\, r d\Omega. \tag{A.22}$$

In the equations, $\Omega = \Omega_{\mathrm{R}} \cup \Omega_{\mathrm{B}} \cup \Omega_{\mathrm{Bf}} \cup \Omega_{\mathrm{C}}$, the terms Ω_{R}, Ω_{B}, Ω_{Bf}, and Ω_{C} represent the spatial domains of the rock, buffer, backfill, and canister, respectively. Additionally, $\Omega \setminus \Omega_{\mathrm{R}}$ is defined as $\Omega_{\mathrm{B}} \cup \Omega_{\mathrm{Bf}} \cup \Omega_{\mathrm{C}}$, indicating the entire spatial domain except for the rock.

A.2 Geometric parameter

This section presents only the components of the separated tensors and vectors that correspond to the geometric parameter as the sole additional dimension. These components are derived from Chapter 4, specifically in Subsection 4.3.2. For the geometric parameter, the domain is divided into two regions: Ω_1, which remains fixed, and Ω_2, which varies based on the geometric parameter. This concept is illustrated in Figure 4.1.

The separated tensor for the thermal part, denoted as $\mathbf{K}_{\mathrm{T}}$, is explained in detail in Chapter 4. The separation of $\mathbf{K}_{\mathrm{T}}$ is presented in Equation (4.26). As for the remaining components of the thermal part, their definitions are as follows:

$$\mathbf{M}^0_{\mathrm{T}} = \int_{\Omega_1} \mathbf{N}^\top_{\mathrm{T}}((1-\phi)\rho_s c_s + \phi\rho_f c_f)\mathbf{N}_{\mathrm{T}} R d\Omega, \tag{A.23}$$

$$\mathbf{M}^1_{\mathrm{T}} = \int_{\Omega_2} \mathbf{N}^\top_{\mathrm{T}}((1-\phi)\rho_s c_s + \phi\rho_f c_f)\mathbf{N}_{\mathrm{T}} R d\Omega, \tag{A.24}$$

$$\mathbf{M}^2_{\mathrm{T}} = \int_{\Omega_2} \mathbf{N}^\top_{\mathrm{T}}((1-\phi)\rho_s c_s + \phi\rho_f c_f)\mathbf{N}_{\mathrm{T}} d\Omega. \tag{A.25}$$

The Hydro-Mechanical (HM) part comprises various components of tensors and vectors, which are presented in Chapter 4 in Equation (4.7). These components are defined in terms of separated tensors and vectors in Subsection 4.3.2. The components of the separated tensors and vectors are as follows, as described in Equations (4.28) to (4.33) and Equations (4.37) to (4.39):

$$\mathbf{M}^0_{\mathrm{pT}} = \int_{\Omega_1} \mathbf{N}^\top_{\mathrm{p}}(3\phi\alpha_f + 3(\alpha-\phi)\alpha_s)\mathbf{N}_{\mathrm{T}} R d\Omega, \tag{A.26}$$

$$\mathbf{M}^1_{\mathrm{pT}} = \int_{\Omega_2} \mathbf{N}^\top_{\mathrm{pT}}(3\phi\alpha_f + 3(\alpha-\phi)\alpha_s)\mathbf{N}_{\mathrm{T}} R d\Omega, \tag{A.27}$$

$$\mathbf{M}^2_{\mathrm{pT}} = \int_{\Omega_2} \mathbf{N}^\top_{\mathrm{pT}}(3\phi\alpha_f + 3(\alpha-\phi)\alpha_s)\mathbf{N}_{\mathrm{T}} d\Omega, \tag{A.28}$$

$$\mathbf{M}^0_{\mathrm{p}} = \int_{\Omega_1} \mathbf{N}^\top_{\mathrm{p}}(\frac{\phi}{K_f} + \frac{\alpha-\phi}{K_s})\mathbf{N}_{\mathrm{p}} R d\Omega, \tag{A.29}$$

$$\mathbf{M}^1_{\mathrm{p}} = \int_{\Omega_2} \mathbf{N}^\top_{\mathrm{pT}}(\frac{\phi}{K_f} + \frac{\alpha-\phi}{K_s})\mathbf{N}_{\mathrm{p}} R d\Omega, \tag{A.30}$$

$$\mathbf{M}^2_{\mathrm{p}} = \int_{\Omega_2} \mathbf{N}^\top_{\mathrm{p}}(\frac{\phi}{K_f} + \frac{\alpha-\phi}{K_s})\mathbf{N}_{\mathrm{p}} d\Omega, \tag{A.31}$$

$$\mathbf{K}^0_{\mathrm{p}} = \int_{\Omega_1} \mathbf{B}^\top_{\mathrm{p}} K \mathbf{B}_{\mathrm{p}} R d\Omega + \int_{\Omega_2} \mathbf{B}^\top_{\mathrm{p}} K \begin{bmatrix} 1 & 0 \\ 0 & 0 \end{bmatrix} \mathbf{B}_{\mathrm{p}} R d\Omega, \tag{A.32}$$

$$\mathbf{K}^1_{\mathrm{p}} = \int_{\Omega_2} \mathbf{B}^\top_{\mathrm{p}} K \begin{bmatrix} 0 & 0 \\ 0 & 1 \end{bmatrix} \mathbf{B}_{\mathrm{p}} R d\Omega, \tag{A.33}$$

$$\mathbf{K}^2_{\mathrm{p}} = \int_{\Omega_2} \mathbf{B}^\top_{\mathrm{p}} K \begin{bmatrix} 1 & 0 \\ 0 & 0 \end{bmatrix} \mathbf{B}_{\mathrm{p}} d\Omega, \tag{A.34}$$

$$\mathbf{K}^3_{\mathrm{p}} = \int_{\Omega_2} \mathbf{B}^\top_{\mathrm{p}} K \begin{bmatrix} 0 & 0 \\ 0 & 1 \end{bmatrix} \mathbf{B}_{\mathrm{p}} d\Omega, \tag{A.35}$$

$$\mathbf{G}^0_{\mathrm{dT}} = \int_{\Omega_1} \mathbf{N}^\top_{\mathrm{d}} 3K_D\alpha_s \mathbf{B}_{\mathrm{T}} R d\Omega, \tag{A.36}$$

$$\mathbf{G}^1_{\mathrm{dT}} = \int_{\Omega_2} \mathbf{N}^\top_{\mathrm{d}} 3K_D\alpha_s \begin{bmatrix} 1 & 0 \\ 0 & 0 \end{bmatrix} \mathbf{B}_{\mathrm{T}} R d\Omega, \tag{A.37}$$

$$\mathbf{G}^2_{\mathrm{dT}} = \int_{\Omega_2} \mathbf{N}^\top_{\mathrm{d}} 3K_D\alpha_s \begin{bmatrix} 0 & 0 \\ 0 & 1 \end{bmatrix} \mathbf{B}_{\mathrm{T}} R d\Omega, \tag{A.38}$$

$$\mathbf{G}^3_{\mathrm{dT}} = \int_\Omega \mathbf{N}^\top_{\mathrm{d}} 3K_D\alpha_s \begin{bmatrix} 1 & 0 \\ 0 & 0 \end{bmatrix} \mathbf{B}_{\mathrm{T}}\, d\Omega, \tag{A.39}$$

$$\mathbf{G}^4_{\mathrm{dT}} = \int_\Omega \mathbf{N}^\top_{\mathrm{d}} 3K_D\alpha_s \begin{bmatrix} 0 & 0 \\ 0 & 1 \end{bmatrix} \mathbf{B}_{\mathrm{T}}\, d\Omega, \tag{A.40}$$

$$\mathbf{G}^0_{\mathrm{dp}} = \int_{\Omega_1} \mathbf{N}^\top_{\mathrm{d}} \alpha \mathbf{B}_{\mathrm{p}} R d\Omega, \tag{A.41}$$

$$\mathbf{G}^1_{\mathrm{dp}} = \int_{\Omega_2} \mathbf{N}^\top_{\mathrm{d}} \alpha \begin{bmatrix} 1 & 0 \\ 0 & 0 \end{bmatrix} \mathbf{B}_{\mathrm{p}} R d\Omega, \tag{A.42}$$

$$\mathbf{G}^2_{\mathrm{dp}} = \int_{\Omega_2} \mathbf{N}^\top_{\mathrm{d}} \alpha \begin{bmatrix} 0 & 0 \\ 0 & 1 \end{bmatrix} \mathbf{B}_{\mathrm{p}} R d\Omega, \tag{A.43}$$

$$\mathbf{G}^3_{\mathrm{dp}} = \int_{\Omega_2} \mathbf{N}^\top_{\mathrm{d}} \alpha \begin{bmatrix} 1 & 0 \\ 0 & 0 \end{bmatrix} \mathbf{B}_{\mathrm{p}}\, d\Omega, \tag{A.44}$$

$$\mathbf{G}^4_{\mathrm{dp}} = \int_{\Omega_2} \mathbf{N}^\top_{\mathrm{d}} \alpha \begin{bmatrix} 0 & 0 \\ 0 & 1 \end{bmatrix} \mathbf{B}_{\mathrm{p}}\, d\Omega, \tag{A.45}$$

$$\mathbf{G}^0_{\mathrm{pd}} = \int_{\Omega_1} \mathbf{N}^\top_{\mathrm{p}} \alpha \mathbf{B}_{\mathrm{v}}\, R d\Omega, \tag{A.46}$$

$$\mathbf{G}^1_{\mathrm{pd}} = \int_{\Omega_2} \mathbf{N}^\top_{\mathrm{p}} \begin{bmatrix} \alpha & 0 \end{bmatrix} \frac{\partial \mathbf{N}_{\mathrm{d}}}{\partial R} R d\Omega + \int_{\Omega_2} \mathbf{N}^\top_{\mathrm{p}} \begin{bmatrix} \alpha & 0 \end{bmatrix} \mathbf{N}_{\mathrm{d}}\, d\Omega, \tag{A.47}$$

$$\mathbf{G}^2_{\mathrm{pd}} = \int_{\Omega_2} \mathbf{N}^\top_{\mathrm{p}} \begin{bmatrix} \alpha & 0 \end{bmatrix} \frac{\partial \mathbf{N}_{\mathrm{d}}}{\partial R}\, d\Omega, \tag{A.48}$$

$$\mathbf{G}^3_{\mathrm{pd}} = \int_{\Omega_2} \mathbf{N}^\top_{\mathrm{p}} \begin{bmatrix} 0 & \alpha \end{bmatrix} \frac{\partial \mathbf{N}_{\mathrm{d}}}{\partial Z} R d\Omega, \tag{A.49}$$

$$\mathbf{G}^4_{\mathrm{pd}} = \int_{\Omega_2} \mathbf{N}^\top_{\mathrm{p}} \begin{bmatrix} 0 & \alpha \end{bmatrix} \frac{\partial \mathbf{N}_{\mathrm{d}}}{\partial Z}\, d\Omega, \tag{A.50}$$

$$\mathbf{K}_{\mathrm{d}}^{0} = \int_{\Omega_1} \mathbf{B}_{\mathrm{d}}^{\top}\mathbf{C}_0(E,\nu)\mathbf{B}_{\mathrm{d}} R d\Omega + \int_{\Omega_2} \frac{\partial \mathbf{N}_{\mathrm{d}}^{\top}}{\partial R}\mathbf{C}_1(E,\nu)\frac{\partial \mathbf{N}_{\mathrm{d}}}{\partial R} R d\Omega + \int_{\Omega_2} \frac{\partial \mathbf{N}_{\mathrm{d}}^{\top}}{\partial R}\mathbf{C}_3(E,\nu)\mathbf{N}_{\mathrm{d}} d\Omega + \int_{\Omega_2} \mathbf{N}_{\mathrm{d}}^{\top}\mathbf{C}_7(E,\nu)\frac{\partial \mathbf{N}_{\mathrm{d}}}{\partial R} d\Omega, \tag{A.51}$$

$$\mathbf{K}_{\mathrm{d}}^{1} = \int_{\Omega_2} \frac{\partial \mathbf{N}_{\mathrm{d}}^{\top}}{\partial R}\mathbf{C}_2(E,\nu)\frac{\partial \mathbf{N}_{\mathrm{d}}}{\partial Z} R d\Omega + \int_{\Omega_2} \frac{\partial \mathbf{N}_{\mathrm{d}}^{\top}}{\partial Z}\mathbf{C}_4(E,\nu)\frac{\partial \mathbf{N}_{\mathrm{d}}}{\partial R} R d\Omega + \int_{\Omega_2} \frac{\partial \mathbf{N}_{\mathrm{d}}^{\top}}{\partial Z}\mathbf{C}_6(E,\nu)\mathbf{N}_{\mathrm{d}} d\Omega + \int_{\Omega_2} \mathbf{N}_{\mathrm{d}}^{\top}\mathbf{C}_8(E,\nu)\frac{\partial \mathbf{N}_{\mathrm{d}}}{\partial R} d\Omega + \int_{\Omega_2} \mathbf{N}_{\mathrm{d}}^{\top}\mathbf{C}_9(E,\nu)\mathbf{N}_{\mathrm{d}}\frac{1}{R} d\Omega, \tag{A.52}$$

$$\mathbf{K}_{\mathrm{d}}^{2} = \int_{\Omega_2} \frac{\partial \mathbf{N}_{\mathrm{d}}^{\top}}{\partial R}\mathbf{C}_2(E,\nu)\frac{\partial \mathbf{N}_{\mathrm{d}}}{\partial z} d\Omega + \int_{\Omega_2} \frac{\partial \mathbf{N}_{\mathrm{d}}^{\top}}{\partial Z}\mathbf{C}_4(E,\nu)\frac{\partial \mathbf{N}_{\mathrm{d}}}{\partial R} d\Omega, \tag{A.53}$$

$$\mathbf{K}_{\mathrm{d}}^{3} = \int_{\Omega_2} \frac{\partial \mathbf{N}_{\mathrm{d}}^{\top}}{\partial Z}\mathbf{C}_5(E,\nu)\frac{\partial \mathbf{N}_{\mathrm{d}}}{\partial Z} R d\Omega, \tag{A.54}$$

$$\mathbf{K}_{\mathrm{d}}^{4} = \int_{\Omega_2} \frac{\partial \mathbf{N}_{\mathrm{d}}^{\top}}{\partial Z}\mathbf{C}_5(E,\nu)\frac{\partial \mathbf{N}_{\mathrm{d}}}{\partial Z} d\Omega, \tag{A.55}$$

$$\mathbf{K}_{\mathrm{d}}^{5} = \int_{\Omega_2} \frac{\partial \mathbf{N}_{\mathrm{d}}^{\top}}{\partial R}\mathbf{C}_1(E,\nu)\frac{\partial \mathbf{N}_{\mathrm{d}}}{\partial R} d\Omega, \tag{A.56}$$

$$\mathbf{K}_{\mathrm{d}}^{6+n} = \int_{\Omega_2} \mathbf{N}_{\mathrm{d}}^{\top}\mathbf{C}_9(E,\nu)\mathbf{N}_{\mathrm{d}}(-1)^{n+1}\frac{(R-b_1)^{n+1}}{R^{n+2}} d\Omega. \tag{A.57}$$

In Equations (A.51) to (A.57), the terms $\mathbf{C}_0(E,\nu)$, $\mathbf{C}_1(E,\nu)$, $\mathbf{C}_2(E,\nu)$, $\mathbf{C}_3(E,\nu)$, $\mathbf{C}_4(E,\nu)$, $\mathbf{C}_5(E,\nu)$, $\mathbf{C}_6(E,\nu)$, $\mathbf{C}_7(E,\nu)$, $\mathbf{C}_8(E,\nu)$, and $\mathbf{C}_9(E,\nu)$ are defined as follows:

$$\mathbf{C}_0(E,\nu) = \frac{E}{(1+\nu)(1-2\nu)}\begin{bmatrix} 1-\nu & \nu & \nu & 0 \\ \nu & 1-\nu & \nu & 0 \\ \nu & \nu & 1-\nu & 0 \\ 0 & 0 & 0 & \frac{1}{2}(1-2\nu) \end{bmatrix}, \tag{A.58}$$

$$\mathbf{C}_1(E,\nu) = \frac{E}{(1+\nu)(1-2\nu)}\begin{bmatrix} 1-\nu & 0 \\ 0 & \frac{1}{2}(1-2\nu) \end{bmatrix}, \tag{A.59}$$

$$\mathbf{C}_2(E,\nu) = \frac{E}{(1+\nu)(1-2\nu)} \begin{bmatrix} 0 & \nu \\ \frac{1}{2}(1-2\nu) & 0 \end{bmatrix}, \tag{A.60}$$

$$\mathbf{C}_3(E,\nu) = \frac{E}{(1+\nu)(1-2\nu)} \begin{bmatrix} \nu & 0 \\ 0 & 0 \end{bmatrix}, \tag{A.61}$$

$$\mathbf{C}_4(E,\nu) = \frac{E}{(1+\nu)(1-2\nu)} \begin{bmatrix} 0 & \frac{1}{2}(1-2\nu) \\ \nu & 0 \end{bmatrix}, \tag{A.62}$$

$$\mathbf{C}_5(E,\nu) = \frac{E}{(1+\nu)(1-2\nu)} \begin{bmatrix} \frac{1}{2}(1-2\nu) & 0 \\ 0 & 1-\nu \end{bmatrix}, \tag{A.63}$$

$$\mathbf{C}_6(E,\nu) = \frac{E}{(1+\nu)(1-2\nu)} \begin{bmatrix} 0 & 0 \\ \nu & 0 \end{bmatrix}, \tag{A.64}$$

$$\mathbf{C}_7(E,\nu) = \frac{E}{(1+\nu)(1-2\nu)} \begin{bmatrix} \nu & 0 \\ 0 & 0 \end{bmatrix}, \tag{A.65}$$

$$\mathbf{C}_8(E,\nu) = \frac{E}{(1+\nu)(1-2\nu)} \begin{bmatrix} 0 & \nu \\ 0 & 0 \end{bmatrix}, \tag{A.66}$$

$$\mathbf{C}_9(E,\nu) = \frac{E}{(1+\nu)(1-2\nu)} \begin{bmatrix} 1-\nu & 0 \\ 0 & 0 \end{bmatrix}. \tag{A.67}$$

Finally, the components of the separated vectors, which are presented in Chapter 4, specifically in Subsection 4.3.2, and described in Equations (4.38) and (4.39), are as follows:

$$\mathbf{f}^0_{\mathbf{b}_f} = \int_{\Omega_1} \mathbf{B}_{\mathrm{p}}^{\top} \frac{K}{\rho_f g} \rho_f \mathbf{g} \; R d\Omega, \tag{A.68}$$

$$\mathbf{f}^1_{\mathbf{b}_f} = \int_{\Omega_2} \mathbf{B}_{\mathrm{p}}^{\top} \frac{K}{\rho_f g} \rho_f \mathbf{g} \begin{bmatrix} 1 & 0 \\ 0 & 0 \end{bmatrix} \; R d\Omega, \tag{A.69}$$

$$\mathbf{f}^2_{\mathbf{b}_f} = \int_{\Omega_2} \mathbf{B}_{\mathrm{p}}^{\top} \frac{K}{\rho_f g} \rho_f \mathbf{g} \begin{bmatrix} 0 & 0 \\ 0 & 1 \end{bmatrix} \, R d\Omega, \tag{A.70}$$

$$\mathbf{f}^3_{\mathbf{b}_f} = \int_{\Omega^2_R} \mathbf{B}_{\mathrm{p}}^{\top} \frac{K}{\rho_f g} \rho_f \mathbf{g} \begin{bmatrix} 1 & 0 \\ 0 & 0 \end{bmatrix} \, d\Omega, \tag{A.71}$$

$$\mathbf{f}^4_{\mathbf{b}_f} = \int_{\Omega_2} \mathbf{B}_{\mathrm{p}}^{\top} \frac{K}{\rho_f g} \rho_f \mathbf{g} \begin{bmatrix} 0 & 0 \\ 0 & 1 \end{bmatrix} \, d\Omega, \tag{A.72}$$

$$\mathbf{f}^0_{\mathbf{d}} = \int_{\Omega_1} \mathbf{N}_{\mathrm{d}}^{\top} \mathbf{b} \, R d\Omega + \int_{\Gamma_{\mathrm{t}_1}} \mathbf{N}_{\mathrm{d}}^{\top} \boldsymbol{\sigma} \, R d\Gamma, \tag{A.73}$$

$$\mathbf{f}^1_{\mathbf{d}} = \int_{\Omega_2} \mathbf{N}_{\mathrm{d}}^{\top} \mathbf{b} \, R d\Omega + \int_{\Gamma_{\mathrm{t}_2}} \mathbf{N}_{\mathrm{d}}^{\top} \boldsymbol{\sigma} \, R d\Gamma, \tag{A.74}$$

$$\mathbf{f}^2_{\mathbf{d}} = \int_{\Omega_2} \mathbf{N}_{\mathrm{d}}^{\top} \mathbf{b} \, d\Omega + \int_{\Gamma_{\mathrm{t}_2}} \mathbf{N}_{\mathrm{d}}^{\top} \boldsymbol{\sigma} \, d\Gamma. \tag{A.75}$$

In Equations (A.73) to (A.75), Γ_{t_1} represents the boundary condition on the top surface corresponding to Ω_1, while Γ_{t_2} represents the boundary condition on the top surface corresponding to Ω_2.

A.3 The four-parameter case

In this section, we will present matrices, tensors, and vectors, taking into account four parameters: three material parameters and one geometric parameter. These parameters act as external dimensions for the simplified engineered barrier system case. First, we will discuss the separated tensor of global terms related to the thermal aspect, as presented in Equation (4.10) (Chapter 4 in Section 4.2). The separated tensor representations for these terms are as follows:

$$\begin{aligned} \mathbf{K}^i_{\mathbf{GT}}(\mu_\kappa, \mu_L) =& \mathbf{K}^i_{\mathbf{GT}}{}^0 + \mathbf{K}^i_{\mathbf{GT}}{}^1 \mu_\kappa + \mathbf{K}^i_{\mathbf{GT}}{}^2 \gamma_1{}^2(\mu_L) + \mathbf{K}^i_{\mathbf{GT}}{}^3 \gamma_1(\mu_L)\gamma_2(\mu_L) + \\ & \mathbf{K}^i_{\mathbf{GT}}{}^4 \mu_\kappa \gamma_1{}^2(\mu_L) + \mathbf{K}^i_{\mathbf{GT}}{}^5 \mu_\kappa \frac{\gamma_2(\mu_L)}{\gamma_1(\mu_L)} + \mathbf{K}^i_{\mathbf{GT}}{}^6 \mu_\kappa \gamma_1(\mu_L)\gamma_2(\mu_L). \end{aligned} \tag{A.76}$$

The definitions of all the terms in Equation (A.76) are as follows:

$$\mathbf{K}^i_{\mathbf{GT}}{}^0 = \mathbf{M}^0_{\mathrm{T}} + \theta \Delta t^i \, \mathbf{K}^0_{\mathrm{T}}, \tag{A.77}$$

$$\mathbf{K}_{\mathbf{GT}}^{i}{}^{1} = \theta \Delta t^i \, \mathbf{K}_{\mathrm{T}}^{1}, \tag{A.78}$$

$$\mathbf{K}_{\mathbf{GT}}^{i}{}^{2} = \mathbf{M}_{\mathrm{T}}^{1}, \tag{A.79}$$

$$\mathbf{K}_{\mathbf{GT}}^{i}{}^{3} = \mathbf{M}_{\mathrm{T}}^{2}, \tag{A.80}$$

$$\mathbf{K}_{\mathbf{GT}}^{i}{}^{4} = \theta \Delta t^i \, \mathbf{K}_{\mathrm{T}}^{2}, \tag{A.81}$$

$$\mathbf{K}_{\mathbf{GT}}^{i}{}^{5} = \theta \Delta t^i \, \mathbf{K}_{\mathrm{T}}^{3}, \tag{A.82}$$

$$\mathbf{K}_{\mathbf{GT}}^{i}{}^{6} = \theta \Delta t^i \, \mathbf{K}_{\mathrm{T}}^{4}. \tag{A.83}$$

The expression $\mathbf{K}_{\mathbf{GT}}^{i*}$ is analogous to Equations (A.76) to (A.83), with the exception that the term θ is replaced by $(\theta-1)$ in their definitions. The components in Equations (A.77) to (A.83) are defined as follows:

$$\mathbf{K}_{\mathrm{T}} = \mathbf{K}_{\mathrm{T}}^{0} + \mathbf{K}_{\mathrm{T}}^{1}\mu_\kappa + \mathbf{K}_{\mathrm{T}}^{2}\mu_\kappa\gamma_1^2(\mu_L) + \mathbf{K}_{\mathrm{T}}^{3}\mu_\kappa\frac{\gamma_2(\mu_L)}{\gamma_1(\mu_L)} + \mathbf{K}_{\mathrm{T}}^{4}\mu_\kappa\gamma_1(\mu_L)\gamma_2(\mu_L), \tag{A.84}$$

$$\mathbf{K}_{\mathrm{T}}^{0} = \int_{\Omega\setminus\Omega_{\mathrm{R}}} \mathbf{B}_{\mathrm{T}}^{\top}\kappa\mathbf{B}_{\mathrm{T}} R d\Omega \tag{A.85}$$

$$\mathbf{K}_{\mathrm{T}}^{1} = \int_{\Omega_{\mathrm{R}}^{1}} \mathbf{B}_{\mathrm{T}}^{\top}\mathbf{B}_{\mathrm{T}} R d\Omega + \int_{\Omega_{\mathrm{R}}^{2}} \mathbf{B}_{\mathrm{T}}^{\top} \begin{bmatrix} 1 & 0 \\ 0 & 0 \end{bmatrix} \mathbf{B}_{\mathrm{T}} R d\Omega, \tag{A.86}$$

$$\mathbf{K}_{\mathrm{T}}^{2} = \int_{\Omega_{\mathrm{R}}^{2}} \mathbf{B}_{\mathrm{T}}^{\top} \begin{bmatrix} 0 & 0 \\ 0 & 1 \end{bmatrix} \mathbf{B}_{\mathrm{T}} R d\Omega, \tag{A.87}$$

$$\mathbf{K}_{\mathrm{T}}^{3} = \int_{\Omega_{\mathrm{R}}^{2}} \mathbf{B}_{\mathrm{T}}^{\top} \begin{bmatrix} 1 & 0 \\ 0 & 0 \end{bmatrix} \mathbf{B}_{\mathrm{T}} d\Omega, \tag{A.88}$$

$$\mathbf{K}_{\mathrm{T}}^{4} = \int_{\Omega_{\mathrm{R}}^{2}} \mathbf{B}_{\mathrm{T}}^{\top} \begin{bmatrix} 0 & 0 \\ 0 & 1 \end{bmatrix} \mathbf{B}_{\mathrm{T}} d\Omega. \tag{A.89}$$

Upon observation, it can be noted that Equations (A.86) to (A.89) encompass two terms related to the spatial domain of rock, specifically labeled as Ω_{R}^1 and Ω_{R}^2. These terms respectively represent the fixed spatial domain of rock in Ω_1 and the spatial domain of rock in Ω_2. In the context of the equations, the spatial domain of rock in Ω_2 undergoes mapping transformations akin to those depicted in Figure 4.2, which cause elongation or shortening of the domain based on the geometric parameter. Essentially, the overall spatial domain of rock, denoted as Ω_{R}, can be defined as the union of Ω_{R}^1 and Ω_{R}^2, thereby forming $\Omega_{\mathrm{R}} = \Omega_{\mathrm{R}}^1 \cup \Omega_{\mathrm{R}}^2$. It should also be noted that in Equations (A.77), (A.79), and (A.77), the terms $\mathbf{M}_{\mathrm{T}}^0$, $\mathbf{M}_{\mathrm{T}}^1$, and $\mathbf{M}_{\mathrm{T}}^2$ bear similarity to those in Equations (A.23), (A.24), and (A.25) respectively.

The global stiffness matrix of the hydro-mechanical part, as presented in Chapter 4 in Section 4.2 by Equation (4.11), can be separated into the following tensor components:

$$
\begin{aligned}
\mathbf{K}_{\mathbf{G}}^{i}(\boldsymbol{\mu}) =& \mathbf{K}_{\mathbf{G}}^{i\ 0} + \mathbf{K}_{\mathbf{G}}^{i\ 1}\gamma_1(\mu_L) + \mathbf{K}_{\mathbf{G}}^{i\ 2}\gamma_2(\mu_L) + \mathbf{K}_{\mathbf{G}}^{i\ 3}{\gamma_1}^2(\mu_L) + \\
& \mathbf{K}_{\mathbf{G}}^{i\ 4}\gamma_1(\mu_L)\gamma_2(\mu_L) + \mathbf{K}_{\mathbf{G}}^{i\ 5}\mu_E(\frac{\mu_L}{b_2})\gamma_1(\mu_L) + \\
& \mathbf{K}_{\mathbf{G}}^{i\ 6}\mu_E(\frac{\mu_L}{b_2})^2\gamma_1(\mu_L) + \mathbf{K}_{\mathbf{G}}^{i\ 7}\mu_E(\frac{\mu_L}{b_2})^3\gamma_1(\mu_L) + \\
& \mathbf{K}_{\mathbf{G}}^{i\ 8}\mu_E(\frac{\mu_L}{b_2})^4\gamma_1(\mu_L) + \mathbf{K}_{\mathbf{G}}^{i\ 9}\mu_E(\frac{\mu_L}{b_2})^5\gamma_1(\mu_L) + \\
& \mathbf{K}_{\mathbf{G}}^{i\ 10}\mu_E(\frac{\mu_L}{b_2})^6\gamma_1(\mu_L) + \\
& \mathbf{K}_{\mathbf{G}}^{i\ 11}\mu_K + \mathbf{K}_{\mathbf{G}}^{i\ 12}\mu_K{\gamma_1}^2(\mu_L) + \mathbf{K}_{\mathbf{G}}^{i\ 13}\mu_K\frac{\gamma_2(\mu_L)}{\gamma_1(\mu_L)} + \\
& \mathbf{K}_{\mathbf{G}}^{i\ 14}\mu_K\gamma_1(\mu_L)\gamma_2(\mu_L) + \mathbf{K}_{\mathbf{G}}^{i\ 15}\mu_E + \\
& \mathbf{K}_{\mathbf{G}}^{i\ 16}\mu_E\gamma_1(\mu_L) + \mathbf{K}_{\mathbf{G}}^{i\ 17}\mu_E\gamma_2(\mu_L) + \mathbf{K}_{\mathbf{G}}^{i\ 18}\mu_E{\gamma_1}^2(\mu_L) + \\
& \mathbf{K}_{\mathbf{G}}^{i\ 19}\mu_E\gamma_1(\mu_L)\gamma_2(\mu_L) + \mathbf{K}_{\mathbf{G}}^{i\ 20}\mu_E\frac{\gamma_2(\mu_L)}{\gamma_1(\mu_L)} + \\
& \mathbf{K}_{\mathbf{G}}^{i\ 21}\frac{1}{\mu_E} + \mathbf{K}_{\mathbf{G}}^{i\ 22}\frac{1}{\mu_E}{\gamma_1}^2(\mu_L) + \mathbf{K}_{\mathbf{G}}^{i\ 23}\frac{1}{\mu_E}\frac{\gamma_2(\mu_L)}{\gamma_1(\mu_L)}.
\end{aligned}
\tag{A.90}
$$

The terms in Equations (A.90) are defined as follows:

$$
\mathbf{K}_{\mathbf{G}}^{i\ 0} = \begin{bmatrix} \mathbf{M}_{\mathrm{p}}^0 + \theta\Delta t^i\,\mathbf{K}_{\mathrm{p}}^0 & \mathbf{G}_{\mathrm{pd}}^0 \\ \theta\mathbf{G}_{\mathrm{dp}}^0 & \theta\mathbf{K}_{\mathrm{d}}^0 \end{bmatrix}, \tag{A.91}
$$

$$
\mathbf{K}_{\mathbf{G}}^{i\ 1} = \begin{bmatrix} \mathbf{0} & \mathbf{G}_{\mathrm{pd}}^1 \\ \theta\mathbf{G}_{\mathrm{dp}}^1 & \mathbf{0} \end{bmatrix}, \tag{A.92}
$$

$$\mathbf{K}_{\mathbf{G}}^{i\ 2} = \begin{bmatrix} \mathbf{0} & \mathbf{G}_{\mathrm{pd}}^{2} \\ \theta\mathbf{G}_{\mathrm{dp}}^{3} & \mathbf{0} \end{bmatrix}, \tag{A.93}$$

$$\mathbf{K}_{\mathbf{G}}^{i\ 3} = \begin{bmatrix} \mathbf{M}_{\mathrm{p}}^{2} & \mathbf{G}_{\mathrm{pd}}^{3} \\ \theta\mathbf{G}_{\mathrm{dp}}^{2} & \mathbf{0} \end{bmatrix}, \tag{A.94}$$

$$\mathbf{K}_{\mathbf{G}}^{i\ 4} = \begin{bmatrix} \mathbf{M}_{\mathrm{p}}^{3} & \mathbf{G}_{\mathrm{pd}}^{4} \\ \theta\mathbf{G}_{\mathrm{dp}}^{4} & \mathbf{0} \end{bmatrix}, \tag{A.95}$$

$$\mathbf{K}_{\mathbf{G}}^{i\ 5} = \begin{bmatrix} \mathbf{0} & \mathbf{0} \\ \mathbf{0} & \theta\mathbf{K}_{\mathrm{d}}^{7} \end{bmatrix}, \tag{A.96}$$

$$\mathbf{K}_{\mathbf{G}}^{i\ 6} = \begin{bmatrix} \mathbf{0} & \mathbf{0} \\ \mathbf{0} & \theta\mathbf{K}_{\mathrm{d}}^{8} \end{bmatrix}, \tag{A.97}$$

$$\mathbf{K}_{\mathbf{G}}^{i\ 7} = \begin{bmatrix} \mathbf{0} & \mathbf{0} \\ \mathbf{0} & \theta\mathbf{K}_{\mathrm{d}}^{9} \end{bmatrix}, \tag{A.98}$$

$$\mathbf{K}_{\mathbf{G}}^{i\ 8} = \begin{bmatrix} \mathbf{0} & \mathbf{0} \\ \mathbf{0} & \theta\mathbf{K}_{\mathrm{d}}^{10} \end{bmatrix}, \tag{A.99}$$

$$\mathbf{K}_{\mathbf{G}}^{i\ 9} = \begin{bmatrix} \mathbf{0} & \mathbf{0} \\ \mathbf{0} & \theta\mathbf{K}_{\mathrm{d}}^{11} \end{bmatrix}, \tag{A.100}$$

$$\mathbf{K}_{\mathbf{G}}^{i\ 10} = \begin{bmatrix} \mathbf{0} & \mathbf{0} \\ \mathbf{0} & \theta\mathbf{K}_{\mathrm{d}}^{12} \end{bmatrix}, \tag{A.101}$$

$$\mathbf{K}_{\mathbf{G}}^{i\ 11} = \begin{bmatrix} \theta\Delta t^{i}\,\mathbf{K}_{\mathrm{p}}^{1} & \mathbf{0} \\ \mathbf{0} & \mathbf{0} \end{bmatrix}, \tag{A.102}$$

$$\mathbf{K}_{\mathbf{G}}^{i\ 12} = \begin{bmatrix} \theta\Delta t^{i}\,\mathbf{K}_{\mathrm{p}}^{2} & \mathbf{0} \\ \mathbf{0} & \mathbf{0} \end{bmatrix}, \tag{A.103}$$

$$\mathbf{K}_{\mathbf{G}}^{i\ 13} = \begin{bmatrix} \theta\Delta t^i\,\mathbf{K}_{\mathrm{p}}^3 & \mathbf{0} \\ \mathbf{0} & \mathbf{0} \end{bmatrix}, \tag{A.104}$$

$$\mathbf{K}_{\mathbf{G}}^{i\ 14} = \begin{bmatrix} \theta\Delta t^i\,\mathbf{K}_{\mathrm{p}}^4 & \mathbf{0} \\ \mathbf{0} & \mathbf{0} \end{bmatrix}, \tag{A.105}$$

$$\mathbf{K}_{\mathbf{G}}^{i\ 15} = \begin{bmatrix} \mathbf{0} & \mathbf{0} \\ \mathbf{0} & \theta\mathbf{K}_{\mathrm{d}}^1 \end{bmatrix}, \tag{A.106}$$

$$\mathbf{K}_{\mathbf{G}}^{i\ 16} = \begin{bmatrix} \mathbf{0} & \mathbf{0} \\ \mathbf{0} & \theta\mathbf{K}_{\mathrm{d}}^2 \end{bmatrix}, \tag{A.107}$$

$$\mathbf{K}_{\mathbf{G}}^{i\ 17} = \begin{bmatrix} \mathbf{0} & \mathbf{0} \\ \mathbf{0} & \theta\mathbf{K}_{\mathrm{d}}^3 \end{bmatrix}, \tag{A.108}$$

$$\mathbf{K}_{\mathbf{G}}^{i\ 18} = \begin{bmatrix} \mathbf{0} & \mathbf{0} \\ \mathbf{0} & \theta\mathbf{K}_{\mathrm{d}}^4 \end{bmatrix}, \tag{A.109}$$

$$\mathbf{K}_{\mathbf{G}}^{i\ 19} = \begin{bmatrix} \mathbf{0} & \mathbf{0} \\ \mathbf{0} & \theta\mathbf{K}_{\mathrm{d}}^5 \end{bmatrix}, \tag{A.110}$$

$$\mathbf{K}_{\mathbf{G}}^{i\ 20} = \begin{bmatrix} \mathbf{0} & \mathbf{0} \\ \mathbf{0} & \theta\mathbf{K}_{\mathrm{d}}^6 \end{bmatrix}, \tag{A.111}$$

$$\mathbf{K}_{\mathbf{G}}^{i\ 21} = \begin{bmatrix} \mathbf{M}_{\mathrm{p}}^1 & \mathbf{0} \\ \mathbf{0} & \mathbf{0} \end{bmatrix}, \tag{A.112}$$

$$\mathbf{K}_{\mathbf{G}}^{i\ 22} = \begin{bmatrix} \mathbf{M}_{\mathrm{p}}^4 & \mathbf{0} \\ \mathbf{0} & \mathbf{0} \end{bmatrix}, \tag{A.113}$$

$$\mathbf{K}_{\mathbf{G}}^{i\ 23} = \begin{bmatrix} \mathbf{M}_{\mathrm{p}}^5 & \mathbf{0} \\ \mathbf{0} & \mathbf{0} \end{bmatrix}. \tag{A.114}$$

The expression $\mathbf{K}^{i}{}^{*}\mathbf{G}(\boldsymbol{\mu})$ is analogous to Equations (A.90) to (A.114), except for the replacement of the term θ with $(\theta-1)$ in their definitions. The components $\mathbf{G}^0_{\mathrm{pd}}$, $\mathbf{G}^1_{\mathrm{pd}}$, $\mathbf{G}^2_{\mathrm{pd}}$, $\mathbf{G}^3_{\mathrm{pd}}$, $\mathbf{G}^4_{\mathrm{pd}}$, $\mathbf{G}^1_{\mathrm{dp}}$, $\mathbf{G}^2_{\mathrm{dp}}$, $\mathbf{G}^3_{\mathrm{dp}}$, $\mathbf{G}^4_{\mathrm{dp}}$ are similar to Equations (A.41) to (A.50), while the remaining components in Equations (A.91) to (A.114) are defined as follows:

$$\mathbf{K}_{\mathrm{p}} = \mathbf{K}^0_{\mathrm{p}} + \mathbf{K}^1_{\mathrm{p}}\mu_K + \mathbf{K}^2_{\mathrm{p}}\mu_K\gamma_1^2(\mu_L) + \mathbf{K}^3_{\mathrm{p}}\mu_K\frac{\gamma_2(\mu_L)}{\gamma_1(\mu_L)} + \mathbf{K}^4_{\mathrm{p}}\mu_K\gamma_1(\mu_L)\gamma_2(\mu_L), \tag{A.115}$$

$$\mathbf{K}^0_{\mathrm{p}} = \int_{\Omega\setminus\Omega_{\mathrm{R}}} \mathbf{B}^{\top}_{\mathrm{p}}(\frac{K}{\rho_f g})\mathbf{B}_{\mathrm{p}} R d\Omega \tag{A.116}$$

$$\mathbf{K}^1_{\mathrm{p}} = \int_{\Omega^1_{\mathrm{R}}} \mathbf{B}^{\top}_{\mathrm{p}}(\frac{1}{\rho_f g})\mathbf{B}_{\mathrm{p}} R d\Omega + \int_{\Omega^2_{\mathrm{R}}} \mathbf{B}^{\top}_{\mathrm{p}}(\frac{1}{\rho_f g}) \begin{bmatrix} 1 & 0 \\ 0 & 0 \end{bmatrix} \mathbf{B}_{\mathrm{p}} R d\Omega, \tag{A.117}$$

$$\mathbf{K}^2_{\mathrm{p}} = \int_{\Omega^2_{\mathrm{R}}} \mathbf{B}^{\top}_{\mathrm{p}}(\frac{1}{\rho_f g}) \begin{bmatrix} 0 & 0 \\ 0 & 1 \end{bmatrix} \mathbf{B}_{\mathrm{p}} R d\Omega, \tag{A.118}$$

$$\mathbf{K}^3_{\mathrm{p}} = \int_{\Omega^2_{\mathrm{R}}} \mathbf{B}^{\top}_{\mathrm{p}}(\frac{1}{\rho_f g}) \begin{bmatrix} 1 & 0 \\ 0 & 0 \end{bmatrix} \mathbf{B}_{\mathrm{p}} d\Omega, \tag{A.119}$$

$$\mathbf{K}^4_{\mathrm{p}} = \int_{\Omega^2_{\mathrm{R}}} \mathbf{B}^{\top}_{\mathrm{p}}(\frac{1}{\rho_f g}) \begin{bmatrix} 0 & 0 \\ 0 & 1 \end{bmatrix} \mathbf{B}_{\mathrm{p}} d\Omega, \tag{A.120}$$

$$\begin{aligned} \mathbf{M}_{\mathrm{p}} =& \mathbf{M}^0_{\mathrm{p}} + \mathbf{M}^1_{\mathrm{p}}\frac{1}{\mu_E} + \mathbf{M}^2_{\mathrm{p}}\gamma_1^2(\mu_L) + \mathbf{M}^3_{\mathrm{p}}\gamma_1(\mu_L)\gamma_2(\mu_L) + \\ & \mathbf{M}^4_{\mathrm{p}}\frac{\gamma_1^2(\mu_L)}{\mu_E} + \mathbf{M}^5_{\mathrm{p}}\frac{\gamma_1(\mu_L)\gamma_2(\mu_L)}{\mu_E}, \end{aligned} \tag{A.121}$$

$$\mathbf{M}^0_{\mathrm{p}} = \int_{\Omega_1} \mathbf{N}^{\top}_{\mathrm{p}}(\frac{\phi}{K_f})\mathbf{N}_{\mathrm{p}} R d\Omega + \int_{\Omega\setminus\Omega_{\mathrm{R}}} \mathbf{N}^{\top}_{\mathrm{p}}\frac{(\alpha-\phi)(1-2\nu)(1-\alpha)}{E}\mathbf{N}_{\mathrm{p}} R d\Omega, \tag{A.122}$$

$$\mathbf{M}^1_{\mathrm{p}} = \int_{\Omega^1_{\mathrm{R}}} \mathbf{N}^{\top}_{\mathrm{p}}(\alpha-\phi)(1-2\nu)(1-\alpha)\mathbf{N}_{\mathrm{p}} R d\Omega, \tag{A.123}$$

$$\mathbf{M}^2_{\mathrm{p}} = \int_{\Omega^2_{\mathrm{R}}} \mathbf{N}^{\top}_{\mathrm{p}}(\frac{\phi}{K_f})\mathbf{N}_{\mathrm{p}} R d\Omega, \tag{A.124}$$

$$\mathbf{M}_{\mathrm{p}}^{3}=\int_{\Omega_{\mathrm{R}}^{2}}\mathbf{N}_{\mathrm{p}}^{\top}(\frac{\phi}{K_{f}})\mathbf{N}_{\mathrm{p}}d\Omega, \tag{A.125}$$

$$\mathbf{M}_{\mathrm{p}}^{4}=\int_{\Omega_{\mathrm{R}}^{2}}\mathbf{N}_{\mathrm{p}}^{\top}(\alpha-\phi)(1-2\nu)(1-\alpha)\mathbf{N}_{\mathrm{p}}Rd\Omega, \tag{A.126}$$

$$\mathbf{M}_{\mathrm{p}}^{5}=\int_{\Omega_{\mathrm{R}}^{2}}\mathbf{N}_{\mathrm{p}}^{\top}(\alpha-\phi)(1-2\nu)(1-\alpha)\mathbf{N}_{\mathrm{p}}d\Omega, \tag{A.127}$$

$$\begin{aligned}\mathbf{K}_{\mathrm{d}}=&\mathbf{K}_{\mathrm{d}}^{0}+\mathbf{K}_{\mathrm{d}}^{1}\mu_{E}+\mathbf{K}_{\mathrm{d}}^{2}\mu_{E}\gamma_{1}(\mu_{L})+\mathbf{K}_{\mathrm{d}}^{3}\mu_{E}\gamma_{2}(\mu_{L})+\mathbf{K}_{\mathrm{d}}^{4}\mu_{E}\gamma_{1}^{2}(\mu_{L})+\\&\mathbf{K}_{\mathrm{d}}^{5}\mu_{E}\gamma_{1}(\mu_{L})\gamma_{2}(\mu_{L})+\mathbf{K}_{\mathrm{d}}^{6}\mu_{E}\frac{\gamma_{2}(\mu_{L})}{\gamma_{1}(\mu_{L})}+\mathbf{K}_{\mathrm{d}}^{7}\mu_{E}\frac{\mu_{L}}{L_{2}}\gamma_{1}(\mu_{L})+\\&\mathbf{K}_{\mathrm{d}}^{8}\mu_{E}(\frac{\mu_{L}}{L_{2}})^{2}\gamma_{1}(\mu_{L})+\mathbf{K}_{\mathrm{d}}^{9}\mu_{E}(\frac{\mu_{L}}{L_{2}})^{3}\gamma_{1}(\mu_{L})+\mathbf{K}_{\mathrm{d}}^{10}\mu_{E}(\frac{\mu_{L}}{L_{2}})^{4}\gamma_{1}(\mu_{L})+\\&\mathbf{K}_{\mathrm{d}}^{11}\mu_{E}(\frac{\mu_{L}}{L_{2}})^{5}\gamma_{1}(\mu_{L})+\mathbf{K}_{\mathrm{d}}^{12}\mu_{E}(\frac{\mu_{L}}{L_{2}})^{6}\gamma_{1}(\mu_{L}),\end{aligned} \tag{A.128}$$

$$\mathbf{K}_{\mathrm{d}}^{0}=\int_{\Omega\setminus\Omega_{\mathrm{R}}}\mathbf{B}_{\mathrm{d}}^{\top}\mathbb{C}(E,\nu)\mathbf{B}_{\mathrm{d}}\ rd\Omega, \tag{A.129}$$

$$\begin{aligned}\mathbf{K}_{\mathrm{d}}^{1}=&\int_{\Omega_{\mathrm{R}}^{1}}\mathbf{B}_{\mathrm{d}}^{\top}\mathbf{C}_{0}(1,\nu)\mathbf{B}_{\mathrm{d}}Rd\Omega+\int_{\Omega_{\mathrm{R}}^{2}}\frac{\partial\mathbf{N}_{\mathrm{d}}^{\top}}{\partial R}\mathbf{C}_{1}(1,\nu)\frac{\partial\mathbf{N}_{\mathrm{d}}}{\partial R}Rd\Omega+\\&\int_{\Omega_{\mathrm{R}}^{2}}\frac{\partial\mathbf{N}_{\mathrm{d}}^{\top}}{\partial R}\mathbf{C}_{3}(1,\nu)\mathbf{N}_{\mathrm{d}}d\Omega+\int_{\Omega_{\mathrm{R}}^{2}}\mathbf{N}_{\mathrm{d}}^{\top}\mathbf{C}_{7}(1,\nu)\frac{\partial\mathbf{N}_{\mathrm{d}}}{\partial R}d\Omega,\end{aligned} \tag{A.130}$$

$$\begin{aligned}\mathbf{K}_{\mathrm{d}}^{2}=&\int_{\Omega_{\mathrm{R}}^{2}}\frac{\partial\mathbf{N}_{\mathrm{d}}^{\top}}{\partial R}\mathbf{C}_{2}(1,\nu)\frac{\partial\mathbf{N}_{\mathrm{d}}}{\partial Z}Rd\Omega+\int_{\Omega_{\mathrm{R}}^{2}}\frac{\partial\mathbf{N}_{\mathrm{d}}^{\top}}{\partial Z}\mathbf{C}_{4}(1,\nu)\frac{\partial\mathbf{N}_{\mathrm{d}}}{\partial R}Rd\Omega+\\&\int_{\Omega_{\mathrm{R}}^{2}}\frac{\partial\mathbf{N}_{\mathrm{d}}^{\top}}{\partial Z}\mathbf{C}_{6}(1,\nu)\mathbf{N}_{\mathrm{d}}d\Omega+\int_{\Omega_{\mathrm{R}}^{2}}\mathbf{N}_{\mathrm{d}}^{\top}\mathbf{C}_{8}(1,\nu)\frac{\partial\mathbf{N}_{\mathrm{d}}}{\partial Z}d\Omega+\\&\int_{\Omega_{\mathrm{R}}^{2}}\mathbf{N}_{\mathrm{d}}^{\top}\mathbf{C}_{9}(1,\nu)\mathbf{N}_{\mathrm{d}}\frac{1}{R}d\Omega,\end{aligned} \tag{A.131}$$

$$\mathbf{K}_{\mathrm{d}}^{3}=\int_{\Omega_{\mathrm{R}}^{2}}\frac{\partial\mathbf{N}_{\mathrm{d}}^{\top}}{\partial R}\mathbf{C}_{2}(1,\nu)\frac{\partial\mathbf{N}_{\mathrm{d}}}{\partial z}d\Omega+\int_{\Omega_{\mathrm{R}}^{2}}\frac{\partial\mathbf{N}_{\mathrm{d}}^{\top}}{\partial Z}\mathbf{C}_{4}(1,\nu)\frac{\partial\mathbf{N}_{\mathrm{d}}}{\partial R}d\Omega, \tag{A.132}$$

$$\mathbf{K}_{\mathrm{d}}^{4}=\int_{\Omega_{\mathrm{R}}^{2}}\frac{\partial\mathbf{N}_{\mathrm{d}}^{\top}}{\partial Z}\mathbf{C}_{5}(1,\nu)\frac{\partial\mathbf{N}_{\mathrm{d}}}{\partial Z}Rd\Omega, \tag{A.133}$$

$$\mathbf{K}_{\mathrm{d}}^{5} = \int_{\Omega_{\mathrm{R}}^{2}} \frac{\partial \mathbf{N}_{\mathrm{d}}^{\top}}{\partial Z} \mathbf{C}_{5}(1,\nu) \frac{\partial \mathbf{N}_{\mathrm{d}}}{\partial Z} d\Omega, \tag{A.134}$$

$$\mathbf{K}_{\mathrm{d}}^{6} = \int_{\Omega_{\mathrm{R}}^{2}} \frac{\partial \mathbf{N}_{\mathrm{d}}^{\top}}{\partial R} \mathbf{C}_{1}(1,\nu) \frac{\partial \mathbf{N}_{\mathrm{d}}}{\partial R} d\Omega, \tag{A.135}$$

$$\mathbf{K}_{\mathrm{d}}^{7} = \int_{\Omega_{\mathrm{R}}^{2}} \mathbf{N}_{\mathrm{d}}^{\top} \mathbf{C}_{9}(1,\nu) \mathbf{N}_{\mathrm{d}}(-1) \frac{(R-L_1)}{R^2} d\Omega, \tag{A.136}$$

$$\mathbf{K}_{\mathrm{d}}^{8} = \int_{\Omega_{\mathrm{R}}^{2}} \mathbf{N}_{\mathrm{d}}^{\top} \mathbf{C}_{9}(1,\nu) \mathbf{N}_{\mathrm{d}} \frac{(R-L_1)^2}{R^3} d\Omega, \tag{A.137}$$

$$\mathbf{K}_{\mathrm{d}}^{9} = \int_{\Omega_{\mathrm{R}}^{2}} \mathbf{N}_{\mathrm{d}}^{\top} \mathbf{C}_{9}(1,\nu) \mathbf{N}_{\mathrm{d}}(-1) \frac{(R-L_1)^3}{R^4} d\Omega, \tag{A.138}$$

$$\mathbf{K}_{\mathrm{d}}^{10} = \int_{\Omega_{\mathrm{R}}^{2}} \mathbf{N}_{\mathrm{d}}^{\top} \mathbf{C}_{9}(1,\nu) \mathbf{N}_{\mathrm{d}} \frac{(R-L_1)^4}{R^5} d\Omega, \tag{A.139}$$

$$\mathbf{K}_{\mathrm{d}}^{11} = \int_{\Omega_{\mathrm{R}}^{2}} \mathbf{N}_{\mathrm{d}}^{\top} \mathbf{C}_{9}(1,\nu) \mathbf{N}_{\mathrm{d}}(-1) \frac{(R-L_1)^5}{R^6} d\Omega, \tag{A.140}$$

$$\mathbf{K}_{\mathrm{d}}^{12} = \int_{\Omega_{\mathrm{R}}^{2}} \mathbf{N}_{\mathrm{d}}^{\top} \mathbf{C}_{9}(1,\nu) \mathbf{N}_{\mathrm{d}} \frac{(R-L_1)^6}{R^7} d\Omega. \tag{A.141}$$

On the right-hand side of the Hydro-Mechanical (HM) component, there is a matrix called $\mathbf{G_T}(\boldsymbol{\mu})$ (Equation (4.9)). This matrix emerges as a result of the influence of the thermal component on the coupled HM part. It contains all the matrices that relate to thermal and hydro, as well as thermal and mechanical (unidirectional coupling from thermal to hydro and mechanical). The separate format of this matrix is as follows:

$$\begin{aligned} \mathbf{G_T}(\boldsymbol{\mu}) =& \mathbf{G}_{\mathbf{T}}^{0} + \mathbf{G}_{\mathbf{T}}^{1} {\gamma_1}^2(\mu_L) + \mathbf{G}_{\mathbf{T}}^{2} \gamma_1(\mu_L)\gamma_2(\mu_L) + \\ & \mathbf{G}_{\mathbf{T}}^{3} \mu_E + \mathbf{G}_{\mathbf{T}}^{4} \mu_E \gamma_1(\mu_L) + \mathbf{G}_{\mathbf{T}}^{5} \mu_E \gamma_2(\mu_L) + \\ & \mathbf{G}_{\mathbf{T}}^{6} \mu_E {\gamma_1}^2(\mu_L) + \mathbf{G}_{\mathbf{T}}^{7} \mu_E \gamma_1(\mu_L)\gamma_2(\mu_L). \end{aligned} \tag{A.142}$$

The terms in Equation (A.142) are as follows:

$$\mathbf{G}_{\mathbf{T}}^{0} = \begin{bmatrix} \mathbf{M}_{\mathrm{pT}}^{0} & -\mathbf{M}_{\mathrm{pT}}^{0} \\ -\theta\mathbf{G}_{\mathrm{dT}}^{0} & (\theta-1)\mathbf{G}_{\mathrm{dT}}^{0} \end{bmatrix}, \tag{A.143}$$

$$\mathbf{G}_{\mathbf{T}}^{1} = \begin{bmatrix} \mathbf{M}_{\mathrm{pT}}^{1} & -\mathbf{M}_{\mathrm{pT}}^{1} \\ \mathbf{0} & \mathbf{0} \end{bmatrix}, \tag{A.144}$$

$$\mathbf{G}_{\mathbf{T}}^{2} = \begin{bmatrix} \mathbf{M}_{\mathrm{pT}}^{2} & -\mathbf{M}_{\mathrm{pT}}^{2} \\ \mathbf{0} & \mathbf{0} \end{bmatrix}, \tag{A.145}$$

$$\mathbf{G}_{\mathbf{T}}^{3} = \begin{bmatrix} \mathbf{0} & \mathbf{0} \\ -\theta\mathbf{G}_{\mathrm{dT}}^{1} & (\theta-1)\mathbf{G}_{\mathrm{dT}}^{1} \end{bmatrix}, \tag{A.146}$$

$$\mathbf{G}_{\mathbf{T}}^{4} = \begin{bmatrix} \mathbf{0} & \mathbf{0} \\ -\theta\mathbf{G}_{\mathrm{dT}}^{2} & (\theta-1)\mathbf{G}_{\mathrm{dT}}^{2} \end{bmatrix}, \tag{A.147}$$

$$\mathbf{G}_{\mathbf{T}}^{5} = \begin{bmatrix} \mathbf{0} & \mathbf{0} \\ -\theta\mathbf{G}_{\mathrm{dT}}^{4} & (\theta-1)\mathbf{G}_{\mathrm{dT}}^{4} \end{bmatrix}, \tag{A.148}$$

$$\mathbf{G}_{\mathbf{T}}^{6} = \begin{bmatrix} \mathbf{0} & \mathbf{0} \\ -\theta\mathbf{G}_{\mathrm{dT}}^{3} & (\theta-1)\mathbf{G}_{\mathrm{dT}}^{3} \end{bmatrix}, \tag{A.149}$$

$$\mathbf{G}_{\mathbf{T}}^{7} = \begin{bmatrix} \mathbf{0} & \mathbf{0} \\ -\theta\mathbf{G}_{\mathrm{dT}}^{5} & (\theta-1)\mathbf{G}_{\mathrm{dT}}^{5} \end{bmatrix}. \tag{A.150}$$

In Equations (A.143) to (A.150), all the terms related to $\mathbf{M}_{\mathrm{pT}}^{0}$, $\mathbf{M}_{\mathrm{pT}}^{1}$, and $\mathbf{M}_{\mathrm{pT}}^{2}$ are already presented in Equations (A.26), (A.27), and (A.28), respectively. However, for $\mathbf{G}_{\mathrm{dT}}$, due to its dependency on both material and geometric parameters, it is necessary to determine its separate definition and its components, which are defined as follows:

$$\begin{aligned} \mathbf{G}_{\mathrm{dT}} =& \mathbf{G}_{\mathrm{dT}}^{0} + \mathbf{G}_{\mathrm{dT}}^{1}\mu_{E} + \mathbf{G}_{\mathrm{dT}}^{2}\mu_{\mathrm{E}}\gamma_{1}(\mu_{L}) + \mathbf{G}_{\mathrm{dT}}^{3}\mu_{\mathrm{E}}\gamma_{1}^{2}(\mu_{L}) + \\ & \mathbf{G}_{\mathrm{dT}}^{4}\mu_{\mathrm{E}}\gamma_{2}(\mu_{L}) + \mathbf{G}_{\mathrm{dT}}^{5}\mu_{\mathrm{E}}\gamma_{1}(\mu_{L})\gamma_{2}(\mu_{L}), \end{aligned} \tag{A.151}$$

$$\mathbf{G}_{\mathrm{dT}}^{0} = \int_{\Omega\setminus\Omega_{\mathrm{R}}} \mathbf{N}_{\mathrm{d}}^{\top}(\frac{\alpha_s}{1-2\nu}) E\, \mathbf{B}_{\mathrm{T}} R d\Omega, \tag{A.152}$$

$$\mathbf{G}_{\mathrm{dT}}^{1} = \int_{\Omega_{\mathrm{R}}^{1}} \mathbf{N}_{\mathrm{d}}^{\top}(\frac{\alpha_s}{1-2\nu}) \mathbf{B}_{\mathrm{T}} R d\Omega, \tag{A.153}$$

$$\mathbf{G}_{\mathrm{dT}}^{2} = \int_{\Omega_{\mathrm{R}}^{2}} \mathbf{N}_{\mathrm{d}}^{\top}(\frac{\alpha_s}{1-2\nu}) \begin{bmatrix} 1 & 0 \\ 0 & 0 \end{bmatrix} \mathbf{B}_{\mathrm{T}} R d\Omega, \tag{A.154}$$

$$\mathbf{G}_{\mathrm{dT}}^{3} = \int_{\Omega_{\mathrm{R}}^{2}} \mathbf{N}_{\mathrm{d}}^{\top}(\frac{\alpha_s}{1-2\nu}) \begin{bmatrix} 0 & 0 \\ 0 & 1 \end{bmatrix} \mathbf{B}_{\mathrm{T}} R d\Omega, \tag{A.155}$$

$$\mathbf{G}_{\mathrm{dT}}^{4} = \int_{\Omega_{\mathrm{R}}^{2}} \mathbf{N}_{\mathrm{d}}^{\top}(\frac{\alpha_s}{1-2\nu}) \begin{bmatrix} 1 & 0 \\ 0 & 0 \end{bmatrix} \mathbf{B}_{\mathrm{T}} d\Omega, \tag{A.156}$$

$$\mathbf{G}_{\mathrm{dT}}^{5} = \int_{\Omega_{\mathrm{R}}^{2}} \mathbf{N}_{\mathrm{d}}^{\top}(\frac{\alpha_s}{1-2\nu}) \begin{bmatrix} 0 & 0 \\ 0 & 1 \end{bmatrix} \mathbf{B}_{\mathrm{T}} d\Omega. \tag{A.157}$$

On the right-hand side of the coupled HM part, there is an additional term denoted as $\mathbf{F}_{*}^{i}(\boldsymbol{\mu})$ in Equation (4.9). This term encompasses the body force terms from the hydro and mechanical parts, as well as the traction force from the mechanical part. The separate vector forms of this term are as follows:

$$\begin{aligned} \mathbf{F}_{*}^{i}(\boldsymbol{\mu}) =& \mathbf{F}_{*}^{i\ 0} + \mathbf{F}_{*}^{i\ 1}{\gamma_1}^2(\mu_L) + \mathbf{F}_{*}^{i\ 2}\gamma_1(\mu_L)\gamma_2(\mu_L) + \\ & \mathbf{F}_{*}^{i\ 3}\mu_K + \mathbf{F}_{*}^{i\ 4}\mu_K\gamma_1(\mu_L) + \mathbf{F}_{*}^{i\ 5}\mu_K{\gamma_1}^2(\mu_L) + \\ & \mathbf{F}_{*}^{i\ 6}\mu_K\gamma_2(\mu_L) + \mathbf{F}_{*}^{i\ 7}\mu_K\gamma_1(\mu_L)\gamma_2(\mu_L). \end{aligned} \tag{A.158}$$

All the terms in Equation (A.158) are as follows:

$$\mathbf{F}_{*}^{i\ 0} = \begin{bmatrix} \Delta t^i\, \mathbf{f}_{\mathbf{b}_{\mathrm{f}}}^{0} \\ \mathbf{f}_{\mathrm{d}}^{0} \end{bmatrix}, \tag{A.159}$$

$$\mathbf{F}_{*}^{i\ 1} = \begin{bmatrix} \mathbf{0} \\ \mathbf{f}_{\mathrm{d}}^{1} \end{bmatrix}, \tag{A.160}$$

$$\mathbf{F}_*^{i\ 2} = \begin{bmatrix} \mathbf{0} \\ \mathbf{f}_{\mathrm{d}}^2 \end{bmatrix}, \tag{A.161}$$

$$\mathbf{F}_*^{i\ 3} = \begin{bmatrix} \Delta t^i\, \mathbf{f}_{\mathbf{b}_\mathrm{f}}^1 \\ \mathbf{0} \end{bmatrix}, \tag{A.162}$$

$$\mathbf{F}_*^{i\ 4} = \begin{bmatrix} \Delta t^i\, \mathbf{f}_{\mathbf{b}_\mathrm{f}}^2 \\ \mathbf{0} \end{bmatrix}, \tag{A.163}$$

$$\mathbf{F}_*^{i\ 5} = \begin{bmatrix} \Delta t^i\, \mathbf{f}_{\mathbf{b}_\mathrm{f}}^3 \\ \mathbf{0} \end{bmatrix}, \tag{A.164}$$

$$\mathbf{F}_*^{i\ 6} = \begin{bmatrix} \Delta t^i\, \mathbf{f}_{\mathbf{b}_\mathrm{f}}^4 \\ \mathbf{0} \end{bmatrix}, \tag{A.165}$$

$$\mathbf{F}_*^{i\ 7} = \begin{bmatrix} \Delta t^i\, \mathbf{f}_{\mathbf{b}_\mathrm{f}}^5 \\ \mathbf{0} \end{bmatrix}. \tag{A.166}$$

The definitions of the components $\mathbf{f}_{\mathbf{d}}^0$, $\mathbf{f}_{\mathbf{d}}^1$, and $\mathbf{f}_{\mathbf{d}}^2$ can be found in Equations (A.73), (A.74), and (A.75), respectively. However, for the remaining components in Equations (A.159) to (A.166), they are defined as follows:

$$\begin{aligned} \mathbf{f}_{\mathbf{b}_\mathrm{f}} =& \mathbf{f}_{\mathbf{b}_\mathrm{f}}^0 + \mathbf{f}_{\mathbf{b}_\mathrm{f}}^1 \mu_K + \mathbf{f}_{\mathbf{b}_\mathrm{f}}^2 \mu_K \gamma_1(\mu_L) + \mathbf{f}_{\mathbf{b}_\mathrm{f}}^3 \mu_K {\gamma_1}^2(\mu_L) + \\ & \mathbf{f}_{\mathbf{b}_\mathrm{f}}^4 \mu_K \gamma_2(\mu_L) + \mathbf{f}_{\mathbf{b}_\mathrm{f}}^5 \mu_K \gamma_1(\mu_L) \gamma_2(\mu_L), \end{aligned} \tag{A.167}$$

$$\mathbf{f}_{\mathbf{b}_\mathrm{f}}^0 = \int_{\Omega \setminus \Omega_\mathrm{R}} \mathbf{B}_\mathrm{p}^\top \frac{K}{\rho_f g} \rho_f \mathbf{g}\, R d\Omega, \tag{A.168}$$

$$\mathbf{f}_{\mathbf{b}_\mathrm{f}}^1 = \int_{\Omega_\mathrm{R}^1} \mathbf{B}_\mathrm{p}^\top \frac{1}{\rho_f g} \rho_f \mathbf{g}\, R d\Omega, \tag{A.169}$$

$$\mathbf{f}_{\mathbf{b}_\mathrm{f}}^2 = \int_{\Omega_\mathrm{R}^2} \mathbf{B}_\mathrm{p}^\top \frac{1}{\rho_f g} \rho_f \mathbf{g} \begin{bmatrix} 1 & 0 \\ 0 & 0 \end{bmatrix}\, R d\Omega, \tag{A.170}$$

$$\mathbf{f}^3_{\mathbf{b}_\mathrm{f}} = \int_{\Omega^2_\mathrm{R}} \mathbf{B}^\top_\mathrm{p} \frac{1}{\rho_f g} \rho_f \mathbf{g} \begin{bmatrix} 0 & 0 \\ 0 & 1 \end{bmatrix} \, R d\Omega, \tag{A.171}$$

$$\mathbf{f}^4_{\mathbf{b}_\mathrm{f}} = \int_{\Omega^2_\mathrm{R}} \mathbf{B}^\top_\mathrm{p} \frac{1}{\rho_f g} \rho_f \mathbf{g} \begin{bmatrix} 1 & 0 \\ 0 & 0 \end{bmatrix} \, d\Omega, \tag{A.172}$$

$$\mathbf{f}^5_{\mathbf{b}_\mathrm{f}} = \int_{\Omega^2_\mathrm{R}} \mathbf{B}^\top_\mathrm{p} \frac{1}{\rho_f g} \rho_f \mathbf{g} \begin{bmatrix} 0 & 0 \\ 0 & 1 \end{bmatrix} \, d\Omega. \tag{A.173}$$

Bibliography

[1] A. A. Abed, M. Laitinen, J. Lämsä, T. Harjupatana, W. T. Solowski, and M. Kataja. Hydro-mechanical modelling of MX-80 bentonite: one dimensional study. *E3S Web Conf.*, 9:180–185, 2016.

[2] E. Alonso, A. Gens, and A. Josa. Constitutive Model for Partially Saturated Soils. *Géotechnique*, 40, 01 1990.

[3] A. Ammar, B. Mokdad, F. Chinesta, and R. Keunings. A new family of solvers for some classes of multidimensional partial differential equations encountered in kinetic theory modeling of complex fluids. *Journal of Non-Newtonian Fluid Mechanics*, 139(3):153–176, 2006.

[4] A. Ammar, B. Mokdad, F. Chinesta, and R. Keunings. A new family of solvers for some classes of multidimensional partial differential equations encountered in kinetic theory modelling of complex fluids: Part II: Transient simulation using space-time separated representations. *Journal of Non-Newtonian Fluid Mechanics*, 144(2):98–121, 2007.

[5] J. Autio, M. Hassan, P. Karttunen, and P. Keto. Backfill Design 2012, December 2013.

[6] I. Babuska. The finite element method with Lagrangian multipliers. *Numer Math*, 20:179–192, 1973.

[7] K. J. Bathe. The inf-sup condition and its evaluation for mixed finite element methods. *Comput Struct*, 79:243–252, 2001.

[8] J. Bear and M. Y. Corapcioglu. A mathematical model for consolidation in a thermoelastic aquifer due to hot water injection or pumping. *Water Resources Research*, 17(3):723–736, 1981.

[9] J. Bear and M. Y. Corapcioglu. *Fundamentals of Transport Phenomena in Porous Media*. Martinus Nijhoff Publishers, Dordecht/ Boston/ Lancaster, 1985.

[10] T. Berlepsch and B. Haverkamp. Salt as a host rock for the geological repository for nuclear waste. *Elements*, 12:257–262, 08 2016.

[11] F. Bernier and B. Neerdael. Overview of in-situ thermomechanical experiments in clay: Concept, results and interpretation. *Engineering Geology*, 41(1):51–64, 1996.

[12] M. A. Biot. General Theory of Three-Dimensional Consolidation. *Journal of Applied Physics*, 12(2):155–164, 1941.

[13] M. A. Biot. Thermoelasticity and Irreversible Thermodynamics. *Journal of Applied Physics*, 27(3):240–253, 1956.

[14] M. Bjorge, P. Kreye, E. Heim, F. Wellmann, and W. Rühaak. The role of geological models and uncertainties in safety assessments. *Environmental Earth Sciences*, 81(7):190–200, 2022.

[15] R. Boer. *Porous Media: Theory and Experiments*. Springer, Dordrecht, the Netherlands, 1999.

[16] R. Boer. *Theory of Porous Media: Highlights in Historical Development and Current State*. Springer, Berlin, Heidelberg, 2000.

[17] F. Brezzi, J. Douglas, and L. D. Marini. Two families of mixed finite elements for second order elliptic problems. *Numer Math*, 47:217–235, 1985.

[18] F. Cavaliere, S. Zlotnik, R. Sevilla, X. Larráyoz, and P. Díez. Nonintrusive reduced order model for parametric solutions of inertia relief problems. *International Journal for Numerical Methods in Engineering*, 122(16):4270 – 4291, 2021.

[19] R. Charlier, J.-P. Radu, and F. Collin. Numerical modelling of coupled transient phenomena. *Revue française de génie civil*, 5:719–741, 09 2001.

[20] A. Chatterjee. An introduction to the proper orthogonal decomposition. *Current Science*, 78, April 2000.

[21] A. H. D. Cheng. *Poroelasticity*. Theory and Application of Transport in Porous Media 27. Springer International Publishing, 2016.

[22] M. Chijimatsu, L. Börgesson, T. Fujita, P. Jussila, S. Nguyen, J. Rutqvist, and L. Jing. Model development and calibration for the coupled thermal, hydraulic and mechanical phenomena of the bentonite. *Environmental Geology*, 57(6):1255–1261, 2009.

[23] M. Chijimatsu, T. Fujita, Y. Sugita, K. Amemiya, and A. Kobayashi. Field experiment, results and THM behavior in the Kamaishi mine experiment. *International Journal of Rock Mechanics and Mining Sciences*, 38(1):67–78, 2001. Decovalex II.

[24] F. Chinesta, A. Ammar, A. Leygue, and R. Keunings. An overview of the proper generalized decomposition with applications in computational rheology. *Journal of Non-Newtonian Fluid Mechanics*, 166(11):578–592, 2011. XVIth International Workshop on Numerical Methods for Non-Newtonian Flows.

[25] F. Chinesta, A. Leygue, F. Bordeu, J. V. Aguado, E. CUETO, D. Gonzalez, I. Alfaro, A. Ammar, and A. Huerta. Pgd-based computational vademecum for efficient design, optimization and control. *Archives of Computational Methods in Engineering*, 20, 03 2013.

[26] K. R. Chinesta, F. and A. Leygue. *The Proper Generalized Decomposition for Advanced Numerical Simulation*. Springer, 2014.

[27] L. Clarkson, D. Williams, and J. Seppälä. Real-time monitoring of tailings dams. *Georisk: Assessment and Management of Risk for Engineered Systems and Geohazards*, 15(2):113–127, 2021.

[28] P. J. Cleall, S. C. Seetharam, and H. R. Thomas. Inclusion of Some Aspects of Chemical Behavior of Unsaturated Soil in Thermo/Hydro/Chemical/Mechanical Models. I: Model Development. *Journal of Engineering Mechanics*, 133(3):338–347, 2007.

[29] F. Collin, X. Li, J. Radu, and R. Charlier. Thermo-hydro-mechanical coupling in clay barriers. *Engineering Geology*, 64(2):179–193, 2002. Key Issues in Waste Isolation Research.

[30] O. Coussy. *Mechanics of Porous Media*. John Wiley, New York, NY, 1995.

[31] O. Coussy. *Poromechanics*. John Wiley, 2004.

[32] C. W. Cryer. A comparison of the three-dimensional consolidation theories of Biot and Terzaghi. *The Quarterly Journal of Mechanics and Applied Mathematics*, 16(4):401–412, November 1963.

[33] S. De Simone, V. Vilarrasa, J. Carrera, A. Alcolea, and P. Meier. Thermal coupling may control mechanical stability of geothermal reservoirs during cold water injection. *Physics and Chemistry of the Earth, Parts A/B/C*, 64:117–126, 2013.

[34] D. Degen, K. Veroy, and F. Wellmann. Certified Reduced Basis Method in Geosciences Addressing the challenge of high dimensional problems, June 2019.

[35] F. Dupray, B. François, and L. Laloui. Analysis of a the FEBEX multi-barrier system including thermoplasticity of unsaturated bentonite. *International Journal For Numerical and Analytical Methods in Geomechanics*, 37, 2011.

[36] R. DuTeau, T. Sprecker, and D. Swenson. Preventing Short-Circuiting of Flow in Hot Dry Rock Reservoirs. *Geothermal Resources Council Transactions*, 18:415–422, 1994.

[37] P. Díez, S. Zlotnik, A. García-González, and A. Huerta. Algebraic PGD for tensor separation and compression: An algorithmic approach. *Comptes Rendus Mécanique*, 346(7):501–514, 2018.

[38] P. Díez, S. Zlotnik, A. García-González, and A. Huerta. Encapsulated PGD Algebraic Toolbox Operating with High-Dimensional Data. *Archives of Computational Methods in Engineering*, 27, 11 2019.

[39] W. Ehlers and J. Bluhm. *Porous Media: Theory, Experimental and Numerical Applications*. Springer, Berlin, Heidelberg, 2002.

[40] EURATOM. Full-scale engineered barriers experiment for a deep geological repository for high-level radioactive waste in crystalline host rock (FEBEX project), 2000.

[41] P. Fillunger. *Erdbaumechanik?* Selbstverlag des Verfassers, Wien, Germany, 1936.

[42] H. Florez. *Domain Decomposition Methods in Geomechanics [doctoral thesis]*. PhD thesis, The University of Texas at Austin, August 2012.

[43] H. Florez and E. Gildin. Model-order reduction applied to coupled flow and geomechanics. 2018(1):1–21, 2018.

[44] B. François and L. Laloui. A Stress-Strain Framework for Modelling the Behaviour of Unsaturated Soils under Non-Isothermal Conditions. *Theoretical and Numerical Unsaturated Soil Mechanics*, pages 119–125, January 2007.

[45] B. François and L. Laloui. ACMEG-TS: A constitutive model for unsaturated soils under non-isothermal conditions. *International Journal for Numerical and Analytical Methods in Geomechanics*, 32, 11 2008.

[46] B. François and L. Laloui. Non-isothermal infiltration in plastic bentonite. *Unsaturated Soils - Proceedings of the 5th International Conference on Unsaturated Soils*, 2, January 2011.

[47] R. Freeze and J. Cherry. *Groundwater*. Prentice Hall, 1979.

[48] S. K. Garg and A. Nur. Effective stress laws for fluid-saturated porous rocks. *Journal of Geophysical Research (1896-1977)*, 78(26):5911–5921, 1973.

[49] H. Garikapati, S. Zlotnik, P. Díez, C. Verhoosel, and H. Van Brummelen. A Proper Generalized Decomposition (PGD) approach to crack propagation in brittle materials: with application to random field material properties. *Computational Mechanics*, 65, February 2020.

[50] J. Geertsma. A remark on the analogy between thermoelasticity and the elasticity of saturated porous media. *Journal of the Mechanics and Physics of Solids*, 6(1):13–16, 1957.

[51] J. Geertsma. The Effect of Fluid Pressure Decline on Volumetric Changes of Porous Rocks. *Transactions of the AIME*, 210(01):331–340, December 1957.

[52] J. Geertsma. Problems of Rock Mechanics In Petroleum Production Engineering. *Int. Soc. Rock Mech*, 1:585–594, September 1966.

[53] A. Gens. *Constitutive Laws*, pages 129–158. Springer Vienna, Vienna, 1995.

[54] A. Gens. The role of geotechnical engineering for nuclear energy utilisation. *Proc. 13th Eur. Conf. Soil Mech. Geotech. Engng, Prague*, 3:25–67, 08 2003.

[55] A. Gens and E. Alonso. A framework for the behavior of unsaturated expansive clays. *Canadian Geotechnical Journal*, 29:1013–1032, 01 1992.

[56] A. Gens and E. Alonso. Aznalcóllar dam failure. Part 2: Stability conditions and failure. *Géotechnique*, 56(3):185–201, 01 2006.

[57] A. Gens, R. De Vasconcelos, and S. Olivella. Towards higher temperatures in nuclear waste repositories. *E3S Web Conferences*, 205(1001):1–8, 2020.

[58] A. Gens, A. J. Garcia-Molina, S. Olivella, E. E. Alonso, and F. Huertas. Analysis of a Full Scale IN SITU test simulating repository conditions. *International Journal For Numerical and Analytical Methods in Geomechanics*, 22:515–548, 1998.

[59] A. Gens and S. Olivella. Clay barriers in radioactive waste disposal. *Revue Française de Génie Civil*, 5(6):845–856, 2001.

[60] A. Gens and S. Olivella. THM phenomena in saturated and unsaturated porous media. *Revue Française de Génie Civil*, 5:693–717, 09 2001.

[61] A. Gens, M. Sánchez, L. Guimaraes, E. E. Alonso, A. Lloret, S. Olivella, M. V. Villar, and F. Huertas. A full-scale in situ heating test for high-level nuclear waste disposal: observations, analysis and interpretation. *Géotechnique*, 59(4):377–399, 2009.

[62] A. Gens, J. Vaunat, B. Garitte, and Y. Wileveau. In situ behaviour of a stiff layered clay subject to thermal loading: observations and interpretation. *Géotechnique*, 57(2):207–228, 2007.

[63] A. Ghassemi, A. Nygren, and A. Cheng. Effects of heat extraction on fracture aperture: A poro-thermoelastic analysis. *Geothermics*, 37(5):525–539, 2008.

[64] W. Hackbusch. *Multigrid Methods for FEM and BEM Applications, booktitle = Encyclopedia of Computational Mechanics*, chapter 20. John Wiley and Sons, Ltd, 2004.

[65] A. Haxaire, M. Aukenthaler, and R. Brinkgreve. Application of a Thermo-hydro-mechanical Model for Freezing and Thawing. *Procedia Engineering*, 191:74–81, 2017. ISRM European Rock Mechanics Symposium EUROCK 2017.

[66] R. G. Hesthaven, J. S. and B. Stamm. *Certified Reduced Basis Methods for Parametrized Partial Differential Equations*. Springer, 2016.

[67] T. Hicks, R. Pine, J. Willis-Richards, S. Xu, A. Jupe, and N. Rodrigues. A hydro-thermo-mechanical numerical model for HDR geothermal reservoir evaluation. *International Journal of Rock Mechanics and Mining Sciences and Geomechanics Abstracts*, 33(5):499–511, 1996.

[68] K. Huebner, D. Dewhirst, D. Smith, and T. Byrom. *The Finite Element Method For Engineers*. A Wiley Interscience Publication, 2001.

[69] H. Hökmark, M. Lönnqvist, and O. Kristensson. Strategy for thermal dimensioning of the final repository for spent nuclear fuel, December 2009.

[70] A. Iollo, G. Sambataro, and T. Taddei. A projection-based model reduction method for nonlinear mechanics with internal variables: application to thermo-hydro-mechanical systems, 2021.

[71] J. I. Israelsson. Short description of FLAC version 3.2. In O. Stephansson, L. Jing, and C.-F. Tsang, editors, *Coupled Thermo-Hydro-Mechanical Processes of Fractured Media*, volume 79 of *Developments in Geotechnical Engineering*, pages 513–522. Elsevier, 1996.

[72] J. I. Israelsson. Short Descriptions of UDEC and 3DEC. In O. Stephansson, L. Jing, and C.-F. Tsang, editors, *Coupled Thermo-Hydro-Mechanical Processes of Fractured Media*, volume 79 of *Developments in Geotechnical Engineering*, pages 523–528. Elsevier, 1996.

[73] C. E. Jacob. On the flow of water in an elastic artesian aquifer. *Eos, Transactions American Geophysical Union*, 21(2):574–586, 1940.

[74] E. Johansson and J. Rautakorpi. Rock mechanics stability at Olkiyto, H sthol-men, Kivetty and Romuvaara., February 2000.

[75] T. E. Jupp and A. Schultz. A poroelastic model for the tidal modulation of seafloor hydrothermal systems. *Journal of Geophysical Research: Solid Earth*, 109(B3), 2004.

[76] P. Khadivipanah, X. Pintado, S. Olivella, and J. Vaunat. Copper canister shearing in spent nuclear fuel repository using Bodner-Partom model. *Geomechanics for Energy and the Environment*, 22:100171, 2020.

[77] J. Koh, H. Roshan, and S. S. Rahman. A numerical study on the long term thermo-poroelastic effects of cold water injection into naturally fractured geothermal reservoirs. *Computers and Geotechnics*, 38(5):669–682, 2011.

[78] T. Kohl and R. Hopkirk. FRACTure - A simulation code for forced fluid flow and transport in fractured, porous rock. *Geothermics*, 24(3):333–343, 1995.

[79] I. Kukkonen. Thermal Properties of the Rocks in Olkiluto: Results of Laboratory Measurements 1994 2010, February 2011.

[80] L. W. Lake. *Enhanced oil recovery*. Prentice Hall, Englewood Cliffs, NJ, 1989.

[81] Y. Larion, G. Chen, S. Zlotnik, P. Dìez, S. Seetharam, and T. Massart. Using Reduced Basis Approximation for Efficient Surrogate-Based Inverse Identification of Thermo-Hydro-Mechanical Parameters from an In Situ Heating Test. *Rock Mechanics and Rock Engineering*, pages 1–19, June 2022.

[82] Y. Larion, S. Zlotnik, T. Massart, and P. Diez. Building a certified reduced basis for coupled thermo-hydro-mechanical systems with goal-oriented error estimation. *Computational mechanics*, 66(3):559–573, September 2020.

[83] B. Lin, H. Meng, J. Pan, and S. Chen. Porothermoelastic response of an oil sand formation subjected to injection and micro-fracturing in horizontal wells. *Petroleum Science*, 17(4):687–700, 2020.

[84] E. Liu, Y. Lai, H. Wong, and J. Feng. An elastoplastic model for saturated freezing soils based on thermo-poromechanics. *International Journal of Plasticity*, 107:246–285, 2018.

[85] A. Lloret and E. Alonso. State surfaces for partially saturated soils. *10th I.C.S.M.F.E., San Francisco*, 2:557–562, January 1985.

[86] A. Lloret and E. Alonso. State surfaces for partially saturated soils. *Proceedings of the International Conference on Soils Mechanics and Foundation Engineering*, 2:557–562, 1995.

[87] A. Manzoni and F. Negri. *Reduced Basis Methods for Partial Differential Equations An Introduction*. Springer, 2016.

[88] J. McNamee and R. E. Gibson. Plain Strain and Axially Symmetric Problems of the Consolidation of a Semi-infinite Clay Stratum. *The Quarterly Journal of Mechanics and Applied Mathematics*, 13(2):210–227, January 1960.

[89] D. F. McTigue. Thermoelastic response of fluid-saturated porous rock. *Journal of Geophysical Research: Solid Earth*, 91(B9):9533–9542, 1986.

[90] O. E. Meinzer. Compressibility and elasticity of artesian aquifers. *Economic Geology*, 23(3):263–291, May 1928.

[91] A. Merxhani. An introduction to linear poroelasticity. July 2016.

[92] A. R. Mitchell and D. F. Griffiths. *The Finite Difference Method in Partial Differential Equations*. John Wiley and Sons Incorporated, 1980.

[93] M. Muskat. *The Flow of Homogeneous Fluids through Porous Media*. McGraw-Hill, New York, 1937.

[94] C. Nasika, P. Dìez, P. Gerard, T. J. Massart, and S. Zlotnik. Discrete empirical interpolation for hyper-reduction of hydro-mechanical problems in groundwater flow through soil. *International Journal for Numerical and Analytical Methods in Geomechanics*, 47(5):667 – 693, 2023.

[95] C. Nasika, P. Díz, P. Gerard, T. J. Massart, and S. Zlotnik. Towards real time assessment of earthfill dams via Model Order Reduction. *Finite Elements in Analysis and Design*, 199:103666, 2022.

[96] T. Nguyen. Description of the computer code FRACON. In O. Stephansson, L. Jing, and C.-F. Tsang, editors, *Coupled Thermo-Hydro-Mechanical Processes of Fractured Media*, volume 79 of *Developments in Geotechnical Engineering*, pages 539–544. Elsevier, 1996.

[97] T. S. Nguyen and A. P. S. Selvadurai. Coupled Thermal-Mechanical-Hydrological Behaviour of Sparsely Fractured Rock: Implications for Nuclear Fuel Waste Disposal. *International Journal of Rock Mechanics and Mining Sciences and Geomechanics Abstracts*, 32:465–479, 1995.

[98] T. S. Nguyen, A. P. S. Selvadurai, and G. Armand. Modelling the FEBEX THM experiment using a state surface approach. *International Journal of Rock Mechanics and Mining Sciences*, 42:639–651, 2005.

[99] L. Nguyen-Tuan, C. Könke, V. Bettzieche, and T. Lahmer. Damage identification using inverse analysis in coupled thermo-hydro-mechanical problems applied to masonry dams. *International Journal for Numerical and Analytical Methods in Geomechanics*, 42(2):256–273, 2018.

[100] D. Nield and A. Bejan. *Convection in Porous Media*. Springery, Berlin, Germany, 2013.

[101] J. Noorishad and C.-F. Tsang. ROCMAS simulator; A thermohydromechanical computer code. In O. Stephansson, L. Jing, and C.-F. Tsang, editors, *Coupled Thermo-Hydro-Mechanical Processes of Fractured Media*, volume 79 of *Developments in Geotechnical Engineering*, pages 551–558. Elsevier, 1996.

[102] J. Noorishad, C. F. Tsang, and P. A. Witherspoon. Coupled thermal-hydraulic-mechanical phenomena in saturated fractured porous rocks: Numerical approach. *Journal of Geophysical Research: Solid Earth*, 89(B12):10365–10373, 1984.

[103] A. Norris. On the correspondence between poroelasticity and thermoelasticity. *Journal of Applied Physics*, 71(3):1138–1141, 1992.

[104] T. Nowak, H. Kunz, D. Dixon, W. Wang, U.-J. Görke, and O. Kolditz. Coupled 3-D thermo-hydro-mechanical analysis of geotechnological in situ tests. *International Journal of Rock Mechanics and Mining Sciences*, 48(1):1–15, 2011.

[105] A. Nur and J. D. Byerlee. An exact effective stress law for elastic deformation of rock with fluids. *Journal of Geophysical Research (1896-1977)*, 76(26):6414–6419, 1971.

[106] Y. Ohnishi and A. Kobayashi. Thames. In O. Stephansson, L. Jing, and C.-F. Tsang, editors, *Coupled Thermo-Hydro-Mechanical Processes of Fractured Media*, volume 79 of *Developments in Geotechnical Engineering*, pages 545–549. Elsevier, 1996.

[107] S. Olivella. *Nonisothermal Multiphase Flow of Brine and Gas through Saline Media*. PhD thesis, Universitat Politècnica de Catalunya, Departament d'Enginyeria del Terreny I Cartogràfica, June 1995.

[108] S. Olivella, J. Carrera, A. Gens, and E. E. Alonso. Nonisothermal Multiphase Flow of Brine and Gas Through Saline Media. *Transport in Porous Media*, 15:271–293, 1994.

[109] S. Olivella and A. Gens. Double structure THM analyses of heating test in a fractured tuff incorporating intrinsic permeability variations. *International Journal of Rock Mechanics and Mining Sciences*, 42:667–679, 2005.

[110] S. Olivella, A. Gens, J. Carrera, and E. E. Alonso. Numerical formulation for a simulator (CODE-BRIGHT) for the coupled analysis of saline media. *Engineering Computations*, 13:87–112, 1996.

[111] O. Ortega-Gelabert, S. Zlotnik, J. C. Afonso, and P. Díez. Fast Stokes Flow Simulations for Geophysical-Geodynamic Inverse Problems and Sensitivity Analyses Based On Reduced Order Modeling. *Journal of Geophysical Research: Solid Earth*, 125(3), 2020.

[112] V. V. Palciauskas and P. A. Domenico. Characterization of drained and undrained response of thermally loaded repository rocks. *Water Resources Research*, 18(2):281–290, 1982.

[113] P. Pan, J. Rutqvist, X.-T. Feng, and F. Yan. An Approach for Modeling Rock Discontinuous Mechanical Behavior Under Multiphase Fluid Flow Conditions. *Rock Mechanics and Rock Engineering*, 47, February 2014.

[114] P.-Z. Pan, J. Rutqvist, X.-T. Feng, and F. Yan. Modeling of caprock discontinuous fracturing during CO2 injection into a deep brine aquifer. *International Journal of Greenhouse Gas Control*, 19:559–575, 2013.

[115] S. Panday and M. Corapcioglu. Reservoir transport equations by compositional approach. *Transport in Porous Media*, 4:369–393, 1989.

[116] S. Pandey, A. Chaudhuri, and S. Kelkar. A coupled thermo-hydro-mechanical modeling of fracture aperture alteration and reservoir deformation during heat extraction from a geothermal reservoir. *Geothermics*, 65:17–31, 2017.

[117] N. M. Pinyol, E. E. Alonso, and S. Olivella. Rapid drawdown in slopes and embankments. *WATER RESOURCES RESEARCH*, 44, 2008.

[118] S. H. Prassetyo and M. Gutierrez. Effect of transient coupled hydro-mechanical response on the longitudinal displacement profile of deep tunnels in saturated ground. *Tunnelling and Underground Space Technology*, 75:11–20, 2018.

[119] W. E. Pratt and W. Johnson, D. Local Subsidence of the Goose Creek Oil Field. *The Journal of Geology*, 34(7):577–590, 1926.

[120] A. Pudewills. *Evaluation and improvement of the THM modelling capabilities for rock salt repositories*, pages 1362–1370. CIMNE, 2011.

[121] R. Pusch, G. Ramqvist, S. Knutsson, and T. Yang. The Role of Crystalline Rock for Disposal of High-Level Radioactive Waste (HLW). *Procedia Earth and Planetary Science*, 15:526–535, 2015. World Multidisciplinary Earth Sciences Symposium, WMESS 2015.

[122] M. Ramoni and G. Anagnostou. The Effect of Consolidation on TBM Shield Loading in Water-Bearing Squeezing Ground. *Rock Mechanics and Rock Engineering*, 44(1):63–68, 2011.

[123] C. A. Rautman and A. H. Treadway. Geologic uncertainty in a regulatory environment: An example from the potential Yucca Mountain nuclear waste repository site. *Environmental Geology and Water Sciences*, 18(3):171–184, 1991.

[124] J. R. Rice and M. P. Cleary. Some basic stress diffusion solutions for fluid-saturated elastic porous media with compressible constituents. *Reviews of Geophysics*, 14:227–241, 1976.

[125] B. Schrefler, L. Simoni, and E. Turska. Standard staggered and staggered Newton schemes in thermo-hydro-mechanical problems. *Computer Methods in Applied Mechanics and Engineering*, 144(1):93–109, 1997.

[126] B. A. Schrefler, R. Matteazzi, D. Gawin, and X. Wang. Two Parallel Computing Methods for Coupled Thermohydromechanical Problems. *Computer-Aided Civil and Infrastructure Engineering*, 15(3):176–188, 2000.

[127] L. Schuler, L. Chamoin, Z. Khatir, M. Bouarroudj Berkani, M. Ouhab, and N. Degrenne. A Reduced Model Based On Proper Generalized Decomposition for the Fast Analysis of Igbt Power Modules Lifetime. *Journal of Electronic Packaging, Transactions of the ASME*, February 2022.

[128] M. Sedighi, D. Bennet, S. Masum, and E. Johansson. Analysis of Temperature Data at the Olkiluoto, March 2014.

[129] A. Selvadurai and A. Suvorov. *Thermo-Poroelasticity and Geomechanics*. Cambridge University Press, 2017.

[130] A. P. S. Selvadurai. Multiphasic Approaches for Estimating THM Properties of Heterogeneous Rocks. In M. Barla, A. Di Donna, and D. Sterpi, editors, *Challenges and Innovations in Geomechanics*, pages 171–182, Cham, 2021. Springer International Publishing.

[131] A. P. S. Selvadurai, A. P. Suvorov, and P. A. Selvadurai. Thermo-hydro-mechanical processes in fractured rock formations during a glacial advance. *Geoscientific Model Development*, 8(7):2167–2185, 2015.

[132] P. Selvadurai and M. Najari. The thermo-hydro-mechanical behavior of the argillaceous Cobourg Limestone: THM Behavior of Rock. *Journal of Geophysical Research: Solid Earth*, 122, April 2017.

[133] P. Selvadurai, P. A. Selvadurai, and M. Nejati. A multi-phasic approach for estimating the Biot coefficient for Grimsel granite. *Solid Earth*, 10(6):2001–2014, 2019.

[134] A. Sibileau, F. Auricchio, S. Morganti, and P. Díez. Explicit parametric solutions of lattice structures with proper generalized decomposition (PGD): Applications to the design of 3D-printed architectured materials. *Computational Mechanics*, 62, October 2018.

[135] B. D. Solomon. Solving a Wicked Problem in Deep Time: Nuclear Waste Disposal. *Science and Engineering Ethics*, 27(2), 2021.

[136] F. Song, A. Rodriguez-Dono, and S. Olivella. Hydro-mechanical modelling and analysis of multi-stage tunnel excavations using a smoothed excavation method. *Computers and Geotechnics*, 135, 2021.

[137] F. Song, A. Rodriguez-Dono, S. Olivella, and A. Gens. Coupled solid-fluid response of deep tunnels excavated in saturated rock masses with a time-dependent plastic behaviour. *Applied Mathematical Modelling*, 100:508–535, 2021.

[138] P. N. Swift and E. J. Bonano. Geological Disposal of Nuclear Waste in Tuff: Yucca Mountain (USA). *Elements*, 12(4):263–268, August 2016.

[139] M. Sánchez, A. Gens, and S. Olivella. Effect of thermo-coupled processes on the behaviour of a clay barrier submitted to heating and hydration. *Anais da Academia Brasileira de Ciencias*, 82:153–68, March 2010.

[140] M. Sánchez, A. Gens, and S. Olivella. THM analysis of a large-scale heating test incorporating material fabric changes. *International Journal for Numerical and Analytical Methods in Geomechanics*, 36:391 – 421, March 2012.

[141] M. Sánchez, B. Pomaro, and A. Gens. Coupled THM analysis of a full-scale test for high-level nuclear waste and spent fuel disposal under actual repository conditions during 18 years of operation. *Géotechnique*, 73(5):418–438, 2023.

[142] K. Terzaghi. *Erdbaumechanik auf Bodenphysikalischen Grundlagen.* Franz Deuticke, Austria, 1925.

[143] C. V. Theis. The relation between the lowering of the Piezometric surface and the rate and duration of discharge of a well using ground-water storage. *Eos, Transactions American Geophysical Union*, 16(2):519–524, 1935.

[144] H. Thomas, Y. He, M. Sansom, and C. Li. On the development of a model of the thermo-mechanical-hydraulic behaviour of unsaturated soils. *Engineering Geology*, 41(1):197–218, 1996.

[145] H. R. Thomas, P. Cleall, Y.-C. Li, C. Harris, and M. Kern-Luetschg. Modelling of cryogenic processes in permafrost and seasonally frozen soils. *Géotechnique*, 59(3):173–184, 2009.

[146] H. R. Thomas and C. L. W. Li. Parallel Computing Solution of Coupled Flow Processes in Soil. *Journal of Computing in Civil Engineering*, 5(4):428–443, 1991.

[147] H. R. Thomas, P. J. Vardon, and Y.-C. Li. Coupled Thermo-Hydro-Chemo-Mechanical Modeling for Geoenvironmental Phenomena. In Y. Chen, L. Zhan, and X. Tang, editors, *Advances in Environmental Geotechnics*, pages 320–327, Berlin, Heidelberg, 2010. Springer Berlin Heidelberg.

[148] E. Toprak. THM modeling of deposition tunnel in Onkalo project, January 2013.

[149] E. Toprak. *Long term response of multi-barrier schemes for underground radioactive waste disposal*. PhD thesis, Universitat Politècnica de Catalunya, Civil and Environmental Department, May 2018.

[150] E. Toprak, S. Olivella, and X. Pintado. Coupled THM modelling of engineered barriers for the final disposal of spent nuclear fuel isolation. *Radioactive Waste Confinement: Clays in Natural and Engineered Barriers. Geological Society, London, Special Publications*, 2016.

[151] E. Toprak, S. Olivella, and X. Pintado. Modelling Engineered Barriers for Spent Nuclear Fuel Repository using a Double Structure Approach for Pellet based Components. *Environmental Geotechnics*, 7:1–70, 04 2018.

[152] M. N. Toprak, E. and S. Olivella. Thermo-Hydro-Mechanical Modeling of Buffer Synthesis Report, August 2013.

[153] S. Tourchi. *THM analysis of argillaceous rocks with application to nuclear waste underground storage*. PhD thesis, UPC, Departament d'Enginyeria Civil i Ambiental, December 2020.

[154] S. Tourchi, J. Vaunat, A. Gens, M.-N. Vu, and F. Bumbieler. Coupled THM analysis of long-term anisotropic convergence in the full-scale micro tunnel excavated in the Callovo-Oxfordian argillite. *VIII International Conference on Computational Methods for Coupled Problems in Science and Engineering*, 2019.

[155] C.-F. Tsang. Coupled hydromechanical-thermochemical processes in rock fractures. *Reviews of Geophysics*, 29(4):537–551, 1991.

[156] A. Verruijt. *Elastic Storage of Aquifers, in: Flow through Porous Media*, pages 331–376. Academic Press, New York, 01 1969.

[157] A. Verruijt. *Theory and Problems of Poroelasticity*. Delft University of Technology, Delft, The Netherlands, 2014.

[158] Vilarrasa, Víctor, Carrera, Jesùs, and Olivella, Sebastià. Two-phase flow effects on the CO_2 injection pressure evolution and implications for the caprock geomechanical stability. *E3S Web Conf.*, 9:04007, 2016.

[159] M. Villar, J. Garcia-Sineriz, I. Barcena, and A. Lloret. State of the bentonite barrier after five years operation of an in situ test simulating a high level radioactive waste repository. *Engineering Geology*, 80(3):175–198, 2005.

[160] M. V. Villar and A. Lloret. Dismantling of the first section of the FEBEX in situ test: THM laboratory tests on the bentonite blocks retrieved. *Physics and Chemistry of the Earth, Parts A/B/C*, 32(8):716–729, 2007. Clay in natural and engineered barriers for radioactive waste confinement - Part 2.

[161] M. V. Villar and A. Lloret. Influence of dry density and water content on the swelling of a compacted bentonite. *Applied Clay Science*, 39(1):38–49, 2008.

[162] H. F. Wang. *Theory of Linear Poroelasticity with Applications to Geomechanics and Hydrogeology*. Princeton University Press, Princeton, NJ, 2000.

[163] W. Wang and O. Kolditz. Object-oriented finite element analysis of thermo-hydro-mechanical (THM) problems in porous media. *International Journal for Numerical Methods in Engineering*, 69(1):162–201, 2007.

[164] W. Wang, G. Kosakowski, and O. Kolditz. A parallel finite element scheme for thermo-hydro-mechanical (THM) coupled problems in porous media. *Computers and Geosciences*, 35(8):1631–1641, 2009.

[165] X. Wang, , D. Gawin, and B. A. Schrefler. A parallel algorithm for thermo-hydro-mechanical analyses of deforming porous media. *Computational Mechanics*, 19(1):94–104, 1996.

[166] N. Watanabe, W. Wang, C. I.McDermott, T. Taniguchi, and O. Kolditz. Uncertainty analysis of thermo-hydro-mechanical coupled processes in heterogeneous porous media. *Computational Mechanics*, 45(4):263–280, 2009.

[167] P. A. Witherspoon. Geological problems in radioactive waste isolation - second worldwide review. 9 1996.

[168] W. Xi-cheng, G. Zeng-jie, and W. Hong-yu. An algebraic multigrid method for coupled thermo-hydro-mechanical problems. *Applied Mathematics and Mechanics*, 23(12):1464–1471, 2002.

[169] W. Xicheng and B. Schrefler. Fully coupled thermo-hydro-mechanics analysis by an algebraic multigrid method. *Engineering Computations*, 20:211–229, 03 2003.

[170] W. Xicheng and B. A. Schrefler. A multi-frontal parallel algorithm for coupled thermo-hydro-mechanical analysis of deforming porous media. *International Journal for Numerical Methods in Engineering*, 43(6):1069–1083, 1998.

[171] W.-M. Ye, Y.-G. Chen, B. Chen, Q. Wang, and J. Wang. Advances on the knowledge of the buffer/backfill properties of heavily-compacted GMZ bentonite. *Engineering Geology*, 116(1):12–20, 2010.

[172] M. T. Zandarín, L. Oldecop, and R. Pacheco. Stability of a tailing dam considering the hydro-mechanical behaviour of tailings and climate factor. *Unsaturated Soils: Advances in Geo-Engineering*, pages 925–931, 01 2008.

[173] A. Zareidarmiyan, H. Salarirad, V. Vilarrasa, S. De Simone, and S. Olivella. Geomechanical Response of Fractured Reservoirs. *Fluids*, 3(4), 2018.

[174] O. Zienkiewicz and R. Taylor. *The Finite Element - The Basis*, volume 1. Butterworth-Heinemann, 2000.

[175] S. Zlotnik, P. Díez, D. Modesto, and A. Huerta. Proper generalized decomposition of a geometrically parametrized heat problem with geophysical applications. *International Journal for Numerical Methods in Engineering*, 103, March 2015.